

August 2012

# The Neutron-Star Equation of State and Gravitational Waves from Compact Binaries

Benjamin David Lackey  
*University of Wisconsin-Milwaukee*

Follow this and additional works at: <https://dc.uwm.edu/etd>

 Part of the [Astrophysics and Astronomy Commons](#), and the [Physics Commons](#)

---

## Recommended Citation

Lackey, Benjamin David, "The Neutron-Star Equation of State and Gravitational Waves from Compact Binaries" (2012). *Theses and Dissertations*. 72.  
<https://dc.uwm.edu/etd/72>

This Dissertation is brought to you for free and open access by UWM Digital Commons. It has been accepted for inclusion in Theses and Dissertations by an authorized administrator of UWM Digital Commons. For more information, please contact [open-access@uwm.edu](mailto:open-access@uwm.edu).

**THE NEUTRON-STAR EQUATION OF STATE AND  
GRAVITATIONAL WAVES FROM COMPACT BINARIES**

By

**Benjamin D. Lackey**

A Dissertation Submitted in  
Partial Fulfillment of the  
Requirements for the Degree of

Doctor of Philosophy

in

Physics

at

The University of Wisconsin–Milwaukee

August 2012

**ABSTRACT**  
**THE NEUTRON-STAR EQUATION OF STATE AND  
GRAVITATIONAL WAVES FROM COMPACT BINARIES**

By  
**Benjamin D. Lackey**

The University of Wisconsin–Milwaukee, 2012  
Under the Supervision of Professor John L. Friedman

The equation of state (EOS) of matter above nuclear density is currently uncertain by almost an order of magnitude. Fortunately, neutron stars (NS) provide an ideal laboratory for studying high density matter. In order to systematize the study of the EOS from NS observations, we introduce a parametrized high-density EOS that accurately fits theoretical candidate EOSs. We then determine the ability of several recent and near-future electromagnetic observations to constrain the parameter space of our EOS. Recent observations include measurements of masses, gravitational redshift, and spin period, and we find that high mass observations are the most useful at constraining the EOS. Reliable simultaneous mass–radius measurements or mass–moment of inertia measurements in the near future, on the other hand, would provide a dramatically stronger constraint by requiring the allowed parameters to lie on a hypersurface of the full parameter space.

In addition to electromagnetic observations, binary neutron star (BNS) and black hole–neutron star (BHNS) coalescence events observed with gravitational-wave detectors offer the potential to dramatically improve our understanding of the EOS. Information about the EOS is encoded in the waveform through tidal interactions, and for BNS systems, the inspiral waveform depends on the EOS through a single parameter called the tidal deformability. Using recent numerical BHNS simulations we find that the entire BHNS inspiral–merger–ringdown waveform also depends on the EOS exclusively through the same tidal deformability parameter. Using these BNS and BHNS waveforms, we examine the ability of second generation detectors now in construction and planned third generation detectors to extract information about the EOS.

© Copyright 2012  
by  
**Benjamin D. Lackey**

*to*  
*Mom, Dad, and Randall*

# Contents

<b>Preface</b>	<b>viii</b>
<b>Acknowledgments</b>	<b>ix</b>
<b>List of Tables</b>	<b>x</b>
<b>List of Figures</b>	<b>xii</b>
<b>1 The equation of state and stellar structure</b>	<b>1</b>
1.1 Thermodynamic relations and the equation of state . . . . .	2
1.2 Evaluating mass, radius, and moment of inertia . . . . .	4
<b>2 Phenomenologically parametrized EOS</b>	<b>7</b>
2.1 Introduction . . . . .	7
2.2 Candidates . . . . .	10
2.3 Piecewise polytrope . . . . .	10
2.4 Fitting the candidate EOSs . . . . .	12
2.5 Astrophysical constraints on the parameter space . . . . .	18
2.5.1 Causality . . . . .	20
2.5.2 Maximum Mass . . . . .	21
2.5.3 Gravitational redshift . . . . .	24
2.5.4 Maximum Spin . . . . .	25
2.5.5 Moment of inertia or radius of a neutron star of known mass . . . . .	28
2.5.6 Combining constraints . . . . .	30
2.6 Discussion . . . . .	32
<b>3 Point-particle waveform approximations</b>	<b>35</b>
3.1 Description of a binary waveform . . . . .	35

3.2	Post-Newtonian approximation . . . . .	37
3.2.1	Energy and luminosity . . . . .	38
3.2.2	Orbital phase of the binary . . . . .	39
3.2.3	Stationary phase approximation . . . . .	41
3.3	Frequency-domain phenomenological waveforms . . . . .	42
3.4	Effective one body formalism . . . . .	44
3.4.1	Hamiltonian dynamics . . . . .	44
3.4.2	Radiation reaction . . . . .	46
3.4.3	Integrating the equations of motion . . . . .	48
3.4.4	Ringdown . . . . .	50
<b>4</b>	<b>Tidal interactions during binary inspiral</b>	<b>52</b>
4.1	Newtonian tidal interactions . . . . .	53
4.1.1	Gravitational potential, multipoles, and tidal fields . . . . .	53
4.1.2	Lagrangian and energy . . . . .	55
4.1.3	Tidal Corrections to the post-Newtonian waveform . . . . .	58
4.2	The tidal deformability for relativistic stars . . . . .	60
<b>5</b>	<b>Gravitational-wave data analysis</b>	<b>64</b>
5.1	Bayesian inference . . . . .	64
5.2	Statistical properties of the output of gravitational-wave detectors . . . . .	66
5.3	Detection . . . . .	68
5.4	Fisher matrix approximation . . . . .	69
5.5	Markov Chain Monte Carlo . . . . .	71
<b>6</b>	<b>Detectability of tidal parameters from the early inspiral of BNS systems</b>	<b>73</b>
6.1	Introduction and summary . . . . .	73
6.2	Love numbers and tidal deformabilities for candidate EOS . . . . .	75
6.3	Measuring effects on gravitational radiation . . . . .	79
6.4	Conclusion . . . . .	87
<b>7</b>	<b>Detectability of tidal parameters from nonspinning BHNS systems</b>	<b>88</b>
7.1	Introduction . . . . .	88
7.2	Parametrized EOS . . . . .	91
7.3	Numerical methods . . . . .	93
7.4	Description of waveforms . . . . .	94
7.5	Hybrid Waveform Construction . . . . .	98

7.5.1	Matching procedure . . . . .	101
7.5.2	Dependence on matching window . . . . .	102
7.6	Parameter estimation . . . . .	104
7.6.1	Broadband aLIGO and ET . . . . .	106
7.6.2	Narrowband aLIGO . . . . .	109
7.7	Discussion . . . . .	110
7.7.1	Results . . . . .	110
7.7.2	Remaining work . . . . .	111
<b>8</b>	<b>Detectability of tidal parameters from aligned-spin BHNS systems</b>	<b>114</b>
8.1	Introduction . . . . .	114
8.2	Simulations . . . . .	116
8.3	Hybrid inspiral-merger-ringdown waveforms . . . . .	120
8.4	Parameter estimation . . . . .	122
8.5	Phenomenological BHNS waveform . . . . .	125
8.5.1	Amplitude fit . . . . .	126
8.5.2	Phase fit . . . . .	127
8.6	Results . . . . .	128
8.7	Discussion . . . . .	129
	<b>Appendices</b>	<b>131</b>
<b>A</b>	<b>Analytic fits to tabulated EOS</b>	<b>131</b>
A.1	Low-density equation of state . . . . .	131
A.2	Comparison table . . . . .	131
<b>B</b>	<b>Accuracy of the tidal correction model</b>	<b>135</b>
<b>C</b>	<b>Numerically evaluating the Fisher matrix</b>	<b>140</b>
C.1	Finite differencing of $h(t; \theta)$ . . . . .	140
C.2	Finite differencing of amplitude and phase . . . . .	141
C.3	Finite differencing of Fourier transform . . . . .	142
C.4	Parameter spacing and numerical resolution . . . . .	143

# Preface

Chapter 2 is based on material from

“Constraints on a phenomenologically parameterized neutron-star equation of state.” Jocelyn S. Read, Benjamin D. Lackey, Benjamin J. Owen, John L. Friedman. *Phys. Rev. D* 79, 124032 (2009).

Chapter 6 is based on material from

“Tidal deformability of neutron stars with realistic equations of state and their gravitational wave signatures in binary inspiral.” Tanja Hinderer, Benjamin D. Lackey, Ryan N. Lang, Jocelyn S. Read. *Phys. Rev. D* 81, 123016 (2010).

Chapter 7 is based on material from

“Extracting equation of state parameters from black hole-neutron star mergers: Nonspinning black holes.” Benjamin D. Lackey, Koutarou Kyutoku, Masaru Shibata, Patrick R. Brady, John L. Friedman. *Phys. Rev. D* 85, 044061 (2012).

# Acknowledgments

Over the last six years I have received help from many people, and this work would not be possible without them. I would first like to thank my undergraduate advisor at Penn State, Ben Owen, for introducing me to gravitational physics, and for suggesting the project that eventually led to the phenomenological equation of state. In addition to carefully reading and editing this dissertation, I have received much help and advice over the years from my advisor John Friedman, and I sincerely thank him. I would also like to thank Jocelyn Read for many useful discussions, research ideas, and for helping me survive some of my most difficult grad school years. I thank Jolien Creighton and Patrick Brady who taught me most of what I know about data analysis. I would also like to thank Tanja Hinderer and Ryan Lang for an enjoyable collaboration on tidal interactions in binary neutron star systems. The last two chapters on black hole-neutron star systems were made possible by the hard work of Masaru Shibata and Koutarou Kyutoku who wrote the **SACRA** code used in the simulations, and I also thank them for happily running over two years of simulations for this project. Evan Ochsner, Chris Pankow, and Richard O’Shaughnessy have also provided significant help in my struggle to learn the LIGO Algorithm Library, and I have enjoyed many useful discussions with Marc Favata on the measurability of tidal parameters. Finally, I thank the Northwestern parameter estimation group, and in particular Vivien Raymond, Ben Farr, Will Farr, and Vicky Kalogera, for their hospitality and for modifying and helping me run their MCMC code.

# List of Tables

1	Average residuals from fitting candidate EOSs . . . . .	14
2	Properties of a $1.4 M_{\odot}$ neutron star for 18 candidate EOS . . . . .	79
3	The rms measurement error in various binary parameters . . . . .	85
4	Neutron star properties for the 21 EOS used in the simulations . . . . .	92
5	Data for the 30 BHNS simulations . . . . .	95
6	Data for the 90 aligned-spin BHNS simulations . . . . .	118
7	Analytic representation of the SLy EOS below nuclear density . . . . .	131
8	Comparison of candidate EOSs and their best fits . . . . .	133

# List of Figures

1	Pressure versus rest mass density for candidate EOS . . . . .	11
2	Parametrized EOS . . . . .	15
3	Optimal dividing densities for subsets of candidate EOS . . . . .	16
4	Best-fit parameters for candidate EOSs . . . . .	17
5	Region in parameter space that allows two stable NS branches . . . . .	19
6	Causality constraint for any density . . . . .	21
7	Causality constraint for densities up to central density of maximum mass NS	22
8	Maximum mass constraint . . . . .	23
9	Gravitational redshift constraint . . . . .	25
10	Constraint from 716 Hz NS spin . . . . .	27
11	Constraint from very high NS spin . . . . .	27
12	Joint mass–moment of inertia constraint . . . . .	29
13	Joint mass–radius constraint . . . . .	30
14	Joint constraint imposed by causality and maximum mass . . . . .	31
15	Joint constraint imposed by causality, maximum mass, and moment of inertia	31
16	Allowed values of $\Gamma_2$ and $\Gamma_3$ . . . . .	32
17	Allowed range of $p_1$ as a function of the moment of inertia . . . . .	33
18	Strong-field and weak-field regions of a compact binary . . . . .	53
19	Sky location and polarization angle of a gravitational wave . . . . .	67
20	Love number for candidate EOS . . . . .	76
21	Tidal deformability and its measurability for aLIGO and ET . . . . .	78

22	Joint mass–tidal deformability constraint . . . . .	80
23	Tidal deformability as a function of chirp mass and symmetric mass ratio . . . . .	81
24	Comparison of tidal interactions to high order PN effects . . . . .	82
25	Tidal deformability and radius contours for 2-parameter EOS . . . . .	93
26	Sample BHNS waveforms . . . . .	96
27	Amplitude of BHNS waveforms . . . . .	97
28	Phase of BHNS waveforms . . . . .	98
29	Amplitude of Fourier transformed BHNS waveforms . . . . .	99
30	Phase of Fourier transformed BHNS waveforms . . . . .	100
31	Dependence of hybrid waveform on matching window . . . . .	103
32	Matching eccentric waveform to zero eccentricity waveform . . . . .	104
33	PSD for several detector configurations . . . . .	106
34	Error ellipses for broadband aLIGO . . . . .	107
35	Error ellipses for ET-D . . . . .	107
36	$1\text{-}\sigma$ uncertainty for broadband aLIGO . . . . .	108
37	$1\text{-}\sigma$ uncertainty for ET-D . . . . .	109
38	$1\text{-}\sigma$ uncertainty for narrowband aLIGO . . . . .	110
39	Dependence of BHNS waveform on EOS . . . . .	119
40	Dependence of BHNS waveform on mass ratio . . . . .	119
41	Dependence of BHNS waveform on BH spin . . . . .	120
42	Joining numerical waveform to inspiral waveform in frequency domain . . . . .	123
43	Uncorrelated uncertainty in $\Lambda$ for merger-ringdown . . . . .	124
44	Uncorrelated uncertainty in $\Lambda$ for inspiral-merger-ringdown . . . . .	125
45	Uncertainty in $\Lambda$ for broadband aLIGO . . . . .	129
46	Uncertainty in $\Lambda$ for ET-D . . . . .	130

## Chapter 1

# The equation of state and stellar structure

At the most fundamental level, the nature of matter near nuclear density ( $2.8 \times 10^{14}$  g/cm<sup>3</sup>) and above is described in terms of an N-body system of quarks and leptons interacting through electromagnetism and the strong and weak interactions. This computationally intractable problem can, however, be simplified because up to a few times nuclear density, quarks are in the form of nucleons (e.g. neutrons, protons, and hyperons) and mesons (e.g. pions and kaons) interacting through nuclear interactions. As the density increases, it becomes energetically favorable to have an increasing fraction of strange quarks, first in hyperons or mesons, then in the form of free quarks when these composite particles eventually dissolve at several times nuclear density. A wide range of approximations exist for the interactions of these exotic particles, and the free parameters can be calibrated to experimental data from, for example, heavy ion collisions. However, there remains much uncertainty in extrapolating to bulk nuclear matter.

Unlike the matter in terrestrial experiments, the cores of neutron stars (NS), consisting of bulk nuclear matter in its ground state with densities that can exceed  $10^{15}$  g/cm<sup>3</sup>, are an ideal subject for understanding ground-state matter as it is described through the equation of state (EOS). This dissertation will focus on several methods for extracting information about the EOS from electromagnetic observations of neutron stars as well as gravitational-wave observations of neutron stars in coalescing compact binary systems, including binary neutron star (BNS) and black hole-neutron star (BHNS) systems.

We will begin in this chapter by discussing several thermodynamic quantities related to the EOS, and then describe how the EOS is related to observable properties of a neutron star through the relativistic stellar structure equations. In the next chapter, we will discuss

a parametrized phenomenological model for the EOS and how a wide range of observations can be used to constrain the parameters of this model. Chapter 3 will focus on point-particle interactions in coalescing binaries, and Chapter 4 will focus on tidal interactions in binaries that contain at least one neutron star. Chapter 5 will then discuss how the parameters of a binary inspiral can be extracted with gravitational-wave detectors. In Chapter 6, we will examine the detectability of EOS information in BNS inspirals through a quantity known as the tidal deformability  $\lambda$ . Finally, in the last two chapters we will examine the EOS information that can be extracted from BHNS inspiral, merger, and ringdown for systems with both nonspinning (Chapter 7) and aligned-spin (Chapter 8) black holes.

*Conventions:* Unless otherwise stated, we set  $G = c = 1$ .

## 1.1 Thermodynamic relations and the equation of state

For the applications in this dissertation, nuclear reactions occur on a timescale much smaller than changes in the neutron-star configuration, and so neutron-star matter is well described by a perfect fluid in equilibrium. The first law of thermodynamics for a fluid element containing  $N$  baryons states that the total energy  $E$ , including the rest-mass energy of the fluid element, is [1]

$$dE = -pdV + TdS + \mu dN. \quad (1.1)$$

Here,  $p$ ,  $V$ ,  $T$ ,  $S$ , and  $\mu$ , are the pressure, volume, temperature, entropy, and baryon chemical potential. The baryon chemical potential is defined as the increase in energy when a baryon is added to the fluid element, and this includes the energy needed to, for example, add other particles to conserve charge.

We can remove the last term in Eq. (1.1) by introducing the Gibbs free energy  $G = E + pV - TS$ , and using the relation, derived in Ref. [2],

$$G = E + pV - TS = \mu N. \quad (1.2)$$

In terms of the rest mass of the fluid element  $M_0$  and the specific Gibbs free energy  $g = G/M_0 = \mu/m_B$ , the last term in Eq. (1.1) becomes

$$\mu dN = \frac{\mu}{m_B} dM_0 = g dM_0, \quad (1.3)$$

where  $m_B = 1.66 \times 10^{-24}$  g is the baryon rest mass. Because we will consider a fluid element that adjusts so that the baryon number  $N$  is constant, the rest mass is conserved as well, and this term is therefore zero [3].

We will find it useful to rewrite the first law of thermodynamics in terms of only intensive quantities. We will use baryon number density  $n = N/V$ , rest mass density  $\rho = M_0/V = m_B n$ , energy density  $\epsilon = E/V$ , and specific entropy  $s = S/M_0$ . The first law becomes

$$d\frac{\epsilon}{\rho} = -pd\frac{1}{\rho} + Tds, \quad (1.4)$$

or equivalently

$$d\epsilon = hd\rho + \rho Tds, \quad (1.5)$$

where the specific enthalpy  $h$  is

$$h = \frac{E + pV}{M_0} = \frac{\epsilon + p}{\rho}. \quad (1.6)$$

In addition to the first law, the various thermodynamic quantities are related by an equation of state

$$\epsilon = \epsilon(\rho, s), \quad p = p(\rho, s). \quad (1.7)$$

For the neutron stars considered in this dissertation, the temperature will be far below the Fermi temperature, and thus we will only need to consider the isentropic one-parameter cold EOS

$$\epsilon = \epsilon(\rho), \quad p = p(\rho). \quad (1.8)$$

The above two expressions in Eq. (1.8) are not independent because the quantities  $\rho$ ,  $\epsilon$ , and  $p$  are related by the first law with  $ds = 0$ . We thus only need to specify a relation between two of the three quantities to get the third quantity using one of the following relations

$$p = \rho^2 \frac{d(\epsilon/\rho)}{d\rho}, \quad \frac{\epsilon}{\rho} = \frac{\epsilon_0}{\rho_0} + \int_{\rho_0}^{\rho} \frac{p}{\rho'^2} d\rho', \quad \rho = \rho_0 \exp\left(\int_{\epsilon_0}^{\epsilon} \frac{d\epsilon'}{\epsilon' + p}\right), \quad (1.9)$$

where  $\epsilon_0$  is the energy density at some rest-mass density  $\rho_0$ . At the surface of the star defined by  $p \rightarrow 0$ ,  $\epsilon_0 \rightarrow 0$  and  $\rho_0 \rightarrow 0$  for a standard EOS, and the ratio  $\epsilon_0/\rho_0 \rightarrow 1$ . Also, if the surface density is used for  $\rho_0$ , then the last expression in Eq. (1.9) is undefined.

In the following chapters we will find it useful in solving stellar structure equations to define two dimensionless, enthalpy-like quantities. The first quantity is the pseudo-enthalpy  $H$  defined by [4, 5]

$$dH = d \ln h = \frac{dp}{\epsilon + p}, \quad (1.10)$$

and therefore

$$h = e^H, \quad H = \int_0^p \frac{dp'}{\epsilon + p'}. \quad (1.11)$$

The second quantity  $\eta$  used in Ref. [5], which we will call the Newtonian specific enthalpy, is defined in terms of the Newtonian energy  $E_{\text{Newt}} = E - M_0$

$$\eta = \frac{E_{\text{Newt}} + pV}{M_0} = h - 1 = e^H - 1. \quad (1.12)$$

The stiffness of an EOS is often defined in terms of the polytropic exponent. For highly degenerate matter, we distinguish between two types of polytropic exponents,  $\Gamma$  and  $\gamma$ , defined by

$$\Gamma = \frac{d \ln p}{d \ln \rho}, \quad \gamma = \frac{d \ln p}{d \ln \epsilon}. \quad (1.13)$$

We note that for a one-parameter EOS with constant entropy,  $\Gamma$  is the adiabatic index. The two quantities can be related to each other using the first law of thermodynamics

$$\Gamma = \frac{\epsilon + p}{p} \frac{dp}{d\epsilon} = \frac{\epsilon + p}{\epsilon} \gamma. \quad (1.14)$$

We define two types of polytropic EOS

$$p = K_\rho \rho^\Gamma, \quad p = K_\epsilon \epsilon^\gamma, \quad (1.15)$$

where  $K_\rho$  and  $K_\epsilon$  are constants. We note that the first type of polytrope is used far more often in the literature because it is more closely associated with the underlying microphysics. For example, a nonrelativistic degenerate Fermi gas has an EOS that scales as  $p \propto \rho^{5/3}$ , and for a highly relativistic degenerate Fermi gas,  $p \propto \rho^{4/3}$  [1].

Equations of state must satisfy the following two conditions. The first, thermodynamic stability, requires the EOS be monotonic ( $dp/d\rho \geq 0$  and  $dp/d\epsilon \geq 0$ ), and therefore the adiabatic indices  $\Gamma$  and  $\gamma$  must be positive. The second, causality, requires the speed of sound  $v_s$  be less than the speed of light

$$v_s = \sqrt{\frac{dp}{d\epsilon}} \leq 1. \quad (1.16)$$

In terms of the polytropic exponents

$$v_s = \sqrt{\frac{p\Gamma}{\epsilon + p}} = \sqrt{\frac{p\gamma}{\epsilon}}, \quad (1.17)$$

and therefore in the limit of very high density, where the majority of the energy density comes from pressure, the EOS is causal only when  $\Gamma \leq 2$  and  $\gamma \leq 1$ .

## 1.2 Evaluating mass, radius, and moment of inertia

The moment of inertia of a rotating star is the ratio  $I = J/\Omega$ , with  $J$  the asymptotically defined angular momentum. In finding the moment of inertia of spherical models, we use

Hartle's slow-rotation equations [6], adapted to piecewise polytropes in a way we describe below. The metric of a slowly rotating star has, to order  $\Omega$ , the form

$$ds^2 = -e^{2\Phi(r)} dt^2 + e^{2\lambda(r)} dr^2 - 2\omega(r)r^2 \sin^2 \theta d\phi dt + r^2 d\theta^2 + r^2 \sin^2 \theta d\phi^2, \quad (1.18)$$

where  $\Phi$  and  $\lambda$  are the metric functions of the spherical star, given by

$$e^{2\lambda(r)} = \left(1 - \frac{2m(r)}{r}\right)^{-1}, \quad (1.19)$$

$$\frac{d\Phi}{dr} = -\frac{1}{\epsilon + p} \frac{dp}{dr}, \quad (1.20)$$

$$\frac{dp}{dr} = -(\epsilon + p) \frac{m + 4\pi r^3 p}{r(r - 2m)}, \quad (1.21)$$

$$\frac{dm}{dr} = 4\pi r^2 \epsilon. \quad (1.22)$$

The frame-dragging  $\omega(r)$  is obtained from the  $t\phi$  component of the Einstein equation in the form

$$\frac{1}{r^4} \frac{d}{dr} \left( r^4 j \frac{d\bar{\omega}}{dr} \right) + \frac{4}{r} \frac{dj}{dr} \bar{\omega} = 0, \quad (1.23)$$

where  $\bar{\omega} = \Omega - \omega$  is the angular velocity of the star measured by a zero-angular-momentum observer and

$$j(r) = e^{-\Phi} \left(1 - \frac{2m}{r}\right)^{1/2}. \quad (1.24)$$

The angular momentum is obtained from  $\omega$ , which has outside the star the form  $\omega = 2J/r^3$ .

In adapting these equations, we roughly follow Lindblom [4], replacing  $r$  as a radial variable by a generalization  $\eta := h - 1$  of the Newtonian enthalpy. Because  $\eta$  is monotonic in  $r$ , one can integrate outward from its central value to the surface, where  $\eta = 0$ .

This replacement exploits the first integral  $he^\Phi = \sqrt{1 - 2M/R}$  of the equation of hydrostatic equilibrium to eliminate the differential equation (1.20) for  $\Phi$ ; and the enthalpy, unlike  $\epsilon$  and  $p$ , is smooth at the surface for a polytropic EOS. Eqs. (1.21–1.23) are then equivalent to the first-order set

$$\frac{dr}{d\eta} = -\frac{r(r - 2m)}{m + 4\pi r^3 p(\eta)} \frac{1}{\eta + 1} \quad (1.25)$$

$$\frac{dm}{d\eta} = 4\pi r^2 \epsilon(\eta) \frac{dr}{d\eta} \quad (1.26)$$

$$\frac{d\bar{\omega}}{d\eta} = \alpha \frac{dr}{d\eta} \quad (1.27)$$

$$\frac{d\alpha}{d\eta} = \left[ -\frac{4\alpha}{r} + \frac{4\pi(\epsilon + p)(r\alpha + 4\bar{\omega})}{1 - 2m/r} \right] \frac{dr}{d\eta} \quad (1.28)$$

where  $\alpha := d\bar{\omega}/dr$ .

The integration to find the mass, radius, and moment of inertia for a star with given central value  $\eta = \eta_c$  proceeds as follows: Use the initial conditions  $r(\eta_c) = m(\eta_c) = \alpha(\eta_c) = 0$  and *arbitrarily* choose a central value  $\bar{\omega}_0$  of  $\bar{\omega}$ . Integrate to the surface where  $\eta = 0$ , to obtain the radius  $R = r(\eta = 0)$  and mass  $M = m(\eta = 0)$ . The angular momentum  $J$  is found from the radial derivative of the equation

$$\bar{\omega} = \Omega - \frac{2J}{r^3}, \quad (1.29)$$

evaluated at  $r = R$ , namely

$$J = \frac{1}{6}R^4\alpha(R), \quad (1.30)$$

and  $\Omega$  is then given by

$$\Omega = \bar{\omega}(R) + \frac{2J}{R^3}. \quad (1.31)$$

These values of  $\Omega$  and  $J$  are each proportional to the arbitrarily chosen  $\bar{\omega}_0$ , implying that the moment of inertia  $J/\Omega$  is independent of  $\bar{\omega}_0$ .

## Chapter 2

# Phenomenologically parametrized EOS

### 2.1 Introduction

Because the temperature of neutron stars is far below the Fermi energy of their constituent particles, neutron-star matter is accurately described by the one-parameter equation of state (EOS) that governs cold matter above nuclear density. The uncertainty in that EOS, however, is notoriously large, with the pressure  $p$  as a function of baryon mass density  $\rho$  uncertain above nuclear density by as much as an order of magnitude. The phase of the matter in the core of a neutron star is similarly uncertain: Current candidates for the EOS include non-relativistic and relativistic mean-field models; models for which neutron-star cores are dominated by nucleons, by hyperons, by pion or kaon condensates, and by strange quark matter (free up, down, and strange quarks); and one cannot yet rule out the possibility that the ground state of cold matter at zero pressure might be strange quark matter and that the term “neutron star” is a misnomer for strange quark stars.

The correspondingly large number of fundamental parameters needed to accommodate the models’ Lagrangians has meant that studies of astrophysical constraints (see, for example, [7, 8, 9, 10, 11] and references therein) present constraints by dividing the EOS candidates into an allowed and a ruled-out list. A more systematic study, in which astrophysical constraints are described as constraints on the parameter space of a parametrized EOS, can be effective only if the number of parameters is smaller than the number of neutron-star properties that have been measured or will have been measured in the next several years. At the same time, the number of parameters must be large enough to accurately approximate the EOS candidates.

A principal aim of this chapter is to show that, if one uses phenomenological rather than fundamental parameters, one can obtain a parametrized EOS that meets these conditions. We exhibit a parametrized EOS, based on specifying the stiffness of the star in three density intervals, characterized by the adiabatic index  $\Gamma = d \log P / d \log \rho$ . A fourth parameter translates the  $p(\rho)$  curve up or down, adding a constant pressure—equivalently fixing the pressure at the endpoint of the first density interval. Finally, the EOS is matched below nuclear density to the (presumed known) low-density EOS. An EOS for which  $\Gamma$  is constant is a polytrope, and the parametrized EOS is then piecewise polytropic. A similar piecewise-polytropic EOS was previously considered by Vuille and Ipson [12]; and, with different motivation, several other authors [13, 14, 5, 15] have used piecewise polytropes to approximate neutron-star EOS candidates. In contrast to this previous work, we use a small number of parameters chosen to fit a wide variety of fundamental EOSs, and we systematically explore a variety of astrophysical constraints. Like most of the previous work, we aim to model equations of state containing nuclear matter (possibly with various phase transitions) rather than pure quark stars, whose EOS is predicted to be substantially different.

As we have noted, enough uncertainty remains in the pressure at nuclear density, that one cannot simply match to a fiducial pressure at  $\rho_{\text{nuc}}$ . Instead of taking as one parameter the pressure at a fiducial density, however, one could match to the pressure of the known subnuclear EOS at, say,  $0.1 \rho_{\text{nuc}}$  and then use as one parameter a value of  $\Gamma_0$  for the interval between  $0.1 \rho_{\text{nuc}}$  and  $\rho_{\text{nuc}}$ . Neutron-star observables are insensitive to the EOS below  $\rho_{\text{nuc}}$ , because the fraction of mass at low density is small. But the new parameter  $\Gamma_0$  would indirectly affect observables by changing the value of the pressure at and above nuclear density, for fixed values of the remaining  $\Gamma_i$ . By choosing instead the pressure at a fixed density  $\rho_1 > \rho_{\text{nuc}}$ , we obtain a parameter more directly connected to physical observables. In particular, as Lattimer and Prakash [8] have pointed out, neutron-star radii are closely tied to the pressure somewhat above nuclear density, and the choice  $p_1 = p(\rho_1)$  is recommended by that relation.

In general, to specify a piecewise polytropic EOS with three density intervals above nuclear density, one needs six parameters: two dividing densities, three adiabatic indices  $\Gamma_i$ , and a value of the pressure at an endpoint of one of the intervals. Remarkably, however, we find (in Sec. 2.4) that the error in fitting the collection of EOS candidates has a clear minimum for a particular choice of dividing densities. With that choice, the parametrized EOS has three free parameters,  $\Gamma_1, \Gamma_2$  and  $p_1$ , for densities below  $10^{15} \text{ g/cm}^3$  (the density range most relevant for masses  $\sim 1.4 M_\odot$ ), and four free parameters (an additional  $\Gamma_3$ ) for

densities between  $10^{15}$  g/cm<sup>3</sup> and the central density of the maximum mass star for each EOS.

With the parameterization in hand, we examine in Sect. 2.5 astrophysical constraints on the EOS parameter space beyond the radius- $p_1$  relation found by Lattimer and Prakash [8]. Our emphasis in this first study is on present and very near-future constraints: those associated with the largest observed neutron-star mass and spin, with a possible observation (as yet unrepeated) of neutron-star redshift, with a possible simultaneous measurement of mass and radius, and with the expected future measurement of the moment of inertia of a neutron star with known mass. (We do not consider other observables, such as those associated with glitches and cooling, which depend not only on the EOS but also on dynamics, transport coefficients, and thermodynamic derivatives. The latter quantities are generally much more uncertain than the EOS and related observables such as the stellar radius, and are always more model dependent.) Ref. [16] investigates constraints obtainable with gravitational-wave observations in a few years.

The constraints associated with the largest observed mass, spin, and redshift have a similar form, each restricting the parameter space to one side of a surface: For example, if we take the largest observed mass to be  $1.93 M_\odot$ , then the allowed parameters correspond to EOSs whose maximum mass is at least  $1.93 M_\odot$ . We can regard  $M_{\max}$  as a function on the 4-dimensional EOS parameter space. The subspace of EOSs for which  $M_{\max} = 1.93 M_\odot$  is then described by a 3-dimensional surface, and constraint is a restriction to the high-mass side of the surface. Similarly, the observation of a 716 Hz pulsar restricts the EOS parameter space to one side of a surface that describes EOSs for which the maximum spin is 716 Hz. Thus we can produce model-independent extended versions of the multidimensional constraints seen in [17].

The potential simultaneous observation of two properties of a single neutron star (for example, moment of inertia and mass) would yield a significantly stronger constraint: It would restrict the parameter space not to one side of a surface but to the surface itself. And a subsequent observation of two different parameters for a different neutron star would then restrict one to the intersection of two surfaces. We exhibit the result of simultaneous observations of mass and moment of inertia (expected within the next decade for one member of the binary pulsar J0737-3039 [18, 19]) and of mass and radius.

*Conventions:* We use cgs units, denoting rest-mass density by  $\rho$ , and (energy density)/ $c^2$  by  $\epsilon$ . We define rest-mass density as  $\rho = m_B n$ , where  $m_B = 1.66 \times 10^{-24}$  g and  $n$  is the baryon number density. In Sec. 2.3, however, we set  $c = 1$  to simplify the equations and add a footnote on restoring  $c$ .

## 2.2 Candidates

A test of how well a parametrized EOS can approximate the true EOS of cold matter at high density is how well it approximates candidate EOSs. We consider a wide array of candidate EOSs, covering many different generation methods and potential species. Because the parametrized EOS is intended to distinguish the parts of parameter space allowed and ruled out by present and future observations, the collection includes some EOSs that no longer satisfy known observational constraints. Many of the candidate EOSs were considered in Refs. [8, 19, 17]; and we call them by the names used in those papers.

For plain  $npe\mu$  nuclear matter, we include:

- Two potential-method EOSs (PAL6 [20] and SLy [21]);
- eight variational-method EOSs (AP1-4 [22], FPS [23], and WFF1-3 [24]);
- one nonrelativistic (BBB2 [25]) and three relativistic (BPAL12 [26], ENG [7] and MPA1 [27]) Brueckner-Hartree-Fock EOSs; and
- three relativistic mean field theory EOSs (MS1-2 and one we call MS1b, which is identical to MS1 except with a low symmetry energy of 25 MeV [28]).

We also consider models with hyperons, pion and kaon condensates, and quarks, and will collectively refer to these EOSs as  $K/\pi/H/q$  models.

- One neutron-only EOS with pion condensates (PS [29]);
- two relativistic mean field theory EOSs with kaons (GS1-2 [30]);
- one effective potential EOS including hyperons (BGN1H1 [31]); eight relativistic mean field theory EOSs with hyperons (GNH3 [32] and seven variants H1-7 [17]; one relativistic mean field theory EOS with hyperons and quarks (PCL2 [33]); and
- four hybrid EOSs with mixed APR nuclear matter and colour-flavor-locked quark matter (ALF1-4 with transition density  $\rho_c$  and interaction parameter  $c$  given by  $\rho_c = 2n_0, c = 0$ ;  $\rho_c = 3n_0, c = 0.3$ ;  $\rho_c = 3n_0, c = 0.0$ ; and  $\rho_c = 4.5n_0, c = 0.3$  respectively [34]).

The tables are plotted in Fig. 1 to give an idea of the range of EOSs considered for this parameterization.

## 2.3 Piecewise polytrope

A polytropic EOS has the form,

$$p(\rho) = K\rho^\Gamma, \tag{2.1}$$

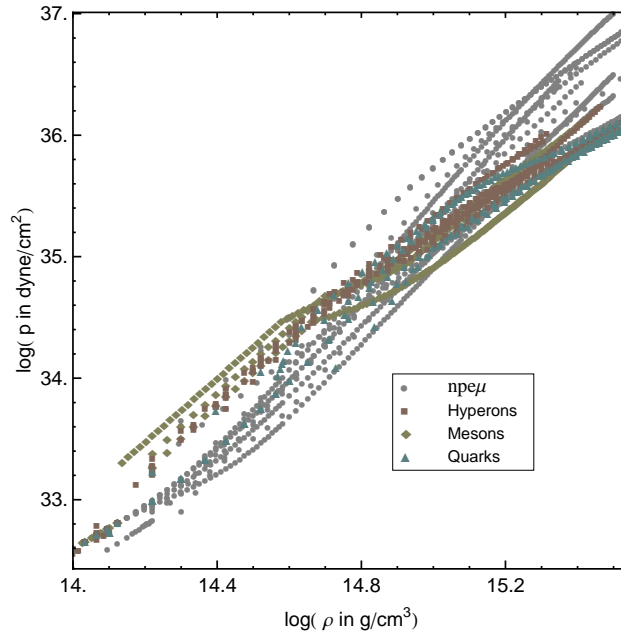


Figure 1 : Pressure versus rest mass density for the set of candidate EOS tables considered in the parametrization.

with  $\rho$  the rest-mass density and  $\Gamma$  the adiabatic index, and with energy density  $\epsilon$  fixed by the first law of thermodynamics,<sup>1</sup>  $d\frac{\epsilon}{\rho} = -p d\frac{1}{\rho}$ . For  $p$  of the form (2.1), the first law has the immediate integral

$$\frac{\epsilon}{\rho} = (1 + a) + \frac{1}{\Gamma - 1} K \rho^{\Gamma-1}, \quad (2.2)$$

where  $a$  is a constant; and the requirement  $\lim_{\rho \rightarrow 0} \epsilon/\rho = 1$  implies  $a = 0$  and the standard relation  $\epsilon = \rho + \frac{1}{\Gamma - 1} p$ .

The parametrized EOSs we consider are piecewise polytropes above a density  $\rho_0$ , satisfying Eqs. (2.1) and (2.2) on a sequence of density intervals, each with its own  $K_i$  and  $\Gamma_i$ : An EOS is piecewise polytropic for  $\rho \geq \rho_0$  if, for a set of dividing densities  $\rho_0 < \rho_1 < \rho_2 < \dots$ , the pressure and energy density are everywhere continuous and satisfy

$$p(\rho) = K_i \rho^{\Gamma_i}, \quad d\frac{\epsilon}{\rho} = -p d\frac{1}{\rho}, \quad \rho_{i-1} \leq \rho \leq \rho_i. \quad (2.3)$$

Then, for  $\Gamma \neq 1$ ,

$$\epsilon(\rho) = (1 + a_i)\rho + \frac{K_i}{\Gamma_i - 1} \rho^{\Gamma_i}, \quad (2.4)$$

<sup>1</sup>In this section, for simplicity of notation,  $c = 1$ . To rewrite the equations in cgs units, replace  $p$  and  $K$  in each occurrence by  $p/c^2$  and  $K/c^2$ . Both  $\epsilon$  and  $\rho$  have units  $\text{g}/\text{cm}^3$ .

with  $a_i = \frac{\epsilon(\rho_{i-1})}{\rho_{i-1}} - 1 - \frac{K_i}{\Gamma_i - 1} \rho_{i-1}^{\Gamma_i-1}$ .

The specific enthalpy<sup>2</sup>  $h := (\epsilon + p)/\rho$ , sound velocity  $v_s = \sqrt{dp/d\epsilon}$ , and internal energy  $e := \epsilon/\rho - 1$ , are given in each density interval by

$$h(\rho) = 1 + a_i + \frac{\Gamma_i}{\Gamma_i - 1} K_i \rho^{\Gamma_i-1}, \quad (2.5)$$

$$v_s(\rho) = \sqrt{\frac{\Gamma_i p}{\epsilon + p}}, \quad (2.6)$$

$$e(\rho) = a_i + \frac{K_i}{\Gamma_i - 1} \rho^{\Gamma_i-1}. \quad (2.7)$$

Each piece of a piecewise polytropic EOS is specified by three parameters: the initial density, the coefficient  $K_i$ , and the adiabatic index  $\Gamma_i$ . However, when the EOS at lower density has already been specified up to the chosen  $\rho_i$ , continuity of pressure determines the value of  $K_{i+1}$ :

$$K_{i+1} = \frac{p(\rho_i)}{\rho_i^{\Gamma_{i+1}}}. \quad (2.8)$$

Thus each additional region requires only two additional parameters,  $\rho_i$  and  $\Gamma_{i+1}$ . Furthermore, if the initial density of an interval is chosen to be a fixed value for the parameterization, specifying the EOS on the density interval requires only a single additional parameter.

## 2.4 Fitting the candidate EOSs

To fit the true neutron-star EOS, we must ensure that a wide variety of candidate EOSs are well fit by some set of parameter values of our parametrized EOS. In this section we describe the fit we use and the results of that fit.

There is general agreement on the low-density EOS for cold matter, and we adopt the version (SLy) given by Douchin and Haensel [21]. Substituting an alternative low-density EOS from, for example, Negele and Vautherin [35], alters by only a few percent the observables we consider in examining astrophysical constraints, both because of the rough agreement among the candidate EOSs and because the low density crust contributes little to the mass, moment of inertia, or radius of the star.

Each choice of a piecewise polytropic EOS above nuclear density is matched to this low-density EOS as follows: The lowest-density piece of the piecewise polytropic  $p(\rho)$  curve is extended to lower densities until it intersects the low-density EOS, and the low-density EOS

---

<sup>2</sup>A note on terminology: When the entropy vanishes, the specific enthalpy,  $h = (\epsilon + p)/\rho$ , and Gibbs free energy,  $g = (\epsilon + p)/\rho - Ts$ , coincide. For nonzero entropy, it is the term  $gdM_0 = \mu dN$  that appears in the first law of thermodynamics, where  $\mu = g/m_B$  is the chemical potential.

is used at densities below the intersection point. This matching method yields a monotonically increasing  $p = p(\rho)$  without introducing additional parameters. It omits EOSs with values of  $p_1$  and  $\Gamma_1$  that are incompatible, i.e. for which the slope of the  $\log p$  vs  $\log \rho$  curve is too shallow to reach the pressure  $p_1$  from the low-density part of the EOS. However it still accommodates a much larger region of parameter space than that spanned by the candidate EOSs. (The precise choice of matching algorithm has little influence on the final fit for the reasons given in the previous paragraph.)

The accuracy with which a piecewise polytrope  $\{\rho_i, K_i, \Gamma_i\}$ , approximates a candidate EOS is measured by the rms residual of the fit to  $m$  tabulated points  $(\rho_j, p_j)$ :

$$\sqrt{\frac{1}{m} \sum_i \sum_{\rho_i < \rho_j \leq \rho_{i+1}} \left[ \log \left( \frac{p_j}{K_i \rho_j^{\Gamma_i}} \right) \right]^2}. \quad (2.9)$$

In each case, we compute the residual only up to  $\rho_{\max}$ , the central density of the maximum mass nonrotating model based on the candidate EOS. Because astrophysical observations can depend on the high-density EOS only up to the value of  $\rho_{\max}$  for that EOS, only the accuracy of the fit below  $\rho_{\max}$  is relevant.

The accuracy of a choice of parameter space is measured by the average residual of its fits to each EOS in the collection. For each EOS, we use a Levenberg-Marquardt algorithm to minimize the residual (2.9) over the parameter space. Even with a robust algorithm, the nonlinear fitting with varying dividing densities is sensitive to initial conditions. Multiple initial parameters for free fits are constructed using fixed-region fits of several possible dividing densities, and the global minimum of the resulting residuals is taken to indicate the best fit for the candidate EOS.

We begin with a single polytropic region in the core, specified by two parameters: the index  $\Gamma_1$  and a pressure  $p_1$  at some fixed density. Here, with a single polytrope, the choice of that density is arbitrary; for more than one polytropic piece, we will for convenience take that density to be the dividing density  $\rho_1$  between the first two polytropic regions. Changing the value of  $p_1$  moves the polytropic  $p(\rho)$  curve up or down, keeping the logarithmic slope  $\Gamma_1 = d \log p / d \log \rho$  fixed. The low-density SLy EOS is fixed, and the density  $\rho_0$  where the polytropic EOS intersects SLy changes as  $p_1$  changes. The polytropic index  $K_1$  is determined by Eq. (2.8). This is referred to as a one free piece fit. We then consider two-piece and three-piece fits: two polytropic regions within the core, specified by the four parameters  $\{p_1, \Gamma_1, \rho_1, \Gamma_2\}$ , as well as three polytropic regions specified by the six parameters  $\{p_1, \Gamma_1, \rho_1, \Gamma_2, \rho_3, \Gamma_3\}$ , where, in each case,  $p_1 \equiv p(\rho_1)$ . Again changing  $p_1$  translates the piecewise-polytropic EOS of the core up or down, keeping its shape fixed.

The accuracy of each parametrization (one, two, or three pieces), measured by the rms residual of Eq. (2.9), is portrayed in Table 1. The Table lists the average and maximum rms residuals over the set of 34 candidate EOSs. (The “fixed” fit is described below.)

Table 1 : Average residuals resulting from fitting the set of candidate EOSs with various types of piecewise polytropes. Free fits allow dividing densities between pieces to vary. The fixed three piece fit uses  $10^{14.7} \text{ g/cm}^3$  or roughly  $1.85\rho_{\text{nuc}}$  and  $10^{15.0} \text{ g/cm}^3$  or  $3.70\rho_{\text{nuc}}$  for all EOSs. Tabled are the RMS residuals of the best fits averaged over the set of candidates. The set of 34 candidates includes 17 candidates containing only  $npe\mu$  matter and 17 candidates with hyperons, pion or kaon condensates, and/or quark matter. Fits are made to tabled points in the high density region between  $10^{14.3} \text{ g/cm}^3$  or  $0.74\rho_{\text{nuc}}$  and the central density of a maximum mass TOV star calculated using that table.

Type of fit	All	$npe\mu$	$K/\pi/h/q$
Mean RMS residual			
One free piece	0.0386	0.0285	0.0494
Two free pieces	0.0147	0.0086	0.0210
Three fixed pieces	0.0127	0.0098	0.0157
Three free pieces	0.0071	0.0056	0.0086
Standard deviation of RMS residual			
One free piece	0.0213	0.0161	0.0209
Two free pieces	0.0150	0.0060	0.0188
Three fixed pieces	0.0106	0.0063	0.0130
Three free pieces	0.0081	0.0039	0.0107

For nucleon EOSs, the four-parameter fit of two free polytropic pieces models the behaviour of candidates well; but this kind of four-parameter EOS does not accurately fit EOSs with hyperons, kaon or pion condensates, and/or quark matter. Many require three polytropic pieces to capture the stiffening around nuclear density, a subsequent softer phase transition, and then final stiffening. On the other hand, the six parameters required to specify three free polytropic pieces exceeds the bounds of what may be reasonably constrained by the small set of model-independent astrophysical measurements. An alternative four parameter fit can be made to all EOSs if the transition densities are held fixed for all candidate EOSs (see below).

The hybrid quark EOS ALF3, which incorporates a QCD correction parameter for quark interactions, exhibits the worst-fit to a one-piece polytropic EOS with residual 0.111, to the three-piece fixed region EOS with residual 0.042, and to the three-piece varying region EOS with residual 0.042. It has a residual from the two-piece fit of 0.044, somewhat less than

the worst fit EOS, BGN1H1, an effective-potential EOS that includes all possible hyperons and has a two-piece fit residual of 0.056.

A good fit is found for three polytropic pieces with fixed divisions: between the first and second pieces at  $\rho_1 = 10^{14.7} \text{ g/cm}^3 = 1.85\rho_{\text{muc}}$  and a division between the second and third pieces fixed at  $\rho_2 = 10^{15.0} \text{ g/cm}^3$ . The EOS is specified by choosing the adiabatic indices  $\{\Gamma_1, \Gamma_2, \Gamma_3\}$  in each region, and the pressure  $p_1$  at the first dividing density,  $p_1 = p_1(\rho_1)$ . A diagram of this parameterization is shown in Fig. 2. For this 4-parameter EOS, best fit parameters for each candidate EOS give a residual of 0.043 or better, with the average residual over 34 candidate EOSs of 0.013. Note that the density of departure from the fixed low-density EOS is still a fitted parameter for this scheme.

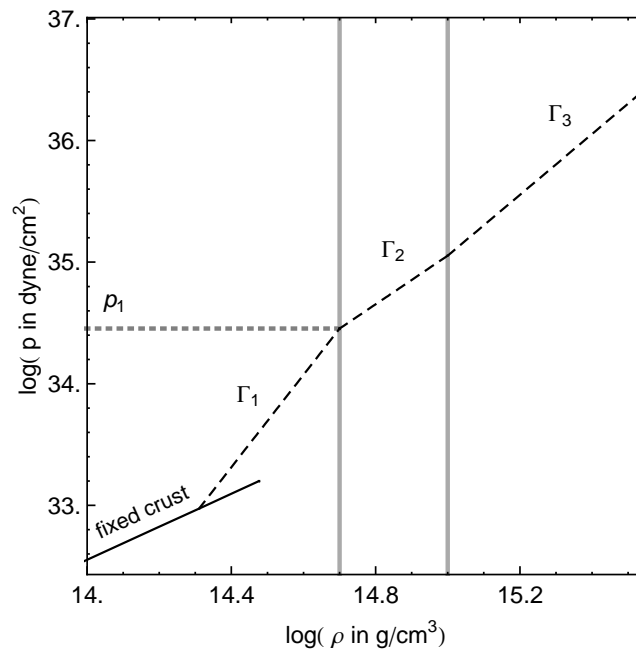


Figure 2 : The fixed-region fit is parametrized by adiabatic indices  $\{\Gamma_1, \Gamma_2, \Gamma_3\}$  and by the pressure  $p_1$  at the first dividing density.

The dividing densities for our parametrized EOS were chosen by minimizing the rms residuals over the set of 34 candidate EOSs. For two dividing densities, this is a two-dimensional minimization problem, which was solved by alternating between minimizing average rms residual for upper or lower density while holding the other density fixed. The location of the best dividing points is fairly robust over the subclasses of EOSs, as illustrated in Fig. 3.

With the dividing points fixed, taking the pressure  $p_1$  to be the pressure at  $\rho_1 = 1.85\rho_{\text{muc}}$ ,

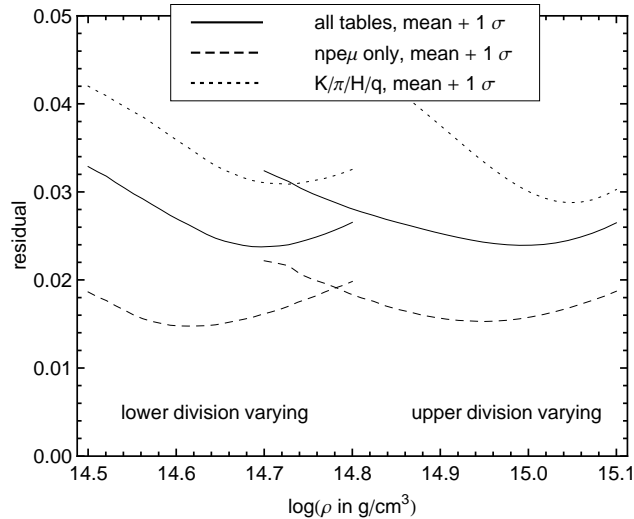


Figure 3 : Subsets of EOSs with and without kaons, hyperons, meson condensates, or quarks, show a fairly robust choice of dividing densities whose fit to the candidate EOSs minimizes residual error. The mean plus one standard deviation of residuals for each subset of candidate EOSs is plotted against the choice of lower and upper dividing densities  $\rho_1$  and  $\rho_2$ . The left curves show mean residual versus  $\rho_1$  with  $\rho_2$  fixed at  $10^{15.0}$  g/cm<sup>3</sup>. The right three curves show mean residual versus  $\rho_2$ , with  $\rho_1$  fixed at  $10^{14.7}$  g/cm<sup>3</sup>.

is indicated by empirical work of Lattimer and Prakash [8] that finds a strong correlation between pressure at fixed density (near this value) and the radius of  $1.4M_{\odot}$  neutron stars. This choice of parameter allows us to examine (in Sec. 2.5.5) the relation between  $p_1$  and the radius; and we expect a similar correlation between  $p_1$  and the frequency at which neutron-star inspiral dramatically departs from point-particle inspiral for neutron stars near this mass.

Since there are not many astrophysical constraints on the EOS, it is desirable to use one of the four-parameter fits (two free pieces or three fixed). Observations of pulsars that are not accreting indicate masses below  $1.45 M_{\odot}$  (see Sec. 2.5), and the central density of these stars is below  $\rho_2$  for almost all EOSs. Then only the three parameters  $\{p_1, \Gamma_1, \Gamma_2\}$  of the fixed piece parameterization are required to specify the EOS for moderate mass neutron stars. This class of observations can then be treated as a set of constraints on a 3-dimensional parameter space. Similarly, because maximum-mass neutron stars ordinarily have most matter in regions with densities greater than the first dividing density, their structure is insensitive to the first adiabatic index. The three piece parameterization does a significantly better job above  $\rho_2$  because phase transitions above that density require a third polytropic index  $\Gamma_3$ . If the remaining three parameters can be determined by pulsar

observations, then observations of more massive, accreting stars can constrain  $\Gamma_3$ .

The best fit parameter values of the candidate EOSs are shown in Fig. 4 and listed in Table 8 of Appendix A. The worst fits of the fixed region fit are the hybrid quark EOSs ALF1 and ALF2, and the hyperon-incorporating EOS BGN1H1. For BGN1H1, the relatively large residual is due to the fact that the best fit dividing densities of BGN1H1 differ strongly from the average best dividing densities. Although BGN1H1 is well fit by three pieces with floating densities, the reduction to a four-parameter fit limits the resolution of EOSs with such structure. The hybrid quark EOSs, however, have more complex structure that is difficult to resolve accurately with a small number of polytropic pieces. Still, the best-fit polytrope EOS is able to reproduce the neutron star properties predicted by the hybrid quark EOS.

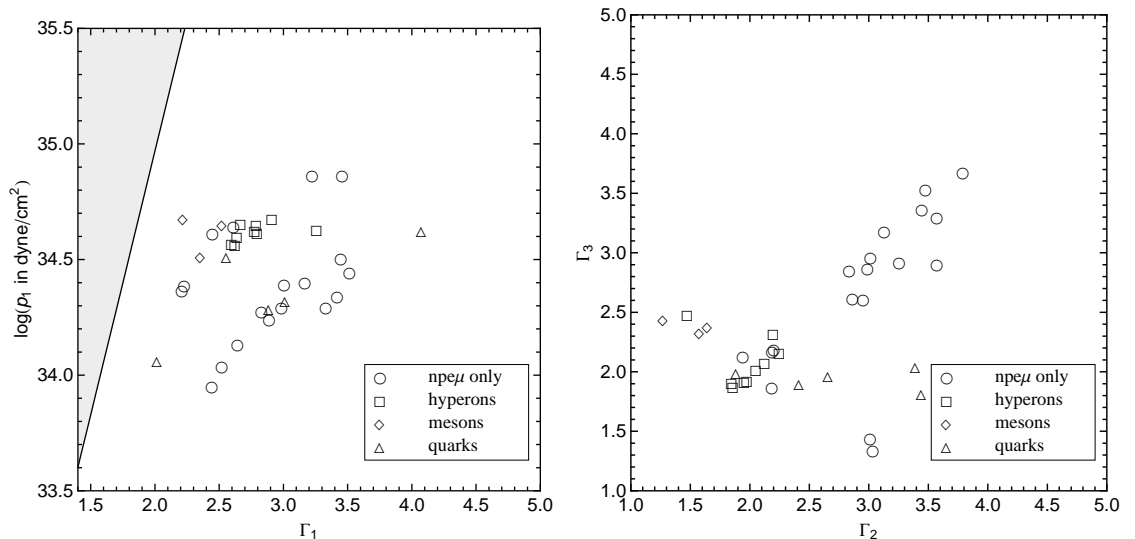


Figure 4 : parametrized EOS fits to the set of 34 candidate EOS tables. There are 17 EOSs with only ordinary nuclear matter (n,p,e, $\mu$ ); 9 have only hyperons in addition to ordinary matter; 3 include meson condensates plus ordinary matter; 5 include quarks plus other matter (PCL2 also has hyperons).  $\Gamma_2 < 3.5$  and  $\Gamma_3 < 2.5$  for all EOSs with hyperons, meson condensates, and/or quark cores. The shaded region corresponds to incompatible values of  $p_1$  and  $\Gamma_1$ , as discussed in the text.

In Appendix A, Table 8 compares neutron-star properties for each EOS to their values for the best-fit piecewise polytrope. The mean error and standard deviation for each characteristic is also listed.

## 2.5 Astrophysical constraints on the parameter space

Adopting a parametrized EOS allows one to phrase each observational constraint as a restriction to a subset of the parameter space. In sections 2.5.1–2.5.4 we find the constraints imposed by causality, by the maximum observed neutron-star mass and the maximum observed neutron-star spin, and by a possible observation of gravitational redshift. We then examine, in section 2.5.5, constraints from the simultaneous measurement of mass and moment of inertia and of mass and radius. We exhibit in section 2.5.6 the combined constraint imposed by causality, maximum observed mass, and a future moment-of-inertia measurement of a star with known mass.

In exhibiting the constraints, we show a region of the 4-dimensional parameter space large enough to encompass the 34 candidate EOSs considered above. The graphs in Fig. 4 display the ranges  $10^{33.5} \text{ dyne/cm}^2 < p_1 < 10^{35.5} \text{ dyne/cm}^2$ ,  $1.4 < \Gamma_1 < 5.0$ ,  $1.0 < \Gamma_2 < 5.0$ , and  $1.0 < \Gamma_3 < 5.0$ . Also shown is the location in parameter space of the best fit to each candidate EOS. The shaded region in the left graph corresponds to incompatible values of  $p_1$  and  $\Gamma_1$  mentioned in Sect. 2.4.

To find the constraints on the parametrized EOS imposed by the maximum observed mass and spin, one finds the maximum mass and spin of stable neutron stars based on the EOS associated with each point of parameter space. A subtlety in determining these maximum values arises from a break in the sequence of stable equilibria—an island of unstable configurations—for some EOSs. The unstable island is typically associated with phase transitions in a way we now describe.

Spherical Newtonian stars described by EOSs of the form  $p = p(\rho)$  are unstable when an average value  $\bar{\Gamma}$  of the adiabatic index falls below  $4/3$ . The stronger-than-Newtonian gravity of relativistic stars means that instability sets in for larger values of  $\bar{\Gamma}$ , and it is ordinarily this increasing strength of gravity that sets an upper limit on neutron-star mass. EOSs with phase transitions, however, temporarily soften above the critical density and then stiffen again at higher densities. As a result, configurations whose inner core has density just above the critical density can be unstable, while configurations with greater central density can again be stable. Models with this behavior are considered, for example, by Glendenning and Kettner [36], Bejger et al. [14] and by Zdunik et al. [13] (these latter authors, in fact, use piecewise polytropic EOSs to model phase transitions).

For our parametrized EOS, instability islands of this kind can occur for  $\Gamma_2 \lesssim 2$ , when  $\Gamma_1 \gtrsim 2$  and  $\Gamma_3 \gtrsim 2$ . A slice of the four-dimensional parameter space with constant  $\Gamma_1$  and  $\Gamma_3$  is displayed in Fig. 5. The shaded region corresponds to EOSs with islands of instability.

Contours are also shown for which the maximum mass for each EOS has the constant value  $1.7M_{\odot}$  (lower contour) and  $2.0M_{\odot}$  (upper contour).

An instability point along a sequence of stellar models with constant angular momentum occurs when the mass is maximum. On a mass-radius curve, stability is lost in the direction for which the curve turns counterclockwise about the maximum mass, regained when it turns clockwise. In the right graph of Fig. 5, mass-radius curves are plotted for six EOSs, labeled A–F, associated with six correspondingly labeled EOSs in the left figure. The sequences associated with EOSs B, C and E have two maximum masses (marked by black dots in the lower figure) separated by a minimum mass. As one moves along the sequence from larger to smaller radius – from lower to higher density, stability is temporarily lost at the first maximum mass, regained at the minimum mass, and permanently lost at the second maximum mass.

It is clear from each graph in Fig. 5 that either of the two local maxima of mass can be the global maximum. On the lower boundary (containing EOSs A and D), the lower density maximum mass first appears, but the upper-density maximum remains the global maximum in a neighborhood of the boundary. Above the upper boundary (containing EOS F), the higher-density maximum has disappeared, and near the upper boundary the lower-density maximum is the global maximum.

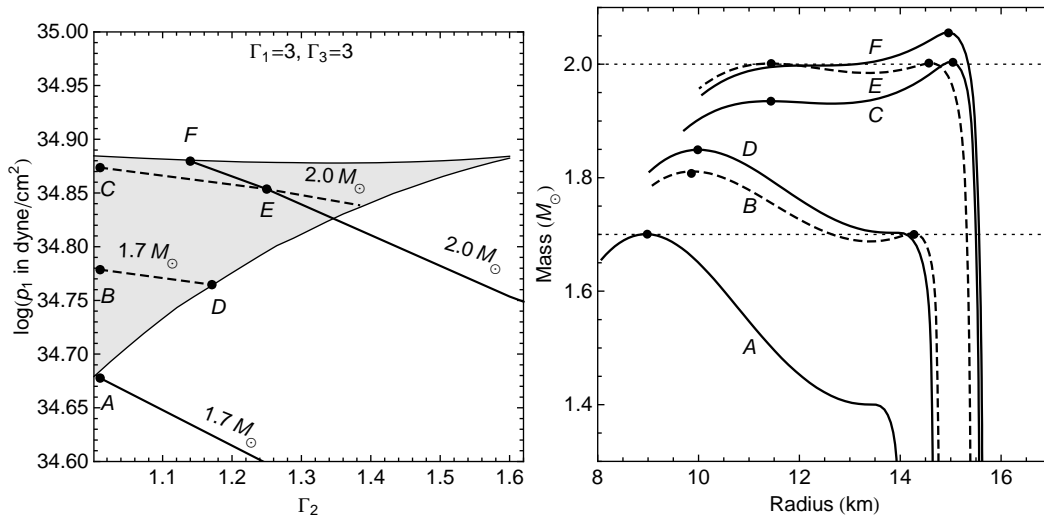


Figure 5 : The region in parameter space where two stable neutron-star sequences can occur is shaded in the left figure. Contours of constant maximum mass are also shown. The higher central density maximum mass contour is solid while the lower central density maximum mass contour is dashed. Mass-radius curves are plotted for several EOSs in the right figure. Although difficult to see, EOS C does in fact have a second stable sequence.

### 2.5.1 Causality

For an EOS to be considered physically reasonable, the adiabatic speed of sound  $v_s$  cannot exceed the speed of light. An EOS is ruled out by causality if  $v_s > 1$  for any density below the central density  $\rho_{\max}$  of the maximum-mass neutron star for that EOS. (If  $v_s > 1$  only above  $\rho_{\max}$ , the EOS is astrophysically indistinguishable from one altered to have  $v_s < 1$  above  $\rho_{\max}$  and thus should not be ruled out.)

We exhibit the causality constraint in two ways, first by simply requiring that each piecewise polytrope be causal at all densities and then by requiring only that it be causal below  $\rho_{\max}$ . The first, unphysically strong, constraint, shown in Fig. 6, is useful for an intuitive understanding of the constraint: The speed of sound is a measure of the stiffness of the EOS, and requiring causality eliminates the largest values of  $\Gamma_i$  and  $p_1$ .

Fig. 7 shows the result of restricting the constraint to densities below  $\rho_{\max}$ , with the speed of sound given by Eq. (2.6). A second surface is shown to account for the inaccuracy with which a piecewise polytropic approximation to an EOS represents the speed of sound. In all but one case (BGN1H1) the fits to the candidate EOSs overpredict the maximum speed of sound, but none of the fits to the candidate EOSs mispredict whether the candidate EOS is causal or acausal by more than 11% (fractional difference between fit and candidate). We adopt as a suitable causality constraint a restriction to a region bounded by the surface  $v_{s,\max} = 1 + \text{mean} + 1\sigma = 1.12$ , corresponding to the mean plus one standard deviation in the error between  $v_{s,\max}$  for the candidate and best fit EOSs.

In the lower parts of each graph in Fig. 7, where  $p_1 < 10^{35}$  dyne/cm<sup>2</sup>, the bounding surface has the character of the first causality constraint, with the restriction on each of the three variables  $p_1$ ,  $\Gamma_2$  and  $\Gamma_3$  becoming more stringent as the other parameters increase, and with  $\Gamma_3$  restricted to be less than about 3. In this low-pressure part of each graph, the surface is almost completely independent of the value of  $\Gamma_1$ : Because the constraint takes the form  $\Gamma_1 p / (\epsilon + p) \leq c^2$  (for  $p \ll \epsilon$ ) and  $p < p_1$  is so low, the constraint rules out values of  $\Gamma_1$  only at or beyond the maximum  $\Gamma_1$  we consider.

In the upper part of each graph, where  $p_1 > 10^{35}$  dyne/cm<sup>2</sup>, unexpected features arise from the fact that we impose the causality constraint only below the maximum density of stable neutron stars – below the central density of the maximum-mass star.

The most striking feature is the way the constraint surface turns over in the upper part of the top graph, where  $p_1 > 10^{35}$  dyne/cm<sup>2</sup>, in a way that allows arbitrarily large values of  $p_1$ . This occurs because, when  $p_1$  is large, the density of the maximum-mass star is small, and a violation of causality typically requires high density. That is, when the density is low, the ratio  $p / (\epsilon + p)$  in Eq. (2.6) is small. As a result, in the left graph,  $v_s$  remains too

small to violate causality before the maximum density is reached. In the right graph, with  $\Gamma_1 = 3.8$ ,  $\Gamma_1$  is now large enough in Eq. (2.6) that the EOS becomes acausal just below the transition to  $\Gamma_2$ . This is the same effect that places the upper limit on  $p_1$  seen in the second graph of Fig. 6.

A second feature of the upper parts of each graph is the exact independence of the bounding surface on  $\Gamma_3$ . The reason is simply that in this part of the parameter space the central density of the maximum mass star is below  $\rho_2$ , implying that no stable neutron stars see  $\Gamma_3$ .

Finally, we note that in both graphs, for small  $\Gamma_2$  (the right of the graph), the EOSs yield the sequences mentioned above, in which an island of instability separates two stable sequences, each ending at a local maximum of the mass. Requiring  $v_{s,\max}$  to satisfy causality for both stable regions rules out EOSs below the lower part of the bifurcated surface.

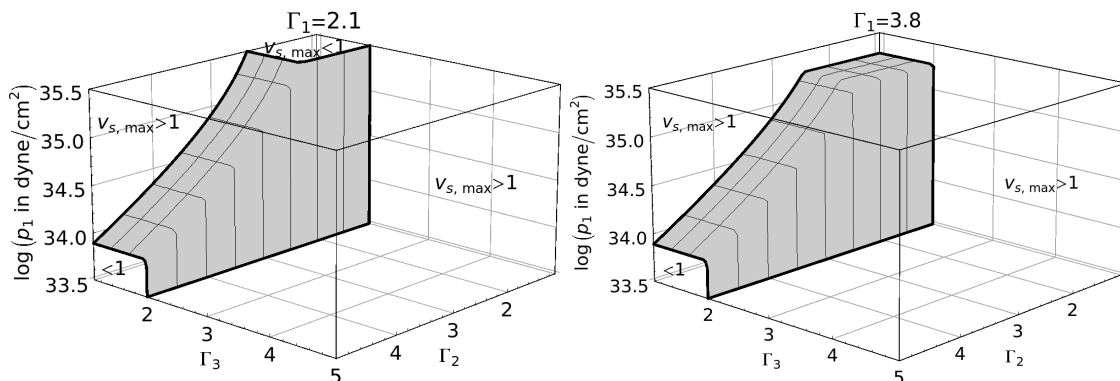


Figure 6 : Causality constraints are shown for two values of  $\Gamma_1$ . For each EOS in the parameter space the maximum speed of sound over all densities is used. The shaded surface separates the EOS parameter space into a region behind the surface allowed by causality (labeled  $v_{s,\max} < 1$ ) and a region in which corresponding EOSs violate causality at any density (labeled  $v_{s,\max} > 1$ ).

### 2.5.2 Maximum Mass

A stringent observational constraint on the EOS parameter space is set by the largest observed neutron-star mass. Unfortunately, the highest claimed masses are also subject to the highest uncertainties and systematic errors. The most reliable measurements come from observations of radio pulsars in binaries with neutron star companions. The masses with tightest error bars (about  $0.01 M_\odot$ ) cluster about  $1.4 M_\odot$  [37]. Recent observations of millisecond pulsars in globular clusters with non-neutron star companions have yielded

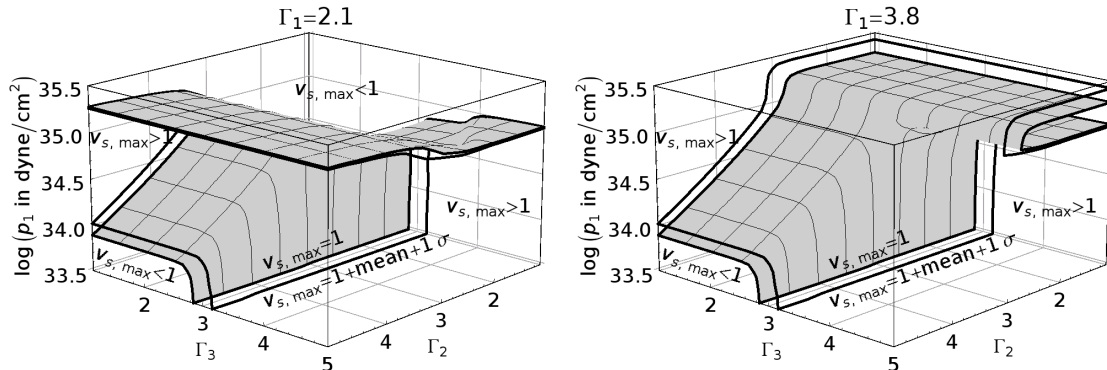


Figure 7 : Causality constraint as in Fig. 6. However, here, only the maximum speed of sound up to the central density of the maximum mass star is considered. A second, outlined surface shows a weaker constraint to accommodate the expected error in the speed of sound associated with a piecewise polytropic approximation to an EOS. With  $\sigma$  the standard deviation in  $v_{s,\max}$  between an EOS and its parametrized representation, as measured by the collection of candidate EOSs, the outlined surface depicts  $v_{s,\max} = 1 + \text{mean} + 1\sigma = 1.12$  constraint.

higher masses: Ter 5I and Ter 5J [38], M5B [39], PSR J1903+0327 [40], and PSR J0437-4715 [41] all have 95% confidence limits of about  $1.7 M_{\odot}$ , and the corresponding limit for NGC 6440B [42] is about  $2.3 M_{\odot}$ . However these systems are more prone to systematic errors: The pulsar mass is obtained by assuming that the periastron advance of the orbit is due to general relativity. Periastron advance can also arise from rotational deformation of the companion, which is negligible for a neutron star but could be much greater for pulsars which have white dwarf or main sequence star companions. Also the mass measurement is affected by inclination angle, which is known only for the very nearby PSR J0437-4715. And with the accumulation of observations of these eccentric binary systems (now about a dozen) it becomes more likely that the anomalously high figure for NGC 6440B is a statistical fluke. Recently, however, a secure measurement was made of a  $1.97 \pm 0.04 M_{\odot}$  neutron star from the Shapiro delay [43]. Fig. 8 shows the constraint on the EOS placed by the existence of  $1.93 M_{\odot}$  neutron stars, which we regard as secure. Also shown in the figure are the surfaces associated with maximum masses of  $1.7 M_{\odot}$  and  $2.3 M_{\odot}$ .

Since all of the candidate high-mass pulsars are spinning slowly enough that the rotational contribution to their structure is negligible, the constraint associated with their observed masses can be obtained by computing the maximum mass of nonrotating neutron stars. Corresponding to each point in the parameter space is a sequence of neutron stars based on the associated parametrized EOS; and a point of parameter space is ruled out if the corresponding sequence has maximum mass below the largest observed mass. We

exhibit here the division of parameter space into regions allowed and forbidden by given values of the largest observed mass.

We plot contours of constant maximum mass in Fig. 8. Because EOSs below a maximum mass contour produce stars with lower maximum masses, the parameter space below these surfaces is ruled out. The error in the maximum mass between the candidate and best fit piecewise polytropic EOSs is  $|\text{mean}| + 1\sigma = 1.7\%$  (the magnitude of the mean error plus one standard deviation in the error over the 34 candidate EOSs), so the parameters that best fit the true EOS are unlikely to be below this surface.

The surfaces of Fig. 8 have minimal dependence on  $\Gamma_1$ , indicating that the maximum mass is determined primarily by features of the EOS above  $\rho_1$ . In Fig. 8 we have set  $\Gamma_1$  to the least constraining value in the range we consider – to the value that gives the largest maximum mass at each point in  $\{p_1, \Gamma_2, \Gamma_3\}$  space. Varying  $\Gamma_1$  causes the contours to shift up, constraining the parameter space further, by a maximum of  $10^{0.2}$  dyne/cm<sup>2</sup>. The dependence of the contour on  $\Gamma_1$  is most significant for large values of  $p_1$  where the average density of a star is lower. The dependence on  $\Gamma_1$  decreases significantly as  $p_1$  decreases.

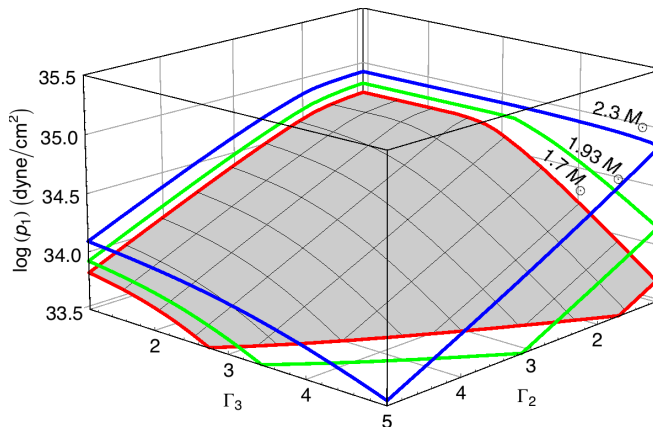


Figure 8 : The above surfaces represent the set of parameters that result in a constant maximum mass. An observation of a massive neutron star constrains the equation of state to lie above the corresponding surface.  $\Gamma_1$  is set to the least constraining value at each point. The lower shaded surface represents  $M_{\text{max}} = 1.7 M_{\odot}$ ; the middle and upper (outlined) surfaces represent  $M_{\text{max}} = 1.93 M_{\odot}$  and  $M_{\text{max}} = 2.3 M_{\odot}$  respectively.

As discussed above, some of the EOSs produce sequences of spherical neutron stars with an island of instability separating two stable sequences, each with a local maximum of the mass. As shown in Fig. 5, this causes a contour in parameter space of constant maximum mass to split into two surfaces, one surface of parameters which has this maximum mass at the lower  $\rho_c$  local maximum and another surface of parameters which has this maximum

mass at higher  $\rho_c$  branches. Since such EOSs allow stable models up to the largest of their local maxima, we use the least constraining surface (representing the global maximum mass) when ruling out points in parameter space.

### 2.5.3 Gravitational redshift

We turn next to the constraint set by an observed redshift of spectral lines from the surface of a neutron star. We consider here only stars for which the broadening due to rotation is negligible and restrict our discussion to spherical models. The redshift is then  $z = (1 - 2M/R)^{-1/2} - 1$ , and measuring it is equivalent to measuring the ratio  $M/R$ . With no independent measurement of mass or radius, the associated constraint again restricts the parameter space to one side of a surface, to the EOSs that allow a redshift as large as the largest observed shift.<sup>3</sup> For spherical models, the configuration with maximum redshift for a given EOS is ordinarily the maximum-mass star. By increasing  $p_1, \Gamma_2$  or  $\Gamma_3$ , one stiffens the core, increasing the maximum mass, but also increasing the radius at fixed mass. The outcome of the competition usually, but not always, yields increased redshift for larger values of these three parameters; that is, the increased maximum mass dominates the effect of increased radius at fixed mass for all but the largest values of  $p_1$ .

Cottam, Paerels, and Mendez [45] claim to have observed spectral lines from EXO 0748-676 with a gravitational redshift of  $z = 0.35$ . With three spectral lines agreeing on the redshift, the identification of the spectral features with iron lines is better founded than other claims involving only a single line. The identification remains in doubt, however, because the claimed lines have not been seen in subsequent bursts [46], and the subsequent observation of a 552 Hz period makes it unlikely that the observed lines originated at the NS surface [47]. There is also a claim of a simultaneous mass-radius measurement of this system using Eddington-limited photospheric expansion x-ray bursts [48] which would rule out many EOSs. This claim is controversial, because the 95% confidence interval is too wide to rule out much of the parameter space, and we believe the potential for systematic error is understated. However, the gravitational redshift is consistent with the earlier claim of 0.35. Thus we treat  $z = 0.35$  as a tentative constraint. We also exhibit the constraint that would be associated with a measurement of  $z = 0.45$ .

Our parameterization can reproduce the maximum redshift of tabulated EOSs to 3.2% (mean+1 $\sigma$ ). Figure 9 displays surfaces of constant redshift  $z = 0.35$  and  $z = 0.45$  for the

---

<sup>3</sup>One could also imagine a measured redshift small enough to rule out a class of EOSs. The minimum redshift for each EOS, however, occurs for a star whose central density is below nuclear density. Its value,  $z \approx 5 \times 10^{-4}$ , thus depends only on the EOS below nuclear density. (See, for example Haensel et al.[44].)

least constraining value of  $\Gamma_1 = 5$  in the range we consider. Surfaces with different values of  $\Gamma_1$  are virtually identical for  $p_1 < 10^{34.8}$  dyne/cm<sup>2</sup>, but diverge for higher pressures when  $\Gamma_1$  is small ( $\lesssim 2.5$ ). In the displayed parameter space, points in front of the  $z = 0.35$  surface, corresponding to stiffer EOSs in the inner core, are allowed by the potential  $z = 0.35$  measurement. From the location of the  $z = 0.35$  and  $z = 0.45$  surfaces, it is clear that, without an upper limit on  $\Gamma_1 \lesssim 2.5$ , an observed redshift significantly higher than 0.35 is needed to constrain the parameter space. In particular, most of the parameter space ruled out by  $z = 0.35$  is already ruled out by the  $M_{\max} = 1.93 M_{\odot}$  constraint displayed in Fig. 8.

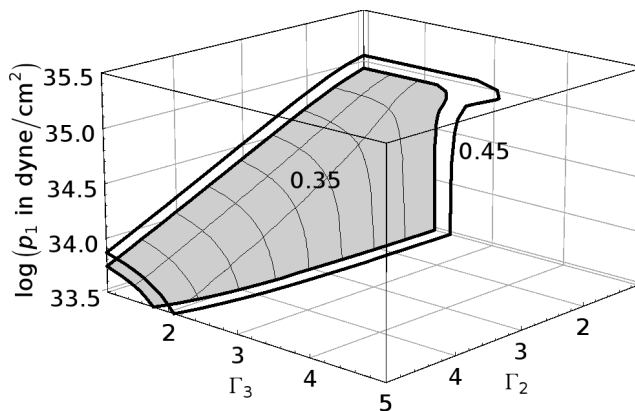


Figure 9 : Surfaces in the EOS parameter space for which the maximum redshift of stable spherical neutron stars has the values 0.35 (shaded surface) and 0.45 (outlined surface). A measured redshift from the surface of a neutron star would exclude the region of parameter space behind the corresponding surface.  $\Gamma_1$  is fixed at 5.0, the least constraining in the range we considered.

#### 2.5.4 Maximum Spin

Observations of rapidly rotating neutron stars can also constrain the EOS. The highest uncontroversial spin frequency is observed in pulsar Ter 5AD at 716 Hz [49]. There is a claim of 1122 Hz inferred from oscillations in x-ray bursts from XTE J1239-285 [50], but this is controversial because the statistical significance is relatively low, the signal could be contaminated by the details of the burst mechanism such as fallback of burning material, and the observation has not been repeated.

The maximum angular velocity of a uniformly rotating star occurs at the Kepler or mass-shedding limit,  $\Omega_K$ , with the star rotating at the speed of a satellite in circular orbit at the equator. For a given EOS, the configuration with maximum spin is the stable configuration with highest central density along the sequence of stars rotating at their Kepler limit. An

EOS thus maximizes rotation if it maximizes the gravitational force at the equator of a rotating star – if it allows stars of large mass and small radius. To allow high mass stars, the EOS must be stiff at high density, and for the radius of the high-mass configuration to be small, the EOS must be softer at low density, allowing greater compression in the outer part of the star [51, 52]. In our parameter space, a high angular velocity then restricts one to a region with large values of  $\Gamma_2$  and  $\Gamma_3$ , and small values of  $p_1$  and  $\Gamma_1$ .

As with the maximum mass, the maximum frequency is most sensitive to the parameter  $p_1$ , but the frequency constraint complements the maximum mass constraint by placing an upper limit on  $p_1$  over the parameter space, rather than a lower limit.

To calculate the maximum rotation frequencies for our parametrized EOS, we used the open-source code `rns` for axisymmetric rapid rotation in the updated form `rns2.0` [53]. For a given EOS, the model with maximum spin is ordinarily close to the model with maximum mass, but that need not be true for EOSs that yield two local mass maxima. The resulting calculation of maximum rotation requires some care, and the method we use is described in Appendix B of Ref. [54]. The error incurred in using the parametrized EOS instead of a particular model is 2.7% (mean+1 $\sigma$ ).

Spin frequencies of 716 Hz and even the possible 1122 Hz turn out to be very weak constraints because both are well below the Kepler frequencies of most EOSs. Thus we plot surfaces of parameters giving maximum rotation frequencies of 716 Hz in Fig. 10 and 1300 Hz and 1500 Hz in Fig. 11. The region of parameter space above the maximum observed spin surface is excluded. In the top figure, maximum mass stars have central densities below  $\rho_2$  so there is no dependence on  $\Gamma_3$ . In the bottom figure the least constraining value of  $\Gamma_1 = 5$  is fixed. The surface corresponding to a rotation of 716 Hz only constrains the parameter space that we consider ( $p_1 < 10^{35.5}$  dyne/cm<sup>3</sup>) if  $\Gamma_1 \lesssim 2.5$ . The minimum observed rotation rate necessary to place a firm upper limit on  $p_1$  is roughly 1200 Hz for  $\Gamma_1 = 5$ . The surface  $f_{\max} = 1500$  Hz for  $\Gamma_1 = 5$  is also displayed in Fig. 11 to demonstrate that much higher rotation frequencies must be observed in order to place strong limits on the parameter space.

Because it is computationally expensive to use `rns` to evaluate the maximum rotation frequency for a wide range of values in a 4-parameter space, one can also use an empirical formula. Haensel and Zdunik [55] found that the maximum stable rotation for a given EOS can be found from the maximum-mass spherically symmetric model for that EOS with mass  $M_s$  and radius  $R_s$  :

$$\left( \frac{\Omega_{\max}}{10^4 \text{ s}^{-1}} \right) \approx \kappa \left( \frac{M_s}{M_\odot} \right)^{\frac{1}{2}} \left( \frac{R_s}{10 \text{ km}} \right)^{-\frac{3}{2}}. \quad (2.10)$$

In other words the maximum rotation is proportional to the square root of the average

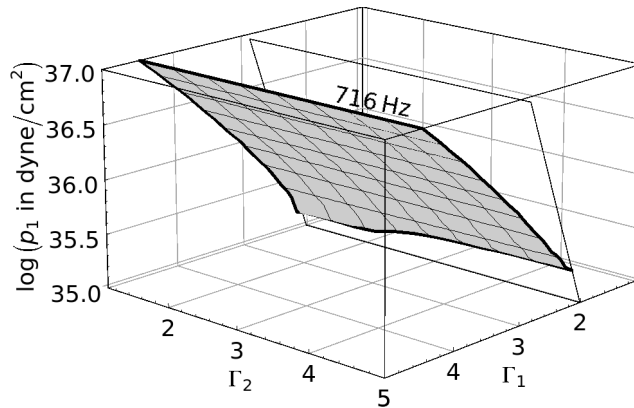


Figure 10 : The above surface represents the set of parameters that result in a maximum spin frequency of 716 Hz for the top surface. For high values of  $p_1$  there is no dependence on  $\Gamma_3$ . The wedge at the back right is the shaded region of Fig. 4, corresponding to incompatible values of  $p_1$  and  $\Gamma_1$ .

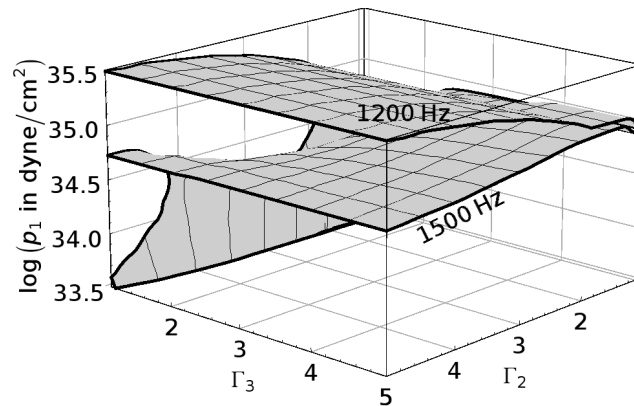


Figure 11 : The above surfaces represent the set of parameters that result in a maximum spin frequency of 1200 Hz for the top surface and 1500 Hz for the bottom surface. That is, observations of such high spin frequencies would constrain the EOS to lie below the corresponding surface. For these surfaces  $\Gamma_1 = 5$ , the least constraining value.

density of the star.

The original calculation of Haensel and Zdunik gave  $\kappa = 0.77$ . An overview of subsequent calculations is given by Haensel et al. in [56], reporting values of  $\kappa = 0.76 - 0.79$  for a range of EOS sets and calculation methods including those of [57, 58, 59]. If we calculate maximum rotations with `rns` as described above, using the 34 tabulated EOSs, we find  $\kappa = 0.786 \pm 0.030$ . The corresponding best fit parametrized EOSs give  $\kappa = 0.779 \pm 0.027$ .

### 2.5.5 Moment of inertia or radius of a neutron star of known mass

The moment of inertia of the more massive component, pulsar A, in the double pulsar PSR J0737-3039 may be determined to an accuracy of 10% within the next few years [18] by measuring the advance of the system’s periastron, and implications for candidate EOSs have been examined in [19, 18, 60]. As noted earlier, by finding both mass and moment of inertia of the same star one imposes a significantly stronger constraint on the EOS parameter space than the constraints associated with measurements of mass or spin alone: The latter restrict the EOS to the region of parameter space lying on one side of a surface, the region associated with the inequality  $M_{\max}(p_1, \Gamma_i) > M_{\text{observed}}$  or with  $\Omega_{\max}(p_1, \Gamma_i) > \Omega_{\text{observed}}$ . The simultaneous measurement, on the other hand, restricts the EOS to a single surface. That is, in an  $n$ -dimensional parameter space, the full  $n$ -dimensional set of EOSs which allow a  $1.338 M_{\odot}$  model, and those EOSs for which that model has moment of inertia  $I_{\text{observed}}$  form the  $(n - 1)$ -dimensional surface in parameter space given by  $I(p_1, \Gamma_i, M = 1.338M_{\odot}) = I_{\text{observed}}$ . (We use here the fact that the 44 Hz spin frequency of pulsar A is slow enough that the moment of inertia is nearly that of the spherical star.) Moreover, for almost all EOSs in the parameter space, the central density of a  $1.338 M_{\odot}$  star is below the transition density  $\rho_2$ . Thus the surfaces of constant moment of inertia have negligible dependence on  $\Gamma_3$ , the adiabatic index above  $\rho_2$ , and the EOS is restricted to the *two-dimensional* surface in the  $p_1$ - $\Gamma_1$ - $\Gamma_2$  space given by  $I(p_1, \Gamma_1, \Gamma_2, M = 1.338M_{\odot}) = I_{\text{observed}}$ .

This difference in dimensionality means that, in principle, the simultaneous equalities that give the constraint from observing two features of the same star are dramatically stronger than the inequalities associated with measurements of mass or spin alone. In practice, however, the two-dimensional constraint surface is thickened by the error of the measurement. The additional thickness associated with the error with which the parametrized EOS can reproduce the moment of inertia of the true EOS is smaller, because the parametrized EOS reproduces the moment of inertia of the 34 candidate EOSs to within 2.8% ( $|\text{mean}| + 1\sigma$ ).

In Fig. 12 we plot surfaces of constant moment of inertia that span the range associated with the collection of candidate EOSs. The lower shaded surface represents  $I = 1.0 \times 10^{45} \text{ g cm}^2$ . This surface has very little dependence on  $\Gamma_1$  because it represents a more compact star, and thus for a fixed mass, most of the mass is in a denser state  $\rho > \rho_1$ . The structures of these stars do depend on  $\Gamma_3$ , and the corresponding dependence of  $I$  on  $\Gamma_3$  is shown by the separation between the surfaces in Fig. 12. The middle outlined surface represents  $I = 1.5 \times 10^{45} \text{ g cm}^2$ , and is almost a surface of constant  $p_1$ . The top outlined surface represents  $I = 2.0 \times 10^{45} \text{ g cm}^2$ . This surface has little dependence on  $\Gamma_2$ , because

a star with an EOS on this surface would be less compact and thus most of its mass would be in a lower density state  $\rho < \rho_1$ .

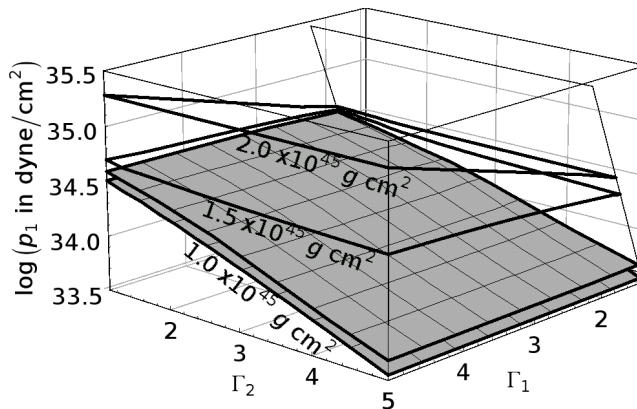


Figure 12 : The above surfaces represent the set of parameters that result in a star with a mass of  $1.338 M_{\odot}$  and a fixed moment of inertia, i.e. possible near-future measurements of PSR J0737-3039A.  $I = 1.0 \times 10^{45} \text{ g cm}^2$  for the shaded surfaces, whose separation corresponds to varying  $\Gamma_3$ .  $I = 1.5 \times 10^{45} \text{ g cm}^2$  for the middle outlined surface.  $I = 2.0 \times 10^{45} \text{ g cm}^2$  for the top outlined surface. The wedge at the back right is the shaded region of Fig. 4, corresponding to incompatible values of  $p_1$  and  $\Gamma_1$ .

If the mass of a neutron star is already known, a measurement of the radius constrains the EOS to a surface of constant mass and radius,  $R(p_1, \Gamma_i) = R_{\text{observed}}$ ,  $M(p_1, \Gamma_i) = M_{\text{observed}}$  in the 4-dimensional parameter space. The thickness of the surface is dominated by the uncertainty in the radius and mass measurements, since our parameterization produces the same radius as the candidate EOSs to within 1.7% ( $|\text{mean}| + 1\sigma$ ). We plot in Fig. 13 surfaces of constant radius for a  $1.4 M_{\odot}$  star that span the range of radii associated with the collection of candidate EOSs. As with the moment of inertia, the radius depends negligibly on  $\Gamma_3$  as long as the radius is greater than 11 km. For smaller radii, the variation with  $\Gamma_3$  is shown by the separation between the surfaces in Fig. 13.

Very recently analyses of time-resolved spectroscopic data during thermonuclear bursts from two neutron stars in low-mass x-ray binaries were combined with distance estimates to yield  $M = 1.4 M_{\odot}$  and  $R = 11 \text{ km}$  or  $M = 1.7 M_{\odot}$  and  $R = 9 \text{ km}$  for EXO 1745-248 [61] and  $M = 1.8 M_{\odot}$  and  $R = 10 \text{ km}$  for 4U 1608-52 [62], both with error bars of about 1 km in  $R$ . These results are more model dependent than the eventual measurement of the moment of inertia of PSR J0737-6069A, but the accuracy of the measurement of  $I$  remains to be seen.

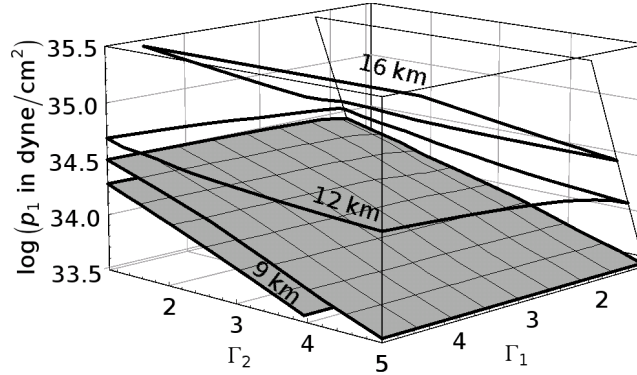


Figure 13 : The above surfaces represent the set of parameters that result in a star with a mass of  $1.4 M_{\odot}$  and a fixed radius.  $R = 9$  km for the shaded surfaces, whose separation corresponds to varying  $\Gamma_3$ .  $R = 12$  km for the middle outlined surface.  $R = 16$  km for the top outlined surface. The wedge at the back right is the shaded region of Fig. 4, corresponding to incompatible values of  $p_1$  and  $\Gamma_1$ .

### 2.5.6 Combining constraints

The simultaneous constraints imposed by causality, a maximum observed mass of  $1.93M_{\odot}$ , and a future measurement of the moment of inertia of PSR J0737-3039A, restrict the parameter space to the intersection of the allowed regions of Figs. 7, 8, and 12. We show in Fig. 14 the projection of the joint constraint from causality and maximum observed mass on the  $p_1 - \Gamma_2 - \Gamma_3$  subspace, and we show in Fig. 15 the joint constraint from including the moment of inertia of PSR J0737-3039A as well. This allows one to see the cutoffs imposed by causality that eliminate large values of  $\Gamma_2$  and  $\Gamma_3$  and (in the left of Fig. 15) the cutoffs imposed by the existence of a  $1.93M_{\odot}$  model that eliminates small values of  $\Gamma_2$  and  $\Gamma_3$ .

We noted above that measuring the moment of inertia of a  $1.338M_{\odot}$  star restricts the EOS at densities below  $\rho_2$  to a two-dimensional surface in the  $p_1 - \Gamma_1 - \Gamma_2$  space. In the full 4-dimensional parameter space, the corresponding surfaces of constant  $M$  and  $I$  of Fig. 15 are then three dimensional and independent of  $\Gamma_3$ . Their projections onto the  $p_1 - \Gamma_2 - \Gamma_3$  subspace are again three-dimensional and independent of  $\Gamma_3$ , their thickness due to the unseen dependence of the mass and moment of inertia on  $\Gamma_1$ . For small moments of inertia there is negligible dependence on  $\Gamma_1$  so the allowed volume in Fig. 15 is thin. The thickness of the allowed volume increases as the moment of inertia increases because the dependence on  $\Gamma_1$  also increases.

In Fig. 16 we explore a relation between the moment of inertia  $I(1.338)$  of PSR J0737-3039A and the maximum neutron star mass, in spite of the fact that the maximum mass is significantly greater than  $1.338 M_{\odot}$ . For three values of the moment of inertia that span the

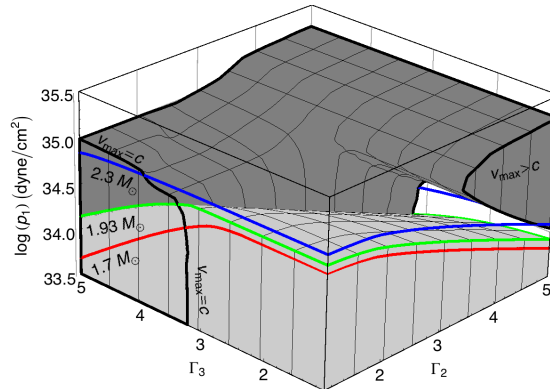


Figure 14 : The figure portrays the joint constraint imposed by causality ( $v_{s,\max} < 1+\text{mean}+1\sigma$ ) and the existence of a  $1.93 M_{\odot}$  neutron star. The dark shaded region is the volume in  $\Gamma_2 - \Gamma_3 - p_1$  space ruled out by the requirement that the EOS be causal, and the light shaded region is the volume ruled out by the  $1.93 M_{\odot}$  neutron star.

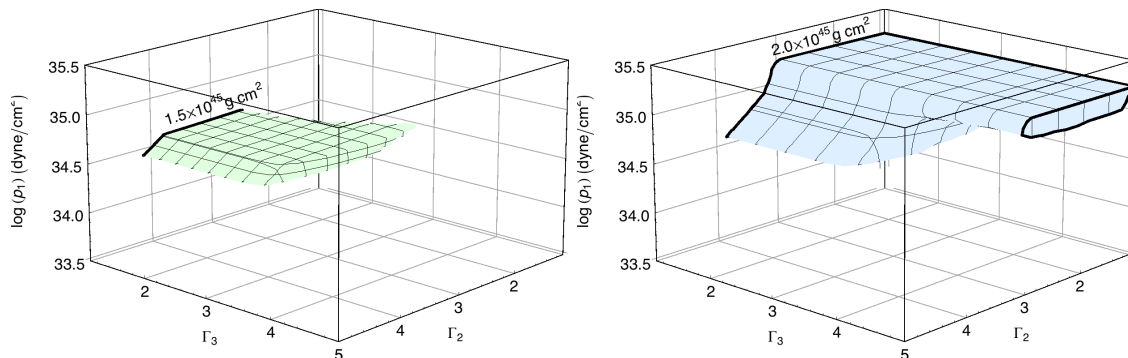


Figure 15 : The figure portrays the joint constraint imposed by causality ( $v_{s,\max} < 1+\text{mean}+1\sigma$ ), the existence of a  $1.93 M_{\odot}$  neutron star, and by a future measurement of the moment of inertia  $I$  of J0737-3039A. Each thick shaded surface is the volume in  $\Gamma_2 - \Gamma_3 - p_1$  space *allowed* by the joint constraint for the labeled value of  $I$ .

full range associated with our collection of candidate EOSs, we show joint constraints on  $\Gamma_2$  and  $\Gamma_3$  including causality and maximum neutron star mass. For  $I(1.338) = 1.0 \times 10^{45} \text{ g cm}^2$ ,  $\Gamma_2$  is nearly unconstrained, while  $\Gamma_3$  is required to lie in a small range between the causality constraint and the reliable observations of stars with mass  $1.7 M_{\odot}$ . However, for the recently measured  $1.93 M_{\odot}$  neutron star, this value for the moment of inertia is completely ruled out. For larger values of  $I(1.338)$ ,  $\Gamma_2$  is more constrained and  $\Gamma_3$  is less constrained.

The allowed range for  $p_1$  as a function of the moment of inertia of J0737-3039A is shown in Fig. 17. The entire shaded range is allowed for a  $1.7 M_{\odot}$  maximum mass. The medium and darker shades are allowed for a  $2.0 M_{\odot}$  maximum mass. Only the range with the darker

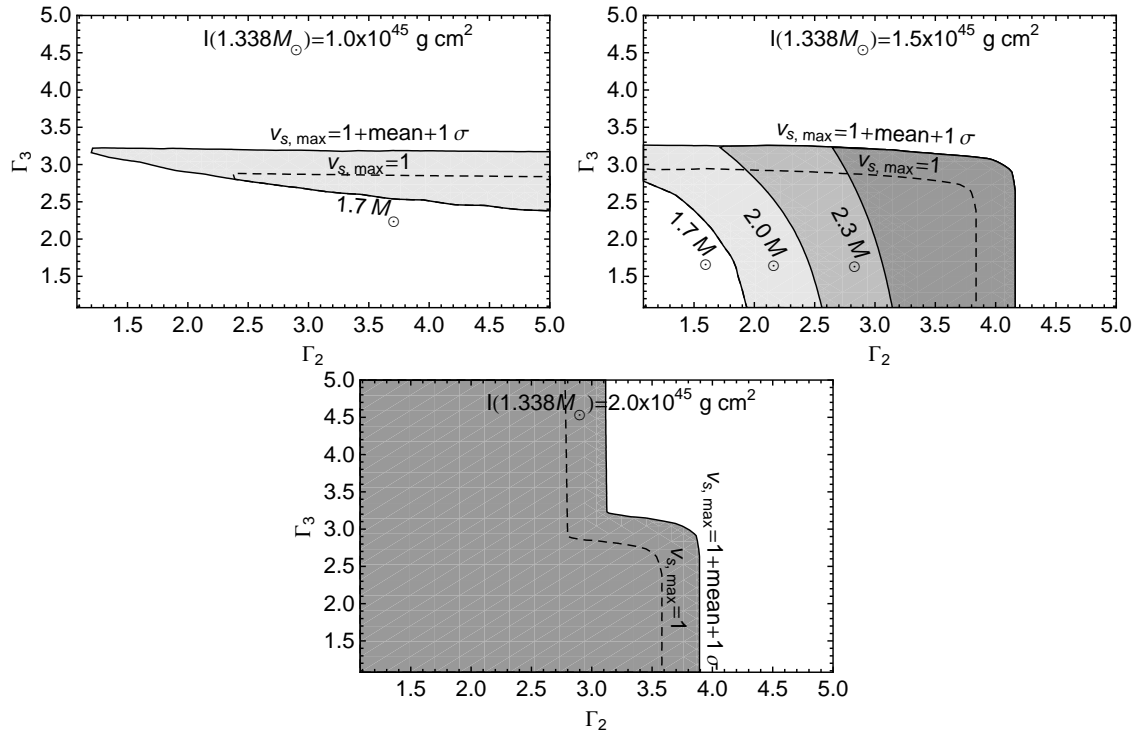


Figure 16 : The allowed values of  $\Gamma_2$  and  $\Gamma_3$  depend strongly on the moment of inertia of PSR J0737-3039A. In top left, top right, and bottom figures, respectively,  $I$  has the values  $1.0 \times 10^{45} \text{ g cm}^2$ ,  $I = 1.5 \times 10^{45} \text{ g cm}^2$  and  $I = 2.0 \times 10^{45} \text{ g cm}^2$ . In each figure the upper curves are the  $v_{s,\text{max}} = 1$  (dotted) and  $v_{s,\text{max}} = 1 + \text{mean} + 1\sigma = 1.12$  (solid) causality constraints. Shading indicates a range of possible maximum mass constraints, with increasing maximum mass leading to a smaller allowed area. All shaded areas are allowed for a  $1.7 M_\odot$  maximum neutron star mass. The medium and dark shades are allowed if a  $2.0 M_\odot$  star is confirmed. Only the darkest shade is allowed if a  $2.3 M_\odot$  star is confirmed.

shade is allowed if a  $2.3 M_\odot$  star is confirmed. It should be noted that for small moments of inertia, this plot overstates the uncertainty in the allowed parameter range. As shown in Fig. 15, the allowed volume in  $\Gamma_2 - \Gamma_3 - p_1$  space for a small moment of inertia observation is essentially two dimensional. If the moment of inertia is measured to be this small, then the EOS would be better parametrized with the linear combination  $\alpha \log(p_1) + \beta \Gamma_2$  instead of two separate parameters  $\log(p_1)$  and  $\Gamma_2$ . We also note that the recent  $1.97 \pm 0.04 M_\odot$  NS observation essentially rules out values of  $I(1.338) < 1.0 \times 10^{45} \text{ g cm}^2$ .

## 2.6 Discussion

We have shown how one can use a parametrized piecewise polytropic EOS to systematize the study of observational constraints on the EOS of cold, high-density matter. We think

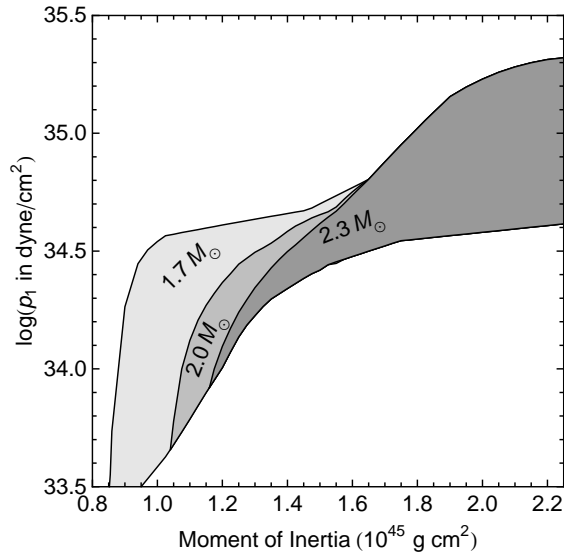


Figure 17 : The allowed range of  $p_1$  as a function of the moment of inertia of J0737-3039A when combined with causality ( $v_{s,\max} = 1 + \text{mean} + 1\sigma$ ) and observed mass constraints. All shaded areas are allowed by a  $1.7 M_\odot$  maximum mass. The medium and dark shades are allowed if a  $2.0 M_\odot$  star is confirmed. Only the darkest shade is allowed if a  $2.3 M_\odot$  star is confirmed.

that our choice of a 4-parameter EOS strikes an appropriate balance between the accuracy of approximation that a larger number of parameters would provide and the number of observational parameters that have been measured or are likely to be measured in the next several years. The simple choice of a piecewise polytrope, with discontinuities in the polytropic index, leads to suitable accuracy in approximating global features of a star. But the discontinuity reduces the expected accuracy with which the parametrized EOS can approximate the local speed of sound. One can largely overcome the problem by using a minor modification of the parametrized EOS in which a fixed smoothing function near each dividing density is used to join the two polytropes.

We see that high-mass neutron stars are likely to provide the strongest constraints from a single measurement. The work dramatizes the significantly more stringent constraints associated with measurements like this, if two (or more) physical features of the same star can be measured, and an  $n$ -dimensional parameter space is reduced by one (or more) dimension(s), to within the error of measurement. In particular, a moment of inertia measurement for PSR J0737-3039 (whose mass is already precisely known) could strongly constrain the maximum neutron star mass.

Finally, we note that the constraints from observations of different neutron star populations constrain different density regions of the EOS. For moderate mass stars such as those

found in binary pulsar systems, the EOS above  $\rho_2 = 10^{15.0} \text{ g/cm}^3$  is unimportant. For near-maximum mass stars, the EOS below  $\rho_1 = 10^{14.7} \text{ g/cm}^3$  has little effect on neutron star properties. This general behavior is independent of the details of our parameterization.

## Chapter 3

# Point-particle waveform approximations

The available electromagnetic observations presented in the last chapter offer useful, but still weak, constraints on the equation of state. Claimed mass–radius measurements offer the potential to provide significantly stronger constraints if they can be confirmed, and mass–moment of inertia measurements will offer similar constraints if they can be measured. Only recently, however, has the potential for gravitational-wave detectors to measure EOS-dependent information from binary inspiral received much attention.

In this chapter we state the results of the post-Newtonian (PN) approximation to the inspiral stage of coalescing binary black hole (BBH) systems, and discuss several methods for obtaining time and frequency domain inspiral waveforms. A more detailed review of the PN formalism can be found in Refs. [63, 64]. We then describe two methods for extending the PN approximation to the merger and ringdown stages of coalescence. In the next chapter we describe how the presence of matter in binary neutron star (BNS) and black hole-neutron star (BHNS) systems modifies the BBH waveform via tidal interactions. First, however, we discuss the general features of a binary waveform.

### 3.1 Description of a binary waveform

In general relativity, a gravitational wave far from a source is a linear perturbation  $h_{\mu\nu}$  of a flat background spacetime  $\eta_{\mu\nu}$  such that the metric is  $g_{\mu\nu} = \eta_{\mu\nu} + h_{\mu\nu}$ . The gauge symmetry of general relativity allows one to choose the Lorenz gauge condition

$$\partial^\nu \bar{h}_{\mu\nu} = 0, \tag{3.1}$$

where  $\bar{h}_{\mu\nu} = h_{\mu\nu} - \frac{1}{2}\eta_{\mu\nu}h$  is the trace reversed perturbation [64]. In the Lorenz gauge, the Einstein equation  $R_{\mu\nu} - \frac{1}{2}g_{\mu\nu}R = 8\pi T_{\mu\nu}$  becomes

$$\square\bar{h}_{\mu\nu} = -16\pi T_{\mu\nu}. \quad (3.2)$$

Outside the source, where the stress energy tensor  $T_{\mu\nu} = 0$  and therefore  $\square\bar{h}_{\mu\nu} = 0$ , an additional coordinate transformation that still preserves the Lorenz gauge condition can be made such that  $\bar{h}$  is transverse and traceless, and the waveform therefore satisfies [64]

$$h_{0\mu} = 0, \quad h_i^i = 0, \quad \partial^i h_{ij} = 0. \quad (3.3)$$

In general, the transverse traceless projection  $h_{ij}^{\text{TT}}$  of a generic perturbation  $h_{ij}$  is given by  $h_{ij}^{\text{TT}} = \Lambda_{ijkl}h_{kl}$ , where  $\Lambda_{ijkl} = P_{ik}P_{jl} - \frac{1}{2}P_{ij}P_{kl}$  is the transverse traceless projection operator and  $P_{ij} = \delta_{ij} - n_in_j$  is the standard projection operator used to project tensors orthogonal to  $n^i$ .

The four constraint equations from the Lorenz gauge condition and the additional four equations from the transverse traceless condition reduce the 10 components of the symmetric perturbation  $h_{\mu\nu}$  to two degrees of freedom. The waveform can therefore be written in terms of the two polarization tensors  $(e_+)_{ij}$  and  $(e_\times)_{ij}$

$$h_{ij}^{\text{TT}} = h_+e_{ij}^+ + h_\times e_{ij}^\times. \quad (3.4)$$

As can be seen by Eq. (3.3), for a source centered at the origin, the + and  $\times$  polarization tensors in spherical coordinates  $(r, \iota, \phi)$  are

$$e_{ij}^+ = \hat{l}_i\hat{l}_j - \hat{\phi}_i\hat{\phi}_j, \quad (3.5)$$

$$e_{ij}^\times = \hat{l}_i\hat{\phi}_j + \hat{l}_j\hat{\phi}_i. \quad (3.6)$$

For a binary in the  $x$ - $y$  plane, the polar angle  $\iota$  is called the inclination angle.

The components of the waveform can be combined into the complex scalar  $h = h_+ - ih_\times$ , which is related to the Weyl scalar  $\Psi_4$ <sup>1</sup> by  $\Psi_4 = \ddot{h}$  for asymptotic values of  $r$ . This scalar can be decomposed in terms of spin-weighted spherical harmonics<sup>2</sup> of spin  $s = -2$

$$h = h_+ - ih_\times = \sum_{\ell=2}^{\infty} \sum_{m=-\ell}^{\ell} -2Y_{\ell m}(\iota, \phi)h_{\ell m}(t, r), \quad (3.7)$$

<sup>1</sup>The 10 independent components of the Weyl tensor  $C_{\alpha\beta\gamma\delta}$  can be represented in terms of 5 complex scalars  $\Psi_0$ - $\Psi_4$ . These scalars are defined by contracting the Weyl tensor with the basis vectors of a null tetrad which can be written in terms of the spherical coordinates used here as  $(\hat{\ell} = \frac{1}{\sqrt{2}}(\hat{t} + \hat{r}), \hat{n} = \frac{1}{\sqrt{2}}(\hat{t} - \hat{r}), \hat{m} = \frac{1}{\sqrt{2}}(\hat{l} + i\hat{\phi}), \hat{m}^* = \frac{1}{\sqrt{2}}(\hat{l} - i\hat{\phi}))$ .  $\Psi_4$  represents outgoing gravitational radiation and is defined by  $\Psi_4 = -C_{\alpha\beta\gamma\delta}\hat{n}^\alpha\hat{m}^{*\beta}\hat{n}^\gamma\hat{m}^{*\delta}$  [65].

<sup>2</sup>Under a rotation of angle  $\psi$  about the radial vector  $\hat{r}$ , the vector  $\hat{m}$  in  $S^2$  transforms as  $\hat{m}' = e^{i\psi}\hat{m}$ . A function  $\eta$  which transforms as  $\eta' = e^{si\psi}\eta$  is said to have spin weight  $s$  [66]. The Weyl scalar  $\Psi_4$ , which transforms as  $\Psi_4' = -C_{\alpha\beta\gamma\delta}\hat{n}^\alpha\hat{m}'^{*\beta}\hat{n}^\gamma\hat{m}'^{*\delta} = e^{-2i\psi}\Psi_4$  where  $\hat{m}'^* = e^{-i\psi}\hat{m}^*$ , therefore has spin weight  $-2$ .

where a general expression for  ${}_s Y_{\ell m}$  and a table for the first few spin weight  $-2$  harmonics is given in Ref. [67]. These spin weighted spherical harmonics are orthogonal over the 2-sphere

$$\int_{S^2} {}_s Y_{\ell m}(\iota, \phi) {}_s Y_{\ell' m'}^*(\iota, \phi) d\Omega = \delta_{\ell\ell'} \delta_{mm'}, \quad (3.8)$$

where  $d\Omega = d\phi \sin \iota d\iota$ , and satisfy the following completeness relation

$$\sum_{\ell=|s|}^{\infty} \sum_{m=-\ell}^{\ell} {}_s Y_{\ell m}(\iota, \phi) {}_s Y_{\ell m}^*(\iota', \phi') = \delta(\phi - \phi') \delta(\cos \iota - \cos \iota'). \quad (3.9)$$

From these relations we see that a generic gravitational waveform, can be decomposed into harmonics with

$$h_{\ell m}(t, r) = \int_{S^2} h(t, r, \iota, \phi) {}_{-2} Y_{\ell m}(\iota, \phi) d\Omega, \quad (3.10)$$

and we also note that  $h_{\ell, m} = (-1)^\ell h_{\ell, -m}^*$ .

For circular orbits in the low-velocity, weak-field approximation, the only nonzero modes are the  $h_{2, \pm 2}$  modes with corresponding spin weighted spherical harmonics

$${}_{-2} Y_{2, \pm 2} = \sqrt{\frac{5}{64\pi}} (1 \pm \cos \iota)^2 e^{\pm 2i\phi}. \quad (3.11)$$

Assuming the observer is in the  $x$ - $z$  plane,  $\phi = 0^3$ , and the waveform is given by

$$h = h_{2, -2} {}_{-2} Y_{2, -2} + h_{2, 2} {}_{-2} Y_{2, 2} \quad (3.12)$$

$$= \sqrt{\frac{5}{64\pi}} [(1 - \cos \iota)^2 h_{2, 2}^* + (1 + \cos \iota)^2 h_{2, 2}], \quad (3.13)$$

and in the special case of an optimally oriented binary ( $\iota = 0$ ),  $h = 4\sqrt{\frac{5}{64\pi}} h_{2, 2}$ . Later in the inspiral, higher modes will begin to contribute. However, for the circular non-precessing orbits that we will consider in this dissertation, the higher modes are usually significantly smaller than the  $\ell = |m| = 2$  modes, and we will therefore focus mainly on this mode for the remainder of the dissertation. Future work will need to incorporate these higher modes.

## 3.2 Post-Newtonian approximation

The post-Newtonian formalism re-expresses the general relativistic description of a system of particles, given in terms of the Einstein field equations and geodesic equation, into the standard equations of motion of Newtonian physics, given in terms of the acceleration of

---

<sup>3</sup>As we will see, the waveform of a binary has an overall phase constant, and this condition is equivalent to redefining the phase constant.

particles through flat Euclidean space. Although far more involved than what is presented here, the equations of motion are found by systematically expanding the metric and the Einstein field equations in powers of the dimensionless parameter  $\epsilon \sim \sqrt{GM/c^2d} \sim v/c$ , where  $M$  is the total mass of the system,  $d$  is the scale of the system, and  $v$  is the characteristic velocity of particles in the system. The metric is then solved iteratively in powers of  $\epsilon$ , and the equations of motion are evaluated from the metric using the geodesic equation.<sup>4</sup> An expansion containing terms up to  $\epsilon^n$  or equivalently  $(1/c)^n$  is denoted an  $\frac{n}{2}$ PN expansion.

### 3.2.1 Energy and luminosity

The equations of motion that result from this expansion will have terms containing even powers of  $1/c$  and terms containing odd powers of  $1/c$ . The terms with even powers of  $1/c$  are time reversal invariant, and therefore admit a Lagrangian with an associated conserved energy. For a binary system of total mass  $M = M_1 + M_2$  in circular orbit with angular velocity  $\Omega$ , the energy in terms of the gauge independent quantity

$$x = (M\Omega)^{2/3}, \quad (3.14)$$

is given to 3.5PN order by [63, 64]

$$E = -\frac{1}{2}M\eta x \left\{ 1 + \left( -\frac{3}{4} - \frac{\eta}{12} \right) x + \left( -\frac{27}{8} + \frac{19\eta}{8} - \frac{\eta^2}{24} \right) x^2 + \left[ -\frac{675}{64} + \left( \frac{34445}{576} - \frac{205\pi^2}{96} \right) \eta - \frac{155\eta^2}{96} - \frac{35\eta^3}{5184} \right] x^3 \right\}, \quad (3.15)$$

where  $\eta = M_1M_2/M^2$  is the symmetric mass ratio.

Terms with odd powers of  $1/c$  in the equations of motion, which begin at 2.5PN ( $1/c^5$ ) order, on the other hand, determine the radiation reaction and are associated with the gravitational-radiation luminosity  $\mathcal{L}$ . For an expansion up to the currently known 3.5PN order, only the 2.5 and 3.5PN terms contribute to the luminosity, and this means that the expression for  $\mathcal{L}$  is only known explicitly to 1PN beyond the leading order. To obtain the luminosity to the same PN order as the energy, we must apply a different method. Although only known to be true to 1PN order, we can reasonably assume that the energy balance equation

$$\frac{dE}{dt} = -\mathcal{L} \quad (3.16)$$

---

<sup>4</sup>See, for example, Ref. [63] for a review of the post-Newtonian expansion, and Ref. [67] for an explicit derivation of the 1PN equations of motion and waveform.

holds at each PN order [63]. Far from the source, where the gravitational perturbation is linear, the luminosity can be calculated from

$$\mathcal{L} = \frac{r^2}{32\pi} \int d\Omega \langle \dot{h}_{ij}^{\text{TT}} \dot{h}_{ij}^{\text{TT}} \rangle. \quad (3.17)$$

We now need to find the waveform in terms of the source. Ignoring significant details in the derivation, which are outlined more thoroughly in Refs. [63, 64], the waveform  $h_{ij}^{\text{TT}}$  can be matched to the post-Newtonian metric by performing a multipole decomposition of both the waveform and PN metric in a shell with inner radius outside the source and outer radius much less than a wavelength from the source. The metric will contain contributions from the instantaneous mass and current multipoles as well as contributions from hereditary tail terms that depend on the past history of the multipoles and result in logarithmic terms. The final result for the luminosity sourced by a binary system in circular orbit is [63, 64]

$$\begin{aligned} \mathcal{L} = & \frac{32}{5} \eta^2 x^5 \left\{ 1 + \left( -\frac{1247}{336} - \frac{35\eta}{12} \right) x + 4\pi x^{3/2} + \left( -\frac{44711}{9072} + \frac{9271\eta}{504} + \frac{65\eta^2}{18} \right) x^2 \right. \\ & + \left( -\frac{8191}{672} - \frac{583\eta}{24} \right) \pi x^{5/2} + \left[ \frac{6643739519}{69854400} + \frac{16\pi^2}{3} - \frac{1712\gamma_E}{105} - \frac{856}{105} \ln(16x) \right. \\ & + \left. \left. \left( -\frac{134543}{7776} + \frac{41\pi^2}{48} \right) \eta - \frac{94403\eta^2}{3024} - \frac{775\eta^3}{324} \right] x^3 \right. \\ & \left. + \left( -\frac{16285}{504} + \frac{214745\eta}{1728} + \frac{193385\eta^2}{3024} \right) \pi x^{7/2} \right\}, \end{aligned} \quad (3.18)$$

where  $\gamma_E \approx 0.5772$  is Euler's constant. The dominant mode of the waveform, decomposed into spin weighted spherical harmonics, is [68, 69]

$$\begin{aligned} h_{22} = & -8\sqrt{\frac{\pi}{5}} \frac{M\eta}{D} e^{-2i\phi} x \left\{ 1 + \left( -\frac{107}{42} + \frac{55\eta}{42} \right) x + 2\pi x^{3/2} \right. \\ & + \left( -\frac{2173}{1512} - \frac{1069\eta}{216} + \frac{2047\eta^2}{1512} \right) x^2 + \left[ -\frac{107\pi}{21} + \left( \frac{34\pi}{21} - 24i \right) \eta \right] x^{5/2} \\ & + \left[ \frac{27027409}{646800} - \frac{856\gamma_E}{105} + \frac{2\pi^2}{3} + \frac{428i\pi}{105} - \frac{428}{105} \ln(16x) \right. \\ & \left. + \left( \frac{41\pi^2}{96} - \frac{278185}{33264} \right) \eta - \frac{20261\eta^2}{2772} + \frac{114635\eta^3}{99792} \right] x^3 \right\}, \end{aligned} \quad (3.19)$$

where  $\phi$  is the phase of the binary orbit. Although not needed for this dissertation, higher order modes are listed in Refs. [68, 69].

### 3.2.2 Orbital phase of the binary

From the energy balance equation we can find the phase  $\phi$  of the orbit by performing a change of variable

$$\mathcal{L} = -\frac{dE}{dt} = -\frac{dE/dx}{dt/dx}. \quad (3.20)$$

Since  $x = \left(M \frac{d\phi}{dt}\right)^{2/3}$ , the phase is found by integrating the following two equations

$$\frac{dx}{dt} = -\frac{\mathcal{L}}{dE/dx}, \quad (3.21)$$

$$\frac{d\phi}{dt} = \frac{x^{3/2}}{M}. \quad (3.22)$$

There are several methods to integrate this system of equations, the four most common of which are labeled TaylorT1–TaylorT4 [67]. In the TaylorT1 method, Eqs. (3.15) and (3.18) are simply plugged into Eq. (3.21), and the system is then integrated numerically starting with the initial conditions  $x_0 = (M\Omega_0)^{2/3}$  and  $\phi_0$ . In the TaylorT2 approach, the equations are written

$$t(x) = t_c + \int_x^{x_c} \frac{dE/dx'}{\mathcal{L}(x')} dx', \quad (3.23)$$

$$\phi(x) = \phi_c + \frac{1}{M} \int_x^{x_c} x'^{3/2} \frac{dE/dx'}{\mathcal{L}(x')} dx' \quad (3.24)$$

The integrands are reexpanded and truncated at the appropriate PN order, then integrated to give analytical series solutions for  $t(x)$  and  $\phi(x)$ . The TaylorT3 method starts with the TaylorT2 result, then inverts the series to obtain  $x$  and  $\phi$  as explicit functions of the auxiliary variable  $\Theta(t) = \frac{\eta}{5M}(t_c - t)$ . To do this, the series solution to  $t(x)$  is inverted to obtain a series solution for  $x(\Theta(t))$ . This solution is then plugged into the series solution for  $\phi(x)$  and reexpanded to give  $\phi(\Theta(t))$ . Finally, in the TaylorT4 method, which appears to agree best with equal mass BBH simulations at 3.5PN order [70], the right side of Eq. (3.21) is reexpanded in a Taylor series and then truncated at 3.5PN order [71]:

$$\begin{aligned} \frac{dx}{dt} = \frac{64}{5} \frac{\eta x^5}{M} \left\{ 1 + \left( -\frac{743}{336} - \frac{11\eta}{4} \right) x + 4\pi x^{3/2} + \left( \frac{34103}{18144} + \frac{13661\eta}{2016} + \frac{59\eta^2}{18} \right) x^2 \right. \\ + \left( -\frac{4159}{672} - \frac{189\eta}{8} \right) \pi x^{5/2} + \left[ \frac{16447322263}{139708800} - \frac{1712\gamma_E}{105} + \frac{16\pi^2}{3} - \frac{856}{105} \ln(16x) \right. \\ + \left. \left( \frac{451\pi^2}{48} - \frac{56198689}{217728} \right) \eta + \frac{541\eta^2}{896} - \frac{5605\eta^3}{2592} \right] x^3 \\ \left. + \left( -\frac{4415}{4032} + \frac{358675\eta}{6048} + \frac{91495\eta^2}{1512} \right) \pi x^{7/2} \right\}. \end{aligned} \quad (3.25)$$

Eqs. 3.25 and 3.22 are then integrated numerically as in the TaylorT1 approach. The waveform can now be evaluated by plugging the solutions for  $x(t)$  and  $\phi(t)$  into the waveform  $h_{22}$  (Eq. 3.19).

### 3.2.3 Stationary phase approximation

As we shall see in later chapters, we will often need the Fourier transform of a waveform. For a generic waveform

$$h_{\ell m}(t) = A_{\ell m}(t)e^{-im\phi(t)} dt, \quad (3.26)$$

the Fourier transform is given by

$$\tilde{h}_{\ell m}(f) = \int_{-\infty}^{\infty} A_{\ell m}(t)e^{i\Phi(t)} dt, \quad (3.27)$$

where  $\Phi(t) = 2\pi ft - m\phi(t)$ . The Fourier transform can be evaluated numerically; however, when the amplitude and frequency are slowly varying with time ( $d \ln A/dt \ll d\phi/dt$  and  $d^2\phi/dt^2 \ll (d\phi/dt)^2$ ), it is possible to use the stationary phase approximation (SPA). When the SPA conditions hold, the main contribution to the integral comes from the region centered on the stationary phase time  $t_{\text{sp}}$  when the integrand is not changing with time [ $\dot{\Phi}(t_{\text{sp}}) = 2\pi f - m\dot{\phi}(t_{\text{sp}}) = 0$ ], while far from the stationary point the integrand is rapidly oscillating and contributes little to the integral. Around this point the phase can be approximated with a Taylor series

$$\Phi(t) \approx 2\pi ft_{\text{sp}} - m\phi(t_{\text{sp}}) - \frac{1}{2!}m\ddot{\phi}(t_{\text{sp}})(t - t_{\text{sp}})^2. \quad (3.28)$$

The Fourier transform now becomes

$$\begin{aligned} \tilde{h}_{\ell m}(f) &\approx A_{\ell m}(t_{\text{sp}}) \sqrt{\frac{2\pi}{m\ddot{\phi}(t_{\text{sp}})}} e^{i\psi_{\ell m}(f)}, \\ \psi_{\ell m}(f) &= 2\pi ft_{\text{sp}} - m\phi(t_{\text{sp}}) - \frac{\pi}{4}, \end{aligned} \quad (3.29)$$

where  $\int_{-\infty}^{\infty} \exp[-ia(t-t_{\text{sp}})^2] dt = \sqrt{\pi/a} \exp(-i\pi/4)$ . The quantities  $t_{\text{sp}}$ ,  $\phi(t_{\text{sp}})$ , and  $A_{\ell m}(t_{\text{sp}})$  can be written as functions of  $f$  using  $x(t_{\text{sp}}) = (M\dot{\phi}(t_{\text{sp}}))^2/3 = (2\pi Mf/m)^2/3$ , and as with time domain post-Newtonian waveforms there are several ways to do this. The most common version known as TaylorF2 closely follows the time domain TaylorT2 approach. The time and phase are written as parametric functions of  $x$

$$t_{\text{sp}} = t_c + \int_{x(t_{\text{sp}})}^{x_c} \frac{dE/dx}{\mathcal{L}(x)} dx, \quad (3.30)$$

$$\phi(t_{\text{sp}}) = \phi_c + \frac{1}{M} \int_{x(t_{\text{sp}})}^{x_c} x^{3/2} \frac{dE/dx}{\mathcal{L}(x)} dx, \quad (3.31)$$

and as in the TaylorT2 approach the ratios in the integral are reexpanded then truncated at the appropriate PN order. The term in the square root of Eq. (3.29) can be written using  $\ddot{\phi}(t_{\text{sp}}) = \frac{3}{2M}x^{1/2}(t_{\text{sp}})\frac{dx(t_{\text{sp}})}{dt}$ , and  $\frac{dx}{dt}$  can be rewritten with the TaylorT1 method, the

TaylorT4 method (3.25), or the entire amplitude term can be reexpanded then truncated. The method that gives the best agreement with the Fourier transform of BBH simulations during the late inspiral is the TaylorT4 method [72]. The TaylorF2 waveform (with TaylorT4 amplitude) is then

$$\tilde{h}_{\ell m}(f) = A_{\ell m}(x(t_{\text{sp}})) \sqrt{\frac{4\pi M}{3mx^{1/2}(t_{\text{sp}}) \left. \frac{dx(t_{\text{sp}})}{dt} \right|_{T4}}} e^{i\psi_{\ell m}(f)}, \quad (3.32)$$

$$\psi_{\ell m}(f) = 2\pi f t_c - m\phi_c - \frac{\pi}{4} + \frac{m}{M} \int_{x(t_{\text{sp}})}^{x_c} [x^{3/2}(t_{\text{sp}}) - x^{3/2}] \frac{dE/dx}{\mathcal{L}(x)} dx. \quad (3.33)$$

The  $\ell = m = 2$  harmonic is, for example,

$$\begin{aligned} \psi_{22}(f) = & 2\pi f t_c - 2\phi_c - \frac{\pi}{4} + \frac{3}{128\eta} (\pi M f)^{-5/3} \left\{ 1 + \left( \frac{3715}{756} + \frac{55\eta}{9} \right) (\pi M f)^{2/3} - 16\pi (\pi M f) \right. \\ & + \left( \frac{15293365}{508032} + \frac{27145\eta}{504} + \frac{3085\eta^2}{72} \right) \pi (\pi M f)^{4/3} \\ & + [1 + \ln(\pi M f)] \left( \frac{38645}{756} - \frac{65\eta}{9} \right) \pi (\pi M f)^{5/3} \\ & + \left[ \frac{11583231236531}{4694215680} - \frac{640\pi^2}{3} - \frac{6848\gamma_E}{21} - \frac{6848}{63} \ln(64\pi M f) \right. \\ & + \left. \left( -\frac{15737765635}{3048192} + \frac{2255\pi^2}{12} \right) \eta + \frac{76055\eta^2}{1728} - \frac{127825\eta^3}{1296} \right] (\pi M f)^2 \\ & \left. + \left( \frac{77096675}{254016} + \frac{378515\eta}{1512} - \frac{74045\eta^2}{756} \right) \pi (\pi M f)^{7/3} \right\}. \end{aligned} \quad (3.34)$$

### 3.3 Frequency-domain phenomenological waveforms

During the late inspiral, the assumptions of slow motion ( $v \ll c$ ) and weak gravitational field ( $\frac{GM}{c^2 d} \ll 1$ ) used in the post-Newtonian formalism no longer hold, and new methods are needed for constructing the waveform. Several methods have been developed to join the post-Newtonian formalism during the inspiral to the results of numerical relativity and perturbation theory during the merger and ringdown stages. In this section we will discuss a frequency-domain phenomenological model which joins numerical waveforms for the merger and ringdown of BBH systems to the stationary phase approximation PN waveform and then constructs an analytic fit to this hybridized waveform. This phenomenological waveform will be used as a starting point for constructing an analytic inspiral-merger-ringdown (IMR) BHNS waveform in Chapter 8. In the next section we will discuss another approach, known as the effective one body (EOB) formalism, for extending the post-Newtonian results to the late inspiral and merger. The EOB formalism will be used in Chapter 7.

Several frequency domain phenomenological models are now available for the complete IMR BBH waveform. These models include the PhenomA [73] model for nonspinning BBH systems, as well as the PhenomB [74] model and improved PhenomC [72] model for aligned-spin BBH systems. Below, we will discuss the PhenomC waveform, which is fit to a wide range of BBH simulations and places an emphasis on controlling errors due to matching the numerical to the PN waveform.

In the models PhenomA–C, the Fourier transform of the waveform is decomposed into an amplitude  $A_{\text{phen}}(f)$  and phase  $\Phi_{\text{phen}}(f)$  as

$$\tilde{h}_{\text{phen}}(f) = A_{\text{phen}}(f)e^{i\Phi_{\text{phen}}(f)}. \quad (3.35)$$

The inspiral is described by the TaylorF2 post-Newtonian waveform with the amplitude given by  $|\tilde{h}_{22}(f)|$  as in Eq. (3.32), and the phase given by  $\psi_{22}(f)$  as in Eq. (3.34)<sup>5</sup>. For aligned-spin waveforms, the spin of both black holes is parametrized by the single parameter

$$\chi = \frac{M_1}{M}\chi_1 + \frac{M_2}{M}\chi_2, \quad (3.36)$$

where  $\chi_A = a_A/M_A \in (-1, 1)$  is the dimensionless spin parameter for black hole  $A$ .

During the premerger stage, defined as  $0.1f_{\text{RD}} < f < f_{\text{RD}}$  where  $f_{\text{RD}}$  is the mass and spin dependent ringdown frequency of the dominant mode given explicitly in Ref. [72], the TaylorF2 waveform will no longer be an accurate description. Instead, the amplitude can be written in terms of the PN amplitude  $A_{\text{PN}}$ , but with an additional phenomenological 3PN correction  $\gamma_1 f^{5/6}$  fit to numerical waveforms

$$A_{\text{PM}}(f) = A_{\text{PN}}(f) + \gamma_1 f^{5/6}. \quad (3.37)$$

The phenomenological phase is written in a form similar to the TaylorF2 expansion (Eq. 3.34)

$$\psi_{\text{PM}}^{22}(f) = \frac{1}{\eta}(\alpha_1 f^{-5/3} + \alpha_2 f^{-1} + \alpha_3 f^{-1/3} + \alpha_4 + \alpha_5 f^{2/3} + \alpha_6 f), \quad (3.38)$$

and the coefficients  $\alpha_1$ – $\alpha_6$  correspond to phenomenological 0PN, 1PN, 2PN, 2.5PN, 3.5PN, and 4 PN corrections respectively.

During the ringdown stage ( $f > f_{\text{RD}}$ ), the amplitude is written as a product of a Lorentzian

$\left(\mathcal{L}(f, f_0, \sigma) = \frac{\sigma^2}{(f-f_0)^2 + \sigma^2/4}\right)$  and the leading  $f^{-7/6}$  PN amplitude term,

$$A_{\text{RD}}(f) = \delta_1 \mathcal{L}(f, f_{\text{RD}}(a, M), \delta_2 Q(a)) f^{-7/6}, \quad (3.39)$$

---

<sup>5</sup>Note that  $A_{22}(x)$  in Eq. (3.32) also has a small phase which is negligible during the inspiral and can be ignored.

where  $Q$  is the ringdown quality factor defined in [72], and  $\delta_1$  and  $\delta_2$  are phenomenological parameters. The phase during ringdown, which grows roughly linearly, is written

$$\psi_{\text{PM}}^{22}(f) = \beta_1 + \beta_2 f. \quad (3.40)$$

The parameters  $\beta_1$  and  $\beta_2$  are determined analytically by matching the value and slope of the premerger phase at  $f_{\text{RD}}$ .

The transitions between the inspiral, premerger, and ringdown regimes are smoothed by means of windowing functions [72]. The 9 phenomenological parameters  $\{\alpha_1, \dots, \alpha_6, \gamma_1, \delta_1, \delta_2\}$  are found by maximizing the overlap with numerical waveforms. Each of the phenomenological parameters are then related to the physical parameters  $\{\eta, \chi\}$  by a polynomial fit with 5 parameters each [72].

### 3.4 Effective one body formalism

In this section we introduce another method for extending the validity of the post-Newtonian formalism to the late inspiral, merger, and ringdown, known as the effective one body (EOB) formalism and first introduced in Ref. [75]. The version used here is exactly that of Ref. [76], and is described in more detail in a review [77]. The only ingredients not listed here are terms for the re-summed waveform in Ref. [78] and coefficients to determine the ringdown waveform found in Ref. [79].

#### 3.4.1 Hamiltonian dynamics

In the EOB formalism the two-body dynamics are replaced by a test particle of reduced mass  $\mu = M_1 M_2 / M$  moving in a modified Schwarzschild metric of total mass  $M = M_1 + M_2$ . In the expressions below, we will use dimensionless coordinates rescaled by the total mass  $M$ , and the dynamical expressions will be rescaled by the test particle mass  $\mu$ <sup>6</sup>. The modified Schwarzschild metric has the form

$$ds^2 = -A(r)dt^2 + B(r)dr^2 + r^2(d\theta^2 + \sin^2\theta d\phi^2). \quad (3.41)$$

---

<sup>6</sup>The coordinates  $(T, R, \phi)$  and conjugate momenta  $(P_R, P_\phi)$  have been rescaled to dimensionless coordinates  $(t, r, \phi)$  and momenta  $(p_r, p_\phi)$  given by:  $t = T/M$  and  $r = R/M$  for the coordinates, and  $p_r = P_R/\mu$ ,  $p_\phi = P_\phi/\mu M$  for the conjugate momenta. Other quantities are then rescaled in the following way:  $\omega = M\Omega = Md\phi/dT$  is the angular velocity,  $\hat{D} = D/M$  is the distance to the source,  $\hat{H} = H/\mu$  and  $\hat{H}_{\text{eff}} = H_{\text{eff}}/\mu$  are the Hamiltonian and effective Hamiltonian, and  $\hat{\mathcal{F}}_\phi = \mathcal{F}_\phi/\mu$  is the radiation reaction force.

The metric potentials  $A$  and  $B$  can be calculated from post-Newtonian theory. The first function is

$$A(u) = P_5^1 \left[ 1 - 2u + 2\eta u^3 + \left( \frac{94}{3} - \frac{41\pi^2}{32} \right) \eta u^4 + a_5 \eta u^5 + a_6 \eta u^6 \right], \quad (3.42)$$

where  $u = 1/r$  and  $P_n^m[\cdot]$  denotes a Padé approximant of order  $m$  in the numerator and  $n$  in the denominator. The 4 and 5 PN coefficients,  $a_5$  and  $a_6$ , are fit to numerical BBH waveforms. The values that give the optimal fit form a degenerate curve in the  $a_5$ - $a_6$  parameter space, and the specific values chosen here are  $(a_5, a_6) = (0, -20)$ . The second potential is rewritten as

$$D(r) = B(r)A(r), \quad (3.43)$$

and has been calculated to 2PN order

$$D(u) = P_3^0 [1 - 6\eta u^2 + 2(3\eta - 26)\eta u^3]. \quad (3.44)$$

The motion of the EOB particle of mass  $\mu$  is determined by the Hamiltonian

$$\hat{H} = \frac{1}{\eta} \sqrt{1 + 2\eta(\hat{H}_{\text{eff}} - 1)}, \quad (3.45)$$

where

$$\hat{H}_{\text{eff}} = \sqrt{A(1/r) \left( 1 + \frac{p_\phi^2}{r^2} + \frac{p_r^2}{B} + 2\eta(4 - 3\eta) \frac{p_r^4}{r^2} \right)} \quad (3.46)$$

is the effective Hamiltonian. The equations of motion given this conservative Hamiltonian  $\hat{H}$  and a dissipative radiation-reaction force  $\hat{\mathcal{F}}_i$  are

$$\frac{dr}{dt} = \frac{\partial \hat{H}}{\partial p_r} \quad (3.47)$$

$$\frac{d\phi}{dt} = \frac{\partial \hat{H}}{\partial p_\phi} = \omega \quad (3.48)$$

$$\frac{dp_r}{dt} = -\frac{\partial \hat{H}}{\partial r} + \hat{\mathcal{F}}_r \quad (3.49)$$

$$\frac{dp_\phi}{dt} = -\frac{\partial \hat{H}}{\partial \phi} + \hat{\mathcal{F}}_\phi. \quad (3.50)$$

Here,  $\frac{\partial \hat{H}}{\partial \phi} = 0$  because the EOB Hamiltonian does not have an explicit  $\phi$  dependence. In addition, for circularized binary inspiral the radial component of the radiation-reaction force  $\hat{\mathcal{F}}_r$  is of higher post-Newtonian order than the tangential component, so it is set to zero.

To increase resolution near the black hole, the radial coordinate can be rewritten in terms of a tortoise coordinate [80] defined by

$$\frac{dr_*}{dr} = \left( \frac{B}{A} \right)^{1/2}. \quad (3.51)$$

The new radial momentum is then  $p_{r_*} = (A/B)^{1/2}p_r$ . Using this definition, the effective Hamiltonian becomes

$$\hat{H}_{\text{eff}} = \sqrt{p_{r_*}^2 + A(1/r) \left( 1 + \frac{p_\phi^2}{r^2} + 2\eta(4 - 3\eta)\frac{p_{r_*}^4}{r^2} \right)} \quad (3.52)$$

where the parts that are 4PN and higher are neglected. (The 4 and 5 PN terms are however accounted for in the free parameters  $a_5$  and  $a_6$  which were fit to numerical waveforms). The equations of motion become

$$\frac{dr}{dt} = \frac{A}{\sqrt{D}} \frac{\partial \hat{H}}{\partial p_{r_*}} \quad (3.53)$$

$$\frac{d\phi}{dt} = \frac{\partial \hat{H}}{\partial p_\phi} = \omega \quad (3.54)$$

$$\frac{dp_{r_*}}{dt} = -\frac{A}{\sqrt{D}} \frac{\partial \hat{H}}{\partial r} \quad (3.55)$$

$$\frac{dp_\phi}{dt} = \hat{\mathcal{F}}_\phi. \quad (3.56)$$

### 3.4.2 Radiation reaction

For the radiation reaction term  $\hat{\mathcal{F}}_\phi$ , which is written in terms of the PN parameter  $x$ , we will need a way to write  $x$  in terms of the dynamical variables. The usual method is to use the Newtonian potential  $1/r$  and velocity squared  $(\omega r)^2$  as PN counting parameters and then rewrite them in terms of the gauge invariant angular velocity  $\omega$  using the Kepler law  $\omega^2 r^3 = 1$  which holds in the Newtonian limit, and for circular orbits, in the Schwarzschild ( $\eta \rightarrow 0$ ) limit. The Kepler relation can be extended to circular orbits in the EOB metric by defining a new radial parameter,  $r_\omega = r\psi^{1/3}$ , where

$$\psi(r, p_\phi) = \frac{2}{r^2} \left( \frac{dA}{dr} \right)^{-1} \left[ 1 + 2\eta \left( \sqrt{A(r) \left( 1 + \frac{p_\phi^2}{r^2} \right)} - 1 \right) \right], \quad (3.57)$$

for which  $\omega^2 r_\omega^3 = 1$  holds for all circular orbits. In addition, for noncircular orbits (in particular for the plunge), this relation also relaxes the quasicircular condition by not requiring that the Kepler relation hold. The specific choice of PN parameter used here is

$$x = (\omega r_\omega)^2. \quad (3.58)$$

See Ref. [81] for an extensive discussion.

The radiation reaction term  $\hat{\mathcal{F}}_\phi$  used in Ref. [76] takes the form of a summation over all multipoles

$$\hat{\mathcal{F}}_\phi = -\frac{1}{8\pi\eta\omega} \sum_{\ell=2}^8 \sum_{m=1}^{\ell} (m\omega)^2 |\hat{D}h_{\ell m}|^2. \quad (3.59)$$

Instead of using the standard Taylor expanded version of  $h_{\ell m}$  which can be found in Ref. [69], Ref. [78] decomposes the waveform into a product of terms

$$h_{22} = h_{22}^{\text{Newt}} \hat{S}_{\text{eff}} T_{22} e^{i\delta_{22}} f_{22}(x) f_{22}^{\text{NQC}} \quad (3.60)$$

for  $\ell = m = 2$ , and

$$h_{\ell m} = h_{\ell m}^{\text{Newt}} \hat{S}_{\text{eff}} T_{\ell m} e^{i\delta_{\ell m}} \rho_{\ell m}^\ell(x) \quad (3.61)$$

for the other values of  $\ell$  and  $m$ . The leading Newtonian part  $h_{\ell m}^{\text{Newt}}$  is given in the usual form as a function of  $x$

$$h_{\ell m}^{\text{Newt}} = \frac{\eta}{\hat{D}} n_{\ell m} c_{\ell+\epsilon}(\eta) x^{(\ell+\epsilon)/2} Y^{\ell-\epsilon, -m} \left( \frac{\pi}{2}, \phi \right) \quad (3.62)$$

where the coefficients  $n_{\ell m}$  and  $c_{\ell+\epsilon}(\eta)$  are defined by Eqs. (5–7) of Ref. [78], and the parity  $\epsilon$  is 0 for  $\ell + m$  even and 1 for  $\ell + m$  odd.

The PN terms in the resummation which had been written as functions of  $x$  in Ref. [78] are now written in terms of the dynamical variables. The effective source term  $\hat{S}_{\text{eff}}$  becomes [82]

$$\hat{S}_{\text{eff}}(r, p_{r_*}, p_\phi) = \begin{cases} \hat{H}_{\text{eff}}(r, p_{r_*}, p_\phi) & \epsilon = 0 \\ \frac{p_\phi}{r_\omega^2 \omega} & \epsilon = 1 \end{cases}. \quad (3.63)$$

The tail term is

$$T_{\ell m}(r, p_{r_*}, p_\phi) = \frac{\Gamma(\ell + 1 - 2i\hat{k})}{\Gamma(\ell + 1)} e^{\pi\hat{k}} e^{2i\hat{k} \ln 2kr_0}, \quad (3.64)$$

where  $\hat{k} = \eta m \hat{H}(r, p_{r_*}, p_\phi) \omega(r, p_{r_*}, p_\phi)$ ,  $k = m\omega(r, p_{r_*}, p_\phi)$ , and  $r_0 = 2$ . The phase of this tail term is corrected with a term of the form  $e^{i\delta_{\ell m}}$ . The first ten  $\delta_{\ell m}$  are given in Eqs. (20–29) of Ref. [78]. The first one is

$$\delta_{22} = \frac{7}{3} y^{3/2} + \frac{428\pi}{105} y^3 - 24\eta \bar{y}^{5/2}, \quad (3.65)$$

where  $y = (\eta \hat{H}(r, p_{r_*}, p_\phi) \omega(r, p_{r_*}, p_\phi))^2$  and  $\bar{y}$ , which has several possible forms, is chosen to be  $\bar{y} = \omega^{2/3}$  [82]. Finally, the remainder term of the resummation  $f_{\ell m}$  is expanded in powers of  $x$ . For  $\ell = m = 2$  this is then re-summed with a Padé approximant

$$f_{22}(x) = P_2^3[f_{22}^{\text{Taylor}}(x)], \quad (3.66)$$

where

$$\begin{aligned}
f_{22}^{\text{Taylor}}(\eta, x) = & 1 + \frac{55\eta - 86}{42}x + \frac{2047\eta^2 - 6745\eta - 4288}{1512}x^2 \\
& + \left( \frac{114635\eta^3}{99792} - \frac{227875\eta^2}{33264} + \frac{41\pi^2\eta}{96} - \frac{34625\eta}{3696} - \frac{856}{105}\text{eulerln}_2(x) + \frac{21428357}{727650} \right) x^3 \\
& + \left( \frac{36808}{2205}\text{eulerln}_2(x) - \frac{5391582359}{198648450} \right) x^4 \\
& + \left( \frac{458816}{19845}\text{eulerln}_2(x) - \frac{93684531406}{893918025} \right) x^5,
\end{aligned} \tag{3.67}$$

and the  $\text{eulerln}_m(x) = \gamma_E + \ln 2 + \frac{1}{2} \ln x + \ln m$  terms are treated as constants when calculating the Padé approximant. For the other values of  $\ell$  and  $m$ ,  $f_{\ell m}$  is re-summed in the form  $f_{\ell m} = \rho_{\ell m}^{\ell}$ . The quantity  $\rho_{\ell m}$  is given in Eqs. (C1–C35) of Ref. [78].  $\rho_{21}$  is for example

$$\begin{aligned}
\rho_{21} = & 1 + \left( \frac{23\eta}{84} - \frac{59}{56} \right) x + \left( \frac{617\eta^2}{4704} - \frac{10993\eta}{14112} - \frac{47009}{56448} \right) x^2 \\
& + \left( \frac{7613184941}{2607897600} - \frac{107}{105}\text{eulerln}_1(x) \right) x^3 \\
& + \left( \frac{6313}{5880}\text{eulerln}_1(x) - \frac{1168617473883}{911303737344} \right) x^4.
\end{aligned} \tag{3.68}$$

The final product in the resummation of  $h_{22}$  is a next-to-quasicircular (NQC) correction term that is used to correct the dynamics and waveform amplitude during the plunge

$$f_{22}^{\text{NQC}}(a_1, a_2) = 1 + \frac{a_1 p_{r_*}^2}{(r\omega)^2} + \frac{a_2 \dot{r}}{r\omega^2}. \tag{3.69}$$

The free parameters  $a_1$  and  $a_2$  are determined by the following conditions: (i) the time when the orbital frequency  $\omega$  is a maximum (the EOB merger time  $t_M$ ) coincides with the time when the amplitude  $|h_{22}|$  is a maximum, and (ii) the value of the maximum amplitude is equal to a fitting function that was fit to several BBH simulations, given by [76]

$$|h_{22}|_{\text{max}}(\eta) = 1.575\eta(1 - 0.131(1 - 4\eta)), \tag{3.70}$$

and is accurate to  $\sim 1\%$ .

### 3.4.3 Integrating the equations of motion

The equations of motion are solved by starting with initial conditions  $\{r_0, \phi_0, p_{r_*0}, p_{\phi 0}\}$  and numerically integrating the equations of motion. In this paper we are interested in long,

zero-eccentricity orbits. This can be achieved in the EOB framework by starting the integration with large  $r$ , where radiation reaction effects are small, and using the quasicircular condition  $p_{r_*} = 0$ . Eq. (3.55) then becomes

$$\frac{\partial H}{\partial r}(r, p_{r_*} = 0, p_\phi) = 0 \quad (3.71)$$

and results in the condition

$$p_\phi^2 = -\frac{\frac{d}{du}A(u)}{\frac{d}{du}(u^2A(u))} \quad (3.72)$$

for  $p_\phi$ . If this quasicircular initial condition is used for smaller  $r$ , the radiation reaction term is no longer negligible, and this initial condition will result in eccentric orbits. If desired, one can use an initial condition that more accurately approximates a zero eccentricity inspiral such as post-circular or post-post-circular initial conditions with nonzero  $p_{r_*}$  [83].

To numerically solve Eqs. (3.53–3.56), they must be written as a system of first order equations. However, the term  $\hat{\mathcal{F}}_\phi$  in Eq. (3.56) which is constructed from Eqs. (3.59–3.69), contains the square of  $\ddot{r}$  from the NQC term  $f_{22}^{\text{NQC}}$  (Eq. 3.69). Since  $f_{22}^{\text{NQC}}$  gives a small correction of order 10% during the plunge, the easiest method, and that used in Ref. [76], is iteration [82]: (i) First solve the system of equations with  $f_{22}^{\text{NQC}}$  set to one. (ii) Use the solution of Eqs. (3.53–3.56) to evaluate  $\ddot{r}$  and the other quantities in  $f_{22}^{\text{NQC}}$ . (iii) Re-solve the equations of motion with the NQC coefficients no longer set to one. (iv) Repeat steps (ii) and (iii) until the solution converges to the desired accuracy. In practice this iteration only needs to be done 2–5 times.

A second method is to directly rewrite Eq. (3.56) as a first order equation. This can be done by replacing  $\ddot{r}$  in the NQC term (Eq. 3.69), contained in the expression for  $\hat{\mathcal{F}}$  on the right hand side of Eq. (3.56), with an expression containing  $\dot{p}_\phi$  and then solving for  $\dot{p}_\phi$ . The equations of motion (3.53–3.56) and the chain rule give

$$\begin{aligned} \ddot{r} &= \frac{d}{dt} \left( \frac{A}{\sqrt{D}} \frac{\partial \hat{H}}{\partial p_{r_*}} \right) \\ &= L + M + N\dot{p}_\phi, \end{aligned} \quad (3.73)$$

where

$$L = \frac{1}{2} \frac{\partial}{\partial r} \left[ \frac{A^2}{D} \left( \frac{\partial \hat{H}}{\partial p_{r_*}} \right)^2 \right] \quad (3.74)$$

$$M = -\frac{A^2}{D} \frac{\partial \hat{H}}{\partial r} \frac{\partial^2 \hat{H}}{\partial p_{r_*}^2} \quad (3.75)$$

$$N = \frac{A}{\sqrt{D}} \frac{\partial^2 \hat{H}}{\partial p_{r_*} \partial p_\phi}. \quad (3.76)$$

Plugging Eq. (3.73) into the expression for  $\hat{\mathcal{F}}$  in Eq. (3.56) yields an equation quadratic in  $\dot{p}_\phi$  which can be solved exactly if desired. To first order in the NQC correction term, Eq. (3.56) now becomes the first order equation

$$\frac{dp_\phi}{dt} = \frac{\hat{\mathcal{F}}_{\phi,\text{Higher}} + \hat{\mathcal{F}}_{\phi,22}^{\text{QC}} \left[ 1 + 2\frac{a_1 p_{r_*}^2}{(r\omega)^2} + 2\frac{a_2}{r\omega^2}(L+M) \right]}{1 - 2\hat{\mathcal{F}}_{\phi,22}^{\text{QC}} \frac{a_2}{r\omega^2} N}, \quad (3.77)$$

where

$$\hat{\mathcal{F}}_{\phi,\text{Higher}} = -\frac{1}{8\pi\eta\omega} \sum_{\ell=2}^8 \sum_{\substack{m=1 \\ (\ell,m) \neq (2,2)}}^{\ell} (m\omega)^2 |\hat{D}h_{\ell m}|^2 \quad (3.78)$$

includes just the higher order terms  $(\ell, m) \neq (2, 2)$ , and

$$\hat{\mathcal{F}}_{\phi,22}^{\text{QC}} = -\frac{1}{8\pi\eta\omega} (2\omega)^2 |\hat{D}h_{22}^{\text{QC}}|^2. \quad (3.79)$$

Here,  $h_{22}^{\text{QC}} = h_{22}/f_{22}^{\text{NQC}}$  is the portion of  $h_{22}$  that does not contain the NQC term.

The solution to the equations of motion  $\{r(t), \phi(t), p_{r_*}(t), p_\phi(t)\}$  are then plugged back into Eqs. (3.60–3.61) to give the waveform  $h_{\ell m}^{\text{inspiral}}(t)$ .

### 3.4.4 Ringdown

In the EOB formalism the ringdown waveform of the final Kerr black hole is smoothly matched onto the inspiral waveform at the EOB merger time  $t_M$ . The mass of the black hole remnant is given by the energy of the EOB particle at the merger time  $t_M$

$$M_{\text{BH}} \equiv \mu \hat{H}(t_M) = M \sqrt{1 + 2\eta(\hat{H}_{\text{eff}}(t_M) - 1)}, \quad (3.80)$$

and the Kerr parameter is given by the final angular momentum of the EOB particle [84]

$$\hat{a}_{\text{BH}} \equiv \frac{P_\phi(t_M)}{M_{\text{BH}}^2} = \frac{\eta p_\phi(t_M)}{1 + 2\eta(\hat{H}_{\text{eff}}(t_M) - 1)}. \quad (3.81)$$

The ringdown waveform is given by the first five positive quasinormal modes (QNM) for a black hole of mass  $M_{\text{BH}}$  and spin  $\hat{a}_{\text{BH}}$ :

$$h_{22}^{\text{ringdown}}(t) = \frac{1}{\hat{D}} \sum_{n=0}^4 C_{22n}^+ e^{-\sigma_{22n}^+(t-t_M)}, \quad (3.82)$$

where  $\sigma_{22n}^+ = \alpha_{22n} + i\omega_{22n}$  is the  $n$ th complex  $\ell = m = 2$  QNM frequency for a Kerr BH with mass  $\hat{M}_{\text{BH}}$  and spin  $\hat{a}_{\text{BH}}$ , and  $C_{22n}^+$  are complex constants that determine the magnitude and phase of each QNM. The amplitude of the negative frequency modes is small [80]. The

first three QNMs have been tabulated in Ref. [79], and fitting formulæ are also provided. The QNM frequency  $\omega_{22n}$  can be approximated by

$$M_{\text{BH}}\omega_{22n} = f_1 + f_2(1 - \hat{a}_{\text{BH}})^{f_3}, \quad (3.83)$$

and the inverse damping time  $\alpha_{22n}$  is given in terms of the quality factor approximated by

$$\frac{1}{2} \frac{\omega_{22n}}{\alpha_{22n}} = q_1 + q_2(1 - \hat{a}_{\text{BH}})^{q_3}. \quad (3.84)$$

The coefficients for  $n = 0-2$  can be found in table VIII of Ref. [79]. For  $n = 3-4$ ,  $\alpha_{22n}$  and  $\omega_{22n}$  can be linearly extrapolated from the values for  $n = 1$  and 2 as was done in Ref. [83].

The constants  $C_{22n}^+$  are determined by requiring that the inspiral and ringdown waveforms be continuous on a “matching comb” centered on the EOB merger time  $t_M$ . Specifically, at the times  $\{t_M - 2\delta, t_M - \delta, t_M, t_M + \delta, t_M + 2\delta\}$  we require  $h_{22}^{\text{inspiral}}(t) = h_{22}^{\text{ringdown}}(t)$ . In Ref. [76],  $\delta$  was chosen to be equal to  $2.3M_{\text{BH}}/M$ . This gives 5 complex equations for the 5 unknown complex coefficients  $C_{22n}^+$ .

The full inspiral plus ringdown waveform is then given by

$$h_{22}(t) = \begin{cases} h_{22}^{\text{inspiral}}(t) & t < t_M \\ h_{22}^{\text{ringdown}}(t) & t > t_M \end{cases}. \quad (3.85)$$

## Chapter 4

# Tidal interactions during binary inspiral

For BNS and BHNS inspiral, tidal interactions are the primary correction to the point-particle dynamics described in the last chapter. These interactions, which to leading order are Newtonian effects, have not received much attention because they are  $\mathcal{O}\left[\left(\frac{R}{M}\right)^5 x^5\right]$  corrections to the leading point-particle interactions where  $M$  is the total mass, and  $R$  is the NS radius, and thus appear to be 5PN effects. However, the additional  $(R/M)^5$  dependence means that they will dominate all PN corrections for systems such as the Earth and Moon, while for BNS systems where  $(R/M)^5 \sim \mathcal{O}(10^4)$ , we will find they have effects of similar magnitude to 3.5PN point-particle terms during the inspiral.

For widely separated relativistic sources, the problem of tidal interactions can be solved by breaking spacetime into two regions as shown in Fig. 18. In the weak-field vacuum region away from a source, the post-Newtonian expansion can be used. However, in the strong-field region containing the source, the full Einstein equations must be solved. The results can then be matched in a buffer region surrounding each source. In the following section we describe tidal interactions in Newtonian gravity based on the discussion in Refs. [85, 86]; then, in the final section using the method developed in Ref. [87], we solve the perturbed Einstein equations for the compact objects in the strong-field region and describe how the solution is matched in a buffer region to the Newtonian description of tidal interactions.

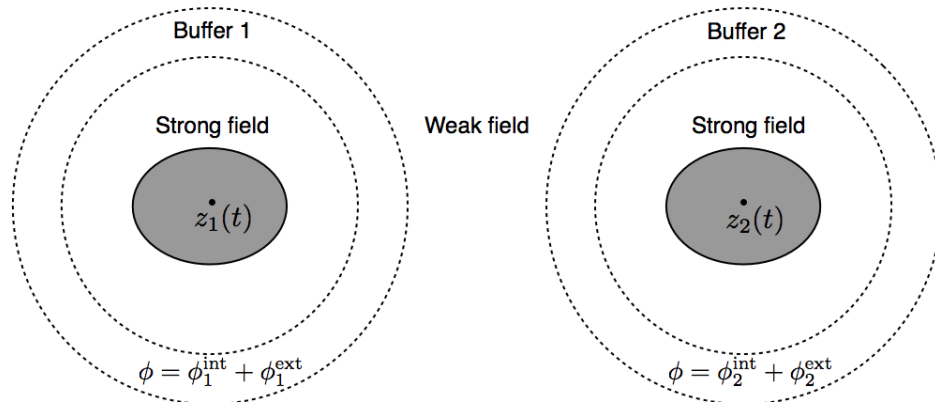


Figure 18 : As shown in Ref. [88], spacetime is decomposed into a weak-field region and a strong-field region surrounding each compact object (gray). The strong-field and weak-field solutions can be matched in a buffer region.

## 4.1 Newtonian tidal interactions

### 4.1.1 Gravitational potential, multipoles, and tidal fields

In Newtonian gravity the gravitational potential due to a system of extended bodies (Fig. 18) with density  $\rho$  is<sup>1</sup>

$$\phi(\vec{x}) = - \int d^3x' \frac{\rho(t, \vec{x}')}{|\vec{x} - \vec{x}'|}. \quad (4.1)$$

To calculate the dynamics of this system, we will find it useful to decompose this potential, in each domain, into an internal part  $\phi_A^{\text{int}}$  sourced by the matter in that domain, which we will write as a sum over multipoles  $M_A^L$ , and an external part  $\phi_A^{\text{ext}}$  sourced by the matter from other bodies, which we will write as a sum over tidal fields  $G_A^L$ . The total potential in domain will therefore be  $\phi = \phi_A^{\text{int}} + \phi_A^{\text{ext}}$ .

We can expand a multivariate function  $f(x^i)$  using a Taylor series

$$f(x^i) = \sum_{\ell=0}^{\infty} \frac{1}{\ell!} (x - a)^L [\partial_L f(x^i)]_{x^i=a^i}, \quad (4.2)$$

where  $L$  is a multi-index representing the  $\ell$  indices  $L = a_1 a_2 \dots a_\ell$ ,  $x^L = x^{a_1} x^{a_2} \dots x^{a_\ell}$ , and  $\partial_L = \frac{\partial^\ell}{\partial x^{a_1} \partial x^{a_2} \dots \partial x^{a_\ell}}$ . Using this, we can expand the denominator of the internal

<sup>1</sup>The gravitational potential energy of a test mass with mass  $m$  in this potential is  $U = m\phi$ . The gravitational potential energy of the entire system will be given by Eq. (4.14).

potential about the center of mass (COM) of the star  $z_A^i$ <sup>2</sup> by expanding in the variable  $x^i$

$$\begin{aligned} \frac{1}{|\vec{x} - \vec{x}'|} &= \sum_{\ell=0}^{\infty} \frac{1}{\ell!} (x' - z)^L \left[ \frac{\partial^\ell}{\partial x'^L} \frac{1}{|\vec{x} - \vec{x}'|} \right]_{\vec{x}' = \vec{z}_A} \\ &= \sum_{\ell=0}^{\infty} \frac{(-1)^\ell}{\ell!} (x' - z)^L \partial_L \frac{1}{|\vec{x} - \vec{z}_A|}, \end{aligned} \quad (4.3)$$

where  $\partial_L = \frac{\partial^\ell}{\partial x^L}$ . We note that  $\partial_L \frac{1}{|\vec{x} - \vec{z}_A|}$  is a symmetric trace free (STF) tensor for  $\vec{x} \neq \vec{z}_A$  because the trace of any pair of indices involves  $\partial_i \partial_i \frac{1}{|\vec{x} - \vec{z}_A|} = \nabla^2 \frac{1}{|\vec{x} - \vec{z}_A|} = -4\pi \delta^{(3)}(\vec{x} - \vec{z}_A)$  is zero unless  $\vec{x}$  coincides with the COM. The internal potential at a point  $\vec{x}$  can now be written in terms of the integral over body A,

$$\begin{aligned} \phi_A^{\text{int}}(t, \vec{x}) &= - \int_A d^3 x' \frac{\rho(t, \vec{x}')}{|\vec{x} - \vec{x}'|} \\ &= - \sum_{\ell=0}^{\infty} \frac{(-1)^\ell}{\ell!} M_A^L(t) \partial_L \frac{1}{|\vec{x} - \vec{z}_A(t)|}, \end{aligned} \quad (4.4)$$

where  $M_A^L$  is the  $\ell$ th multipole of the body defined by

$$M_A^L(t) = \int_A d^3 x \rho(t, \vec{x}) (x - z_A(t))^{(L)}. \quad (4.5)$$

The notation  $T^{(L)}$  denotes the STF part of a tensor  $T^L$ . Using the fact that for any two tensors  $S^L$  and  $T^L$ ,  $S^L T^{(L)} = S^{(L)} T^{(L)}$ , we have defined  $M_A^L$  as STF because  $\partial_L \frac{1}{|\vec{x} - \vec{z}_A|}$  is already STF. The first four moments are the mass, dipole, quadrupole, and octopole, defined in terms of  $\bar{x}^i = x^i - z^i$  by

$$M = \int d^3 x \rho, \quad (4.6)$$

$$M^i = \int d^3 x \rho \bar{x}^i = 0, \quad (4.7)$$

$$M^{ij} = \int d^3 x \rho (\bar{x}^i \bar{x}^j - \frac{1}{3} \delta^{ij} |\bar{x}|^2) = Q^{ij}, \quad (4.8)$$

$$M^{ijk} = \int d^3 x \rho [\bar{x}^i \bar{x}^j \bar{x}^k - \frac{1}{5} (\delta^{ij} \bar{x}^k + \delta^{jk} \bar{x}^i + \delta^{ki} \bar{x}^j) |\bar{x}|^2] = O^{ijk}. \quad (4.9)$$

The dipole is zero because  $z^i$  is the COM.

We similarly can expand the external potential about the COM of body A

$$\begin{aligned} \phi_A^{\text{ext}}(t, \vec{x}) &= \sum_{\ell=0}^{\infty} \frac{1}{\ell!} (x - z_A(t))^L [\partial_L \phi_A^{\text{ext}}(t, \vec{x})]_{\vec{x} = \vec{z}_A} \\ &= - \sum_{\ell=0}^{\infty} \frac{1}{\ell!} G_A^L(t) (x - z_A(t))^L, \end{aligned} \quad (4.10)$$

---

<sup>2</sup>The COM of body A is defined by  $z_A^i(t) = \frac{1}{M_A} \int_A d^3 x \rho(t, \vec{x}) x^i$ .

where the  $\ell$ th order tidal field  $G_A^L$  due to the potential from body B is

$$\begin{aligned}
G_A^L(t) &= -[\partial_L \phi_A^{\text{ext}}(t, \vec{x})]_{\vec{x}=\vec{z}_A} \\
&= -[\partial_L \phi_B^{\text{int}}(t, \vec{x})]_{\vec{x}=\vec{z}_A} \\
&= -\left[ \partial_L \left( -\sum_{k=0}^{\infty} \frac{(-1)^k}{k!} M_B^K(t) \partial_K \frac{1}{|\vec{x} - \vec{z}_B(t)|} \right) \right]_{\vec{x}=\vec{z}_A} \\
&= \sum_{k=0}^{\infty} \frac{(-1)^k}{k!} M_B^K(t) \partial_{KL}^{(A)} \frac{1}{|\vec{z}_A(t) - \vec{z}_B(t)|},
\end{aligned} \tag{4.11}$$

and  $\partial_{KL}^{(A)} = \frac{\partial^{k+\ell}}{\partial z_A^{KL}}$ . As an example, the  $\ell = 2$  tidal field  $G_A^{ij}$  leads to a quadratic potential relative to the COM of body A. This tidal field includes contributions from the monopole, quadrupole, octopole, ... moments of body B, and these contributions scale with the separation  $r$  of the two bodies as  $1/r^3$ ,  $1/r^5$ ,  $1/r^6$ , ... respectively.

#### 4.1.2 Lagrangian and energy

Given the above expressions for the matter distribution and gravitational potential, we can determine the kinetic and potential energy of the system and then write down the corresponding Lagrangian  $L = T - U$ . The Lagrangian can then be used to find the equations of motion (EOM) via the Euler-Lagrange equations.

The total kinetic energy of the system can be decomposed into contributions from the COM of each body as well as from the internal kinetic energy from motion about the COM of each body

$$\begin{aligned}
T(t) &= \frac{1}{2} \int d^3x \rho(t, \vec{x}) v^2(t, \vec{x}) \\
&= \sum_A \frac{1}{2} \int_A d^3x \rho(t, \vec{x}) v^2(t, \vec{x}) \\
&= \sum_A \frac{1}{2} \int_A d^3x \rho [z_A^i + (v - \dot{z}_A)^i] [z_A^i + (v - \dot{z}_A)^i] \\
&= \sum_A \left( \frac{1}{2} M_A \dot{z}_A^2 + T^{\text{int}} \right),
\end{aligned} \tag{4.12}$$

where we used the definition of the COM, and the internal kinetic energy is defined as

$$T_A^{\text{int}}(t) = \frac{1}{2} \int_A d^3x \rho(t, \vec{x}) [v(t, \vec{x}) - \dot{z}_A(t)]^2. \tag{4.13}$$

For a closed system of gravitationally interacting, extended bodies, the total potential

energy is

$$\begin{aligned}
U(t) &= \frac{1}{2} \int d^3x \rho(t, \vec{x}) \phi(t, \vec{x}) \\
&= \sum_A \frac{1}{2} \int_A d^3x \rho(t, \vec{x}) \phi(t, \vec{x}) \\
&= \sum_A (U_A^{\text{int}}(t) + U_A^{\text{ext}}(t)).
\end{aligned} \tag{4.14}$$

We have broken up the potential at each body A into a contribution  $\phi_A^{\text{int}}$  due to sources inside the body and a contribution  $\phi_A^{\text{ext}}$  due to sources outside the body. The corresponding internal and external contributions to the potential energy associated with each body are therefore

$$U_A^{\text{int}}(t) = \frac{1}{2} \int_A d^3x \rho(t, \vec{x}) \phi_A^{\text{int}}(t, \vec{x}), \tag{4.15}$$

and

$$\begin{aligned}
U_A^{\text{ext}}(t) &= \frac{1}{2} \int_A d^3x \rho(t, \vec{x}) \phi_A^{\text{ext}}(t, \vec{x}) \\
&= -\frac{1}{2} \sum_{\ell=0}^{\infty} \frac{1}{\ell!} \int_A d^3x \rho(t, \vec{x}) [x - z_A(t)]^L G_A^L(t) \\
&= -\frac{1}{2} \sum_{\ell=0}^{\infty} \frac{1}{\ell!} M_A^L(t) G_A^L(t).
\end{aligned} \tag{4.16}$$

In the last line we again used the fact that  $G_A^L$  is STF to rewrite the integral as a STF multipole.

The Lagrangian for the system can now be written

$$L = \sum_A \left( \frac{1}{2} M_A \dot{z}_A^2 + \frac{1}{2} \sum_{\ell=0}^{\infty} \frac{1}{\ell!} M_A^L G_A^L + L_A^{\text{int}} \right), \tag{4.17}$$

where the internal Lagrangian for each body is defined as  $L_A^{\text{int}} = T_A^{\text{int}} - U_A^{\text{int}}$ .

The internal dynamics of body A can be determined from the Poisson, Euler, and continuity equations as well as the equation of state (EOS), or for relativistic stars, the Einstein equation, conservation of stress-energy, and the EOS. However, we would like instead to describe the dynamics in terms of a set of canonical variables so that we can use the Lagrangian formalism. To do this, we use the fact that perturbations of a stable spherical star (both nonrelativistic and relativistic) can be decomposed into modes  $n$ , each belonging to a single spherical harmonic, and each oscillating with a characteristic frequency  $\omega_{An}$ . The EOM for the contribution to the  $\ell$ th multipole of body A due to mode  $n$  ( $M_{An}^L$ ) is

$$\ddot{M}_{An}^L + \omega_{An}^2 M_{An}^L = 0. \tag{4.18}$$

The quantities  $M_{An}^L$  can therefore be the canonical variables. The Lagrangian that produces this EOM via the Euler-Lagrange equations is, up to a constant  $\alpha_{A\ell n}$ ,

$$L_{A\ell n}^{\text{int}} = \alpha_{A\ell n}(\dot{M}_{An}^L \dot{M}_{An}^L - \omega_{An}^2 M_{An}^L M_{An}^L), \quad (4.19)$$

so that the total internal Lagrangian of body A is  $L_A^{\text{int}} = \sum_{\ell=0}^{\infty} \sum_n L_{A\ell n}^{\text{int}}$ . Since this Lagrangian is derived from the kinematic assumption of simple harmonic motion and not from Newtonian dynamics, it will be true for relativistic stars as well, (assuming the completeness of outgoing modes for describing the fluid, and ignoring additional gravitational wave degrees of freedom).

The constant can be found by assuming a situation in which the modes of body A evolve adiabatically [89]—driven by the motion of body B at a frequency much slower than the mode frequency. The time derivatives  $\dot{M}_{An}^L$  will therefore be zero, and the Euler-Lagrange equation for the entire Lagrangian will be

$$\begin{aligned} \frac{d}{dt} \frac{\partial L}{\partial \dot{M}_{An}^L} &= \frac{\partial L}{\partial M_{An}^L} \\ 0 &= \frac{\partial}{\partial M_{An}^L} \sum_A \left[ \frac{1}{2} M_A \dot{z}_A^2 + \frac{1}{2} \sum_{\ell=0}^{\infty} \frac{1}{\ell!} \left( \sum_n M_{An}^L \right) G_A^L - \sum_{\ell=0}^{\infty} \sum_n \alpha_{A\ell n} \omega_{An}^2 M_{An}^L M_{An}^L \right] \\ &= \frac{1}{\ell!} G_A^L - 2\alpha_{A\ell n} \omega_{An}^2 M_{An}^L, \end{aligned} \quad (4.20)$$

where the multipoles  $M_A^K$  are hidden in the definition of  $G_B^L$ , and we used the fact that

$$\frac{1}{2} \sum_A \sum_{\ell=0}^{\infty} \frac{1}{\ell!} M_A^L G_A^L = \sum_{\ell=0}^{\infty} \frac{1}{\ell!} M_1^L G_1^L = \sum_{\ell=0}^{\infty} \frac{1}{\ell!} M_2^L G_2^L \quad (4.21)$$

for a two body system as can be shown by writing  $G_A^L$  explicitly in terms of  $M_B^L$  using Eq. (4.11). Eq. (4.20) demonstrates that the  $\ell$ th multipole  $M_{An}^L$  can be written explicitly in terms of the  $\ell$ th tidal field  $G_A^L$  with only a single EOS dependent constant

$$M_{An}^L = \lambda_{A\ell n} G_A^L. \quad (4.22)$$

Summing over n we obtain<sup>3</sup>

$$M_A^L = \lambda_{A\ell} G_A^L, \quad (4.23)$$

where  $\lambda_{A\ell} = \sum_n \lambda_{A\ell n}$  is called the tidal deformability of star A, and  $\lambda_{A\ell n}$  is the component that contributes to  $M_{An}^L$ . We will derive this quantity from the perturbed Einstein equations

---

<sup>3</sup>We emphasize that this relation holds only for adiabatic changes in the tidal field. When the tidal field changes at a rate close to the mode frequency, resonance can occur as will be discussed below.

and an EOS model in the next section. The constant  $\alpha_{A\ell n}$  in the Lagrangian can finally be written

$$\alpha_{A\ell n} = \frac{1}{2\ell!\lambda_{A\ell n}\omega_{An}}. \quad (4.24)$$

In general, the energy of a system with canonical variables  $q^\alpha$  is

$$E = \frac{\partial L}{\partial \dot{q}^\alpha} \dot{q}^\alpha - L. \quad (4.25)$$

For the Lagrangian here, this is equivalent to reversing the sign on the potential energy terms, so that the total energy is

$$E = \sum_A \left[ \frac{1}{2} M_A \dot{z}_A^2 - \frac{1}{2} \sum_{\ell=0}^{\infty} \frac{1}{\ell!} M_A^L G_A^L + \sum_{\ell=0}^{\infty} \sum_n \frac{1}{2\ell!\lambda_{A\ell n}\omega_{An}^2} (\dot{M}_{An}^L \dot{M}_{An}^L + \omega_{An}^2 M_{An}^L M_{An}^L) \right]. \quad (4.26)$$

### 4.1.3 Tidal Corrections to the post-Newtonian waveform

In order to derive the lowest order corrections to the post-Newtonian waveform, we now specialize to the case of circular orbits and include only monopole–monopole and monopole–quadrupole interactions. We also assume that for body A the majority of the quadrupole oscillates with a natural frequency  $\omega_A$ . The Lagrangian for such a system is

$$L = \frac{1}{2} \mu \dot{z}^2 + \frac{\mu M}{r} + \frac{1}{2!} Q_1^{ij} M_2 \partial_{ij} \frac{1}{r} + \mathcal{O}\left(\frac{1}{r^4}\right) + \frac{1}{4\lambda_1 \omega_1^2} (\dot{Q}_1^{ij} \dot{Q}_1^{ij} - \omega_1^2 Q_1^{ij} Q_1^{ij}), \quad (4.27)$$

where  $z^i = z_2^i - z_1^i$ ,  $\mu = M_1 M_2 / M$  is the reduced mass, and we have moved to the center of mass frame of the system ( $M_1 z_1^i + M_2 z_2^i = 0$ ). We have also simplified notation by redefining  $\lambda_A$  as the  $\ell = 2$  tidal deformability of body A, and we have suppressed the contribution from the quadrupole of body 2 which will have the same form as that from body 1 and can simply be added to the final results. The Euler-Lagrange equations now give the following equations of motion

$$\ddot{Q}_1^{ij} + \omega_1^2 Q_1^{ij} = M_2 \lambda_1 \omega_1^2 \partial_{ij} \frac{1}{r}, \quad (4.28)$$

$$\ddot{z}^i = -\frac{M n^i}{r^2} + \frac{M_2}{2\mu} Q_1^{jk} \partial_{ijk} \frac{1}{r}. \quad (4.29)$$

The first equation represents forced oscillations. Under the assumption of circular orbits  $z^i(t) = r n^i(t)$  where  $n^i = (\cos \phi, \sin \phi, 0)$ , and using the fact that

$$\partial_L \frac{1}{r} = (-1)^\ell (2\ell - 1)!! \frac{n^{(L)}}{r^{\ell+1}}, \quad (4.30)$$

we find that the forcing function has a frequency of twice the orbital frequency  $\Omega$  where  $\phi(t) = \Omega t$  because

$$n^{(ij)} = n^i n^j - \frac{1}{3} \delta^{ij} = \begin{bmatrix} \frac{1}{2} \cos 2\phi + \frac{1}{6} & \frac{1}{2} \sin 2\phi & 0 \\ \frac{1}{2} \sin 2\phi & -\frac{1}{2} \cos 2\phi + \frac{1}{6} & 0 \\ 0 & 0 & -\frac{1}{3} \end{bmatrix}. \quad (4.31)$$

The solution to the quadrupole is

$$Q_1^{ij}(t) = \frac{3M_2\lambda_1}{r^3} \begin{bmatrix} \frac{1}{2} \frac{1}{1-4\xi^2} \cos 2\phi + \frac{1}{6} & \frac{1}{2} \frac{1}{1-4\xi^2} \sin 2\phi & 0 \\ \frac{1}{2} \frac{1}{1-4\xi^2} \sin 2\phi & -\frac{1}{2} \frac{1}{1-4\xi^2} \cos 2\phi + \frac{1}{6} & 0 \\ 0 & 0 & -\frac{1}{3} \end{bmatrix}, \quad (4.32)$$

where  $\xi = \Omega/\omega_1$ . Note that resonance will occur if the orbital frequency approaches half the mode frequency.

Using this result and  $\ddot{z}^i = -r\Omega^2 n^i$  for circular orbits, the second equation becomes

$$-r\Omega^2 n^i = -\frac{Mn^i}{r^2} - \frac{9}{4} \frac{M_2^2 \lambda_1}{\mu r^7} \left(1 + \frac{3}{1-4\xi^2}\right) n^i. \quad (4.33)$$

To first order in  $\lambda$  we find

$$r(x) = Mx^{-1} \left[1 + \frac{3}{4} \left(1 + \frac{3}{1-4\xi^2}\right) \frac{M_2}{M_1} \frac{\lambda_1 x^5}{M^5} + 1 \leftrightarrow 2\right], \quad (4.34)$$

where  $x = (M\Omega)^{2/3}$  is the standard post-Newtonian parameter.

With these solutions, the energy can be found from the Lagrangian by reversing the sign on the potential energy terms. The result is

$$E(x) = -\frac{1}{2} M\eta x \left[1 - \frac{9}{4} \left(1 + \frac{3-4\xi^2}{1-4\xi^2}\right) \frac{M_2}{M_1} \frac{\lambda_1 x^5}{M^5} + 1 \leftrightarrow 2\right]. \quad (4.35)$$

The rate of energy loss due to gravitational radiation can be found from the quadrupole formula  $\dot{E} = -\frac{1}{5} \langle \ddot{Q}_T^{ij} \ddot{Q}_T^{ij} \rangle$ . The quantity  $Q_T^{ij}$  is the total quadrupole of the system, and can be calculated using the parallel-axis theorem for the total quadrupole of the system

$$Q_T^{ij}(t) = \int d^3x \rho(t, \vec{x}) x^{(ij)} \quad (4.36)$$

$$= \sum_A \int_A d^3x \rho(t, \vec{x}) x^{(ij)} \quad (4.37)$$

$$= \sum_A [M_A z_A^{(ij)}(t) + Q_A^{ij}(t)], \quad (4.38)$$

where the first term in the sum is the multipole due to the monopole of body A, and the second term  $Q_A^{ij}$  is the multipole about the COM of body A as defined in Eq. (4.5). (The

parallel-axis theorem does not hold for higher multipoles, and in general, the expression for the total multipole  $M_T^L$  in terms of the individual multipoles  $M_A^L$  will be more complicated.) The total radiated energy is then

$$\dot{E} = -\frac{32}{5}\eta^2 x^5 \left[ 1 + 6 \left( \frac{M/M_2 + 2 - 2\xi^2}{1 - 4\xi^2} \right) \frac{M_2}{M_1} \frac{\lambda_1 x^5}{M^5} + 1 \leftrightarrow 2 \right]. \quad (4.39)$$

The post-Newtonian waveforms incorporating tidal interactions can now be readily evaluated from the above expressions for the energy of the binary  $E$  and the luminosity  $\mathcal{L} = -\dot{E}$ . The TaylorT1 expressions are obtained by simply adding the point-particle PN and tidal corrections together

$$E(x) = -\frac{1}{2}M\eta x \left[ 1 + (\text{PP-PN}) - 9\frac{m_2}{m_1} \frac{\lambda_1}{M^5} x^5 + 1 \leftrightarrow 2 \right], \quad (4.40)$$

$$\mathcal{L}(x) = \frac{32}{5}\eta^2 x^5 \left[ 1 + (\text{PP-PN}) + 6\frac{m_1 + 3m_2}{m_1} \frac{\lambda_1}{M^5} x^5 + 1 \leftrightarrow 2 \right], \quad (4.41)$$

then evaluating  $dE/dx$  to obtain  $\frac{dx}{dt} = -\frac{\mathcal{L}}{dE/dx}$ . The TaylorT4 waveform expands this ratio to obtain

$$\frac{dx}{dt} = \frac{64}{5} \frac{\eta x^5}{M} \left[ 1 + (\text{PP-PN}) - 156 \frac{\tilde{\lambda}}{M^5} x^5 \right], \quad (4.42)$$

and  $\tilde{\lambda}$  is the mass weighted total tidal deformability defined by

$$\tilde{\lambda} = \frac{1}{26} \left( \frac{M_1 + 12M_2}{M_1} \lambda_1 + \frac{M_2 + 12M_1}{M_2} \lambda_2 \right), \quad (4.43)$$

which has the property that  $\tilde{\lambda} = \lambda_1 = \lambda_2$  when  $M_1 = M_2$ . The TaylorF2 phase correction can be found by using the methods of Section 3.2.3. The phase can then be written

$$\psi_{22}(f) = 2\pi f t_c - 2\phi_c - \frac{\pi}{4} + \frac{3}{128\eta} (\pi M f)^{-5/3} \left[ 1 + (\text{PP-PN}) - 624 \frac{\tilde{\lambda}}{M^5} (\pi M f)^{10/3} \right]. \quad (4.44)$$

## 4.2 The tidal deformability for relativistic stars

We will now describe the method used in Ref. [87] for determining the  $\ell = 2$  tidal deformability  $\lambda$  of a star from the equation of state. As in [87], we consider a static, spherically symmetric star, placed in a static external quadrupolar tidal field  $G^{ij}$ . To linear order, we define the tidal deformability  $\lambda$  relating the star's induced quadrupole moment  $Q^{ij}$  to the external tidal field,

$$Q^{ij} = \lambda G^{ij}. \quad (4.45)$$

The coefficient  $\lambda$  is related to the  $l = 2$  dimensionless tidal Love number  $k_2$  by

$$k_2 = \frac{3}{2} \lambda R^{-5}. \quad (4.46)$$

The star's quadrupole moment  $Q^{ij}$  and the external tidal field  $G^{ij}$  are defined to be coefficients in an asymptotic expansion of the total metric at large distances  $r$  from the star. This expansion includes, for the metric component  $g_{tt}$  in asymptotically Cartesian, mass-centered coordinates, the standard gravitational potential  $M/r$ , plus two leading order terms arising from the perturbation, one describing an external tidal field growing with  $r^2$  and one describing the resulting tidal distortion decaying with  $r^{-3}$ :

$$-\frac{(1+g_{tt})}{2} = \phi^{\text{int}} + \phi^{\text{ext}} \quad (4.47)$$

$$= -\frac{M}{r} - \frac{3Q^{ij}}{2r^3}n^in^j + \mathcal{O}\left(\frac{1}{r^4}\right) + \frac{G^{ij}}{2}r^2n^in^j, \quad (4.48)$$

where  $n^i = z^i/r$  and both  $Q_{ij}$  and  $G_{ij}$  are symmetric and traceless. The relative size of these multipole components of the perturbed spacetime gives the constant  $\lambda$  relating the quadrupole deformation to the external tidal field as in Eq. (4.45).

To compute the metric (4.48), we use the method discussed in [87]. We consider the problem of a linear static perturbation expanded in spherical harmonics following [90]. In the quasiequilibrium limit, the tidal deformation will be axisymmetric around the line connecting the two stars which we take as the axis for the spherical harmonic decomposition. The only azimuthal number will therefore be  $m = 0$ .

A static (zero-frequency) linear  $\ell = 2$  perturbation of a spherically symmetric star is associated with an even-parity perturbation of the metric, which in the Regge-Wheeler gauge [91] can be simplified [87] to give

$$ds^2 = -e^{2\Phi(r)} [1 + H(r)Y_{20}(\theta, \phi)] dt^2 + e^{2\Lambda(r)} [1 - H(r)Y_{20}(\theta, \phi)] dr^2 \\ + r^2 [1 - K(r)Y_{20}(\theta, \phi)] (d\theta^2 + \sin^2\theta d\phi^2), \quad (4.49)$$

where  $K(r)$  is related to  $H(r)$  by  $K'(r) = H'(r) + 2H(r)\Phi'(r)$ . Here primes denote derivatives with respect to  $r$ . The corresponding perturbations of the perfect fluid stress-energy tensor components are  $\delta T_0^0 = -\delta\epsilon(r)Y_{20}(\theta, \phi)$  and  $\delta T_i^i = \delta p(r)Y_{20}(\theta, \phi)$ , where  $\epsilon$  is the energy density and  $p$  the pressure. The function  $H(r)$  satisfies the differential equation

$$\left(-\frac{6e^{2\Lambda}}{r^2} - 2(\Phi')^2 + 2\Phi + \frac{3}{r}\Lambda' + \frac{7}{r}\Phi' - 2\Phi'\Lambda' + \frac{f}{r}(\Phi' + \Lambda')\right) + \left(\frac{2}{r} + \Phi' - \Lambda'\right) H' + H'' = 0. \quad (4.50)$$

Here  $f$  is given by

$$\delta\epsilon = f\delta p \quad (4.51)$$

which for slow changes in matter configurations corresponds to  $f = d\epsilon/dp$ .

The method of calculating the tidal perturbation for a general equation of state table is similar to the method of calculating moment of inertia in the slow rotation approximation [92]. The specific implementation we use follows the moment of inertia calculation in Appendix A of [54], via an augmentation of the OV system of equations<sup>4</sup>:

$$e^{2\Lambda} = \left(1 - \frac{2m}{r}\right)^{-1}, \quad (4.52)$$

$$\frac{d\Phi}{dr} = -\frac{1}{\epsilon + p} \frac{dp}{dr}, \quad (4.53)$$

$$\frac{dp}{dr} = -(\epsilon + p) \frac{m + 4\pi r^3 p}{r(r - 2m)}, \quad (4.54)$$

$$\frac{dm}{dr} = 4\pi r^2 \epsilon. \quad (4.55)$$

The second-order differential equation for  $H$  is separated into a first-order system of ODEs in terms of the usual OV quantities  $m(r)$ ,  $p(r)$ , and  $\epsilon(p)$ , as well as the additional functions  $H(r)$ ,  $\beta(r) = dH/dr$ , and the equation of state function  $f(p) = d\epsilon/dp$

$$\frac{dH}{dr} = \beta \quad (4.56)$$

$$\begin{aligned} \frac{d\beta}{dr} = & 2 \left(1 - 2\frac{m}{r}\right)^{-1} H \left\{ -2\pi [5\epsilon + 9p + f(\epsilon + p)] + \frac{3}{r^2} + 2 \left(1 - 2\frac{m}{r}\right)^{-1} \left(\frac{m}{r^2} + 4\pi r p\right)^2 \right\} \\ & + \frac{2\beta}{r} \left(1 - 2\frac{m}{r}\right)^{-1} \left[ -1 + \frac{m}{r} + 2\pi r^2 (\epsilon - p) \right]. \end{aligned} \quad (4.57)$$

These are combined with Eqs. (4.52)–(4.55), and the augmented system is solved simultaneously. The system is integrated outward starting just outside the center using the expansions  $H(r) = a_0 r^2$  and  $\beta(r) = 2a_0 r$  as  $r \rightarrow 0$ . The constant  $a_0$  determines how much the star is deformed and can be chosen arbitrarily as it cancels in the expression for the Love number.

The ODE for  $H(r)$  outside the star, where  $T_{\mu\nu} = 0$ , has a general solution in terms of associated Legendre functions of the first  $P_n^m(x)$  and second  $Q_n^m(x)$  kind for  $n = m = 2$  and  $x > 1$  given by

$$H = c_1 Q_2^2(r/M - 1) + c_2 P_2^2(r/M - 1). \quad (4.58)$$

These functions are defined by

$$P_2^2(x) = 3(1 - x^2) \quad (4.59)$$

$$Q_2^2(x) = \frac{3}{2}(x^2 - 1) \ln\left(\frac{x+1}{x-1}\right) - \frac{3x^3 - 5x}{z^2 - 1} \quad (4.60)$$

---

<sup>4</sup>Here we present the equations in terms of the radial coordinate  $r$ ; the extension to the enthalpy variable  $\eta$  used in [54] is straightforward.

and have the asymptotic properties  $Q_2^2\left(\frac{r}{M} - 1\right) \sim \frac{8}{5}\left(\frac{M}{r}\right)^3$  and  $P_2^2\left(\frac{r}{M} - 1\right) \sim -3\left(\frac{r}{M}\right)^2$  at large  $r$ . We can now compare this solution to the asymptotic behavior of  $g_{tt}$  given in Eq. (4.48) to relate the coefficients  $c_1$  and  $c_2$  to the external tidal field. Writing the tidal field and quadrupole moments in terms of the corresponding  $\ell = 2, m = 0$  spherical harmonic coefficients,  $G_0 Y_{20}(\theta, \phi) = G^{ij} n^i n^j$ , and  $Q_0 Y_{20}(\theta, \phi) = Q^{ij} n^i n^j = -\lambda G^{ij} n^i n^j = -\lambda G_0 Y_{20}(\theta, \phi)$ , as was done in [87], we obtain the result

$$c_1 = \frac{15}{8} \frac{\lambda G_0}{M^3}, \quad c_2 = -\frac{1}{3} M^2 G_0. \quad (4.61)$$

We can now determine the strength of the tidal field  $G_0$  that caused the perturbation by matching the solution for  $H$  and its derivative at the boundary of the star  $r = R$ . This will then give us an expression for the tidal Love number  $k_2$ . Defining the quantity

$$y = \frac{R \beta(R)}{H(R)} \quad (4.62)$$

for the internal solution, the  $l = 2$  Love number is finally

$$\begin{aligned} k_2 = & \frac{8C^5}{5} (1 - 2C)^2 [2 + 2C(y - 1) - y] \\ & \times \left\{ 2C[6 - 3y + 3C(5y - 8)] + 4C^3[13 - 11y + C(3y - 2) + 2C^2(1 + y)] \right. \\ & \left. + 3(1 - 2C)^2 [2 - y + 2C(y - 1)] \ln(1 - 2C) \right\}^{-1}, \end{aligned} \quad (4.63)$$

where  $C = m/R$  is the compactness of the star.

For stars with a nonzero density at the surface (for example strange quark matter or an incompressible  $n = 0$  polytrope), the term  $(f/r)(\Phi' + \Lambda')$  in Eq. (4.50) blows up at the surface  $r = R$  and  $H'(r)$  is no longer continuous across the surface. Following the discussion in [93] for an  $n = 0$  polytrope, this discontinuity leads to an extra term in the expression above for  $y$

$$y = \frac{R \beta(R)}{H(R)} - \frac{4\pi R^3 \epsilon_-}{M}, \quad (4.64)$$

where  $\epsilon_-$  is the density just inside the surface.

## Chapter 5

# Gravitational-wave data analysis

The interpretation of data in gravitational-wave astronomy differs in many ways from that in other fields. In particle physics, for example, one can often perform an ensemble of experiments with carefully controlled parameters. A frequentist interpretation of probability can then be used: in the limit of a large number of experiments the probability  $P(A)$  of outcome  $A$  is the ratio of the number of times  $A$  was the outcome to the total number of outcomes. Gravitational-wave astronomy is fundamentally different in that we cannot set up an ensemble of identical binary inspiral events, for example, and we are often interested in estimating the parameters themselves (sky location, binary orientation, masses, spins, and tidal parameters) of individual events. A natural method for answering such a question is that of Bayesian inference.

### 5.1 Bayesian inference

The key theorem in Bayesian inference is Bayes' theorem

$$P(B|A) = \frac{P(B)P(A|B)}{P(A)}, \quad (5.1)$$

where  $P(A|B)$  denotes the conditional probability that  $A$  is true given that  $B$  is true. This theorem can be used for performing parameter estimation in the following way. Given a data set  $D$  from a detector and prior information  $I$ , the posterior probability density function (PDF) for the parameters  $\vec{\theta}$  of a model  $\mathcal{H}$  are given by [94]

$$p(\vec{\theta}|D, \mathcal{H}, I) = \frac{p(\vec{\theta}|\mathcal{H}, I)p(D|\vec{\theta}, \mathcal{H}, I)}{p(D|\mathcal{H}, I)}. \quad (5.2)$$

The quantity  $p(D|\vec{\theta}, \mathcal{H}, I)$  is known as the likelihood, and can be calculated in the frequentist sense; given a hypothetical ensemble of events with parameters in the volume  $d\vec{\theta}$ , the

likelihood is the probability density of obtaining the data  $D$  from a detector. The prior distribution of the parameters  $p(\vec{\theta}|\mathcal{H}, I)$  is determined by the hypothesis and prior information. In the denominator, the evidence  $Z = p(D|\mathcal{H}, I)$  is a normalization constant, and if needed, can be evaluated explicitly by integrating Eq. (5.2) over the parameter space and using the fact that the integral over the left hand side is 1

$$Z = p(D|\mathcal{H}, I) = \int p(\vec{\theta}|\mathcal{H}, I)p(D|\vec{\theta}, \mathcal{H}, I) d\vec{\theta}. \quad (5.3)$$

Because  $Z$  is the prior weighted integral over the likelihood, it is also called the marginalized likelihood. For a high dimensional parameter space this integration is computationally challenging, although there exist methods such as nested sampling and thermodynamic integration that can perform it (see for example Refs. [95] and [96] for their use in gravitational wave data analysis).

If one is only interested in a subset of the parameters  $\vec{\theta}^A$  where  $\vec{\theta} = \{\vec{\theta}^A, \vec{\theta}^B\}$ , the other parameters  $\vec{\theta}^B$  can be integrated out to obtain a marginalized PDF over only the parameters of interest

$$p(\vec{\theta}^A|D, \mathcal{H}, I) = \int p(\vec{\theta}|D, \mathcal{H}, I) d\vec{\theta}^B. \quad (5.4)$$

This is done, as we shall see, if we are only concerned with the PDF for the intrinsic parameters of a binary system such as masses and tidal parameters, and are not concerned with the extrinsic parameters such as sky location and orientation relative to Earth.

In addition to estimating the parameters of a specific model, we can also in principle calculate the posterior probability  $P(\mathcal{H}_i|D, I)$  that model  $\mathcal{H}_i$  is true using the model selection form of Bayes' theorem

$$P(\mathcal{H}_i|D, I) = \frac{P(\mathcal{H}_i|I)P(D|\mathcal{H}_i, I)}{P(D|I)}. \quad (5.5)$$

The quantity  $Z = P(D|\mathcal{H}_i, I)$  is the evidence or marginalized likelihood given by Eq. (5.3).  $P(\mathcal{H}_i|I)$  is the prior probability of  $\mathcal{H}_i$  which is sometimes a subjective measure of one's prior belief that hypothesis  $\mathcal{H}_i$  is true. The quantity in the denominator  $P(D|I)$  is the marginalized probability of obtaining the data  $D$ . It can be calculated if there exists a complete set of independent hypotheses ( $\sum_i P(\mathcal{H}_i|D, I) = 1$  and  $\mathcal{H}_i \cap \mathcal{H}_j = \emptyset$  for  $i \neq j$ ). The marginalized probability is then<sup>1</sup>

$$P(D|I) = \sum_i P(\mathcal{H}_i|I)P(D|\mathcal{H}_i, I). \quad (5.6)$$

---

<sup>1</sup>The prior was left out of the corresponding expression in Ref. [94].

In practice we don't always have a complete set of hypotheses, so we cannot calculate the posterior for each model. We can, however, calculate the ratio of posteriors for two models known as the odds ratio

$$\begin{aligned} O_{i,j} &= \frac{P(\mathcal{H}_i|D, I)}{P(\mathcal{H}_j|D, I)} \\ &= \frac{P(\mathcal{H}_i|I)}{P(\mathcal{H}_j|I)} \Lambda_{i,j}, \end{aligned} \quad (5.7)$$

where

$$\Lambda_{i,j} = \frac{P(D|\mathcal{H}_i, I)}{P(D|\mathcal{H}_j, I)} \quad (5.8)$$

is the Bayes factor or likelihood ratio.

## 5.2 Statistical properties of the output of gravitational-wave detectors

We will now briefly describe in this section the output of gravitational-wave detectors in the possible presence of a gravitational wave as well as detector noise, and then derive the probability that a gravitational wave is present. In the remainder of the chapter we will then apply the above Bayesian techniques to address the questions of parameter estimation.

As discussed in Chapter 3 the gravitational wave  $h_{ij} = h_+ e_{ij}^+ + h_\times e_{ij}^\times$  has two transverse polarizations  $e_{ij}^+$  and  $e_{ij}^\times$ . In the  $\hat{X}$ - $\hat{Y}$ - $\hat{n}$  coordinate system of a gravitational wave traveling in the  $\hat{n}$  direction, the polarization tensors are

$$e_{ij}^+ = \hat{X}^i \hat{X}^j - \hat{Y}^i \hat{Y}^j \quad (5.9)$$

$$e_{ij}^\times = \hat{X}^i \hat{Y}^j + \hat{Y}^i \hat{X}^j. \quad (5.10)$$

The response of the detector arms of length  $L$ , expressed in terms of the scalar strain  $h = \Delta L/L$ , can be expressed by contracting the waveform with a tensor  $D_{ij}$

$$h = D_{ij} h_{ij}. \quad (5.11)$$

For a Michelson interferometer with arms in the  $\hat{p}$  and  $\hat{q}$  directions [67]

$$D_{ij} = \frac{1}{2}(\hat{p}_i \hat{p}_j - \hat{q}_i \hat{q}_j). \quad (5.12)$$

In terms of the components  $h_+$  and  $h_\times$ , the strain can be written

$$h = F_+ h_+ + F_\times h_\times, \quad (5.13)$$

where  $F_+$  and  $F_\times$  are the response functions for the two polarizations. For a detector with a  $90^\circ$  opening angle between the arms, they can be expressed as functions of the sky position

$(\theta, \phi)$  relative to the detector and polarization angle  $\psi$  (see Fig. 19) as [97]

$$\begin{aligned}
F_+ &= D_{ij}e_{ij}^+ \\
&= \frac{1}{2}(\hat{p}^i\hat{p}^j - \hat{q}^i\hat{q}^j)(\hat{X}^i\hat{X}^j - \hat{Y}^i\hat{Y}^j) \\
&= -\frac{1}{2}(1 + \cos^2\theta)\cos 2\phi\cos 2\psi - \cos\theta\sin 2\phi\sin 2\psi,
\end{aligned} \tag{5.14}$$

$$\begin{aligned}
F_\times &= D_{ij}e_{ij}^\times \\
&= \frac{1}{2}(\hat{p}^i\hat{p}^j - \hat{q}^i\hat{q}^j)(\hat{X}^i\hat{Y}^j + \hat{Y}^i\hat{X}^j) \\
&= \frac{1}{2}(1 + \cos^2\theta)\cos 2\phi\sin 2\psi - \cos\theta\sin 2\phi\cos 2\psi.
\end{aligned} \tag{5.15}$$

As an example, in the optimally oriented  $\theta = 0$  configuration, a waveform written as the complex quantity  $h_+(t) - ih_\times(t) = A(t)e^{-i\Phi(t)}$  results in the strain  $h(t) = -A(t)\cos[2(\phi - \psi) - \Phi(t)]$ .

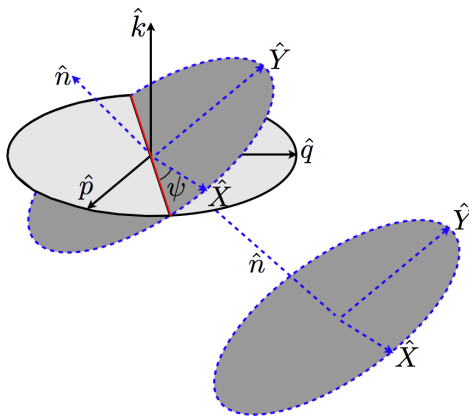


Figure 19 : For detector arms in the  $\hat{p}$  and  $\hat{q}$  directions, the sky location of a source  $-\hat{n}$  is given by the usual spherical coordinates  $(\theta, \phi)$ , where  $\theta$  is the polar angle from the axis normal to the detector,  $\phi$  is the azimuthal angle from the  $\hat{p}$  direction, and  $\hat{n} = (-\theta, \phi + \pi)$  is the direction of propagation of the gravitational wave. The polarization angle  $\psi$  is the angle measured counterclockwise about the direction of propagation  $\hat{n}$  from the line of nodes  $(\hat{k} \times \hat{n})$  to  $\hat{x}$ .

In addition to the GW signal  $h(t)$ , a real detector will have noise  $n(t)$  such that the output  $s(t)$  of the detector is

$$s(t) = n(t) + h(t), \tag{5.16}$$

where we have assumed the noise is additive (the presence of a GW does not affect the statistical properties of the noise). We will also assume that the noise is stationary, which means the statistical properties of the noise do not change with time.

An important property of the noise is its power spectrum. The power in the noise is defined as the time average of  $n^2(t)$  over some large time interval  $T$ :

$$\langle n^2 \rangle = \lim_{T \rightarrow \infty} \frac{1}{T} \int_{-T/2}^{T/2} n^2(t) dt. \quad (5.17)$$

For stationary noise, this average will be independent of the time. The power can be reexpressed in terms of the power spectral density (PSD)  $S_n(f)$  by [67]

$$\langle n^2 \rangle = \int_0^\infty S_n(f) df, \quad (5.18)$$

where the PSD

$$S_n(f) = \lim_{T \rightarrow \infty} \frac{2}{T} \left| \int_{-T/2}^{T/2} n(t) e^{-2\pi i f t} dt \right|^2 \quad (5.19)$$

is the absolute square of the Fourier transform of the signal. The PSD can equivalently be expressed in terms of the Fourier transform  $\tilde{R}_n(f)$  of the autocorrelation function  $R_n(\tau) = \langle n(t)n(t+\tau) \rangle$  as

$$S_n(f) = 2 \int_{-\infty}^{\infty} R_n(\tau) e^{-2\pi i f \tau} d\tau = 2\tilde{R}_n(f). \quad (5.20)$$

Another equivalent expression is

$$\langle \tilde{n}^*(f') \tilde{n}(f) \rangle = \frac{1}{2} S_n(f) \delta(f - f'). \quad (5.21)$$

Another assumption that we will make is that the noise is Gaussian. For Gaussian noise  $n(t)$ , the discretely sampled noise time series is a sequence of correlated Gaussian random variables  $\{n_i\}$  measured at times  $i\Delta t$ . In the limit  $\Delta t \rightarrow 0$ , the joint probability distribution for this noise sequence is given by [67]

$$p_n[n(t)] \propto e^{-(n,n)/2}, \quad (5.22)$$

where

$$(a, b) = 4\text{Re} \int_0^\infty \frac{\tilde{a}(f) \tilde{b}^*(f)}{S_n(f)} df \quad (5.23)$$

is an inner product weighted by the noise PSD.

### 5.3 Detection

To determine if there is a gravitational wave present in the data, we can compare the two mutually exclusive hypotheses

$$\mathcal{H}_0 : s(t) = n(t) \text{ (There is no gravitational wave),}$$

$$\mathcal{H}_1 : s(t) = n(t) + h(t) \text{ (There is a gravitational wave).}$$

The probability that there is a gravitational wave is given by

$$\begin{aligned} P(\mathcal{H}_1|D, I) &= \frac{P(\mathcal{H}_1|I)P(D|\mathcal{H}_1, I)}{P(D|I)} \\ &= \frac{\Lambda_{1,0}}{\Lambda_{1,0} + P(\mathcal{H}_0|I)/P(\mathcal{H}_1|I)}, \end{aligned} \quad (5.24)$$

where  $P(D|I) = P(\mathcal{H}_0|I)P(D|\mathcal{H}_0, I) + P(\mathcal{H}_1|I)P(D|\mathcal{H}_1, I)$  and  $\Lambda_{1,0}$  is the Bayes factor (or likelihood ratio) defined in Eq. (5.8). In addition, when assigning priors we must obey the constraint  $P(\mathcal{H}_0|I) + P(\mathcal{H}_1|I) = 1$ . For a GW signal that can be described by the unknown parameters  $\vec{\theta}$  and noise which in this case has no unknown parameters, the Bayes factor can be reexpressed as [98]

$$\Lambda_{1,0} = \int \Lambda(\vec{\theta}) d\vec{\theta}, \quad (5.25)$$

where

$$\begin{aligned} \Lambda(\vec{\theta}) &= \frac{p(\vec{\theta}|\mathcal{H}_1, I)p(D|\vec{\theta}, \mathcal{H}_1, I)}{p(D|\mathcal{H}_0, I)} \\ &= \frac{p(\vec{\theta}|\mathcal{H}_1, I)p_n[s(t) - h(t; \vec{\theta})]}{p_n[s(t)]} \\ &= p(\vec{\theta}|\mathcal{H}_1, I)e^{(s, h(\vec{\theta}))} e^{-(h(\vec{\theta}), h(\vec{\theta}))/2}. \end{aligned} \quad (5.26)$$

Another quantity that we will be interested in is the signal to noise ratio (SNR), which is defined as the ratio of the matched filter  $(s, h)$  (a Gaussian random variable) when a GW is present to the standard deviation of the matched filter when a GW is not present ( $\sqrt{(h, h)}$ ):

$$\rho = \frac{(s, h)}{\sqrt{(h, h)}}. \quad (5.27)$$

When a GW is not present,  $\rho$  is a Gaussian random variable with  $\langle \rho \rangle = 0$  and  $\text{Var}(\rho) = 1$ , while when a GW is present,  $\langle \rho \rangle = \sqrt{(h, h)}$  and  $\text{Var}(\rho) = 1$ . The quantity  $\langle \rho \rangle = \sqrt{(h, h)}$  is sometimes referred to as the characteristic SNR of the signal, and describes the characteristic strength of a GW for a given detector configuration [67].

## 5.4 Fisher matrix approximation

Although we now have in principle all the tools necessary to estimate the parameters of a binary, this task is still computationally challenging. In this section we will discuss an analytical approximation for estimating the parameters known as the Fisher matrix approximation which applies to signals with high SNR, and then discuss in the next section a more general method known as Markov Chain Monte Carlo (MCMC).

For a binary event with actual parameters  $\tilde{\theta}$ , we can choose as our best estimate of the parameters  $\hat{\theta}$  the value, known as the mode, that maximizes  $\Lambda(\vec{\theta})$  and is given by the solution to  $\partial_i \Lambda(\vec{\theta}) = 0$ . It is possible for there to be multiple local maxima, however for signals with high SNR,  $\Lambda(\vec{\theta})$  will be a narrowly peaked function and the mode  $\hat{\theta}$  will be close to the actual parameters  $\tilde{\theta}$ . Using the fact that the log of a function has the same mode as the function, the relation  $s = n + h(\tilde{\theta})$ , and the shorthand  $p_0(\vec{\theta}) = p(\vec{\theta}|\mathcal{H}_1, I)$ , the mode can be found from Eq. (5.26) [98]

$$\begin{aligned} 0 &= \partial_i \ln \Lambda(\hat{\theta}) \\ &= \partial_i \left[ \ln p_0(\hat{\theta}) + (n + h(\tilde{\theta}), h(\hat{\theta}) - \frac{1}{2}(h(\hat{\theta}), h(\hat{\theta}))) \right] \\ -v_i &= \partial_i \ln p_0(\hat{\theta}) + (h(\tilde{\theta}) - h(\hat{\theta}), \partial_i h(\hat{\theta})), \end{aligned} \quad (5.28)$$

where

$$v_i = (n, \partial_i h(\hat{\theta})). \quad (5.29)$$

Because  $n(t)$  is a sequence of zero mean ( $\langle n(t) \rangle = 0$ ) Gaussian random variables, each  $v_i$  is a zero mean Gaussian as well. The joint distribution of  $v_i$  over all parameters will therefore be a multivariate Gaussian with covariance  $\Gamma_{ij}$  known as the Fisher matrix

$$\begin{aligned} \Gamma_{ij} &= \text{Cov}(v_i, v_j) = \langle (v_i - \langle v_i \rangle)(v_j - \langle v_j \rangle) \rangle \\ &= \langle v_i v_j \rangle \\ &= \langle (n, \partial_i h(\hat{\theta}))(n, \partial_j h(\hat{\theta})) \rangle \\ &= (\partial_i h(\hat{\theta}), \partial_j h(\hat{\theta})), \end{aligned} \quad (5.30)$$

where we used Eq. (5.21) in going to the last line.

If the signal has high SNR and is narrowly peaked, the true parameters  $\tilde{\theta}$  will be close to the mode  $\hat{\theta}$ , and we can linearize the difference in the corresponding waveforms

$$h(\tilde{\theta}) = h(\hat{\theta}) + \partial_i h(\hat{\theta}) \Delta \theta_i + \mathcal{O}(\Delta \theta^2), \quad (5.31)$$

where  $\Delta \theta_i = \tilde{\theta}_i - \hat{\theta}_i$ . Eq. (5.28) can now be used to provide an explicit expression for  $\tilde{\theta}$

$$\Delta \theta_i = -\Gamma_{ij}^{-1} (v_j + \partial_j \ln p). \quad (5.32)$$

The random variables  $\Delta \theta_i$  have means

$$\langle \Delta \theta_i \rangle = -\Gamma_{ij}^{-1} \partial_j \ln p(\hat{\theta}) \quad (5.33)$$

and covariance

$$\begin{aligned}\Sigma_{ij} &= \text{Cov}(\Delta\theta_i, \Delta\theta_j) = \langle (\Delta\theta_i - \langle \Delta\theta_i \rangle)(\Delta\theta_j - \langle \Delta\theta_j \rangle) \rangle \\ &= \Gamma_{ij}^{-1}.\end{aligned}\tag{5.34}$$

Note that when the prior is uniform,  $\langle \Delta\theta_i \rangle = 0$  and  $\Sigma_{ij} = \text{Cov}(\Delta\theta_i, \Delta\theta_j) = \langle \Delta\theta_i \Delta\theta_j \rangle$ . The joint probability distribution for  $\Delta\theta_i$  given the mode  $\hat{\theta}_i$  is therefore

$$p(\Delta\theta_i | \hat{\theta}_i) = \frac{1}{\sqrt{(2\pi)^N \det(\Sigma_{ij})}} e^{-\frac{1}{2} \Sigma_{ij}^{-1} (\Delta\theta_i - \langle \Delta\theta_i \rangle)(\Delta\theta_j - \langle \Delta\theta_j \rangle)}.\tag{5.35}$$

The  $n$ - $\sigma$  error ellipsoid which is a contour of  $p(\Delta\theta_i | \hat{\theta}_i)$  is defined by

$$(\Delta\theta_i - \langle \Delta\theta_i \rangle)(\Delta\theta_j - \langle \Delta\theta_j \rangle) \Sigma_{ij}^{-1} = n^2.\tag{5.36}$$

The variance in  $\Delta\theta_i$  is

$$\sigma_i^2 = \langle (\Delta\theta_i - \langle \Delta\theta_i \rangle)^2 \rangle = \Sigma_{ii},\tag{5.37}$$

and the correlation coefficients  $r_{ij}$  are

$$r_{ij} = \frac{\langle (\Delta\theta_i - \langle \Delta\theta_i \rangle)(\Delta\theta_j - \langle \Delta\theta_j \rangle) \rangle}{\sigma_i \sigma_j} = \frac{\Sigma_{ij}}{\sigma_i \sigma_j}.\tag{5.38}$$

The correlation  $r_{ij}$  ranges from -1 to 1, with  $r_{ij} = 0$  indicating no correlation between the parameters and  $r_{ij} = \pm 1$  indicating the parameters are completely degenerate.

## 5.5 Markov Chain Monte Carlo

In general, the PDF for the parameters of a gravitational-wave event cannot be approximated as a multivariate Gaussian centered on the maximum likelihood (for some parameters the marginalized PDF is even multimodal), and so the Fisher matrix will fail to give an accurate estimate of the uncertainty in the parameters. What we need to understand the overall structure of the PDF is to sufficiently sample the entire PDF instead of just the region around the maximum likelihood. Sampling a  $D$  dimensional parameter space with  $N$  points in each parameter requires  $\mathcal{O}(N^D)$  evaluations of the posterior, and this rapidly becomes an intractable problem. Fortunately there are adaptive techniques for sampling more finely regions where the PDF is larger. One such technique is known as Markov Chain Monte Carlo (MCMC). The essential idea of MCMC is to sample each point in the parameter space with a probability proportional to the PDF itself. If this is done, then the marginalized PDF over the parameters  $\theta^B$  is found by simply binning the sampled points and making a histogram over the remaining 1 or 2 parameters of interest  $\theta^A$ .

The algorithm is as follows<sup>2</sup>. Begin at the point  $\vec{\theta}_{i-1}$  and draw a new point  $\vec{\theta}_i$  from a distribution  $p(\vec{\theta}_i|\vec{\theta}_{i-1})$ . (Because the new point depends on only the previous point, the sequence of points that results from repeating this process is called a Markov Chain.) If the distribution  $p(\vec{\theta}_i|\vec{\theta}_{i-1})$  satisfies the detailed balance equation

$$\pi(\vec{\theta}_{i-1})p(\vec{\theta}_i|\vec{\theta}_{i-1}) = \pi(\vec{\theta}_i)p(\vec{\theta}_{i-1}|\vec{\theta}_i), \quad (5.39)$$

then each point  $\vec{\theta}_i$  will eventually be visited with probability  $\pi(\vec{\theta})$ . This can be seen by integrating both sides of Eq. (5.39) over all possible choices for the previous point  $\vec{\theta}_{i-1}$  in the chain to obtain

$$\int \pi(\vec{\theta}_{i-1})p(\vec{\theta}_i|\vec{\theta}_{i-1}) d\vec{\theta}_{i-1} = \pi(\vec{\theta}_i). \quad (5.40)$$

This indicates that if  $\vec{\theta}_{i-1}$  is drawn from  $\pi(\vec{\theta}_{i-1})$  then so is  $\vec{\theta}_i$ .

There are several possible ways to draw the new point  $\vec{\theta}_i$  such that the transition probability function  $p(\vec{\theta}_i|\vec{\theta}_{i-1})$  satisfies the detailed balance equation (5.39). The most common is given by the Metropolis-Hastings algorithm. In this algorithm a new point is drawn from some proposal distribution  $q(\vec{\theta}_i|\vec{\theta}_{i-1})$  for example a Gaussian. This new point will be accepted with probability

$$\alpha(\vec{\theta}_{i-1}, \vec{\theta}_i) = \min \left( 1, \frac{\pi(\vec{\theta}_i)q(\vec{\theta}_{i-1}|\vec{\theta}_i)}{\pi(\vec{\theta}_{i-1})q(\vec{\theta}_i|\vec{\theta}_{i-1})} \right). \quad (5.41)$$

If this new point is not accepted, then set  $\vec{\theta}_i = \vec{\theta}_{i-1}$  instead. The transition probability will therefore be

$$p(\vec{\theta}_{i-1}|\vec{\theta}_i) = q(\vec{\theta}_i|\vec{\theta}_{i-1})\alpha(\vec{\theta}_{i-1}, \vec{\theta}_i). \quad (5.42)$$

This can be shown to satisfy the detailed balance equation.

There are many methods available to find proposal distributions  $q$  that efficiently sample the entire parameter space. Furthermore, the proposal  $q$  can be changed after each iteration and still satisfy the detailed balance equation. In addition, methods such as parallel tempering [100] are available which make it easier for a chain to jump between different modes of a PDF.

---

<sup>2</sup>The discussion in this section is based on that in Section 15.8 of Ref. [99].

## Chapter 6

# Detectability of tidal parameters from the early inspiral of BNS systems

### 6.1 Introduction and summary

The observation of inspiraling binary neutron stars (NSs) with ground-based gravitational-wave detectors such as LIGO and Virgo may provide significantly more information about neutron-star structure and the highly uncertain equation of state (EOS) of neutron-star matter than is currently available. The available electromagnetic observations of neutron stars provide weak constraints from properties such as the star's mass, spin, and gravitational redshift (see for example [37, 54]). Simultaneous measurements of both the mass and radius of a neutron star [48, 101, 61, 62, 102], on the other hand, have the potential to make significantly stronger constraints. These measurements, however, depend on detailed modeling of the radiation mechanisms at the neutron-star surface and absorption in the interstellar medium, and they are subject to systematic uncertainties.

In contrast, information about the neutron star EOS obtained from gravitational-wave observations of binary inspiral is model independent. The tidal distortion of neutron stars in a binary system links the EOS describing neutron-star matter to the gravitational-wave emission during the inspiral. Initial estimates showed that for LIGO, tidal effects change the phase evolution only at the end of inspiral, and that point particle post-Newtonian waveforms can be used for template-based detection [103, 104, 105]. With the projected sensitivities of later-generation detectors, however, effects which can be neglected for the purpose of detection may become measurable in the strongest observed signals.

While EOS effects are largest during the late inspiral and merger of two neutron stars where numerical simulations must be used to predict the signal, Flanagan and Hinderer showed that a small but clean tidal signature arises in the inspiral below 400 Hz [86]. This signature amounts to a phase correction which can be described in terms of a single EOS-dependent tidal deformability parameter  $\lambda$ , namely the ratio of each star's induced quadrupole to the tidal field of its companion. The fact that the EOS-dependence enters only via a single parameter was worked out previously in the context of Newtonian gravity in Refs. [103, 106]. The parameter  $\lambda$  depends on the EOS via both the NS radius  $R$  and a dimensionless quantity  $k_2$ , called the Love number [107, 108, 109]:  $\lambda = 2/(3G)k_2R^5$ .

The relativistic Love numbers of polytropic<sup>1</sup> EOS were examined first by Flanagan and Hinderer [86, 87] and later by others in more detail [93, 110]. Flanagan and Hinderer also examined the measurability of the tidal deformability of polytropes and suggested that Advanced LIGO could start to place interesting constraints on  $\lambda$  for nearby events. However, they used incorrect values for  $k_2$ , which overestimated  $\lambda$  by a factor of  $\sim 2 - 3$  and were therefore overly optimistic about the potential measurability. In addition, polytropes are known to be a poor approximation to the neutron star equation of state, and there may be significant differences in the tidal deformability between polytropes and realistic candidates for the neutron-star EOS. In this paper, we calculate the deformability for candidate EOS, and show that a tidal signature is actually only marginally detectable with Advanced LIGO from the early-inspiral waveform.

In Sec. 4.2 we described a method based on Ref. [87] for calculating the relativistic Love number and tidal deformability for an arbitrary EOS. In Sec. 6.2 we calculate  $k_2$  and  $\lambda$  as a function of mass for several EOS commonly found in the literature. We find that, in contrast to the Love number, the tidal deformability has a wide range of values, spanning roughly an order of magnitude over the observed mass range of neutron stars in binary systems.

As discussed above, the direct practical importance of the stars' tidal deformability for gravitational wave observations of NS binary inspirals is that it encodes the EOS influence on the waveform's phase evolution during the early portion of the signal, where it is accurately modeled by post-Newtonian (PN) methods. In this regime, the influence of tidal

---

<sup>1</sup>Polytropes are often written in two forms. The first form is expressed as  $p = K\epsilon^{1+1/n}$ , where  $p$  is the pressure,  $\epsilon$  is the energy density,  $K$  is a pressure constant, and  $n$  is the polytropic index. The second form, is given by  $p = K\rho^{1+1/n}$ , where  $\rho$  is the rest-mass density, defined as the baryon number density times the baryon rest mass. The first form was mainly used in the recent papers [87, 93, 110]. However, the second form is more commonly used in the neutron-star literature and is more closely tied to the thermodynamics of a Fermi gas. We will use both forms as was done in Ref. [93].

effects is only a small correction to the point-particle dynamics. However, when the signal is integrated against a theoretical waveform template over many cycles, even a small contribution to the phase evolution can be detected and could give information about the NS structure.

Following [86], we calculate in Sec. 6.3 the measurability of the tidal deformability for a wide range of equal- and unequal- mass binaries, covering the entire expected range of NS masses and EOS, and with proposed detector sensitivity curves for second- and third- generation detectors. We show that the tidal signature is optimistically detectable in Advanced LIGO only for binaries with neutron star masses below  $1.4 M_{\odot}$  for gravitational frequencies below 450 Hz. In third-generation detectors, however, the tenfold increase in sensitivity allows a finer discrimination between equations of state leading to potential measurability of a large portion of proposed EOSs over most of the expected neutron star mass range.

We conclude by briefly considering how the errors could be improved with a more careful analysis of the detectors and extension of the understanding of EOS effects to higher frequencies.

Finally, in Appendix B we compute the leading order EOS-dependent corrections to our model of the tidal effect and derive explicit expressions for the resulting corrections to the waveform's phase evolution, extending the analysis of Ref. [86]. Estimates of the size of the phase corrections show that the main source of error are post-1 Newtonian corrections to the Newtonian tidal effect itself, which are approximately twice as large as other, EOS-dependent corrections at a frequency of 450 Hz. Since these point-particle corrections do not depend on unknown NS physics, they can easily be incorporated into the analysis. A derivation of the explicit post-Newtonian correction terms is the subject of Ref. [85, 111].

*Conventions:* We set  $G = c = 1$ .

## 6.2 Love numbers and tidal deformabilities for candidate EOS

Differences between candidate EOS can have a significant effect on the tidal interactions of neutron stars. In this paper we consider a sample of EOS from Refs. [8, 54] with a variety of generation methods and particle species. The sample is chosen to include EOS with the largest range of behaviors for  $k_2(M/R)$ ,  $k_2(M)$  and  $\lambda(M)$  rather than to fairly represent the different generation methods. We also restrict ourselves to stars with a maximum mass greater than  $1.5 M_{\odot}$ , which is conservatively low given recent neutron-star mass observations [112, 39, 40, 41, 42, 43]. We consider 7 EOS with just normal  $npe\mu$  matter (SLY [21], AP1 and AP3 [22], FPS [23], MPA1 [27], MS1 and MS2 [28]), 8 EOS that

also incorporate some combination of hyperons, pion condensates, and quarks (PS [29], BGN1H1 [31], GNH3 [32], H1 and H4 [17], PCL2 [33], ALF1 and ALF2 [34]), and 3 self-bound strange quark matter EOS (SQM1–3 [33]). A brief description of these EOS and their properties can be found in [8, 54].

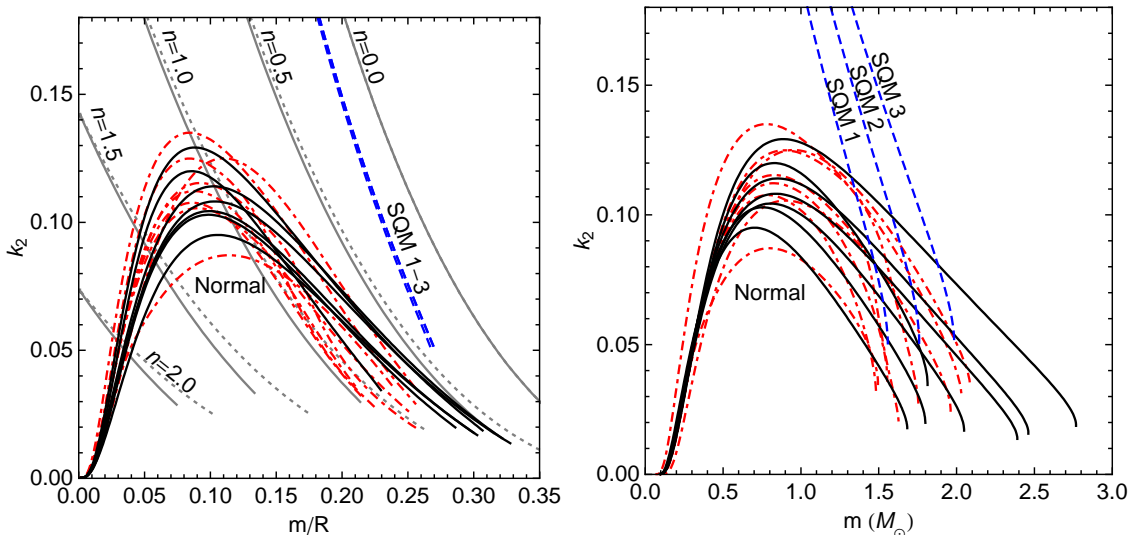


Figure 20 : Left panel: Love number as a function of compactness. Gray dotted curves are energy density polytropes ( $p = K\epsilon^{1+1/n}$ ), and gray solid curves are rest-mass density polytropes ( $p = K\rho^{1+1/n}$ ). Both polytropes are the same for  $n = 0$ . EOS with only  $npe\mu$  matter are solid and those that also incorporate  $\pi$ /hyperon/quark matter are dot-dashed. The three SQM EOS are dashed and overlap. They approach the  $n = 0$  curve at low compactness, where  $k_2$  has a maximum value of 0.75 as  $M/R \rightarrow 0$ . Right panel: Love number as a function of mass for the same set of realistic EOS. Note that there is more variation in  $k_2$  between different EOS for fixed mass than for fixed compactness.

The generic behavior of the Love number  $k_2$  is shown in the left panel of Fig. 20 as a function of compactness  $M/R$  for different types of EOS. The two types of polytropes, energy and rest-mass density polytropes, are shown in gray. They coincide in the limit  $M/R \rightarrow 0$  where  $\epsilon \rightarrow \rho$  as the star’s density goes to zero, and in the limit  $n \rightarrow 0$  where  $\epsilon(p)$  and  $\rho(p)$  are both constant. This can be seen from the first law of thermodynamics,

$$d\frac{\epsilon}{\rho} = -pd\frac{1}{\rho}, \quad (6.1)$$

which relates  $\epsilon$  to  $\rho$ .

The sequences labeled “Normal” correspond to the 15 EOS with a standard nuclear matter crust, and the 3 sequences labeled “SQM” correspond to the crustless EOS SQM1-3 where the pressure is zero below a few times nuclear density. Within these two classes, there is little variation in behavior, so we do not explicitly label each candidate EOS.

The left panel of Fig. 20 shows  $k_2(M)$  for the realistic EOS, which is more astrophysically relevant because mass, not compactness, is the measurable quantity during binary inspiral. Unlike the quantity  $k_2(M/R)$ ,  $k_2(M)$  depends on the constant  $K$  for polytropes, so polytropic EOS are not shown. There is more variation in  $k_2$  for fixed mass than for fixed compactness.

The behavior of these curves can be understood as follows: The Love number  $k_2$  measures how easily the bulk of the matter in a star is deformed. If most of the star's mass is concentrated at the center (centrally condensed), the tidal deformation will be smaller. For polytropes, matter with a higher polytropic index  $n$  is softer and more compressible, so these polytropes are more centrally condensed. As a result,  $k_2$  decreases as  $n$  increases. The limiting case  $n = 0$  represents a uniform density star and has the largest Love number possible. The Love number also decreases with increasing compactness, and from Eq. (4.63) it can be seen that  $k_2$  vanishes at the compactness of a black hole ( $M/R = 0.5$ ) regardless of the EOS dependent quantity  $y$  [93, 110].

Normal matter EOS behave approximately as polytropes for large compactness. However, for smaller compactness, the softer crust becomes a greater fraction of the star, so the star is more centrally condensed and  $k_2$  smaller. For strange quark matter, the EOS is extremely stiff near the minimum density, and the star behaves approximately as an  $n = 0$  polytrope for small compactness. As the central density and compactness increase, the softer, higher density part of the EOS has a larger effect, and the star becomes more centrally condensed.

The parameter that is directly measurable by gravitational wave observations of a binary neutron star inspiral is proportional to the tidal deformability  $\lambda$ , which is shown for each candidate EOS in Fig. 21. The values of  $\lambda$  for the candidate EOS show a much wider range of behaviors than for  $k_2$  because  $\lambda$  is proportional to  $k_2 R^5$ , and the candidate EOS produce a wide range of radii (9.4–15.5 km for a  $1.4 M_\odot$  star for normal EOS and 8.9–10.9 km for the SQM EOS). See Table 2.

For normal matter,  $\lambda$  becomes large for stars near the minimum mass configuration at roughly  $0.1 M_\odot$  because they have a large radius. For masses in the expected mass range for binary inspirals, there are several differences between EOS with only  $npe\mu$  matter and those with condensates. EOS with condensates have, on average, a larger  $\lambda$ , primarily because they have, on average, larger radii. The quark hybrid EOS ALF1 with a small radius (9.9 km for a  $1.4 M_\odot$  star) and the nuclear matter only EOSs MS1 and MS2 with large radii (14.9 km and 14.5 km, respectively, at  $1.4 M_\odot$ ) are exceptions to this trend.

For strange quark matter stars, there is no minimum mass, so the radius (and therefore

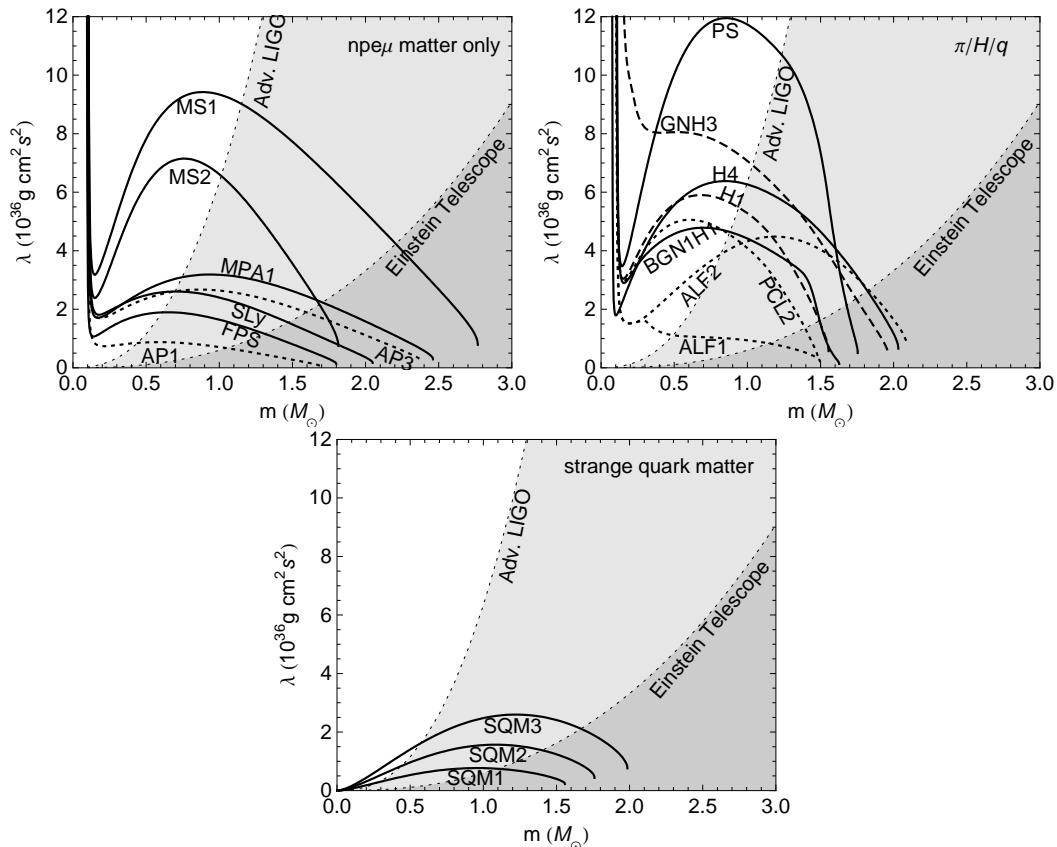


Figure 21 : Tidal deformability  $\lambda$  of a single neutron star as a function of neutron-star mass for a range of realistic EOS. The top left figure shows EOS that only include  $npe\mu$  matter; the top right figure shows EOS that also incorporate  $\pi$ /hyperon/quark matter; the bottom figure shows strange quark matter EOS. The dashed lines between the various shaded regions represent the expected uncertainties in measuring  $\lambda$  for an equal-mass binary inspiral at a distance of  $D = 100$  Mpc as it passes through the gravitational wave frequency range 10 Hz–450 Hz. Observations with Advanced LIGO will be sensitive to  $\lambda$  in the unshaded region, while the Einstein Telescope will be able to measure  $\lambda$  in the unshaded and light shaded regions. See text below.

$\lambda$ ) approaches zero as the mass approaches zero. At larger masses, the tidal deformability of SQM stars remains smaller than most normal matter stars because, despite having large Love numbers, the radii of SQM stars are typically smaller.

Error estimates  $\Delta\lambda$  for an equal-mass binary inspiral at 100 Mpc are also shown in Fig. 21 for both Advanced LIGO and the Einstein Telescope. They will be discussed in the next section.

In addition to these candidate EOS, we also calculate tidal deformability for the piecewise polytropic EOS introduced in Chapter 2. As shown in Fig. 22, the constraint imposed

Table 2 : Properties of a  $1.4 M_{\odot}$  neutron star for the 18 EOS discussed in the text.

EOS	$R(\text{km})$	$M/R$	$k_2$	$\lambda(10^{36} \text{ g cm}^2 \text{ s}^2)$
SLY	11.74	0.176	0.0763	1.70
AP1	9.36	0.221	0.0512	0.368
AP3	12.09	0.171	0.0858	2.22
FPS	10.85	0.191	0.0663	1.00
MPA1	12.47	0.166	0.0924	2.79
MS1	14.92	0.139	0.110	8.15
MS2	13.71	0.151	0.0883	4.28
PS	15.47	0.134	0.104	9.19
BGN1H1	12.90	0.160	0.0868	3.10
GNH3	14.20	0.146	0.0867	5.01
H1	12.86	0.161	0.0738	2.59
H4	13.76	0.150	0.104	5.13
PCL2	11.76	0.176	0.0577	1.30
ALF1	9.90	0.209	0.0541	0.513
ALF2	13.19	0.157	0.107	4.28
SQM1	8.86	0.233	0.098	0.536
SQM2	10.03	0.206	0.136	1.38
SQM3	10.87	0.190	0.166	2.52

by a measurement of  $\lambda$  is very similar to that of a radius (Fig. 13) or moment of inertia (Fig. 12) observation. This occurs because  $\lambda \propto k_2 R^5$  is strongly dependent on the neutron star radius.

### 6.3 Measuring effects on gravitational radiation

We wish to calculate the contribution from realistic tidal effects to the phase evolution and resulting gravitational wave spectrum of an inspiraling neutron star binary. In the secular limit, where the orbital period is much shorter than the gravitational radiation reaction timescale, we consider the tidal contribution to the energy  $E$  and energy flux  $dE/dt$  for a quasi-circular inspiral using the formalism developed by Flanagan and Hinderer [86], which adds the following leading-order terms to the post-Newtonian point-particle corrections

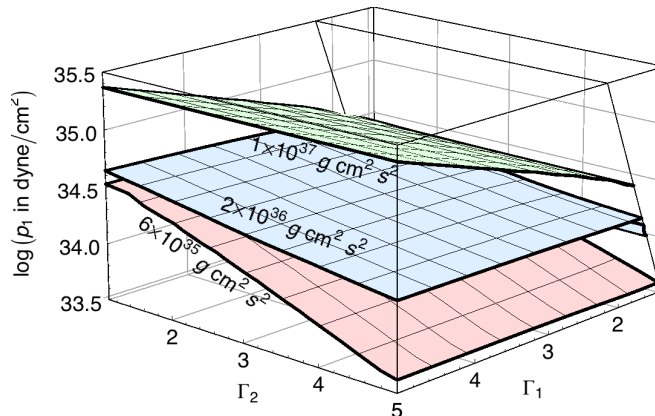


Figure 22 : The above surfaces represent the set of parameters that result in a star with a mass of  $1.4 M_{\odot}$  and a fixed tidal deformability.  $\lambda = 6 \times 10^{35} \text{ g cm}^2 \text{ s}^2$  for the bottom surface.  $\lambda = 2 \times 10^{36} \text{ g cm}^2 \text{ s}^2$  for the middle surface.  $\lambda = 1 \times 10^{37} \text{ g cm}^2 \text{ s}^2$  for the top surface. The wedge at the back right is the shaded region of Fig. 4, corresponding to incompatible values of  $p_1$  and  $\Gamma_1$ .

(PN-PP corr.):

$$E(x) = -\frac{1}{2}M\eta x \left[ 1 + (\text{PN-PP corr.}) - 9 \frac{M_2}{M_1} \frac{\lambda_1}{M^5} x^5 + 1 \leftrightarrow 2 \right], \quad (6.2)$$

$$\dot{E}(x) = -\frac{32}{5}\eta^2 x^5 \left[ 1 + (\text{PN-PP corr.}) + 6 \frac{M_1 + 3M_2}{M_1} \frac{\lambda_1}{M^5} x^5 + 1 \leftrightarrow 2 \right]. \quad (6.3)$$

Here  $\lambda_1 = \lambda(M_1)$  and  $\lambda_2 = \lambda(M_2)$  are the tidal deformabilities of stars 1 and 2, respectively.  $M = M_1 + M_2$  is the total mass,  $\eta = M_1 M_2 / M^2$  is the symmetric mass ratio, and  $x$  is the post-Newtonian dimensionless parameter given by  $x = (\Omega M)^{2/3}$ , where  $\Omega$  is the orbital angular frequency. One can then use

$$dx/dt = \frac{\dot{E}}{dE/dx} \quad (6.4)$$

to estimate the evolution of the quadrupole gravitational wave phase  $\Phi$  via  $d\Phi/dt = 2\Omega = 2x^{3/2}/M$ . The effect of the tidal distortion on these quantities was previously computed in Refs. [104, 103, 106] in terms of the gauge-dependent orbital separation. When these results are converted to the gauge invariant quantity  $x$ , taking into account the tidal correction to the radius-frequency relation, the expressions obtained in the previous studies agree with our Eqs. (6.2) and (6.3).

Each equation of state gives in this approximation a known phase contribution as a function of  $M_1$  and  $M_2$ , or as a function of the total mass  $M = M_1 + M_2$  and the mass ratio  $M_2/M_1$ , via  $\lambda(M_1)$  and  $\lambda(M_2)$  for that EOS. Although we calculated  $\lambda$  for individual neutron stars, the universality of the neutron star core equation of state allows us to predict

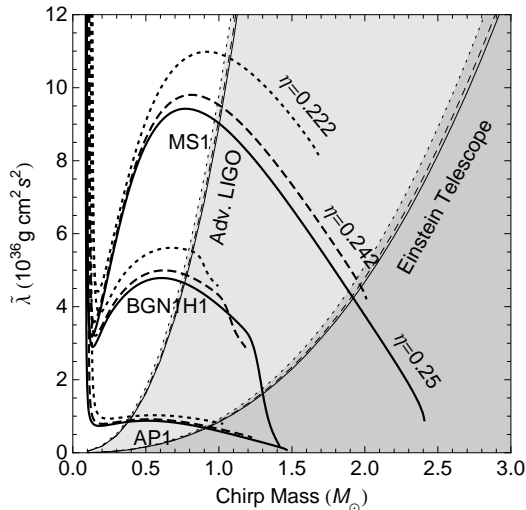


Figure 23 : Weighted  $\tilde{\lambda}$  for a range of chirp mass  $\mathcal{M}$  and symmetric mass ratio  $\eta$ , for three of the EOSs considered above. The values of  $\eta$  equal to  $\{0.25, 0.242, 0.222\}$  correspond to the mass ratios  $M_2/M_1 = \{1.0, 0.7, 0.5\}$ . Also plotted (as in Fig. 21) are the uncertainties  $\Delta\tilde{\lambda}$  in measuring  $\tilde{\lambda}$  for a binary at 100 Mpc between 10 Hz–450 Hz. The solid, dashed, and dotted curves correspond to  $\Delta\tilde{\lambda}$  for  $\eta = 0.25, 0.242$ , and  $0.222$  respectively.

the tidal phase contribution for a given binary system from each EOS. Following [86], we discuss the constraint on the weighted average

$$\tilde{\lambda} = \frac{1}{26} \left[ \frac{M_1 + 12M_2}{M_1} \lambda_1 + \frac{M_2 + 12M_1}{M_2} \lambda_2 \right], \quad (6.5)$$

which reduces to  $\lambda$  in the equal mass case. The contribution to  $d\Phi/dx$  from the tidal deformation, which adds linearly to the known point particle phase evolution, is

$$\left. \frac{d\Phi}{dx} \right|_T = -\frac{195}{8} \frac{x^{3/2} \tilde{\lambda}}{M^5 \eta}. \quad (6.6)$$

The weighted average  $\tilde{\lambda}$  is plotted as a function of chirp mass  $\mathcal{M} = (M_1 M_2)^{3/5} / M^{1/5}$  in Fig. 23 for three of the EOS and for three values of  $\eta$ : equal mass ( $\eta = 0.25$ ), large but plausible mass ratio [113] ( $\eta = 0.242$ ), and extremely large mass ratio ( $\eta = 0.222$ ).

We can determine the significance of the tidal effect on gravitational waveforms in a given frequency range by considering the resulting change in phase accumulated as a function of frequency. In the case of template-based searches, for example, a drift in phase of half a cycle leads to destructive interference between the signal and template, halting the accumulation of signal to noise ratio. The phase contributions to binary neutron stars of various masses from a range of realistic tidal deformabilities are plotted in Fig. 24.

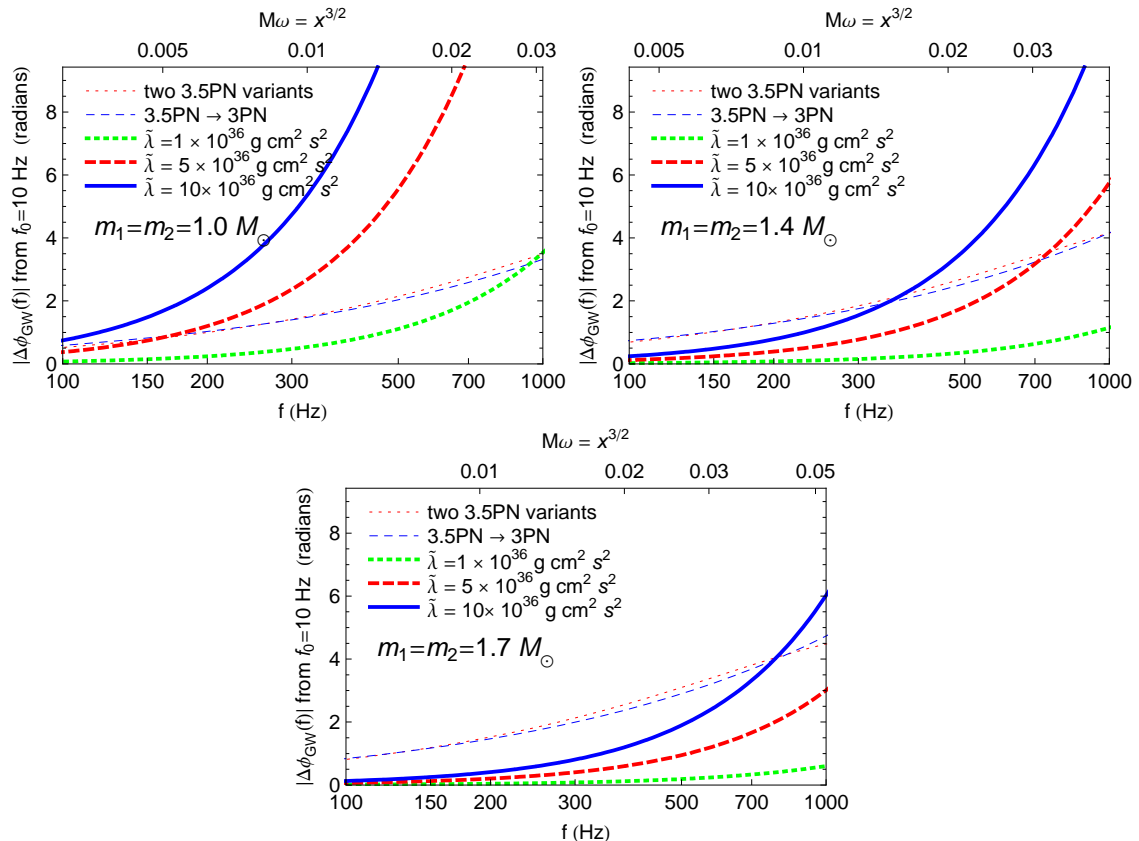


Figure 24 : The reduction in accumulated gravitational wave phase due to tidal effects,  $\Phi_{3.5,PP}(f_{GW}) - \Phi_{3.5,\lambda}(f_{GW})$ , is plotted with thick lines as a function of gravitational wave frequency, for a range of  $\lambda$  appropriate for realistic neutron star EOS and the masses considered. The 3.5 post-Newtonian TaylorT4 PN specification is used as the point-particle reference for the phase calculations. For reference, the difference in accumulated phase between 3.0 and 3.5 post-Newtonian orders of T4 (thin dashed line), and the difference between 3.5 post-Newtonian T4 and 3.5 post-Newtonian T1 (thin dotted line) are also shown. Phase accumulations are integrated from a starting frequency of 10 Hz.

The post-Newtonian formalism itself is sensitive to high-order corrections at the frequencies at which the tidal effect becomes significant; as reference, we show in Fig. 24 the phase difference between the 3.0PN and 3.5PN expansions, as well as that from varying the form of the post-Newtonian Taylor expansion from T4 to T1.<sup>2</sup> An accurate knowledge of the underlying point-particle dynamics will be important to resolve the effects of tidal deformation on the gravitational wave phase evolution at these frequencies.

The half-cycle or more contribution to the gravitational wave phase at relatively low frequencies suggests that this effect could be measurable. Flanagan and Hinderer [86]

<sup>2</sup>For an explanation of the differences between T4 and T1, see Chapter 3.

first calculated the measurability for frequencies below 400 Hz, where the approximations leading to the tidal phase correction are well-justified. We extend the same computation of measurability to a range of masses and mass ratios. We take noise curves from the projected NS-NS optimized Advanced LIGO configuration [114], as well as a proposed noise spectrum of the Einstein Telescope [115]. These noise curves are representative of the anticipated sensitivities of the two detectors. Our results do not change significantly for alternate configurations which have similar sensitivities in the frequency range of interest.

We also extend the computation to a slightly higher cutoff frequency. As estimated in Appendix B, our calculation should still be fairly robust at 450 Hz, as the contributions to the phase evolution from various higher order effects are  $O(10\%)$  of the leading order tidal contribution. The uncertainty in the phase contribution from a given EOS is therefore significantly smaller than the order of magnitude range of phase contributions over the full set of realistic EOS.

The rms uncertainty  $\Delta\tilde{\lambda}$  in the measurement of  $\tilde{\lambda}$  is computed using the standard Fisher matrix formalism [116]. Assuming a strong signal  $h$  and Gaussian detector noise, the signal parameters  $\theta^i$  have probability distribution  $p(\theta^i) \propto \exp(-(1/2)\Gamma_{ij}\delta\theta^i\delta\theta^j)$ , where  $\delta\theta^i = \theta^i - \hat{\theta}^i$  is the difference between the parameters and their best-fit values  $\hat{\theta}^i$  and  $\Gamma_{ij} = (\partial h/\partial\theta^i, \partial h/\partial\theta^j)$  is the Fisher information matrix. The parentheses denote the inner product defined in [116]. The rms measurement error in  $\theta^i$  is given by a diagonal element of the inverse Fisher, or covariance, matrix:  $\Delta\theta^i = \sqrt{(\Gamma^{-1})^{ii}}$ .

Using the stationary phase approximation and neglecting post-Newtonian corrections to the amplitude, the Fourier transform of the waveform for spinning point masses is given by  $\tilde{h}(f) = \mathcal{A}f^{-7/6}\exp(i\Psi)$ , where the point-mass contribution to the phase  $\Psi$  is given to 3.5 post-Newtonian order in Ref. [63]. The tidal term

$$\delta\Psi^{\text{tidal}} = -\frac{117\tilde{\lambda}x^{5/2}}{8\eta M^5} \quad (6.7)$$

obtained from Eq. (B.5) adds linearly to this, yielding a phase model with 7 parameters  $(t_c, \phi_c, \mathcal{M}, \eta, \beta, \sigma, \tilde{\lambda})$ , where  $\beta$  and  $\sigma$  are spin parameters. We incorporate the maximum spin constraint for the NSs by assuming a Gaussian prior for  $\beta$  and  $\sigma$  as in [116]. The uncertainties computed will depend on the choice of point-particle phase evolution, but we assume this to be exactly the 3.5PN form for the current analysis.

The rms measurement uncertainty of  $\tilde{\lambda}$ , along with the uncertainties in chirp mass  $\mathcal{M}$  and symmetric mass ratio  $\eta$ , are given in Table 3 and plotted in Figs. 21 and 23, from a single-detector observation of a binary at 100 Mpc distance with amplitude averaged over inclinations and sky positions. If the best-fit  $\tilde{\lambda}$  is zero, this represents a  $1-\sigma$  upper bound

on the physical  $\tilde{\lambda}$ . A signal with best-fit  $\tilde{\lambda} \geq \Delta\tilde{\lambda}$  would allow a measurement rather than a constraint of  $\tilde{\lambda}$ , with  $1\text{-}\sigma$  uncertainty of  $\Delta\tilde{\lambda}$ .

We obtain the following approximate formula for the rms measurement uncertainty  $\Delta\tilde{\lambda}$ , which is accurate to better than 4% for the range of masses  $0.1 M_\odot \leq m_1, m_2 \leq 3.0 M_\odot$  and cutoff frequencies  $400 \text{ Hz} \leq f_{\text{end}} \leq 500 \text{ Hz}$ :

$$\Delta\tilde{\lambda} \approx \alpha \left( \frac{M}{M_\odot} \right)^{2.5} \left( \frac{m_2}{m_1} \right)^{0.1} \left( \frac{f_{\text{end}}}{\text{Hz}} \right)^{-2.2} \left( \frac{D}{100 \text{ Mpc}} \right), \quad (6.8)$$

where  $\alpha = 1.0 \times 10^{42} \text{ g cm}^2 \text{ s}^2$  for a single Advanced LIGO detector and  $\alpha = 8.4 \times 10^{40} \text{ g cm}^2 \text{ s}^2$  for a single Einstein Telescope detector.

Our results show that the measurability of tidal effects decreases steeply with the total mass of the binary. Estimates of the measurement uncertainty for an equal-mass binary inspiral in a single detector with projected sensitivities of Advanced LIGO and the Einstein Telescope, at a volume-averaged distance of 100 Mpc and using only the portion of the signal between 10 – 450 Hz, are shown in Fig. 21, together with the values of  $\lambda$  predicted by various EOS models. Measurability is less sensitive to mass ratio, as seen in Fig. 23. Comparing the magnitude of the resulting upper bounds on  $\lambda$  with the expected range for realistic EOS, we find that the predicted  $\lambda$  are greatest and the measurement uncertainty  $\Delta\lambda$  is smallest for neutron stars at the low end of the expected mass range for NS-NS inspirals of  $(1 M_\odot - 1.7 M_\odot)$  [117].

In a single Advanced LIGO detector, only extremely stiff EOS could be constrained with a typical 100 Mpc observation. However, a rare nearby event could allow more interesting constraints, as the uncertainty scales as the distance to the source. Rate estimates for detection of binary neutron stars are often given in terms of a minimum signal-to-noise  $\rho_c = 8$ ; a recent estimate [118] is between 2 and 64 binary neutron star detections per year for a single Advanced LIGO interferometer with a volume averaged range of 187 Mpc. The rate of binaries with a volume averaged distance smaller than 100 Mpc translates to roughly  $(100/187)^3 \simeq 15\%$  of this total detection rate, but over multiple years of observation a rare event could give measurements of  $\tilde{\lambda}$  with uncertainties smaller than the values in Table 3 (e.g. with half the tabled uncertainty at 1.9% the total NS-NS rate).

Using information from a network of  $N$  detectors with the same sensitivity decreases the measurement uncertainty by approximately a factor of  $1/\sqrt{N}$  [119], giving more reason for optimism. However, we should also note that, in some ways, our estimates of uncertainty are already too optimistic. First,  $\Delta\lambda$  only represents a 68% confidence in the measurement; a  $2\Delta\lambda$  error bar would give a more reasonable 95% confidence. In addition, our Fisher matrix estimates are likely to somewhat underestimate the measurement uncertainty in

real non-Gaussian noise.

In contrast to Advanced LIGO, an Einstein Telescope detector with currently projected noise would be sensitive to tidal effects for typical binaries, using only the signal below 450 Hz at 100 Mpc. The tidal signal in this regime would provide a clean signature of the neutron star core equation of state. However, an accurate understanding of the underlying point-particle phase evolution is still important to confidently distinguish EOS effects.

Table 3 : The rms measurement error in various binary parameters (chirp mass  $\mathcal{M}$ , symmetric mass ratio  $\eta$ , and weighted average  $\tilde{\lambda}$  of the tidal deformabilities) for a range of total mass  $M$  and mass ratio  $M_2/M_1$ , together with the signal to noise ratio  $\rho$ , using only the information in the portion of the inspiral signal between  $10 \text{ Hz} \leq f \leq 450 \text{ Hz}$ . The distance is set at 100 Mpc, and the amplitude is averaged over sky position and relative inclination.

Advanced LIGO					
$M (M_\odot)$	$M_2/M_1$	$\Delta\mathcal{M}/\mathcal{M}$	$\Delta\eta/\eta$	$\Delta\tilde{\lambda}(10^{36} \text{ g cm}^2 \text{ s}^2)$	$\rho$
2.0	1.0	0.00028	0.073	8.4	27
2.8	1.0	0.00037	0.055	19.3	35
3.4	1.0	0.00046	0.047	31.3	41
2.0	0.7	0.00026	0.058	8.2	26
2.8	0.7	0.00027	0.058	18.9	35
3.4	0.7	0.00028	0.055	30.5	41
2.8	0.5	0.00037	0.06	17.8	33
Einstein Telescope					
$M (M_\odot)$	$M_2/M_1$	$\Delta\mathcal{M}/\mathcal{M}$	$\Delta\eta/\eta$	$\Delta\tilde{\lambda}(10^{36} \text{ g cm}^2 \text{ s}^2)$	$\rho$
2.0	1.0	0.000015	0.0058	0.70	354
2.8	1.0	0.000021	0.0043	1.60	469
3.4	1.0	0.000025	0.0038	2.58	552
2.0	0.7	0.000015	0.0058	0.68	349
2.8	0.7	0.000021	0.0045	1.56	462
3.4	0.7	0.000025	0.0038	2.52	543
2.8	0.5	0.000020	0.0048	1.46	442

Expected measurement uncertainty will decrease if we can extend the calculation later into the inspiral. From Eq. (6.8),  $\Delta\tilde{\lambda}$  at 500 Hz is approximately 79% of its value at 450 Hz. The dominant source of error in the tidal phasing at these frequencies are post-Newtonian effects which scale as  $\lambda x^{7/2}$  and do not depend on any additional EOS parameters. These

terms are computed in Refs. [85, 111], and when they are incorporated into the analysis, the resulting phase evolution model can be used at slightly higher frequencies. These terms also add  $\sim 10\%(f/450 \text{ Hz})^{2/3}$  to the strength of the tidal signature.

Higher-order tidal effects and nonlinear hydrodynamic couplings, which depend on unknown NS microphysics, are smaller than post-Newtonian effects by factors of  $\sim x$  and  $\sim x^2$ , so they become important later in the inspiral, where the adiabatic approximation that the mode frequency is large compared to the orbital frequency also breaks down. At this point we can no longer measure only  $\tilde{\lambda}$ , but an EOS-dependent combination of effects including higher multipoles, nonlinearity, and tidal resonances.

However, information in the late inspiral could also constrain the underlying neutron-star EOS. Read et al. [16] estimated potential measurability of EOS effects in the last few orbits of binary inspiral, where the gravitational wave frequency is above 500 Hz, using full numerical simulations. The EOS used for the simulation was systematically varied by shifting the pressure in the core while keeping the crust fixed. The resulting models were parameterized, either by a fiducial pressure or by the radius of the isolated NS model, and measurability in Advanced LIGO was estimated. Such numerical simulations include all the higher order EOS effects described above, but the  $l = 2$  tidal deformability parameter  $\lambda$  should remain the dominant source of EOS-dependent modification of the phase evolution. We therefore expect it to be a better choice for a single parameter to characterize EOS effects on the late inspiral.

The numerically simulated models of [16] can be re-parameterized by the  $\lambda$  of the  $1.35 M_{\odot}$  neutron stars considered<sup>3</sup>. The uncertainty of measurement for the new parameter  $\lambda$  can be estimated from Tables II-V of [16]. In the broadband Advanced LIGO configuration of Table IV, it is between 0.3 and  $4 \times 10^{36} \text{ g cm}^2 \text{ s}^2$  for an optimally oriented 100 Mpc binary, or between 0.7 and  $9 \times 10^{36} \text{ g cm}^2 \text{ s}^2$  averaged over sky position and orientation. However, in the NS-NS optimized LIGO configuration of Table III, which is most similar to the Advanced LIGO configuration considered in this paper, the expected measurement uncertainty is more than several times  $\lambda$  for all models. These estimates should be considered order-of-magnitude, as numerical simulation errors are significant, and the discrete sampling of a parameter space allows only a coarse measurability estimate which neglects parameter correlations. In contrast to the perturbative/post-Newtonian estimate of EOS effects calculated in this paper, EOS information in the signal before the start of numerical simulations is neglected. The estimate is complementary to the measurability below 450 Hz

---

<sup>3</sup>The piecewise polytropic EOS {2B, B, HB, H, 2H} have  $\lambda_{1.35M_{\odot}}$  of {0.588, 1.343, 1.964, 2.828, 10.842}  $\times 10^{36} \text{ g cm}^2 \text{ s}^2$ , respectively.

estimated in this paper.

## 6.4 Conclusion

We have calculated the relativistic  $l = 2$  Love number  $k_2$  and resulting tidal deformability  $\lambda$  for a wide range of realistic EOS in addition to polytropes. These EOS have tidal deformabilities that differ by up to an order of magnitude in the mass range relevant for binary neutron stars. However, the estimated uncertainty  $\Delta\tilde{\lambda}$  for a binary neutron star inspiral at 100 Mpc using the Advanced LIGO sensitivity below 450 Hz is greater than the largest values of  $\tilde{\lambda}$  except for very low-mass binaries. The uncertainty for the Einstein Telescope, on the other hand, is approximately an order of magnitude smaller than for Advanced LIGO, and a measurement of  $\tilde{\lambda}$  will rule out a significant fraction of the EOS.

Advanced LIGO can place a constraint on the space of possible EOS by obtaining a 95% confidence upper limit of  $\tilde{\lambda}(\mathcal{M}, \eta) \lesssim 2\Delta\tilde{\lambda}(\mathcal{M}, \eta)$ . The tables in Sec. 6.3 can also be scaled as follows: For a network of  $N$  detectors the uncertainty scales roughly as  $\Delta\tilde{\lambda}/\sqrt{N}$ , and for a closer signal we have  $\Delta\tilde{\lambda}(D/100 \text{ Mpc})$ .

## Chapter 7

# Detectability of tidal parameters from nonspinning BHNS systems

### 7.1 Introduction

Construction of the second-generation Advanced LIGO (aLIGO) detectors is underway and will soon begin for Advanced VIRGO and LCGT, making it likely that gravitational waveforms from compact binaries will be observed in this decade. Plans are also in development for the third generation Einstein Telescope (ET) detector with an order-of-magnitude increase in sensitivity over aLIGO. Population synthesis models predict that with a single aLIGO detector binary neutron star (BNS) systems will be observed with a signal-to-noise ratio (SNR) of 8, at an event rate between 0.4 and 400 times per year and with a most likely value of 40 per year [120]. Black hole–neutron star (BHNS) systems are also expected, but with a more uncertain rate of between 0.2 and 300 events per year at the same SNR and with a most likely value of 10 events per year for a canonical  $1.4 M_{\odot}$ – $10 M_{\odot}$  system [120]. The expected mass ratios  $Q = M_{\text{BH}}/M_{\text{NS}}$  of BHNS systems are also highly uncertain and may range from just under 3 to more than 20 [121, 122].

A major goal of the gravitational-wave (GW) program is to extract from observed waveforms the physical characteristics of their sources and, in particular, to use the waveforms of inspiraling and merging BNS and BHNS systems to constrain the uncertain EOS of neutron-star matter. During inspiral the tidal interaction between the two stars leads to a small drift in the phase of the gravitational waveform relative to a point particle system. Specifically the tidal field  $\mathcal{E}_{ij}$  of one star will induce a quadrupole moment  $Q_{ij}$  in the other star given by  $Q_{ij} = -\lambda\mathcal{E}_{ij}$  where  $\lambda$ <sup>1</sup> is an EOS dependent quantity that describes how easily the star

---

<sup>1</sup>The tidal deformability for the  $\ell$ th multipole is often defined in terms of the NS radius  $R$  and its

is distorted. A method for determining  $\lambda$  for relativistic stars was found by Hinderer [87]; its effect on the waveform was calculated to Newtonian order (with the relativistic value of  $\lambda$ ) by Flanagan and Hinderer [86] and to first post-Newtonian (PN) order by Vines, Flanagan, and Hinderer [85, 111]. This tidal description has also been extended to higher order multipoles [93, 110].

The detectability of EOS effects have been examined for both BNS and BHNS systems using this analytical description of the inspiral. For BNS systems, the detectability of  $\lambda$  with aLIGO was examined for polytropic EOS [86] as well as a range of theoretical EOS commonly found in the NS literature for aLIGO and ET [123]. These studies considered only the waveform up to frequencies of 400–500 Hz ( $\sim 30$ – $20$  GW cycles before merger for  $1.4 M_{\odot}$  equal-mass NSs). For this early part of inspiral, they find that the tidal deformability is detectable by aLIGO only for an unusually stiff EOS and for low neutron-star masses ( $< 1.2 M_{\odot}$ ). ET on the other hand would have an order of magnitude improvement in estimating  $\lambda$ , allowing ET to distinguish between different classes of EOS. For BHNS systems, using the recently calculated 1PN corrections, Pannarale et al. [124] examined detectability for a range of mass ratios, finding that aLIGO will be able to distinguish between BHNS and binary black hole (BBH) systems only for low mass ratios and stiff EOS when considering the full inspiral waveform up to the point of tidal disruption.

In sharp contrast to these analytic post-Newtonian results, analysis of just the last few orbits of BNS inspiral from numerical simulations has shown that the NS radius may be extracted to a higher accuracy, of  $\mathcal{O}(10\%)$  with aLIGO [16], and this is confirmed by a study based on a set of longer and more accurate waveforms from two different codes [125]. In addition, comparisons between the analytical tidal description and BNS quasiequilibrium sequences [126] as well as long BNS numerical waveforms [127, 128] suggest that corrections beyond the 1PN quadrupole description are significant and substantially increase the tidal effect during the late inspiral.

Numerical BHNS simulations have also been done to examine the dependence of the waveform on mass ratio, BH spin, NS mass, and the neutron-star EOS [129, 130, 131, 132, 133, 134, 135, 136, 137, 138, 139, 140]. However, an analysis of the detectability of EOS information with GW detectors using these simulations has not yet been done, and the present chapter presents the first results of this kind. EOS information from tidal interactions is present in the inspiral waveform. For BHNS systems, however, the stronger signal is likely to arise from a sharp drop in the GW amplitude arising from tidal

---

dimensionless  $\ell$ th Love number  $k_{\ell}$  by  $\lambda_{\ell} = \frac{2}{(2\ell-1)!!G} k_{\ell} R^{2\ell+1}$ . Here we will discuss only the  $\ell = 2$  term so we write  $\lambda := \lambda_2$ .

disruption prior to merger or, when there is negligible disruption, from the cutoff frequency at merger [141].

We find from simulations of the last few orbits, merger, and ringdown of BHNS systems with varying EOS that, to within numerical accuracy, the EOS parameter extracted from the waveform is the same tidal parameter  $\Lambda$  that determines the departure from point particle behavior during inspiral; here  $\Lambda$  is a dimensionless version of the tidal parameter:

$$\Lambda := G\lambda \left( \frac{c^2}{GM_{\text{NS}}} \right)^5 = \frac{2}{3} k_2 \left( \frac{c^2 R}{GM_{\text{NS}}} \right)^5, \quad (7.1)$$

where  $k_2$  is the quadrupole Love number. This parameter is similar to the dimensionless parameter  $\kappa_2^T$  introduced in Eq. (26) of Ref. [126]. However, we have chosen to make  $\Lambda$  independent of the mass ratio so that it depends on only the neutron star mass and EOS.

The constraint on the EOS imposed by gravitational-wave observations of BHNS inspiral and merger is essentially a restriction of the space of EOS  $p = p(\rho)$  to a hypersurface of constant  $\Lambda$ , thickened by the uncertainty in the measurement (that is, a restriction to the set of EOS for which a spherical neutron star of the mass observed in the inspiral has tidal parameter  $\Lambda$ ). We use a parametrized EOS based on piecewise polytropes [54], to delineate this region in the EOS space, but the result can be used to constrain any choice of parameters for the EOS space.

In Sec. 7.2 we discuss the parametrized EOS used in the simulations. We give in Sec. 7.3 an overview of the numerical methods used and, in Sec. 7.4, a description of the waveforms from the simulations. We then discuss the analytical waveforms used for the early inspiral and issues related to joining the analytical and numerical waveforms to create hybrids in Sec. 8.3, and we then estimate the uncertainty in extracting EOS parameters in Sec. 7.6. Finally, we discuss in Sec. 7.7 remaining work, including spinning black holes, which will be addressed in Chapter 8. In an appendix we describe methods for numerically evaluating the Fisher matrix.

*Conventions:* Unless otherwise stated we set  $G = c = 1$ . Base 10 and base  $e$  logarithms are denoted  $\log$  and  $\ln$  respectively. We define the Fourier transform  $\tilde{x}(f)$  of a function  $x(t)$  by

$$\tilde{x}(f) = \int_{-\infty}^{\infty} x(t) e^{-2\pi i f t} dt, \quad (7.2)$$

and the inverse Fourier transform by

$$x(t) = \int_{-\infty}^{\infty} \tilde{x}(f) e^{2\pi i f t} df. \quad (7.3)$$

## 7.2 Parametrized EOS

To understand the dependence of the BHNS waveform on the EOS we systematically vary the free parameters of a parametrized EOS and then simulate a BHNS inspiral for each set of parameters. We choose the piecewise polytropic EOS introduced in Ref [54]. Within each density interval  $\rho_{i-1} < \rho < \rho_i$ , the pressure  $p$  is given in terms of the rest mass density  $\rho$  by

$$p(\rho) = K_i \rho^{\Gamma_i}, \quad (7.4)$$

where the adiabatic index  $\Gamma_i$  is constant in each interval, and the pressure constant  $K_i$  is chosen so that the EOS is continuous at the boundaries  $\rho_i$  between adjacent segments of the EOS. The energy density  $\epsilon$  is found using the first law of thermodynamics,

$$d\frac{\epsilon}{\rho} = -pd\frac{1}{\rho}. \quad (7.5)$$

Ref. [54] uses a fixed low density EOS for the NS crust. The parametrized high density EOS is then joined onto the low density EOS at a density  $\rho_0$  that depends on the values of the high-density EOS parameters. The high-density EOS consists of a three-piece polytrope with fixed dividing densities  $\rho_1 = 10^{14.7}$  g/cm<sup>3</sup> and  $\rho_2 = 10^{15}$  g/cm<sup>3</sup> between the three polytropes. The resulting EOS has four free parameters. The first parameter, the pressure  $p_1$  at the first dividing density  $\rho_1$ , is closely related to the radius of a  $1.4 M_\odot$  NS [8]. The other three parameters are the adiabatic indices  $\{\Gamma_1, \Gamma_2, \Gamma_3\}$  for the three density intervals. This parametrization accurately fits a wide range of theoretical EOS and reproduces the corresponding NS properties such as radius, moment of inertia, and maximum mass to a few percent [54].

Following previous work on BNS [16] and BHNS simulations [137, 140] we use a simplified two-parameter version of the piecewise-polytrope parametrization and uniformly vary each of these parameters. For our two parameters we use the pressure  $p_1$  as well as a single fixed adiabatic index  $\Gamma = \Gamma_1 = \Gamma_2 = \Gamma_3$  for the core. The crust EOS is given by a single polytrope with the constants  $K_0 = 3.5966 \times 10^{13}$  in cgs units and  $\Gamma_0 = 1.3569$  so that the pressure at  $10^{13}$  g/cm<sup>3</sup> is  $1.5689 \times 10^{31}$  dyne/cm<sup>2</sup>. (For most values of  $p_1$ ,  $\Gamma_1$ , and  $\Gamma_2$ , the central density of a  $1.4 M_\odot$  star is below or just above  $\rho_2$ , so the parameter  $\Gamma_3$  is irrelevant anyway for BNS before merger and BHNS for all times.)

We list in Table 4 the 21 EOS used in the simulations along with some of the NS properties. In addition, we plot the EOS as points in parameter space in Fig. 25 along with contours of constant radius, tidal deformability  $\Lambda$ , and maximum NS mass. The  $1.93 M_\odot$  maximum mass contour corresponds to the recently observed pulsar with a mass

of  $1.97 \pm 0.04 M_{\odot}$  measured using the Shapiro delay [43]. In this two-parameter cross section of the full four-parameter EOS space, parameters below this curve are ruled out because the corresponding EOS cannot support the observed NS with  $M > 1.93 M_{\odot}$ .

Table 4 : Neutron star properties for the 21 EOS used in the simulations. The original EOS names [16, 137, 140] are also listed.  $p_1$  is given in units of  $\text{dyne/cm}^2$ , maximum mass is in  $M_{\odot}$ , and neutron star radius  $R$  is in km.  $R$ ,  $k_2$ , and  $\Lambda$  are given for the two masses used:  $\{1.20, 1.35\} M_{\odot}$ . The values listed for  $\log p_1$  are rounded to three digits. The exact values used in the simulations can be found by adding  $\log(c/\text{cm s}^{-1})^2 - 20.95 \approx 0.00364$  (e.g. 34.3 becomes 34.30364).

EOS		$\log p_1$	$\Gamma$	$M_{\text{max}}$	$R_{1.20}$	$k_{2,1.20}$	$\Lambda_{1.20}$	$R_{1.35}$	$k_{2,1.35}$	$\Lambda_{1.35}$
p.3 $\Gamma$ 2.4	Bss	34.3	2.4	1.566	10.66	0.0765	401	10.27	0.0585	142
p.3 $\Gamma$ 2.7	Bs	34.3	2.7	1.799	10.88	0.0910	528	10.74	0.0751	228
p.3 $\Gamma$ 3.0	B	34.3	3.0	2.002	10.98	0.1010	614	10.96	0.0861	288
p.3 $\Gamma$ 3.3		34.3	3.3	2.181	11.04	0.1083	677	11.09	0.0941	334
p.4 $\Gamma$ 2.4	HBss	34.4	2.4	1.701	11.74	0.0886	755	11.45	0.0723	301
p.4 $\Gamma$ 2.7	HBs	34.4	2.7	1.925	11.67	0.1004	828	11.57	0.0855	375
p.4 $\Gamma$ 3.0	HB	34.4	3.0	2.122	11.60	0.1088	872	11.61	0.0946	422
p.4 $\Gamma$ 3.3		34.4	3.3	2.294	11.55	0.1151	903	11.62	0.1013	454
p.5 $\Gamma$ 2.4		34.5	2.4	1.848	12.88	0.1000	1353	12.64	0.0850	582
p.5 $\Gamma$ 2.7		34.5	2.7	2.061	12.49	0.1096	1271	12.42	0.0954	598
p.5 $\Gamma$ 3.0	H	34.5	3.0	2.249	12.25	0.1165	1225	12.27	0.1029	607
p.5 $\Gamma$ 3.3		34.5	3.3	2.413	12.08	0.1217	1196	12.17	0.1085	613
p.6 $\Gamma$ 2.4		34.6	2.4	2.007	14.08	0.1108	2340	13.89	0.0970	1061
p.6 $\Gamma$ 2.7		34.6	2.7	2.207	13.35	0.1184	1920	13.32	0.1051	932
p.6 $\Gamma$ 3.0		34.6	3.0	2.383	12.92	0.1240	1704	12.97	0.1110	862
p.6 $\Gamma$ 3.3		34.6	3.3	2.537	12.63	0.1282	1575	12.74	0.1155	819
p.7 $\Gamma$ 2.4		34.7	2.4	2.180	15.35	0.1210	3941	15.20	0.1083	1860
p.7 $\Gamma$ 2.7		34.7	2.7	2.362	14.26	0.1269	2859	14.25	0.1144	1423
p.7 $\Gamma$ 3.0	1.5H	34.7	3.0	2.525	13.62	0.1313	2351	13.69	0.1189	1211
p.7 $\Gamma$ 3.3		34.7	3.3	2.669	13.20	0.1346	2062	13.32	0.1223	1087
p.9 $\Gamma$ 3.0	2H	34.9	3.0	2.834	15.12	0.1453	4382	15.22	0.1342	2324

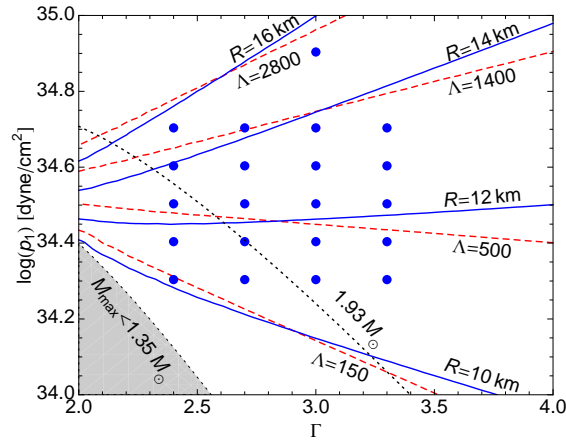


Figure 25 : The 21 EOS used in the simulations are represented by blue points in the parameter space. For a NS of mass  $1.35 M_{\odot}$ , contours of constant radius are solid blue and contours of constant tidal deformability  $\Lambda$  are dashed red. Also shown are dotted contours of maximum NS mass. The shaded region does not allow the  $1.35 M_{\odot}$  NS used in our simulations, while the region below the  $1.93 M_{\odot}$  contour is inconsistent with high-mass NS observations.

### 7.3 Numerical methods

We employ BHNS binaries in quasiequilibrium states for the initial conditions of our numerical simulations. We compute a quasiequilibrium state of the BHNS binary as a solution of the initial value problem of general relativity, employing the piecewise polytropic EOS described in the previous section. The details of the formulation and numerical methods are described in Refs. [142, 137]. Computations of the quasiequilibrium states are performed using the spectral-method library LORENE [143].

Numerical simulations are performed using an adaptive-mesh refinement code SACRA [144]. SACRA solves the Einstein evolution equations in the BSSN formalism with the moving puncture gauge, and solves the hydrodynamic equations with a high-resolution central scheme. The formulation, the gauge conditions, and the numerical scheme are the same as those described in Ref. [137]. For the EOS, we decompose the pressure and energy density into cold and thermal parts as

$$p = p_{\text{cold}} + p_{\text{th}}, \quad \epsilon = \epsilon_{\text{cold}} + \epsilon_{\text{th}}, \quad (7.6)$$

as was done in, for example, [145] and references therein. We calculate the cold parts of both variables using the piecewise polytropic EOS from  $\rho$ , and then the thermal part of the energy density is defined from  $\epsilon$  as  $\epsilon_{\text{th}} = \epsilon - \epsilon_{\text{cold}}$ . Because  $\epsilon_{\text{th}}$  vanishes in the absence of shock heating,  $\epsilon_{\text{th}}$  is regarded as the finite temperature part. In our simulations, we adopt

a  $\Gamma$ -law ideal gas EOS

$$p_{\text{th}} = (\Gamma_{\text{th}} - 1)\epsilon_{\text{th}}, \quad (7.7)$$

to determine the thermal part of the pressure, and choose  $\Gamma_{\text{th}}$  equal to the adiabatic index in the crust region,  $\Gamma_0$ , for simplicity.

In our numerical simulations, gravitational waves are extracted by calculating the outgoing part of the Weyl scalar  $\Psi_4$  at finite coordinate radii  $\sim 400M_\odot$ , and by integrating  $\Psi_4$  twice in time as

$$h_+(t) - ih_\times(t) = \int_{-\infty}^t dt' \int_{-\infty}^{t'} dt'' \Psi_4(t''), \quad (7.8)$$

where we will focus on the  $(\ell, m) = (2, 2)$  multipole evaluated on the orbital axis. Other multipoles measured along the axis are one or two orders of magnitude smaller. In this work, we perform this time integration with a “fixed frequency integration” method to eliminate unphysical drift components in the waveform [146]. In this method, we first perform a Fourier transformation of  $\Psi_4$  as

$$\tilde{\Psi}_4(f) = \int_{-\infty}^{\infty} dt \Psi_4(t) e^{-2\pi i f t}. \quad (7.9)$$

Using this, Eq. (7.8) is rewritten as

$$h_+(t) - ih_\times(t) = -\frac{1}{(2\pi)^2} \int_{-\infty}^{\infty} df \frac{\tilde{\Psi}_4(f)}{f^2} e^{2\pi i f t}. \quad (7.10)$$

We then replace  $1/f^2$  of the integrand with  $1/f_0^2$  for  $|f| < f_0$ , where  $f_0$  is a free parameter in this method. By appropriately choosing  $f_0$ , this procedure suppresses unphysical, low-frequency components of gravitational waves. As proposed in Ref. [146], we choose  $f_0$  to be  $\sim 0.8m\Omega_0/2\pi$ , where  $\Omega_0$  is the initial orbital angular velocity and  $m(=2)$  is the azimuthal quantum number.

## 7.4 Description of waveforms

Using the 21 EOS described in Table 4, we have performed 30 BHNS inspiral and merger simulations with different mass ratios  $Q = M_{\text{BH}}/M_{\text{NS}}$  and neutron star masses  $M_{\text{NS}}$ . A complete list of these simulations is given in Table 6. For the mass ratio  $Q = 2$  and NS mass  $M_{\text{NS}} = 1.35 M_\odot$ , we performed a simulation for each of the 21 EOS. In addition, we performed simulations of a smaller NS mass ( $Q = 2$ ,  $M_{\text{NS}} = 1.20 M_\odot$ ) and a larger mass ratio ( $Q = 3$ ,  $M_{\text{NS}} = 1.35 M_\odot$ ), in which we only varied the pressure  $p_1$  over the range  $34.3 \leq \log(p_1/(\text{dyne cm}^{-2})) \leq 34.9$  while holding the core adiabatic index fixed at  $\Gamma = 3.0$ .

Table 5 : Data for the 30 BHNS simulations. NS mass is in units of  $M_{\odot}$ , and  $\Omega_0 M$  is the angular velocity used in the initial data where  $M = M_{\text{BH}} + M_{\text{NS}}$ .

$Q$	$M_{\text{NS}}$	EOS	$\Omega_0 M$	$Q$	$M_{\text{NS}}$	EOS	$\Omega_0 M$
2	1.35	p.3 $\Gamma$ 2.4	0.028	2	1.35	p.6 $\Gamma$ 3.3	0.025
2	1.35	p.3 $\Gamma$ 2.7	0.028	2	1.35	p.7 $\Gamma$ 2.4	0.025
2	1.35	p.3 $\Gamma$ 3.0	0.028	2	1.35	p.7 $\Gamma$ 2.7	0.025
2	1.35	p.3 $\Gamma$ 3.3	0.025	2	1.35	p.7 $\Gamma$ 3.0	0.028
2	1.35	p.4 $\Gamma$ 2.4	0.028	2	1.35	p.7 $\Gamma$ 3.3	0.025
2	1.35	p.4 $\Gamma$ 2.7	0.028	2	1.35	p.9 $\Gamma$ 3.0	0.025
2	1.35	p.4 $\Gamma$ 3.0	0.028	2	1.20	p.3 $\Gamma$ 3.0	0.028
2	1.35	p.4 $\Gamma$ 3.3	0.025	2	1.20	p.4 $\Gamma$ 3.0	0.028
2	1.35	p.5 $\Gamma$ 2.4	0.025	2	1.20	p.5 $\Gamma$ 3.0	0.028
2	1.35	p.5 $\Gamma$ 2.7	0.025	2	1.20	p.9 $\Gamma$ 3.0	0.022
2	1.35	p.5 $\Gamma$ 3.0	0.028	3	1.35	p.3 $\Gamma$ 3.0	0.030
2	1.35	p.5 $\Gamma$ 3.3	0.025	3	1.35	p.4 $\Gamma$ 3.0	0.030
2	1.35	p.6 $\Gamma$ 2.4	0.025	3	1.35	p.5 $\Gamma$ 3.0	0.030
2	1.35	p.6 $\Gamma$ 2.7	0.025	3	1.35	p.7 $\Gamma$ 3.0	0.030
2	1.35	p.6 $\Gamma$ 3.0	0.025	3	1.35	p.9 $\Gamma$ 3.0	0.028

Two of the gravitational waveforms are shown in Fig. 26 below. The waveforms are compared with EOB BBH waveforms of the same mass ratio and NS mass which are also shown. Specifically we use the EOB formalism discussed in Sec. 3.4. The most significant differences begin just before the merger of the black hole and neutron star. For neutron stars with a small radius, the black hole does not significantly distort the neutron star which crosses the event horizon intact. As a result, the merger and ringdown of these waveforms are very similar to the BBH waveform. However, a larger NS may be completely tidally disrupted just before merger resulting in a suppressed merger and ringdown waveform. Disruption suppresses the ringdown for two reasons related to the spreading of the matter: The ringdown is primarily a superposition of nonaxisymmetric quasinormal modes, dominated by the  $l = m = 2$  mode (axisymmetric modes are more than an order of magnitude smaller [147]), while the disrupted matter is roughly axisymmetric as it accretes onto the black hole; and the accretion timescale of the spread-out matter is long compared to the periods of the dominant modes decreasing the amplitude further.

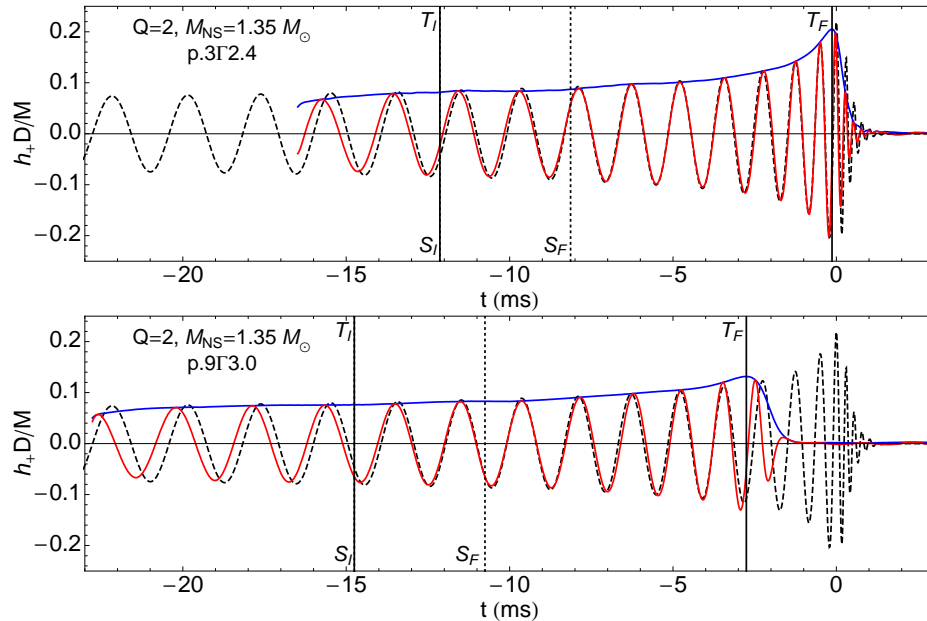


Figure 26 :  $h_+$  and  $|h| = |h_+ - ih_\times|$  for BHNS waveforms for ( $Q = 2, M_{\text{NS}} = 1.35 M_\odot$ ) with two different EOS are represented by solid red and blue curves respectively. The softest EOS p.3 $\Gamma$ 2.4 is on top and the stiffest EOS p.9 $\Gamma$ 3.0 is on bottom. An EOB BBH waveform (dashed) with the same values of  $Q$  and  $M_{\text{NS}}$  is matched to each numerical waveform within the matching window  $T_I < t < T_F$  bounded by solid vertical lines. A hybrid EOB BBH–Numerical BHNS waveform is generated by splicing the waveforms together within a splicing window  $S_I < t < S_F$  bounded by dotted vertical lines. The matching window is 12 ms long and ends at the numerical merger time  $t_M^{\text{NR}}$  (time when the numerical waveform reaches its maximum amplitude), while the splicing window is 4 ms long and begins at the start of the matching window ( $S_I = T_I$ ).

The dependence of the waveform on the EOS can be seen more clearly by decomposing each waveform into amplitude  $A(t)$  and phase  $\Phi(t)$  with the relation  $h_+(t) - ih_\times(t) = A(t)e^{-i\Phi(t)}$ . In Fig. 27, the amplitude as a function of time for each BHNS waveform is compared to a BBH waveform of the same value of  $Q$  and  $M_{\text{NS}}$ . At early times, the waveform is almost identical to the BBH waveform. However, a few ms before the maximum amplitude is reached, the amplitude begins to depart from the BBH case. For each  $Q$  and  $M_{\text{NS}}$ , this departure from the BBH waveform is approximately monotonic in  $\Lambda$  and  $R$ . Neutron stars with large values of  $\Lambda$  merge earlier, and as a result the waveforms reach a smaller maximum amplitude. The phase of each waveform is compared to that of the EOB BBH waveform  $\Phi_{\text{EOB}}$  in Fig. 28. At early times the phase oscillates about the EOB phase due to initial eccentricity in the numerical waveform discussed in Sec. 7.5.2. At later times, closer to the merger, tidal interactions lead to a higher frequency orbit; this, together with

correspondingly stronger gravitational wave emission, means the BHNS phase accumulates faster than the EOB phase. This continues for 1–2 ms after the waveform reaches its maximum amplitude (indicated by the dot on each curve). Eventually the amplitude drops significantly, and numerical errors dominate the phase. We truncate the curves when the amplitude drops below 0.01.

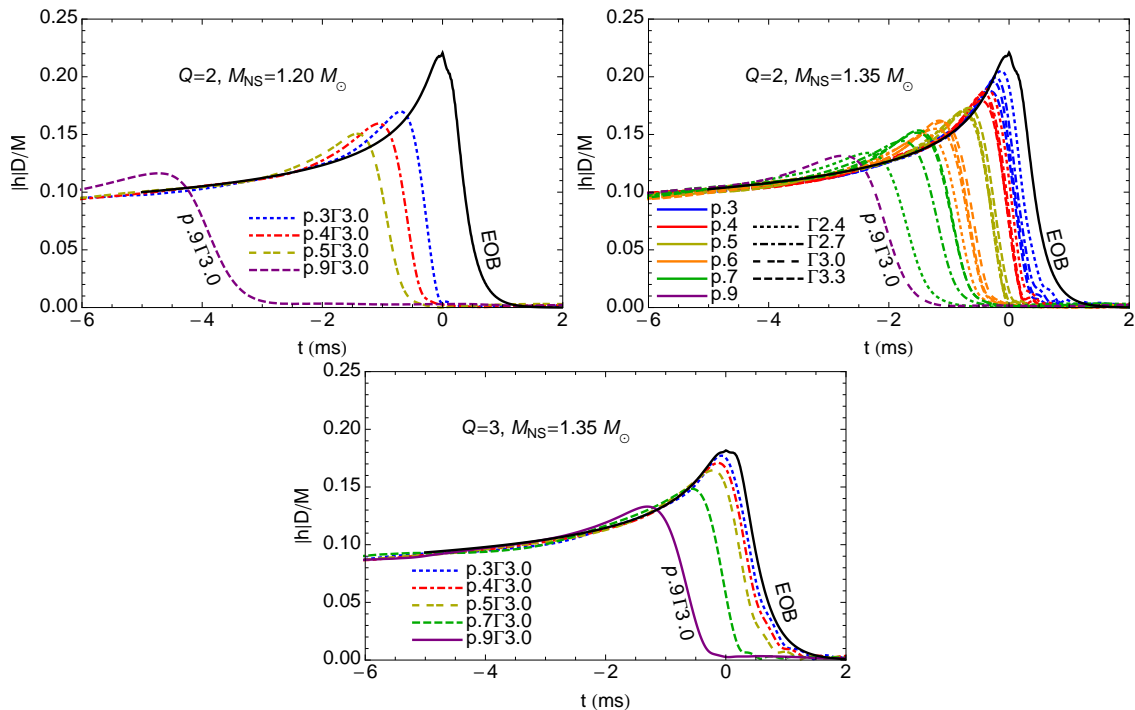


Figure 27 : (Color online) Amplitude of the complex waveform  $h = h_+ - ih_\times$ . Solid black curves are EOB waveforms with the same  $Q$  and  $M_{\text{NS}}$ . Matching and splicing conventions are those of Fig. 26. Top right panel: color indicates the value of  $\log(p_1)$  while the line style indicates the value of  $\Gamma$ . With the exception of the four closely spaced waveforms where  $\log(p_1/(\text{dyne cm}^{-2})) = 35.5$  and the difference in  $\Lambda$  and  $R$  between waveforms is small, the BHNS waveforms monotonically approach the EOB waveform as  $\Lambda$  and  $R$  decrease.

The monotonic dependence of the waveform on  $\Lambda$  can again be seen in its Fourier transform  $\tilde{h}$ , shown in Figs. 29 and 30, which is decomposed into amplitude and phase by  $\tilde{h}(f) = A(f)e^{-i\Phi(f)}$ . The predicted EOS dependent frequency cutoff in the waveform [141] is clearly shown in the amplitude<sup>2</sup>. Neutron stars that are more easily disrupted (larger  $\Lambda$ ) result in an earlier and lower frequency drop in their waveform amplitude than NS

<sup>2</sup>Tidal disruption occurs after the onset of mass shedding of the neutron star. The frequency at the onset of mass shedding is usually much lower than that of tidal disruption for BHNS binaries [132]. In Ref. [141], mass-shedding frequency was identified as the cutoff frequency but this underestimates the true cutoff frequency. See also Refs. [148, 106] for a discussion of dynamical mass transfer.

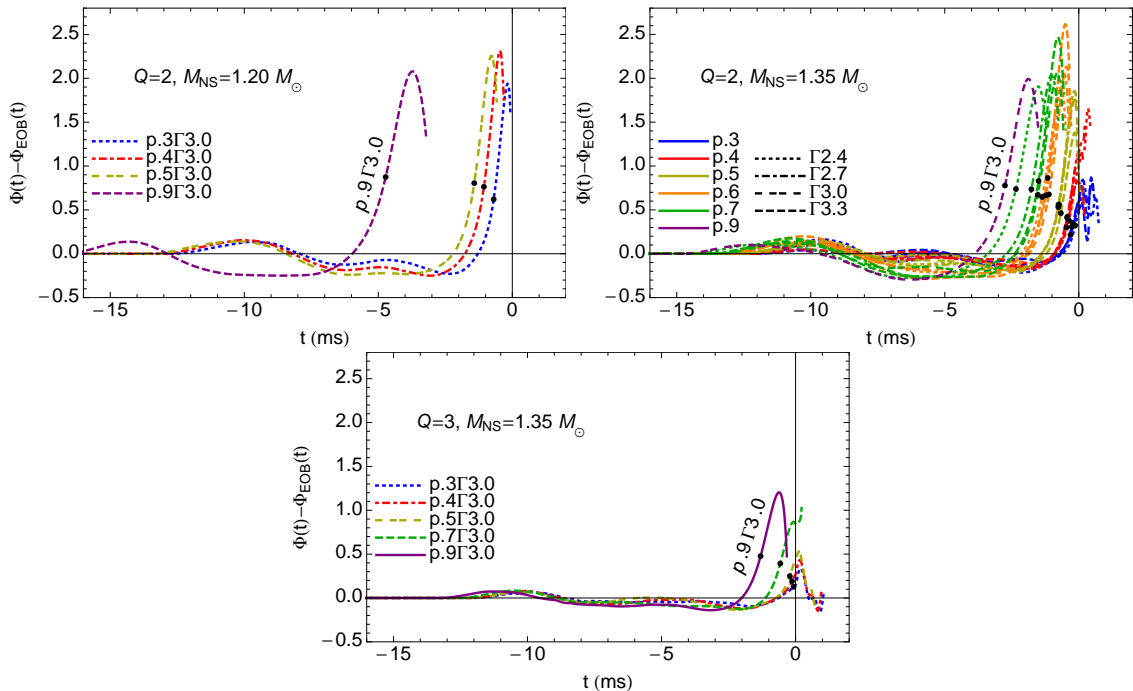


Figure 28 : (Color online) Cumulative phase difference  $\Phi - \Phi_{\text{EOB}}$  between BHNS waveform and EOB BBH waveform with the same  $Q$  and  $M_{\text{NS}}$ . The phase is defined by breaking up each complex waveform into amplitude and cumulative phase  $h_+(t) - ih_\times(t) = A(t)e^{-i\Phi(t)}$ . The black point on each curve indicates the BHNS merger time  $t_M^{\text{NR}}$  defined as the time of maximum amplitude  $A(t_M^{\text{NR}})$ . The curve is truncated when the amplitude  $AD/M$  drops below 0.01. Matching and splicing conventions are those of Fig. 26. Ordering of waveforms are those of Fig. 27.

with smaller  $\Lambda$ . The phase  $\Phi(f)$  relative to the corresponding BBH waveform has a much smoother behavior than the phase of the time domain waveform. This feature will be useful in evaluating the Fisher matrix in Sec. 7.6. The noise that is seen at frequencies above  $\sim 3000$  Hz is the result of numerical errors in the simulation and has no effect on the error estimates below.

## 7.5 Hybrid Waveform Construction

Since our numerical simulations typically begin  $\sim 5$  orbits before merger, it is necessary to join the numerical waveforms to analytic waveforms representing the earlier inspiral. There is a substantial literature comparing analytic and phenomenological waveforms with numerical waveforms extracted from simulations of BBH coalescence. For example, it has been shown that the 3.5 post-Newtonian (TaylorT4) waveform agrees well with equal mass BBH waveforms up to the last orbit before merger [70]. For unequal mass systems, the EOB

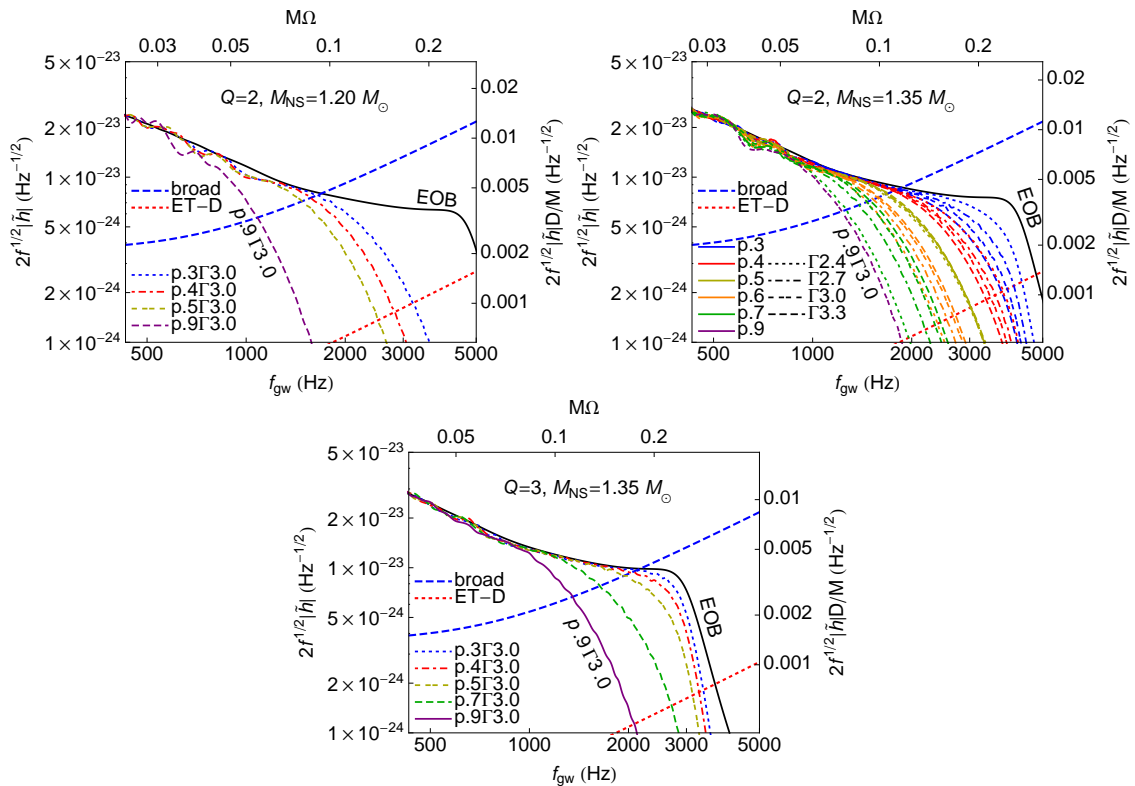


Figure 29 : (Color online) Weighted Fourier transform  $2f^{1/2}|\tilde{h}(f)|$  of numerical waveforms where  $\tilde{h} = \frac{1}{2}(\tilde{h}_+ + \tilde{h}_\times)$ . Solid black curves are EOB waveforms with the same  $Q$  and  $M_{\text{NS}}$ . The left axis is scaled to a distance of 100 Mpc, and the noise  $S_n^{1/2}(f)$  for broadband aLIGO and ET-D are shown for comparison. In each plot the numerical waveform monotonically approaches the EOB waveform as the tidal parameter  $\Lambda$  decreases. Matching and splicing conventions are those of Fig. 26. Ordering of waveforms are those of Fig. 27.

formalism (see Ref. [77] for a review) has proven to be a powerful tool to generate analytic waveforms that agree with numerical simulations. Free parameters in the EOB formalism have been fit to numerical BBH waveforms to provide analytic (phenomenological) waveforms that extend to the late, non-adiabatic inspiral as well as the ringdown. These EOB waveforms appear to be in good agreement with numerical BBH waveforms for mass ratios at least up to  $Q = 4$  [76]. Although we have not explored them in this context, other approaches have also been taken for constructing phenomenological inspiral-merger-ringdown waveforms [73, 74, 72, 149, 150].

For equal-mass BNS, Read et al. [16] compared the numerical BNS waveform during inspiral to a point particle post-Newtonian waveform. Specifically, they used the 3.5 post-Newtonian (TaylorT4) waveforms matched on to the numerical waveforms to study the

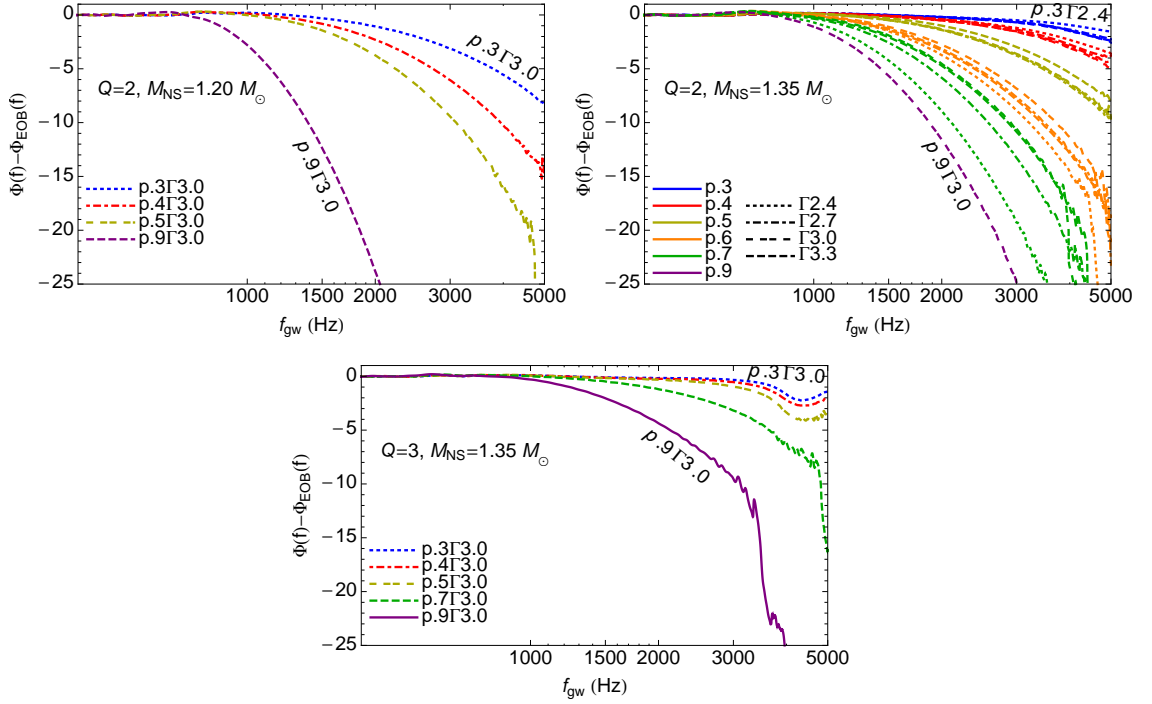


Figure 30 : (Color online) Cumulative phase difference  $\Phi - \Phi_{\text{EOB}}$  of the Fourier transform between BHNS waveform and EOB BBH waveform of the same mass and mass ratio. The phase is defined by breaking up the Fourier transform  $\tilde{h} = \frac{1}{2}(\tilde{h}_+ + \tilde{h}_\times)$  of each waveform into amplitude and cumulative phase  $\tilde{h}(f) = A(f)e^{-i\Phi(f)}$ . Matching and splicing conventions are those of Fig. 26. Ordering of waveforms are those of Fig. 27.

measurability of EOS parameters. They found that differences between the analytic and numerical waveforms become apparent 4 – 8 cycles before the post-Newtonian coalescence time.

The leading and post-1-Newtonian quadrupole tidal effects have recently been incorporated into the post-Newtonian formalism and used to compute corrections to the point-particle gravitational waveforms [86, 85, 111]. These post-Newtonian contributions along with a fit to the 2PN tidal contribution have also been incorporated into the EOB formalism and compared to long simulations ( $\sim 20$  GW cycles), where they find agreement with the simulations to  $\pm 0.15$  rad over the full simulation up to merger [128].

For the BHNS systems discussed here, we have matched the numerical waveforms to EOB waveforms that include inspiral, merger, and ringdown phases instead of post-Newtonian waveforms which are often not reliable during the last few cycles for higher mass ratios. This choice also allows us to use longer matching windows that average over

numerical noise and the effects of eccentricity as shown in Sec. 7.5.2. We have chosen to use the EOB formalism to generate inspiral-merger-ringdown waveforms, although we note that other phenomenological waveforms would probably work. For simplicity, and because it appears that an accurate description of the late inspiral dynamics just before merger requires 2PN tidal corrections [126, 127, 128] which are not yet known, we will use the EOB waveforms without tidal corrections. Our results will therefore be lower limits on the measurability of EOS parameters since the EOS dependence is coming solely from the numerical waveforms.

### 7.5.1 Matching procedure

We use a method similar to that described by Read et al. [16] to join each of the numerical BHNS waveforms to a reference EOB waveform, generating a hybrid EOB–numerical waveform. Denote a complex numerical waveform by  $h_{\text{NR}}(t) = h_{+}^{\text{NR}}(t) - ih_{\times}^{\text{NR}}(t)$  and an EOB waveform with the same  $Q$  and  $M_{\text{NS}}$  by  $h_{\text{EOB}}(t) = h_{+}^{\text{EOB}}(t) - ih_{\times}^{\text{EOB}}(t)$ . A constant time-shift  $\tau$  and phase-shift  $\Phi$  can be applied to the EOB waveform to match it to a section of the numerical waveform by rewriting it as  $h_{\text{EOB}}(t - \tau)e^{-i\Phi}$ . We hold the numerical waveform fixed because we must specify a matching window  $T_I < t < T_F$ , and as discussed below, there is only a small region of the numerical waveforms over which a valid match can be performed. Once the values of  $\tau$  and  $\Phi$  are determined, we will then choose to instead hold the EOB waveform fixed and shift the numerical waveform in the opposite direction by rewriting it as  $h_{\text{NR}}^{\text{shift}}(t) = h_{\text{NR}}(t + \tau)e^{+i\Phi}$ . This is done so that all of the numerical waveforms with the same  $Q$  and  $M_{\text{NS}}$  are aligned relative to a single fixed reference EOB waveform.

Over a matching window  $T_I < t < T_F$  (bounded by solid vertical lines in Fig. 26), the normalized match between the waveforms is defined as

$$m(\tau, \Phi) = \frac{\text{Re} [z(\tau)e^{i\Phi}]}{\sigma_{\text{NR}}\sigma_{\text{EOB}}(\tau)}, \quad (7.11)$$

where

$$z(\tau) = \int_{T_I}^{T_F} h_{\text{NR}}(t)h_{\text{EOB}}^*(t - \tau) dt \quad (7.12)$$

and the normalizations for each waveform in the denominator are defined as

$$\sigma_{\text{NR}}^2 = \int_{T_I}^{T_F} |h_{\text{NR}}(t)|^2 dt \quad (7.13)$$

and

$$\sigma_{\text{EOB}}^2(\tau) = \int_{T_I}^{T_F} |h_{\text{EOB}}(t - \tau)|^2 dt. \quad (7.14)$$

The time-shift  $\tau$  and phase  $\Phi$  are chosen to maximize the match  $m(\tau, \Phi)$  for a fixed matching window. Explicitly, the phase is determined analytically to be  $\Phi = -\arg[z(\tau)]$ ; plugging this result back into Eq. (7.11), the time-shift is given by maximizing  $|z(\tau)|/[\sigma_{\text{NR}}\sigma_{\text{EOB}}(\tau)]$  over  $\tau$ . As stated above, once  $\tau$  and  $\Phi$  are found we shift the numerical waveform in the opposite direction to generate  $h_{\text{NR}}^{\text{shift}}(t) = h_{\text{NR}}(t + \tau)e^{+i\Phi}$ .

A hybrid waveform is generated by smoothly turning off the EOB waveform and smoothly turning on the shifted numerical waveform over a splicing window  $S_I < t < S_F$  (bounded by dotted vertical lines in Fig. 26) which can be chosen independently of the matching window. As in Ref. [16], we employ Hann windows

$$w_{\text{off}}(t) = \frac{1}{2} \left[ 1 + \cos \left( \frac{\pi[t - S_I]}{S_F - S_I} \right) \right] \quad (7.15)$$

$$w_{\text{on}}(t) = \frac{1}{2} \left[ 1 - \cos \left( \frac{\pi[t - S_I]}{S_F - S_I} \right) \right]. \quad (7.16)$$

The hybrid waveform is then written

$$h_{\text{hybrid}}(t) = \begin{cases} h_{\text{EOB}}(t) & t < S_I \\ w_{\text{off}}(t)h_{\text{EOB}}(t) + w_{\text{on}}(t)h_{\text{NR}}^{\text{shift}}(t) & S_I < t < S_F \\ h_{\text{NR}}^{\text{shift}}(t) & t > S_F \end{cases} \quad (7.17)$$

As shown in Fig. 26, we choose the start of the splicing interval to be the same as the start of the matching window  $S_I = T_I$  and choose the end of the splicing window to be  $S_F = T_I + 4$  ms. It is also necessary to use these windows to smoothly turn on the hybrid waveform at low frequency when performing a discrete Fourier transform to avoid the Gibbs phenomenon. Unlike the case for BNS waveforms, it is not necessary to window the end of the hybrid waveform as the amplitude rapidly decays to zero anyway during the ringdown.

For concreteness we define  $t = 0$  as the EOB BBH merger time  $t_M^{\text{EOB}}$  when the EOB waveform reaches its maximum amplitude. After matching to the EOB waveform, the time when the numerical BHNS waveform reaches its maximum amplitude is  $t_M^{\text{NR}}$ .

### 7.5.2 Dependence on matching window

Because the numerical BHNS waveforms are close but not identical to the EOB BBH waveform during the inspiral and because there is some noise in the BHNS waveforms, the time shift that maximizes the match depends on the choice of matching window. The matching window should exclude the first couple of cycles of the numerical waveform during which time the simulation is settling down from the initial conditions. It should also exclude the merger/ringdown which are strongly dependent on the presence of matter. The window

must also be wide enough to average over numerical noise and, as we shall see below, the effects of eccentricity in the simulations.

The numerical merger time  $t_M^{\text{NR}}$  relative to the EOB BBH merger time  $t_M^{\text{EOB}}$  as a function of the end of the matching window  $T_F - t_M^{\text{NR}}$  provides a useful diagnostic of the matching procedure. Results for matching two  $Q = 2, M_{\text{NS}} = 1.35M_\odot$  waveforms with different equations of state to an EOB waveform are shown in Fig. 31. The horizontal axis is the end time  $T_F$  of the matching window relative to the numerical merger time  $t_M^{\text{NR}}$ . For negative values, the matching window contains the BHNS inspiral only. For positive values, the matching window also contains part of the BHNS ringdown. The vertical axis is the location of the shifted numerical merger time  $t_M^{\text{NR}}$  after finding the best match. Four different window durations  $\Delta t = T_F - T_I$  are shown. The drift in the best fit merger time  $t_M^{\text{NR}}$  most likely arises from the neglect of tidal effects in the EOB waveform which lead to an accumulating phase shift in the waveform. This is consistent with the fact that the amount of drift increases with the tidal deformability, although some of the drift may also arise from numerical angular momentum loss from finite resolution of the simulations. Further work is in progress to understand this issue [125]. We also note that the amount of offset from the  $t_M^{\text{NR}} = 0$  line depends monotonically on the tidal deformability, and arises from the fact that stars with a large value of  $\Lambda$  will be tidally disrupted a few ms before stars with small  $\Lambda$ .

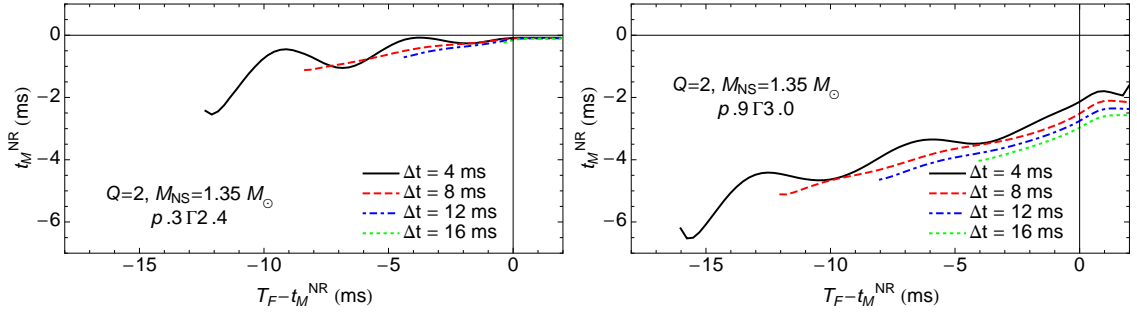


Figure 31 : Dependence of time shift between numerical and EOB waveform on the end time  $T_F - t_M^{\text{NR}}$  and width  $\Delta t$  of the matching window.  $Q = 2$  and  $M_{\text{NS}} = 1.35M_\odot$  for each waveform. The EOS used are p.3 $\Gamma$ 2.4 (left panel), and p.9 $\Gamma$ 3.0 (right panel). The EOB waveform has zero eccentricity.

When the matching window duration is approximately one orbital period or shorter, the time-shift oscillates as a function of  $T_F - t_M^{\text{NR}}$ . We attribute this effect to the eccentricity in the numerical waveform that results from initial data with no radial velocity. For larger matching-window durations, the effect of eccentricity is averaged out.

To demonstrate concretely that the decaying oscillations for  $\Delta t = 4$  ms are the result of eccentricity, we matched an EOB BBH waveform with eccentricity to the equivalent zero

eccentricity EOB BBH waveform. EOB waveforms can be generated with small eccentricity by starting the EOB equations of motion with quasicircular (zero radial velocity) initial conditions late in the inspiral. The result is shown in Fig. 32 for an EOB waveform with the same quasicircular initial conditions as the simulation for the EOS p.3 $\Gamma$ 2.4 shown in Fig. 31. The oscillations take exactly the form of those shown in Fig. 31, except without the drift and offset.

We estimate that the initial eccentricities in the simulations used in this chapter are  $e_0 \sim 0.03$ . Decreasing the initial eccentricity by about an order of magnitude, possibly using an iterative method that adjusts the initial radial velocity [151], will remove this issue and allow one to determine the phase shift due to tidal interactions during the inspiral part of the simulation.

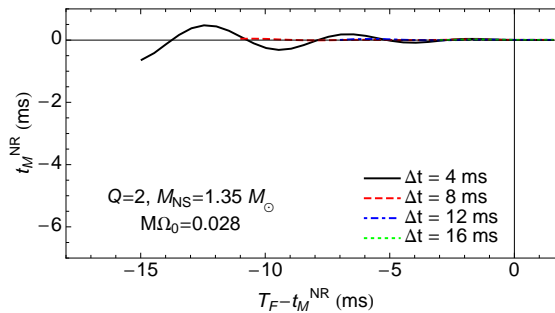


Figure 32 : Same as Fig. 31, but matching an eccentric EOB BBH waveform with the quasicircular initial condition  $M\Omega_0 = 0.028$  to a zero eccentricity EOB BBH waveform.

## 7.6 Parameter estimation

The output of a gravitational-wave detector  $s(t) = n(t) + h(t)$  is the sum of detector noise  $n(t)$  and a possible gravitational-wave signal  $h(t)$ . Stationary, Gaussian noise is characterized by its power spectral density (PSD)  $S_n(|f|)$  defined by

$$\langle \tilde{n}(f) \tilde{n}^*(f') \rangle = \frac{1}{2} \delta(f - f') S_n(|f|). \quad (7.18)$$

The gravitational wave signal is given in terms of the two polarizations of the gravitational wave by

$$h(t) = F_+ h_+(t) + F_\times h_\times(t), \quad (7.19)$$

where  $F_{+,\times}$  are the detector response functions and depend on the location of the binary and the polarization angle of the waves. We assume the binary is optimally located at the

zenith of the detector and optimally oriented with its orbital plane parallel to that of the detector. This condition is equivalent to averaging  $h_+$  and  $h_\times$  ( $F_+ = F_\times = 1/2$ ).

It is well known [152] that the optimal statistic for detection of a known signal  $h(t)$  in additive Gaussian noise is

$$\rho = \frac{(h|s)}{\sqrt{(h|h)}} \quad (7.20)$$

where the inner product between two signals  $h_1$  and  $h_2$  is given by

$$(h_1|h_2) = 4\text{Re} \int_0^\infty \frac{\tilde{h}_1(f)\tilde{h}_2^*(f)}{S_n(f)} df. \quad (7.21)$$

In searches for gravitational-wave signals from compact binary mergers, a parametrized signal  $h(t; \theta^A)$  is known in advance of detection, and the parameters  $\theta^A$  must be estimated from the measured detector output  $s(t)$ . The parameters  $\theta^A$  of an inspiral are estimated by maximizing the inner product of the signal  $s(t)$  over the template waveforms  $h(t; \theta^A)$ . In the high signal-to-noise limit, the statistical uncertainty in the estimated parameters  $\hat{\theta}^A$  arising from the instrumental noise can be estimated using the Fisher matrix

$$\Gamma_{AB} = \left( \frac{\partial h}{\partial \theta^A} \left| \frac{\partial h}{\partial \theta^B} \right. \right) \Big|_{\hat{\theta}^A}. \quad (7.22)$$

Note that  $\hat{\theta}^A$  are the parameter values that maximize the signal-to-noise. The variance  $\sigma_A^2 = \sigma_{AA} = \langle (\Delta\theta^A)^2 \rangle$  and covariance  $\sigma_{AB} = \langle \Delta\theta^A \Delta\theta^B \rangle$  of the parameters are then given in terms of the Fisher matrix by

$$\langle \Delta\theta^A \Delta\theta^B \rangle = (\Gamma^{-1})^{AB}. \quad (7.23)$$

For hybrid waveforms, the partial derivatives in the Fisher matrix must be approximated with finite differences. It is most robust to compute the derivatives of the Fourier transforms used in the inner product. We rewrite the Fourier transform of each waveform in terms of the amplitude  $A$  and phase  $\Phi$  as  $\exp[\ln A - i\Phi]$  as given in Eq. (C.9). The derivatives  $\partial \ln A / \partial \theta^A$  and  $\partial \Phi / \partial \theta^A$  are then evaluated with finite differencing. More details of this and the other methods we tested are given in Appendix C.

In general, errors in the parameters  $\theta^A$  are correlated with each other forming an error ellipsoid in parameter space determined by the Fisher matrix  $\Gamma_{AB}$ . The uncorrelated parameters that are best extracted from the signal are found by diagonalizing  $\Gamma_{AB}$ . These new parameters are linear combinations of the original parameters  $\theta^A$ . We focus attention below on the two parameters  $\log(p_1)$  and  $\Gamma$ , and fix all other parameters as follows. We use the masses and spins determined from the numerical simulations and fix the time and phase shifts as determined during the hybrid waveform construction. We therefore construct the

error ellipses in  $\{\log(p_1), \Gamma\}$  parameter space and identify the parameter with the smallest statistical errors. We will leave an analysis of correlations due to uncertainty in masses and BH spin to future work.

### 7.6.1 Broadband aLIGO and ET

For the BHNS systems discussed here, the greatest departure from BBH behavior occurs for gravitational-wave frequencies in the range 500–5000 Hz. As a result, detector configurations optimized for detection of BHNS systems with low noise in the region below 500 Hz are not ideal for estimating EOS parameters. We therefore present results for the broadband aLIGO noise curve [114] and the ET-D noise curve [153] shown in Fig. 33. The broadband aLIGO configuration uses zero-detuning of the signal recycling mirror and a high laser power, resulting in significantly lower noise above 500 Hz at the expense of slightly higher noise at lower frequencies. Several noise curves have been considered for the Einstein Telescope denoted ET-B [115], ET-C [154], and ET-D [153]. We will use the most recent ET-D configuration, and note that in the 500–5000 Hz range all of the ET configurations have a similar sensitivity. The published noise curves, and those used in this chapter, are for a single interferometer of 10 km with a  $90^\circ$  opening angle. The current ET proposal is to have three individual interferometers each with a  $60^\circ$  opening angle. This will shift the noise curve down approximately 20% [153].

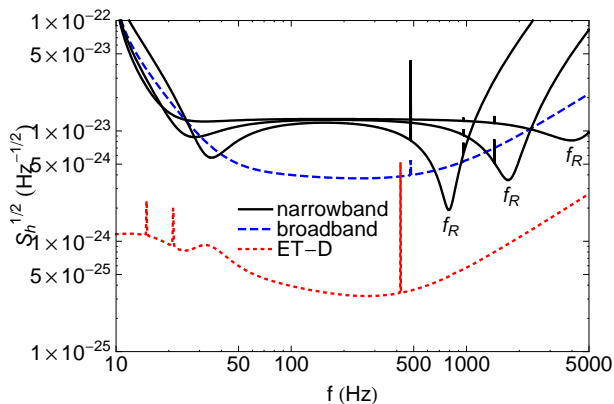


Figure 33 : Noise PSD for broadband aLIGO, ET-D, and various configurations of narrowband aLIGO. The minima of the narrowband configuration are labeled  $f_R$ .

In Figs. 34 and 35, we show the resulting  $1\text{-}\sigma$  error ellipses in the 2-dimensional parameter space  $\{\log(p_1), \Gamma\}$  for an optimally oriented BHNS with  $Q = 2$  and  $M_{\text{NS}} = 1.35M_\odot$  at a distance of 100 Mpc. Surfaces of constant  $\Lambda^{1/5}$  and NS radius, which are almost parallel

to each other, are also shown. One can see that the error ellipses are aligned with these surfaces. This indicates that, as expected,  $\Lambda^{1/5}$  is the parameter that is best extracted from BHNS gravitational-wave observations. Because  $\Lambda^{1/5}$  and  $R$  are so closely aligned we will use these two parameters interchangeably.

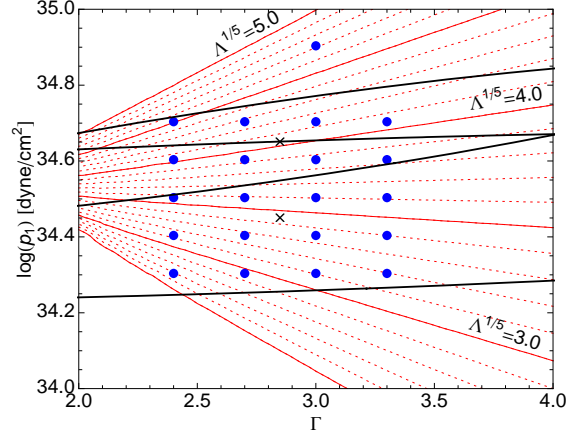


Figure 34 : Two  $1-\sigma$  error ellipses for broadband aLIGO. Evenly spaced contours of constant  $\Lambda^{1/5}$  are also shown. Each ellipse is centered on the estimated parameter  $\hat{\theta}^A$  denoted by a  $\times$ . The semimajor axes are significantly longer than the width of the figure, so each ellipse appears as a pair of parallel lines. Matching and splicing conventions are those of Fig. 26.

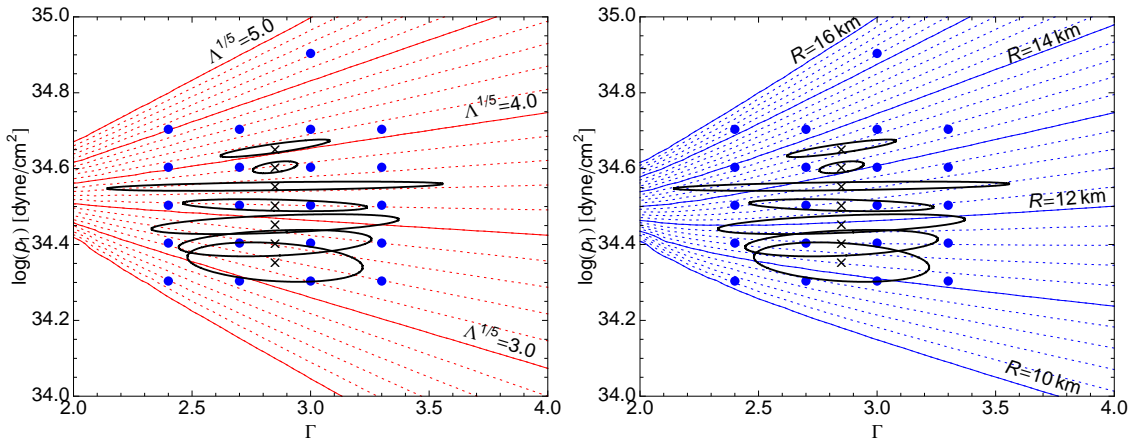


Figure 35 :  $1-\sigma$  error ellipses for ET-D. Evenly spaced contours of constant  $\Lambda^{1/5}$  ( $R$ ) are also shown on the left (right). Matching and splicing conventions are those of Fig. 26.

As mentioned above, there is some freedom in construction of the hybrid waveforms. The size and orientation of the error ellipses also depend on the details of this construction. We find that as long as the matching window is longer than approximately four

gravitational-wave cycles to average out the effects of eccentricity and does not include the first two gravitational-wave cycles, the orientation of the error ellipses does not change significantly. As expected, the size of the ellipses decreases as more of the numerical waveform is incorporated into the hybrid waveform. We therefore adopt the last 12 ms before merger of each numerical waveform as the matching window and the first 4 ms of the matching window for splicing as shown in Fig. 26.

We have emphasized that, to within present numerical accuracy, the late-inspiral waveform is determined by the single parameter  $\Lambda^{1/5}$ . This implies that, by using contours of constant  $\Lambda$  in the EOS space, one could have obtained the constraint on the EOS, summarized in Figs. 34 and 35 by varying only a single EOS parameter. For the simulations with other mass ratios and neutron star masses, we have used as our single parameter  $\log(p_1)$  and not  $\Gamma$  because contours of constant  $p_1$  more closely coincide with contours of constant  $\Lambda$  and because  $\Lambda$  is a one to one function of  $\log(p_1)$  throughout the parameter space. The one-parameter Fisher matrix can then be evaluated with finite differencing using the waveforms and values of  $\Lambda$  at two points in EOS parameter space with different  $\log(p_1)$ .

The uncertainties in  $\Lambda^{1/5}$  and  $R$  are shown in Figs. 36 and 37 for broadband aLIGO and for ET respectively. The uncertainty in these quantities is  $\sim 10\text{--}50\%$  for broadband aLIGO and  $\sim 1\text{--}5\%$  for ET-D. The uncertainties for the higher mass ratio  $Q = 3$  are somewhat larger than for  $Q = 2$ , but not significantly so. It is not clear how rapidly the uncertainty in  $\Lambda^{1/5}$  and  $R$  will increase as the mass ratio is increased toward more realistic values. On the one hand the tidal distortion is likely to be much smaller for larger  $Q$ . On the other hand the overall signal will be louder, and the merger and ringdown will occur at lower frequencies where the noise is lower. Additional simulations for higher  $Q$  are needed to address this question.

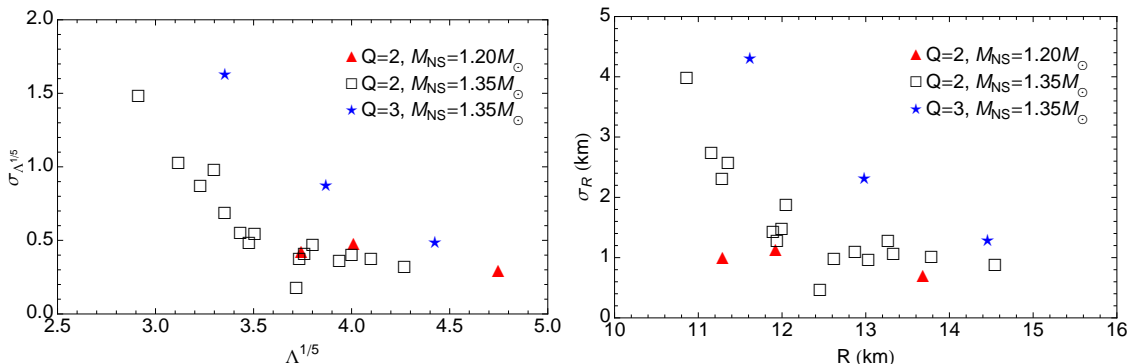


Figure 36 : 1- $\sigma$  uncertainty  $\sigma_{\Lambda^{1/5}}$  and  $\sigma_R$  as a function of the parameters  $\Lambda^{1/5}$  or  $R$  for the broadband aLIGO noise PSD. Matching and splicing conventions are those of Fig. 26.

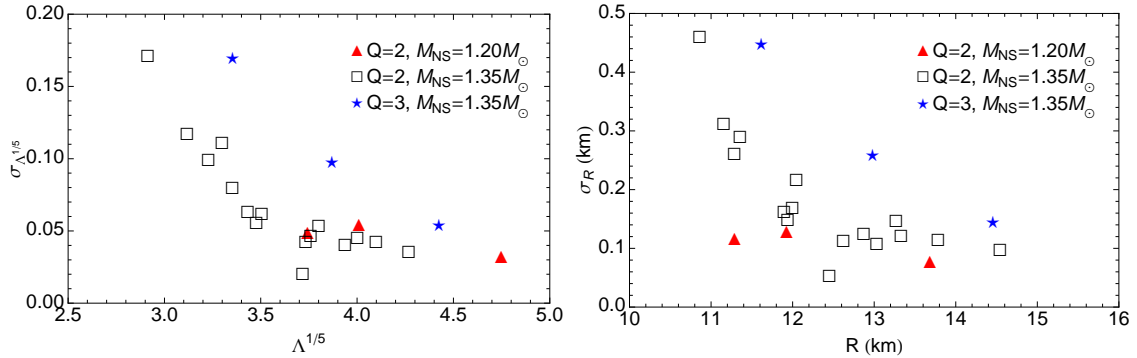


Figure 37 : Same as Fig. 36, but with the ET-D noise PSD. Error estimates are an order of magnitude smaller than for broadband aLIGO.

### 7.6.2 Narrowband aLIGO

The presence of a signal-recycling cavity in the aLIGO instruments will allow them to be tuned to have improved narrowband sensitivity at the expense of bandwidth. Two parameters control the narrowband capabilities of the instruments [155, 156, 67]: the signal recycling mirror transmissivity effectively sets the frequency bandwidth of the instrument, while the length of the signal recycling cavity (or equivalently the signal-recycling cavity tuning phase) controls the central frequency  $f_R$  of the best sensitivity. By tuning one or more of the aLIGO detectors to operate in narrowband mode, it may be possible to improve estimates of the EOS parameters.

We have examined several narrowband tunings with central frequencies that vary between approximately  $f_R = 500$  Hz and 4000 Hz. These noise curves use a signal recycling mirror transmissivity of 0.011 and a signal-recycling cavity tuning phase ranging from  $10^\circ$  down to  $1^\circ$ , and were generated using the program `gwinc` [157]. Three of these noise curves are shown in Fig. 33. In Fig. 38 we plot the  $1-\sigma$  uncertainty in NS radius  $\sigma_R$  as a function of the narrowband central frequency  $f_R$ . For the waveforms considered in this chapter the optimal narrowband frequency is in the range  $1000 \text{ Hz} \lesssim f_R \lesssim 2500 \text{ Hz}$  and depends on the mass ratio, NS mass, and EOS. Narrowband configurations usually give smaller errors than the broadband configuration if  $f_R$  happens to be tuned to within a few hundred Hz of the minimum for that BHNS event. In Ref. [158], Hughes discussed a method for determining the best frequency  $f_R$  to tune a narrowbanded detector to extract an EOS dependent cutoff frequency from a sequence of identical BNS inspirals. While this technique is not directly applicable to BHNS systems, which have different masses and spins, a similar approach could be used to combine multiple BHNS observations.

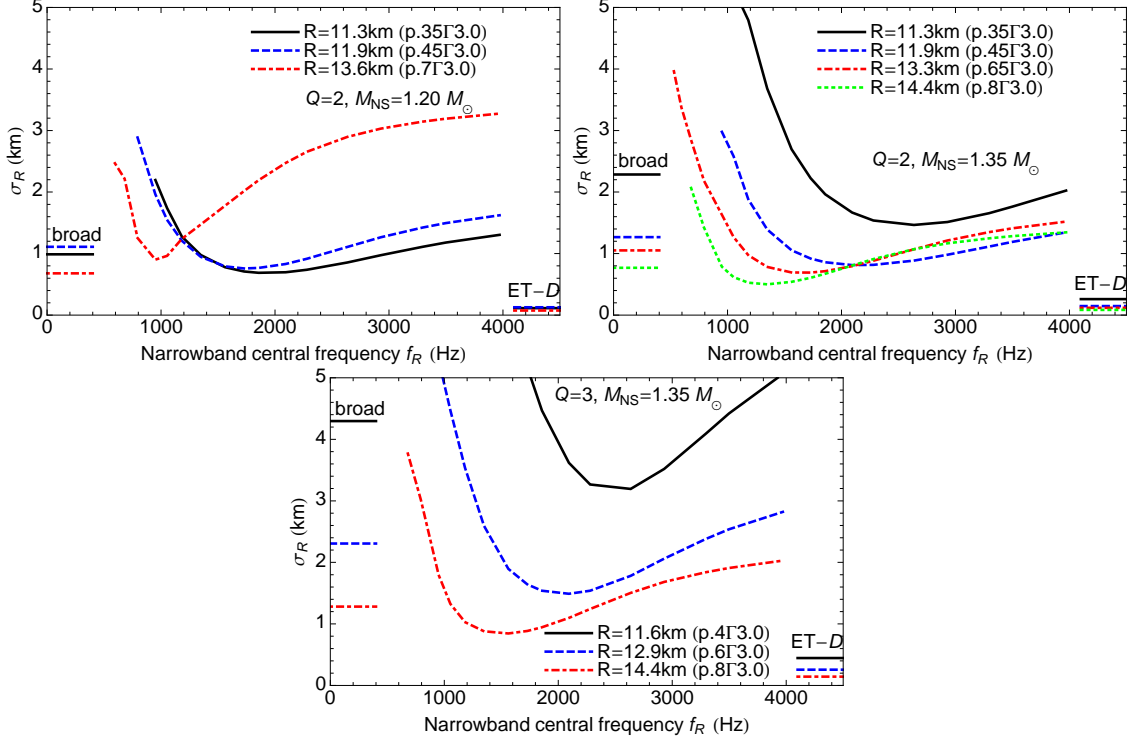


Figure 38 :  $1\text{-}\sigma$  uncertainty in  $R$  for different configurations of narrowband aLIGO and for different EOS.  $f_R$  defines the frequency where  $S_n$  is a minimum as shown in Fig. 33. Horizontal lines on the left and right indicate the corresponding  $1\text{-}\sigma$  errors for broadband aLIGO and ET-D respectively. Matching and splicing conventions are those of Fig. 26.

## 7.7 Discussion

### 7.7.1 Results

Using a large set of simulations incorporating a two-parameter EOS, we have found that the tidal deformability  $\Lambda^{1/5}$ , or equivalently the NS radius  $R$ , is the parameter that will be best extracted from BHNS waveforms. These parameters can be estimated to 10–50% with broadband aLIGO for an optimally oriented BHNS binary at 100 Mpc. The narrowband aLIGO configuration can do slightly better if it is tuned to within a few hundred Hz of the ideal frequency for a given BHNS event. The proposed Einstein Telescope will have an order-of-magnitude better sensitivity to the EOS parameters.

Although we have used a particular EOS parametrization to show that  $\Lambda$  is the parameter that is observed during BHNS coalescence, this result can be used to constrain any EOS model—an EOS based on fundamental nuclear theory in addition to a parametrized

phenomenological EOS. In particular, several parametrizations have recently been developed, including a spectral representation [159], a reparametrization of the piecewise polytrope [160], and a generalization that also includes nuclear parameters [161].

The results presented here can be compared with recent work to determine the mass and radius of individual NS in Type-1 X-ray bursts. Özel et al. [162] have obtained mass and radius measurements from several systems by simultaneously measuring the flux  $F$ , which is likely close to the Eddington value, and the blackbody temperature  $T$  during X-ray bursts of systems with accurately determined distances. During the burst, the emission area of the photosphere  $F/(\sigma T^4)$  expands, contracts, then reaches a constant value, and Özel et al. have argued that the final area corresponds to that of the NS surface. They obtain estimates of NS mass and radii with  $\mathcal{O}(10\%)$   $1-\sigma$  uncertainty. Steiner et al. [161] have also considered these systems, but argue that the final emission area does not necessarily correspond to that of the NS surface, and as a result obtain slightly smaller NS radii and larger uncertainties in the mass and radius. These radius error estimates are slightly smaller than those for the BHNS systems we have considered at 100 Mpc. However, we note that binary inspiral observations are subject to less systematic uncertainty due to questions of composition of the photosphere and associating it with the NS surface.

The uncertainty in NS radius for the merger and ringdown of BHNS systems examined here is of roughly the same size as that found for the last few orbits up to merger of BNS systems at the same 100 Mpc distance [16, 125]. BNS inspirals, however, will likely occur more frequently, and, including a tidally corrected inspiral–numerical hybrid, BNS systems are likely to have uncertainties that are smaller than BHNS systems by a factor of a few. Considering the post-merger phase for BNS waveforms may also provide additional information. Expected NS masses in both BNS and BHNS systems are slightly smaller than those measured for X-ray bursters which have accreted matter from their companion, so BNS and BHNS GW observations may complement X-ray burst observations by better constraining the lower density range of the EOS which is not well constrained from X-ray burst observations [160, 162].

### 7.7.2 Remaining work

We have used in this chapter several simplifications and conventions which can significantly affect the accuracy to which EOS parameters can be extracted. We list them below and describe how changing them would affect the parameter error estimates.

1. *Finite length of numerical waveforms*

The BHNS waveforms used here include only the last  $\sim 10$  GW cycles of inspiral as well as the merger and ringdown, of which the first few cycles of inspiral are unreliable due to inexact initial data. Matching the numerical waveform to a tidally corrected inspiral waveform instead of just the point-particle waveform will increase the overall departure from point-particle behavior by (i) creating a phase shift during the early inspiral, and more importantly (ii) adding to the phase of the late inspiral and merger the accumulated phase shift from the early inspiral – a phase shift that is not already included in the stronger signal of the late inspiral. The tidal corrections are now known up to 1PN order during inspiral, and using the 1PN corrections, the distinguishability between BHNS and BNS waveforms during the inspiral was calculated in [124]. We estimate that for a mass ratio of  $Q = 3$  the distinguishability between BHNS and BNS waveforms is roughly (to within a factor of two) the same when tidal information is incorporated into only the inspiral versus only the merger-ringdown, indicating that uncertainty in  $\Lambda$  may be decreased by a factor of two or more using a full inspiral-merger-ringdown BHNS waveform. We leave the issue of generating these tidally corrected inspiral-merger-ringdown waveforms to the next chapter.

## 2. *Event rates*

Estimates of the detectability of EOS parameters in BNS systems are often given for an event at a distance of 100 Mpc, and we have used the same convention here to state the results above. The relevant event rate is, therefore, the expected number of detected events that will have an effective distance  $D_{\text{eff}} \leq 100$  Mpc. (The effective distance  $D_{\text{eff}}$  depends on the location of the binary and its inclination relative to the detector. For an optimally oriented and located binary, one finds  $D = D_{\text{eff}}$  while typically  $D \leq D_{\text{eff}}$ .) The aLIGO inspiral rates for BNS systems are highly uncertain with {low, most likely, high} estimates of {0.01, 1, 10}  $\text{Mpc}^{-3} \text{Myr}^{-1}$  [120] or {0.004, 0.4, 4}  $\text{yr}^{-1}$  with effective distance  $D_{\text{eff}} \leq 100$  Mpc. Rates are even more uncertain for BHNS systems with rate estimates of {0.0002, 0.01, 0.4}  $\text{yr}^{-1}$  with effective distance  $D_{\text{eff}} \leq 100$  Mpc [120]. Since the uncertainty in EOS parameters scales linearly with distance [ $\sigma_{\Lambda^{1/5}} = \sigma_{\Lambda^{1/5}, 100\text{Mpc}}(D/100\text{Mpc})$ ] and the event rate scales as  $D^3$ , the estimated detection rates of systems with effective distance  $D_{\text{eff}} \leq 400$  Mpc are {0.01, 1, 30}  $\text{yr}^{-1}$  with a four-fold increase in uncertainty of  $\Lambda^{1/5}$ . Fortunately, for  $N_{\text{obs}}$  identical events and  $N_{\text{det}}$  identical detectors, the uncertainty also scales as  $\sigma_{\Lambda^{1/5}}/\sqrt{N_{\text{obs}}N_{\text{det}}}$ .

## 3. *Expected NS masses and mass ratios*

The simulations we used included realistic mass neutron stars of 1.2 and 1.35  $M_{\odot}$ . On

the other hand, black hole masses are expected to be many times larger [122], with likely mass ratios closer to  $Q \sim 7$  (for the canonical  $10 M_{\odot}$ – $1.4 M_{\odot}$  system) than the  $Q = 2$  and 3 systems we examined here. Additional simulations for mass ratios of 4 and 5 are in progress.

#### 4. *Spinning BH*

In this chapter we have not examined the effect of a spinning BH. The analytic results of Ref. [124] indicated that spin does not significantly improve the sensitivity to  $\Lambda$  for the inspiral up to the point of tidal disruption. However, numerical simulations [134, 139, 140] have shown that spin can strongly affect the dynamics near tidal disruption and the amount of matter left over in an accretion disk. We have performed several tens of simulations of non-precessing BHNS systems with spinning BH with various BH spins, mass ratios, NS masses, and EOS parameters, and an analysis of how BH spin affects the detectability of EOS parameters will be the subject of the next chapter.

#### 5. *Correlations between parameters*

In our Fisher analysis we have assumed that the mass ratio, NS mass, and BH spin will be determined to sufficient accuracy during the inspiral to separate them from EOS effects during the merger and ringdown. A full Fisher analysis using all of the BHNS parameters should be done to find the extent to which uncertainties in the other parameters alter measurability estimates of the EOS parameters.

Because BHNS waveforms smoothly deviate from corresponding BBH waveforms as  $\Lambda$  increases, it should be expected that one can find a good analytical approximation for the full inspiral, merger, and ringdown waveform by modifying analytical BBH waveforms. Accurate waveforms for non-spinning BBH systems using the EOB approach have been developed [76, 163], and work to find EOB waveforms for spinning BBH systems is in progress [164, 165]. Tidal interactions have also been incorporated into the EOB approach for BNS systems with good agreement with the inspiral waveform from numerical simulations when parametrized 2PN tidal interactions are fit to the numerical waveform [127, 128]. Another approach is to use phenomenological waveforms that fit the frequency domain post-Newtonian inspiral waveform to a phenomenological merger and ringdown for both spinning and non-spinning BBH systems [72]. Both of these approaches may work for generating full analytic BHNS waveforms as well. A complete description of the BHNS waveform will likely include corrections for the  $l = 3$  tidal field and other higher order corrections. However, it is not clear given the current set of simulations that these effects would be observable with either aLIGO or a third generation detector such as ET.

## Chapter 8

# Detectability of tidal parameters from aligned-spin BHNS systems

### 8.1 Introduction

By the end of the decade a network of second generation gravitational-wave detectors, including the two Advanced LIGO (aLIGO) detectors, Advanced Virgo, KAGRA (formerly LCGT), and possibly LIGO-India, will likely be making routine detections. Future ground based detectors such as the third generation Einstein Telescope (ET), with an order of magnitude higher sensitivity, are also in the planning stages, and may be operational in the next decade. A primary goal of these detectors is extracting from the gravitational waveform information about the sources. Of particular interest are compact binaries whose waveform encodes the sky location, orientation, distance, masses, spins, and for compact binaries containing neutron stars (NS), information about the neutron-star equation of state (EOS).

The study of EOS effects during binary inspiral has focused mainly on binary neutron star (BNS) systems. Work by [103, 106, 108, 109] showed that EOS information could be imprinted in the gravitational waveform through monopole–quadrupole interactions that depended on the equation of state through the tidal Love number of the neutron stars. The leading ( $\ell = 2$ ) relativistic tidal Love number was first calculated in Ref. [87], and its effect on the binary inspiral including the contribution due to tidally excited modes was calculated to leading order [86], and later extended to 1PN order [85, 111]. The gravitoelectric and gravitomagnetic tidal Love numbers for higher multipoles were calculated in [93, 110], and the waveform has now been calculated to 2PN order in the tidal corrections, including  $\ell = 2$  and 3 gravitoelectric interactions and the  $\ell = 2$  gravitomagnetic interaction, using the

effective action approach [166, 167].

The measurability of tidal parameters was examined for BNS inspiral for gravitational wave frequencies below 450Hz [86] using polytropic EOS, and this was extended to include theoretical nuclear and strange quark matter EOS [123]. They found that tidal interactions were only observable during this early inspiral stage (ignoring the last  $\sim 20$  gravitational wave cycles before merger) for stiff EOS and NS masses below  $1.4 M_{\odot}$ . On the other hand, using 2PN accurate tidal corrections in the effective one body approach, it was found that tidal parameters are in fact observable when including the extra  $\sim 20$  gravitational wave cycles up to the point of contact [167].

Numerical simulations have also been used to study tidal interactions during the late inspiral. The measurability of EOS information has been examined during the last few orbits using numerical simulations assuming that non EOS parameters were known to sufficient accuracy that they did not couple significantly with EOS parameters [16, 125]. They found that the NS radius could be measured using only the last few orbits to an accuracy of  $\sim 10\%$ . Other numerical simulations using both quasiequilibrium sequences [126] and full hydrodynamic simulations [127, 128, 168] have shown that by fitting effective one body (EOB) waveforms with parametrized higher order PN corrections to the simulations, the higher order PN corrections can significantly increase the strength of tidal interactions during the late inspiral. These results were confirmed by the analytic 2PN calculation [166, 167].

Comparably little work has been done to understand the measurability of tidal parameters in black hole-neutron star (BHNS) systems. Using the inspiral waveform with tidal corrections up to 1PN order, it was found that BHNS waveforms were not distinguishable from BBH waveforms during the inspiral before the point of tidal disruption [124]. Furthermore, this result did not improve for spinning black holes which tidally disrupt later. On the other hand, early work examining a possible cutoff in the gravitational wave amplitude due to tidal disruption of the neutron star by the black hole suggested that the NS radius may, in fact, be measurable [141] with second generation detectors. In Chapter 7 we examined numerical simulations of the last few orbits, merger, and ringdown for systems with non-spinning black holes and low mass ratios of  $Q = 2$  and  $3$ . We found that when considering only the merger and ringdown, the tidal deformability was the best measured EOS parameter and was marginally measurable for second generation detectors.

We have now run simulations with mass ratios up to  $Q = 5$ , which is closer to the canonical  $10 M_{\odot}-1.4 M_{\odot}$  ( $Q = 7.1$ ) BHNS system; and, we have also run simulations for black holes with spin aligned with the orbital angular momentum axis with values

from  $\chi_{\text{BH}} = a/M_{\text{BH}} = -0.5$  to  $0.75$ . In this chapter we will also address many of the simplifications used in Chapter 7 that can have a dramatic impact on the detectability of EOS parameters. Previously, we considered only the tidal information that could be obtained from the merger and ringdown, ignoring the small accumulating phase drift during the inspiral that results from tidal interactions. We will find that coherently adding the slow tidal phase drift from the inspiral to the tidal effect during the merger and ringdown can improve the measurability of tidal parameters by as much as a factor of 4 over just the merger and ringdown.

In the previous chapter we also ignored possible correlations between the tidal parameter  $\Lambda$  and the other binary parameters when estimating the measurability of  $\Lambda$  using the Fisher matrix. We have addressed this problem by developing a frequency domain analytic BHNS waveform, fitted to our BHNS simulations, and based on the phenomenological BBH waveform developed in Ref. [72]. This allows us to accurately evaluate derivatives in the Fisher matrix and evaluate correlations between the tidal parameter and the other parameters. We find that although these correlations are not nearly as strong as with other pairs of parameters, they can increase uncertainty by up to a factor of  $\sim 4$ . Overall, we find that the estimates of measurability of tidal parameters using the improvements presented in this paper are about the same as those presented in the previous chapter where only the merger and ringdown was considered and the uncertainty in the other parameters was presumed to be negligible.

*Conventions:* We use the following sign convention for the Fourier transform of a signal  $x(t)$

$$\tilde{x}(f) = \int_{-\infty}^{\infty} x(t)e^{+2\pi ift} dt, \quad (8.1)$$

and we will decompose the complex Fourier transform into amplitude and phase as  $\tilde{h}(f) = |\tilde{h}(f)|e^{+i\Phi(f)}$ . These conventions are opposite those of Chapter 7, and are chosen to agree with those of the PhenomC waveform model [72]. In addition, we set  $G = c = 1$  unless otherwise stated.

## 8.2 Simulations

Following the previous chapter on nonspinning BHNS systems, we perform a large set of simulations where we systematically vary the parameters of a parametrized EOS, then look for the combination of parameters that are best extracted from gravitational wave observations. Specifically we choose a simplified two-parameter version of the piecewise polytrope introduced in [54]. For this EOS, the pressure  $p$  in the rest-mass density interval

$\rho_{i-1} < \rho < \rho_i$  is

$$p(\rho) = K_i \rho^{\Gamma_i}, \quad (8.2)$$

Where  $K_i$  is a constant, and  $\Gamma_i$  is the adiabatic index. We fix the crust EOS defined by densities below the transition density  $\rho_0$ . In the crust,  $K_0 = 3.5966 \times 10^{13}$  in cgs units and  $\Gamma_0 = 1.3569$ , such that the pressure at  $10^{13}$  g/cm<sup>3</sup> is  $1.5689 \times 10^{31}$  dyne/cm<sup>2</sup>. Above the transition density  $\rho_0$  the core EOS is parametrized by the two parameters  $p_1$  and  $\Gamma_1$ . The pressure  $p_1$  is defined as the pressure at  $\rho_1 = 10^{14.7}$  g/cm<sup>3</sup> and the adiabatic index  $\Gamma_1$  of the core will, for simplicity, be written  $\Gamma$ . The constant  $K_1$  for the core is then given by  $K_1 = p_1/\rho_1^\Gamma$ . Once the two parameters  $p_1$  and  $\Gamma$  are set, the dividing density  $\rho_0$  between the crust and the core is given by the density where the crust and core EOS intersect:  $\rho_0 = (K_0/K_1)^{1/(\Gamma-\Gamma_0)}$ . Finally, given this EOS, the energy density  $\epsilon$  can be evaluated by integrating the first law of thermodynamics

$$d\frac{\epsilon}{\rho} = -pd\frac{1}{\rho}. \quad (8.3)$$

As discussed in more detail in [169], quasiequilibrium configurations are used as initial data for the simulations, and are computed using the spectral-method library `LORENE` [143]. The numerical simulations are performed using the adaptive-mesh refinement code `SACRA` [144]. To obtain the gravitational waveform  $h_+ - ih_\times$ , the outgoing part of the Weyl scalar  $\Psi_4 = \ddot{h}_+ - i\ddot{h}_\times$  is extracted from these simulations at a finite coordinate radius, and is then integrated twice using a method known as Fixed Frequency Integration [146]. Specifically, we take the Fourier transform of  $\Psi_4$ , then integrate twice in time by dividing by  $(2\pi if)^2$ . Low frequency components are filtered out as in [169], and the inverse Fourier transform is then taken to find  $h_+ - ih_\times$  in the time domain.

We have performed 90 simulations of the late inspiral, merger, and ringdown of BHNS systems, using 21 sets of parameters for our two-parameter EOS. We have also varied the mass ratio from  $Q = 2$  to 5, the neutron star mass from  $1.20 M_\odot$  to  $1.45 M_\odot$ , and the spin of the black hole from  $\chi_{\text{BH}} = -0.5$  to 0.75. The EOS parameters used as well as the corresponding NS radius, Love number, and tidal deformability can be found in Table 4. A list of all the simulations is given in Table 6.

Because trends in the BHNS waveform are most apparent in terms of the amplitude and phase of the Fourier transform, and because data analysis is usually done in the frequency domain, we will focus our discussion of the waveforms below on the frequency domain. Several representative waveforms with varying tidal deformability  $\Lambda$ , mass ratio  $Q$ , and spin  $\chi_{\text{BH}}$  are shown in Figs. 39–41.

Table 6 : Data for the 90 BHNS simulations. NS mass is in units of  $M_{\odot}$ .

$\chi_{\text{BH}}$	$Q$	$M_{\text{NS}}$	EOS	$\chi_{\text{BH}}$	$Q$	$M_{\text{NS}}$	EOS	$\chi_{\text{BH}}$	$Q$	$M_{\text{NS}}$	EOS
-0.5	2	1.35	p.3 $\Gamma$ 3.0	0	3	1.35	p.3 $\Gamma$ 3.0	0.5	4	1.35	p.3 $\Gamma$ 3.0
-0.5	2	1.35	p.4 $\Gamma$ 3.0	0	3	1.35	p.4 $\Gamma$ 3.0	0.5	4	1.35	p.4 $\Gamma$ 3.0
-0.5	2	1.35	p.5 $\Gamma$ 3.0	0	3	1.35	p.5 $\Gamma$ 3.0	0.5	4	1.35	p.5 $\Gamma$ 3.0
-0.5	2	1.35	p.9 $\Gamma$ 3.0	0	3	1.35	p.7 $\Gamma$ 3.0	0.5	4	1.35	p.9 $\Gamma$ 3.0
-0.5	3	1.35	p.4 $\Gamma$ 3.0	0	3	1.35	p.9 $\Gamma$ 3.0	0.75	2	1.2	p.3 $\Gamma$ 3.0
0	2	1.2	p.3 $\Gamma$ 3.0	0.5	2	1.35	p.3 $\Gamma$ 3.0	0.75	2	1.2	p.4 $\Gamma$ 3.0
0	2	1.2	p.4 $\Gamma$ 3.0	0.5	2	1.35	p.4 $\Gamma$ 3.0	0.75	2	1.2	p.5 $\Gamma$ 3.0
0	2	1.2	p.5 $\Gamma$ 3.0	0.5	2	1.35	p.5 $\Gamma$ 3.0	0.75	2	1.2	p.9 $\Gamma$ 3.0
0	2	1.2	p.9 $\Gamma$ 3.0	0.5	2	1.35	p.7 $\Gamma$ 3.0	0.75	2	1.35	p.3 $\Gamma$ 3.0
0	2	1.35	p.3 $\Gamma$ 2.4	0.5	2	1.35	p.9 $\Gamma$ 3.0	0.75	2	1.35	p.4 $\Gamma$ 3.0
0	2	1.35	p.3 $\Gamma$ 2.7	0.5	3	1.35	p.3 $\Gamma$ 2.4	0.75	2	1.35	p.5 $\Gamma$ 3.0
0	2	1.35	p.3 $\Gamma$ 3.0	0.5	3	1.35	p.3 $\Gamma$ 2.7	0.75	2	1.35	p.7 $\Gamma$ 3.0
0	2	1.35	p.3 $\Gamma$ 3.3	0.5	3	1.35	p.3 $\Gamma$ 3.0	0.75	2	1.35	p.9 $\Gamma$ 3.0
0	2	1.35	p.4 $\Gamma$ 2.4	0.5	3	1.35	p.3 $\Gamma$ 3.3	0.75	2	1.45	p.3 $\Gamma$ 3.0
0	2	1.35	p.4 $\Gamma$ 2.7	0.5	3	1.35	p.4 $\Gamma$ 2.4	0.75	2	1.45	p.4 $\Gamma$ 3.0
0	2	1.35	p.4 $\Gamma$ 3.0	0.5	3	1.35	p.4 $\Gamma$ 2.7	0.75	2	1.45	p.5 $\Gamma$ 3.0
0	2	1.35	p.4 $\Gamma$ 3.3	0.5	3	1.35	p.4 $\Gamma$ 3.0	0.75	2	1.45	p.9 $\Gamma$ 3.0
0	2	1.35	p.5 $\Gamma$ 2.4	0.5	3	1.35	p.4 $\Gamma$ 3.3	0.75	3	1.35	p.3 $\Gamma$ 3.0
0	2	1.35	p.5 $\Gamma$ 2.7	0.5	3	1.35	p.5 $\Gamma$ 2.4	0.75	3	1.35	p.4 $\Gamma$ 3.0
0	2	1.35	p.5 $\Gamma$ 3.0	0.5	3	1.35	p.5 $\Gamma$ 2.7	0.75	3	1.35	p.5 $\Gamma$ 3.0
0	2	1.35	p.5 $\Gamma$ 3.3	0.5	3	1.35	p.5 $\Gamma$ 3.0	0.75	3	1.35	p.7 $\Gamma$ 3.0
0	2	1.35	p.6 $\Gamma$ 2.4	0.5	3	1.35	p.5 $\Gamma$ 3.3	0.75	3	1.35	p.9 $\Gamma$ 3.0
0	2	1.35	p.6 $\Gamma$ 2.7	0.5	3	1.35	p.6 $\Gamma$ 2.4	0.75	4	1.35	p.3 $\Gamma$ 3.0
0	2	1.35	p.6 $\Gamma$ 3.0	0.5	3	1.35	p.6 $\Gamma$ 2.7	0.75	4	1.35	p.4 $\Gamma$ 3.0
0	2	1.35	p.6 $\Gamma$ 3.3	0.5	3	1.35	p.6 $\Gamma$ 3.3	0.75	4	1.35	p.5 $\Gamma$ 3.0
0	2	1.35	p.7 $\Gamma$ 2.4	0.5	3	1.35	p.7 $\Gamma$ 2.4	0.75	4	1.35	p.9 $\Gamma$ 3.0
0	2	1.35	p.7 $\Gamma$ 2.7	0.5	3	1.35	p.7 $\Gamma$ 2.7	0.75	5	1.35	p.3 $\Gamma$ 3.0
0	2	1.35	p.7 $\Gamma$ 3.0	0.5	3	1.35	p.7 $\Gamma$ 3.0	0.75	5	1.35	p.4 $\Gamma$ 3.0
0	2	1.35	p.7 $\Gamma$ 3.3	0.5	3	1.35	p.7 $\Gamma$ 3.3	0.75	5	1.35	p.5 $\Gamma$ 3.0
0	2	1.35	p.9 $\Gamma$ 3.0	0.5	3	1.35	p.9 $\Gamma$ 3.0	0.75	5	1.35	p.9 $\Gamma$ 3.0

As was found in Chapter 7, the waveform monotonically departs from a BBH ( $\Lambda = 0$ ) waveform as  $\Lambda$  increases, and this is true for systems with spinning black holes as well, as we see from Fig. 39 where  $\chi_{\text{BH}} = 0.5$ . In particular, the cutoff frequency, where the waveform begins a sharp drop in the amplitude, decreases monotonically with increasing  $\Lambda$ , and the BHNS phase  $\Phi_{\text{BHNS}}$  monotonically departs from that of a BBH waveform  $\Phi_{\text{BBH}}$  with increasing  $\Lambda$ . In Fig. 40, the difference in phase  $\Delta\Phi$  between the BHNS and BBH waveform decreases as the mass ratio  $Q$  increases. However, in Fig. 41,  $\Delta\Phi$  increases with increasing BH spin.

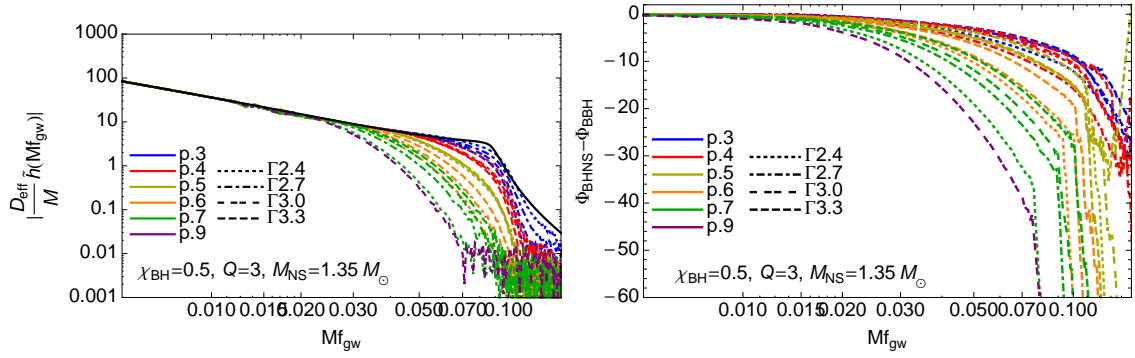


Figure 39 : The difference between a BHNS waveform and a BBH waveform (solid black curve on left) grows monotonically as  $\Lambda$  increases. For the EOS, the value of  $\log(p_1)$  is represented by the color of the curve, and the value of  $\Gamma$  is represented by its line style.

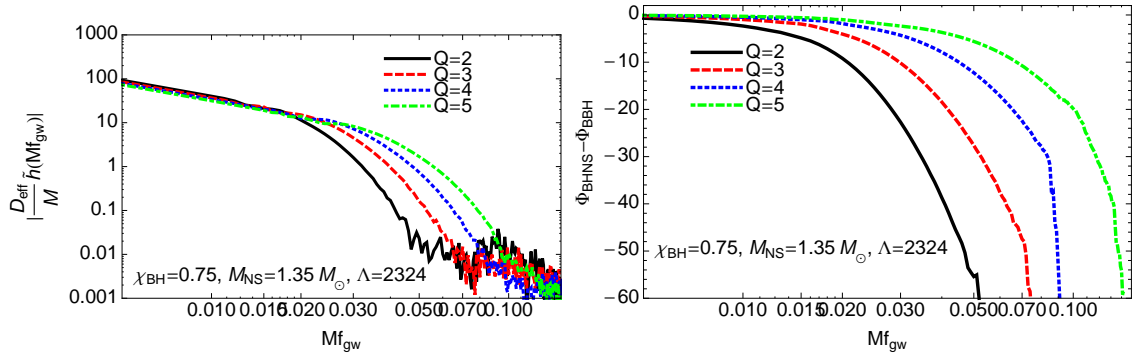


Figure 40 : As mass ratio  $Q$  increases, the dependence of the waveform on matter decreases.

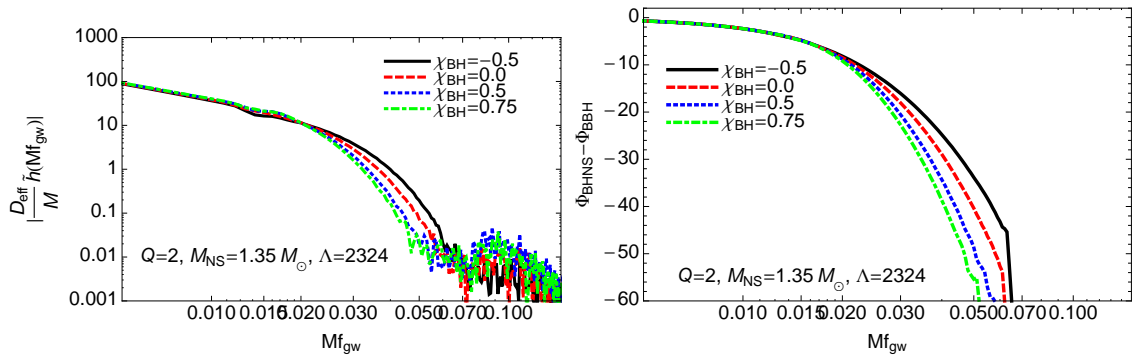


Figure 41 : As black hole spin  $\chi_{\text{BH}}$  increases, the dependence of the waveform on matter increases.

### 8.3 Hybrid inspiral-merger-ringdown waveforms

To obtain as much information as possible about a BHNS coalescence, we will construct a hybrid waveform that joins the analytic inspiral to the numerical merger and ringdown. In the previous chapter, we constructed hybrid waveforms using effective one body (EOB) BBH waveforms as an approximation for the inspiral. However, in order to take full advantage of the tidal interactions in the inspiral as well as the merger and ringdown, we will need a tidally corrected inspiral waveform. Tidal corrections during the inspiral have been computed for post-Newtonian [111] as well as EOB [166, 167] waveforms in both the time and frequency domains. For BHNS systems with spinning BH, we will also need waveforms that incorporate spin. Post-Newtonian waveforms include spin, but can be unreliable for high mass ratios during the last few orbits where matching to numerical waveforms is done. Recently, time domain EOB waveforms with aligned spin have been calculated, and are currently being calibrated to numerical waveforms [164, 165]. Another approach, as discussed in Section 3.3, is to use frequency domain phenomenological waveforms that include the complete inspiral-merger-ringdown (IMR), and are calibrated to aligned-spin numerical waveforms [74, 72]. Tidal corrections can then be added to these phenomenological waveforms using the stationary phase approximation (SPA) [111] to generate BHNS inspiral waveforms that have accurate point particle terms in the matching region.

In this chapter, we will choose the phenomenological IMR waveform referred to as PhenomC [72] and a SPA tidal correction as our inspiral waveform for two main reasons. The first reason is that, as we will find in Section 8.5, we can use this BBH waveform model as a starting point for generating phenomenological BHNS IMR waveforms with only minor corrections. The second reason is that data analysis is typically done in the

frequency domain. Since the waveform enters the detector band starting at frequencies as low as 10 Hz for aLIGO and 1 Hz for ET, it is much easier to start in the frequency domain instead of evaluate the Fourier transform for a long waveform. In particular, we have in mind future parameter estimation studies where the waveform must be evaluated  $\mathcal{O}(10^6)$  times in the frequency domain.

The frequency domain PhenomC waveform is, in terms of the amplitude  $A_{\text{phen}}(f)$  and phase  $\Phi_{\text{phen}}(f)$ ,  $\tilde{h}_{\text{phen}}(f) = A_{\text{phen}}(f)e^{i\Phi_{\text{phen}}(f)}$ , where the expressions for the amplitude and phase are given explicitly in Ref. [72]. The 1PN accurate TaylorF2 tidal phase correction is [111]

$$\psi_T(f) = \frac{3}{128\eta}(\pi Mf)^{-5/3} \left[ -\frac{24}{X_{\text{NS}}}(1 + 11X_{\text{BH}})\frac{\lambda}{M^5}(\pi Mf)^{10/3} - \frac{5}{28X_{\text{NS}}}(3179X_{\text{NS}} - 919X_{\text{NS}}^2 + 260X_{\text{NS}}^3)\frac{\lambda}{M^5}(\pi Mf)^{12/3} \right], \quad (8.4)$$

where  $X_{\text{BH}} = M_{\text{BH}}/M$  and  $X_{\text{NS}} = M_{\text{NS}}/M$ . We then write the inspiral waveform as  $\tilde{h}_{\text{insp}}(f) = A_{\text{phen}}(f)e^{i\Phi_{\text{phen}+\text{T}}(f)}$ , where  $\Phi_{\text{phen}+\text{T}}(f) = \Phi_{\text{phen}}(f) + \psi_T(f)$ .

To join our numerical waveforms to the frequency domain inspiral waveform, we follow the least-squares method used in [72]. When matching waveforms, a time constant  $\tau$  and phase constant  $\phi$  are free parameters that need to be fixed. For a generic waveform  $h(t)$ , the time and phase can be adjusted to produce a shifted waveform  $h^{\text{shift}}(t; \tau, \phi) = h(t - \tau)e^{i\phi}$ . The Fourier transformed waveform, which can be written in terms of amplitude and phase as  $\tilde{h}(f) = |\tilde{h}(f)|e^{i\Phi(f)}$ , has a corresponding shifted waveform  $\tilde{h}^{\text{shift}}(f; \tau, \phi) = |\tilde{h}(f)|e^{i\Phi^{\text{shift}}(f; \tau, \phi)}$ , where  $\Phi^{\text{shift}}(f; \tau, \phi) = \Phi(f) + 2\pi f\tau + \phi$ . When joining the inspiral and numerical waveforms, we hold the phase of the inspiral waveform  $\Phi_{\text{phen}+\text{T}}(f)$  fixed and adjust the phase of the numerical waveform  $\Phi_{\text{NR}}(f)$ , such that  $\Phi_{\text{NR}}^{\text{shift}}(f; \tau, \phi) = \Phi_{\text{NR}}(f) + 2\pi f\tau + \phi$ . We then perform a least-squares fit in the matching interval  $f_l < f < f_h$  by minimizing the quantity

$$\int_{f_l}^{f_h} [\Phi_{\text{NR}}^{\text{shift}}(f; \tau, \phi) - \Phi_{\text{phen}+\text{T}}(f)]^2 df \quad (8.5)$$

with respect to the free parameters  $\tau$  and  $\phi$ . This minimization can be done analytically up to two numerical integrals. The result is

$$\tau = \frac{3(f_h + f_l)I_0 - 6I_1}{\pi(f_h - f_l)^3}, \quad (8.6)$$

$$\phi = \frac{-4(f_h^2 + f_h f_l + f_l^2)I_0 + 6(f_h + f_l)I_1}{(f_h - f_l)^3}, \quad (8.7)$$

where

$$I_0 = \int_{f_l}^{f_h} [\Phi_{\text{NR}}(f) - \Phi_{\text{phen+T}}(f)] df, \quad (8.8)$$

$$I_1 = \int_{f_l}^{f_h} [\Phi_{\text{NR}}(f) - \Phi_{\text{phen+T}}(f)] f df. \quad (8.9)$$

Once the time and phase shifts are found, we smoothly turn on the numerical waveform and smoothly turn off the phenomenological waveform within a splicing window  $s_l < f < s_h$  using Hann windows

$$w_{\text{off}}(f) = \frac{1}{2} \left[ 1 + \cos \left( \frac{\pi[f - s_i]}{s_f - s_i} \right) \right], \quad (8.10)$$

$$w_{\text{on}}(f) = \frac{1}{2} \left[ 1 - \cos \left( \frac{\pi[f - s_i]}{s_f - s_i} \right) \right]. \quad (8.11)$$

The amplitude of the hybrid waveform is then

$$|\tilde{h}_{\text{hybrid}}(f)| = \begin{cases} |\tilde{h}_{\text{phen}}(f)| & f < s_i \\ w_{\text{off}}(f)|\tilde{h}_{\text{phen}}(f)| + w_{\text{on}}(f)|\tilde{h}_{\text{NR}}(f)| & s_i < f < s_f \\ |\tilde{h}_{\text{NR}}(f)| & f > s_f \end{cases}, \quad (8.12)$$

and the phase is

$$\Phi_{\text{hybrid}}(f) = \begin{cases} \Phi_{\text{phen+T}}(f) & f < s_i \\ w_{\text{off}}(f)\Phi_{\text{phen+T}}(f) + w_{\text{on}}(f)[\Phi_{\text{NR}}(f) + 2\pi f\tau + \phi] & s_i < f < s_f \\ \Phi_{\text{NR}}(f) + 2\pi f\tau + \phi & f > s_f \end{cases}. \quad (8.13)$$

A hybrid waveform for the system ( $\chi_{\text{BH}} = 0.75$ ,  $Q = 2$ ,  $M_{\text{NS}} = 1.35 M_{\odot}$ ,  $\text{EOS} = p.9\Gamma 3.0$ ) is shown in Fig. 42. We note that the linear matching term  $2\pi f\tau + \phi$  in the hybrid phase can have a large effect on the post-splice waveform. In particular, as shown in the left panel of Fig. 42, the inclusion of the tidal term  $\psi_T$  in the inspiral waveform leads to an additional linearly growing deviation in the phase  $\Delta\Phi = \Phi_{\text{hybrid}} - \Phi_{\text{BBH}}$  which would not be present if we simply ignored the small tidal term  $\psi_T(f)$  during the inspiral as was done in Chapter 7. As we will see below, this has a large impact on the measurability of tidal parameters.

## 8.4 Parameter estimation

As discussed in Chapters 5 and 7, for Gaussian noise and high signal to noise ratio, the uncertainties in the parameters  $\theta^A$  can be calculated from the Fisher matrix

$$\Gamma_{AB} = \left( \frac{\partial h}{\partial \theta^A} \middle| \frac{\partial h}{\partial \theta^B} \right) \bigg|_{\hat{\theta}^A}, \quad (8.14)$$

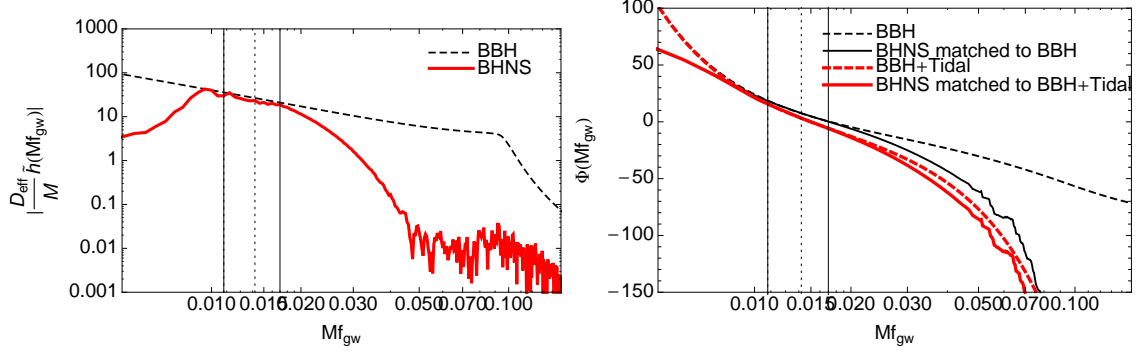


Figure 42 : Amplitude  $\left| \frac{D_{\text{eff}}}{M} \tilde{h}(Mf) \right|$  (left) and phase  $\Phi(Mf)$  (right) for a numerical BHNS waveform matched to the PhenomC BBH waveform with and without the tidal correction  $\psi_T$ . The waveform parameters are  $(\chi_{\text{BH}} = 0.75, Q = 2, M_{\text{NS}} = 1.35 M_{\odot}, \text{EOS} = p.9\Gamma 3.0)$ . The matching window  $f_i < f < f_f$  is bounded by solid vertical lines, and the splicing window  $s_i < f < s_f$ , which begins at  $s_i = f_i$ , is bounded by dotted vertical lines. Note that matching the numerical BHNS waveform to a BBH waveform without tidal corrections, as was done in Chapter 7, results in a phase error that accumulates linearly even after the matching region, and underestimates the effect of matter. The amplitude and phase of the numerical waveform are unreliable for  $Mf \gtrsim 0.05$ .

where we note that  $\hat{\theta}^A$  are the parameter values that maximize the signal-to-noise ratio. The variance  $\sigma_A^2 = \sigma_{AA} = \langle (\Delta\theta^A)^2 \rangle$  and covariance  $\sigma_{AB} = \langle \Delta\theta^A \Delta\theta^B \rangle$  of the parameters are then given in terms of the Fisher matrix by

$$\langle \Delta\theta^A \Delta\theta^B \rangle = (\Gamma^{-1})^{AB}. \quad (8.15)$$

In Chapter 7 we evaluated the two-parameter Fisher matrix for the EOS parameters  $\log(p_1)$  and  $\Gamma$  using hybrid waveforms that ignored the inspiral tidal correction  $\psi_T$  and only included EOS information from the merger and ringdown of the numerical part of the waveform. We also assumed that uncertainties in the non-EOS parameters did not correlate with the EOS parameters. In the remainder of this section we will compare the estimates of EOS parameters for only the merger and ringdown to a waveform that includes EOS information in the full IMR hybrid waveform. In the next two sections we will address the issue of correlations between all of the parameters by constructing an analytic BHNS waveform and calculating the complete Fisher matrix.

As in Chapter 7, we can evaluate the measurability of EOS effects from just the merger and ringdown by matching each numerical BHNS waveform to an inspiral waveform that does not include tidal corrections. We can then evaluate the Fisher matrix by differentiating the waveform with respect to each EOS parameter using finite differencing with two or more waveforms for each parameter. Specifically we follow the third method in Appendix C

which results in the greatest accuracy given the sometimes large phase difference between waveforms. Specifically, we break up each Fourier transformed waveform into the log of the amplitude  $\ln A(f; \theta^A)$  and accumulated phase  $\Phi(f; \theta^A)$

$$\tilde{h}(f; \theta^A) = e^{\ln A(f; \theta^A) + i\Phi(f; \theta^A)}. \quad (8.16)$$

The derivative is now approximated by

$$\frac{\partial \tilde{h}}{\partial \theta^A} = e^{\ln A + i\Phi} \left( \frac{\Delta \ln A}{\Delta \theta^A} + i \frac{\Delta \Phi}{\Delta \theta^A} \right). \quad (8.17)$$

where  $\Delta/\Delta\theta^A$  represents finite differencing, and  $\ln A$  and  $\Phi$  are evaluated at the midpoint using interpolation.

The  $1\text{-}\sigma$  uncertainty contours in the EOS parameter space,  $\Delta\theta^A \Delta\theta^B \Gamma_{AB} = 1$ , are shown in Fig. 43 for the ET-D noise PSD for both spinning and nonspinning simulations. As in Chapter 7 we find the uncertainty contours are aligned with tidal deformability contours  $\Lambda^{1/5}$ , and this holds for systems with spinning black holes as well. In contrast, when the tidal correction  $\psi_T$  is added to the inspiral of the hybrid waveform, there is an improvement of roughly a factor of 3 in the measurability of  $\Lambda$  as shown in Fig. 44. The majority of the improvement arises because, as discussed above, the inspiral tidal correction also adds a linearly growing term to the merger and ringdown which is not present when the numerical waveform is joined to an inspiral waveform without tidal corrections.

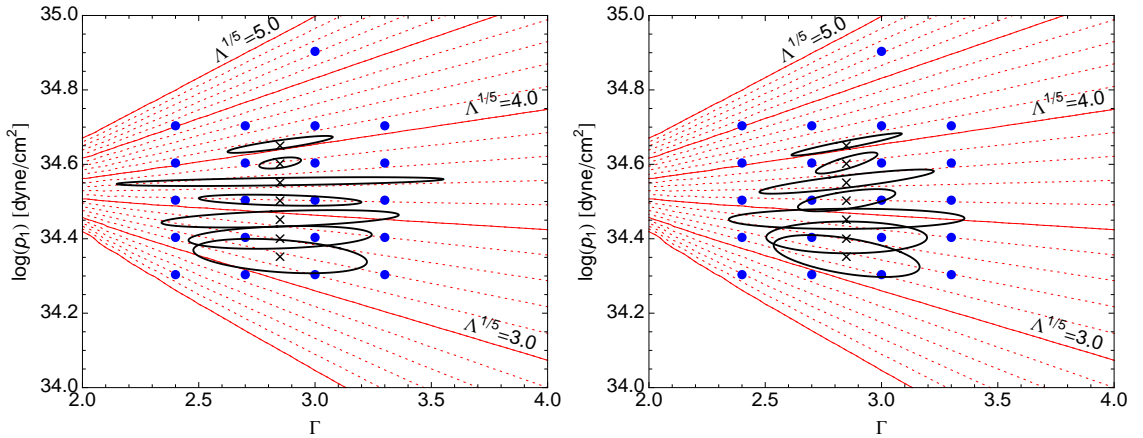


Figure 43 :  $1\text{-}\sigma$  error ellipses using the ET-D noise curve when only tidal effects during the merger-ringdown are included, and assuming non-EOS parameters are known exactly as was done in [169]. Binary is optimally oriented and at a distance of 100 Mpc. Left:  $\chi_{\text{BH}} = 0$ ,  $Q = 2$ , and  $M_{\text{NS}} = 1.35M_{\odot}$ . Right:  $\chi_{\text{BH}} = 0.5$ ,  $Q = 3$ , and  $M_{\text{NS}} = 1.35M_{\odot}$ . Evenly spaced contours of constant  $\Lambda^{1/5}$  are also shown. Each ellipse is centered on the estimated parameter  $\hat{\theta}^A$  denoted by a  $\times$ .

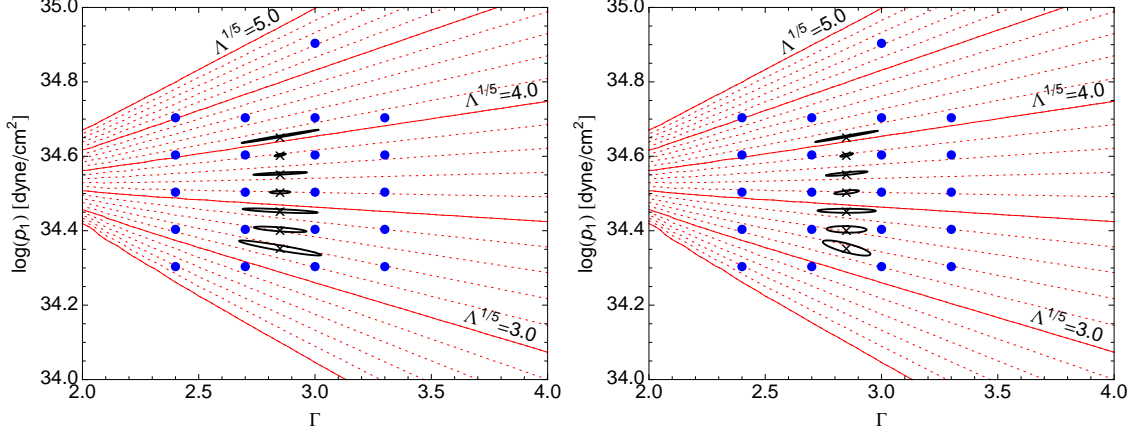


Figure 44 : Same as Fig. 43, but including tidal information from the inspiral in addition to the merger-ringdown. Left:  $\chi_{\text{BH}} = 0$ ,  $Q = 2$ , and  $M_{\text{NS}} = 1.35M_{\odot}$ . Right:  $\chi_{\text{BH}} = 0.5$ ,  $Q = 3$ , and  $M_{\text{NS}} = 1.35M_{\odot}$ .

## 8.5 Phenomenological BHNS waveform

In the previous chapter and in Section 8.4 we assumed that the correlation between EOS parameters and the other parameters is negligible. To test this assumption, we must calculate the complete Fisher matrix for all parameters, and this requires us to evaluate partial derivatives with respect to all parameters at a single point. For an aligned-spin BHNS system with negligible NS spin and a single detector, there are 7 parameters. The 4 intrinsic parameters are the chirp mass  $\mathcal{M} = (M_{\text{BH}}M_{\text{NS}})^{3/5}/M^{1/5}$ , symmetric mass ratio  $\eta = M_{\text{BH}}M_{\text{NS}}/M^2$ , black hole spin  $\chi_{\text{BH}}$ <sup>1</sup>, and tidal deformability  $\Lambda$ . The 3 extrinsic parameters, which can be differentiated analytically, are time of coalescence  $t_c$ , phase of coalescence  $\phi_c$ , and an effective distance  $D_{\text{eff}}$  that incorporates the true distance  $D$  as well as the orientation and sky location of the binary. For an optimally oriented binary,  $D_{\text{eff}} = D$ . If using central differencing, this requires 8 waveforms for the 4 numerical derivatives at each point in the waveform parameter space, and is computationally expensive. Also, in contrast to the EOS parameters, small changes in  $\mathcal{M}$ ,  $\eta$ , and  $\chi_{\text{BH}}$  can result in a large change in the phase of the waveform. This means that the simulations must be closely spaced in parameter space in order to accurately calculate derivatives. However, closely spaced waveforms which have

<sup>1</sup>The NS spin will likely have a negligible effect on the waveform because the NS mass is smaller than the BH mass by a factor of  $Q$ , and the angular velocity of the NS is bounded by the Kepler frequency. In addition, NS are expected to spin down to a small fraction of the Kepler frequency by the time the binary reaches the detector band. Furthermore, there is a strong degeneracy between the two spins in a binary, so we can simply treat the total spin as an effective BH spin, and ignoring the NS spin as a separate parameter is therefore justified.

numerical errors can lead to large subtraction errors in the finite differences.

Another approach is to construct an analytic BHNS waveform model, then fit the free parameters of the model to the hybridized numerical simulations. This will allow us to interpolate between the available simulations as well as evaluate derivatives used in the Fisher matrix. For aligned-spin BBH systems, significant work has gone into developing phenomenological waveforms that include the complete inspiral, merger, and ringdown. We will use the most modern version of these waveforms, PhenomC [72], as the basis for our BHNS waveform model.

As found in Section 8.4 (Figs. 43 and 44) and hinted at in Fig. 39, a BHNS waveform is well approximated by a one-parameter deformation from a BBH waveform where  $\Lambda = 0$  [110]. As shown in Fig. 39, throughout the inspiral, merger, and ringdown, both the amplitude and phase of the Fourier transformed waveform monotonically decrease with respect to a BBH waveform as frequency increases and as  $\Lambda$  increases. We thus write the BHNS waveform as a modification to a BBH waveform

$$\tilde{h}_{\text{BHNS}}(Mf; \theta^A) = \tilde{h}_{\text{BBH}}(Mf; \theta^A) e^{[\Delta \ln A(Mf; \theta^A) + i\Delta\Phi(Mf; \theta^A)]}, \quad (8.18)$$

where  $\Delta \ln A(Mf) = \ln |\tilde{h}_{\text{BHNS}}(Mf)| - \ln |\tilde{h}_{\text{BBH}}(Mf)|$  is an amplitude correction factor,  $\Delta\Phi(Mf) = \Phi_{\text{BHNS}}(Mf) - \Phi_{\text{BBH}}(Mf)$  is a phase correction factor, and the 3 physical parameters that we will fit our waveforms to are  $\theta^A = \{\eta, \chi_{\text{BH}}, \Lambda\}$ . In the next two subsections, we will fit the quantities  $\Delta \ln A(Mf)$  and  $\Delta\Phi(Mf)$  to the 90 hybrid waveforms listed in Table 6.

### 8.5.1 Amplitude fit

During the inspiral, parameter estimation is much more sensitive to the phase of the waveform than to the amplitude, so we ignore the very small amplitude correction from tidal interactions. During the merger and ringdown, however, they are important. We therefore write the amplitude correction as

$$\Delta \ln A(Mf; \theta^A) = \begin{cases} 0 & Mf \leq Mf_0 \\ -\eta\Lambda B(Mf; \theta^A) & Mf > Mf_0 \end{cases}, \quad (8.19)$$

where  $Mf_0$  is the boundary, chosen below, between the inspiral and merger, and we have extracted the quantity  $\eta\Lambda$  because as  $\eta \rightarrow 0$  (extreme mass ratio limit) or  $\Lambda \rightarrow 0$ , the waveform should approach that of a BBH waveform. We now impose two requirements on the function  $B(Mf; \theta^A)$ . (i) The amplitude must be continuous at the frequency  $Mf_0$ , so  $B(Mf_0; \theta^A) = 0$ . (ii) Because the amplitude of the BHNS waveform is always less than that

of the corresponding BBH waveform, we require  $B(Mf; \theta^A) \geq 0$  for  $Mf \geq Mf_0$  and for all physical values of the parameters:  $\eta \in [0, 0.25]$ ,  $\chi_{\text{BH}} \in [-1, 1]$ , and  $\Lambda \geq 0$ .

Given the above restrictions, we find that a useful fitting function for the amplitude correction is  $B(Mf; \theta^A) = C(Mf - Mf_0)^D$ , where  $C$  and  $D$  are free parameters, and  $Mf_0 = 0.01$ . With this ansatz, we then do a least-squares fit to determine the parameters  $C$  and  $D$ . We find that over the 90 simulations,  $D$  has a mean and standard deviation of  $D \sim 3 \pm 0.7$ , and because these parameters are highly correlated, we fix  $D = 3$  so that  $B = C(Mf - Mf_0)^3$ . We then fit each waveform with the single parameter  $C$ . The parameter  $C$  is then fit to the physical parameters with the function  $C(\eta, \chi_{\text{BH}}, \Lambda) = c_0 \Lambda e^{1+c_1\eta+c_2\chi_{\text{BH}}}$ , where the parameters  $c_0$ ,  $c_1$ , and  $c_2$  are found with a least-squares fit, and we note that this function is positive for all physical values of the parameters  $\eta$ ,  $\chi_{\text{BH}}$ , and  $\Lambda$ . Another useful feature of the exponential form of this function is that it is nonlinear and allows for coupling between  $\eta$  and  $\chi_{\text{BH}}$  while still having a small number of parameters. In other words, when expanded, it leads to nonlinear terms (e.g. terms proportional to  $\chi_{\text{BH}}^2$ ) and cross terms (e.g. terms proportional to  $\eta\chi_{\text{BH}}$ ). The final form of  $B$  can therefore be written

$$B(Mf; \theta^A) = c_0 \Lambda e^{1+c_1\eta+c_2\chi_{\text{BH}}}(Mf - Mf_0)^3, \quad (8.20)$$

and the best-fit parameters are  $\{c_0, c_1, c_2\} = \{2.09650 \times 10^{-5}, 35.4859, 1.12893\}$ .

### 8.5.2 Phase fit

For the phase of the waveform we choose the following ansatz

$$\Delta\Phi(Mf; \theta^A) = \begin{cases} \psi_T(Mf; \theta^A) & Mf \leq Mf_0 \\ -\eta\Delta E(Mf; \theta^A) + \psi_T(Mf_0; \theta^A) + (Mf - Mf_0)\psi'_T(Mf_0; \theta^A) & Mf > Mf_0 \end{cases}, \quad (8.21)$$

where  $\psi_T$  is the frequency domain tidal phase correction for the inspiral, and a  $'$  denotes a derivative with respect to  $Mf$ . In this paper we will use the 1PN accurate TaylorF2 tidal correction (Eq. 8.4) for the inspiral. However, a key feature of this ansatz is that an improved inspiral tidal phase term  $\psi_T$  can be swapped in without requiring one to redo the hybridization or the following phase fit. This is because the hybridization procedure of Section 8.3 matches the phase and derivative of the inspiral and numerical waveforms by adjusting the parameters  $\phi$  and  $\tau$  to generate a shifted numerical waveform with a linear correction term:  $\Phi_{\text{NR}}^{\text{shift}}(f; \tau, \phi) = \Phi_{\text{NR}}(f) + 2\pi f\tau + \phi$ . By explicitly pulling out the linear quantity  $\psi_T(Mf_0) + (Mf - Mf_0)\psi'_T(Mf_0)$  in the phenomenological fit, the hybridization procedure will not need to be repeated for an improved inspiral tidal correction, and the coefficients given below for the fit will remain the same. As in the amplitude fit, we have

extracted the quantity  $\eta\Lambda$  in the first term because the phase of the BHNS waveform should approach that of a BBH waveform as  $\eta \rightarrow 0$  or  $\Lambda \rightarrow 0$ . The above discussion then demands the remaining function  $E(Mf; \theta^A)$  satisfy the following conditions: (i)  $E(Mf_0; \theta^A) = 0$ , (ii)  $E'(Mf_0; \theta^A) = 0$ , and (iii)  $E(Mf; \theta^A) \geq 0$  for  $Mf \geq Mf_0$  and for all physical values of  $\eta$ ,  $\chi_{\text{BH}}$ , and  $\Lambda$ .

We find that each waveform can be accurately fit with a function of the form  $E = G(Mf - Mf_0)^H$ , where  $G$  and  $H$  are free parameters, and unlike the amplitude fit, we choose  $Mf_0 = 0.015$  for the phase fit. For the 90 BHNS waveforms the best fit for the parameter  $H$  has a relatively narrow range of approximately  $5/3 \pm 0.3$  which is consistent with the leading frequency dependence of the tidal correction in Eq. (8.4). In addition, the free parameters  $G$  and  $H$  in this fit are highly correlated. We thus rewrite  $E = G(Mf - Mf_0)^{5/3}$  and fit each waveform with the single parameter  $G$ . The parameter  $G$  is then fit to the physical parameters with the positive function  $G(\eta, \chi_{\text{BH}}, \Lambda) = g_0 e^{1+g_1\eta+g_2\chi_{\text{BH}}}$ , where  $G$  has only a weak dependence on  $\Lambda$ . The function  $E$  can then be written

$$E(Mf; \eta, \chi_{\text{BH}}) = g_0 e^{1+g_1\eta+g_2\chi_{\text{BH}}} (Mf - Mf_0)^{5/3}, \quad (8.22)$$

and the best-fit parameters are  $\{g_0, g_1, g_2\} = \{0.078655, 16.35086, 0.730279\}$ . As with the amplitude fit, this parametrization is well defined for all possible values of  $\eta$ ,  $\chi_{\text{BH}}$ , and  $\Lambda$ .

## 8.6 Results

Using the analytic IMR waveform developed in the previous section, we can now evaluate the Fisher matrix for a single gravitational-wave detector using the complete set of waveform parameters  $\{\ln D_{\text{eff}}, f_1 t_c, \phi_c, \ln \mathcal{M}, \ln \eta, \chi_{\text{BH}}, \Lambda^{1/5}\}$ , where  $f_1$  is some fiducial frequency such as 1 Hz, and as in Chapter 7 we use  $\Lambda^{1/5}$  because it is closely related to the more familiar NS radius. We have calculated the  $1\text{-}\sigma$  uncertainty in  $\Lambda^{1/5}$  for both the broadband aLIGO [114] and ET-D detector configurations [153] shown in Fig. 33. Errors are shown in Figs. 45 and 46 for broadband aLIGO and ET-D respectively, and are scaled to an effective distance of 100 Mpc as was done in Chapter 7. We note that the results shown here for the  $Q = 2$  and 3 nonspinning waveforms are similar to those presented in the previous chapter (Figs. 36 and 37). This indicates that including tidal interactions in the inspiral as well as the merger and ringdown and considering correlations between  $\Lambda$  and the other parameters roughly cancel each other.

There are several trends to notice in the uncertainty  $\sigma_{\Lambda^{1/5}}$ . In general,  $\sigma_{\Lambda^{1/5}}$  increases with increasing mass ratio  $Q$ . This is not surprising since the tidal contribution to the phase  $\psi_T$  (Eq. 8.4) is a strongly decreasing function of the mass ratio. In addition, the amount

of tidal disruption before the plunge, as well as its imprint on the waveform, decreases as the mass ratio increases. However, there are two additional competing effects. First, the amplitude during the inspiral which scales as  $|\tilde{h}(f)| \propto \mathcal{M}^{5/6} f^{-7/6}$  increases as the mass ratio increases for a fixed NS mass. Second, for higher mass ratios, the EOS dependent merger dynamics occur at a lower frequency closer to the minimum of the noise PSD (Fig. 33). These two effects help to minimize the increase in uncertainty  $\sigma_{\Lambda^{1/5}}$  as  $Q$  increases.

On the other hand, as the black hole spin  $\chi_{\text{BH}}$  increases  $\sigma_{\Lambda^{1/5}}$  decreases. This effect can be understood from Fig. 41. As the BH spin increases, the phase difference  $\Delta\Phi = \Phi_{\text{BHNS}} - \Phi_{\text{BBH}}$  increases and the amplitude cutoff occurs at a lower frequency where the detector is more sensitive.

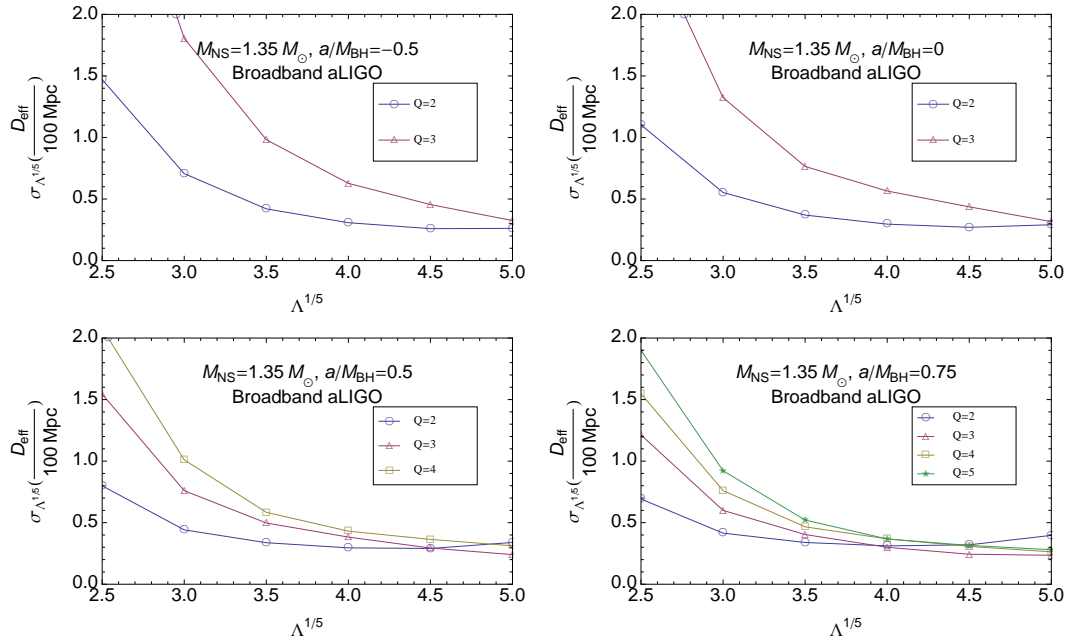


Figure 45 : 1- $\sigma$  error  $\sigma_{\Lambda^{1/5}}$  for various values of the mass ratio, BH spin, and tidal deformability. NS mass is fixed at  $1.35 M_{\odot}$ . PSD is broadband aLIGO.

## 8.7 Discussion

We have examined the ability of gravitational wave detectors to extract information about the equation of state from observations of BHNS coalescence for black holes with aligned spin. As in Chapter 7, we found that the EOS parameter that is best measured is the tidal deformability  $\Lambda$ . This is true for spinning as well as nonspinning black holes, and it is true for the merger and ringdown as well as for the inspiral. Furthermore, coherently

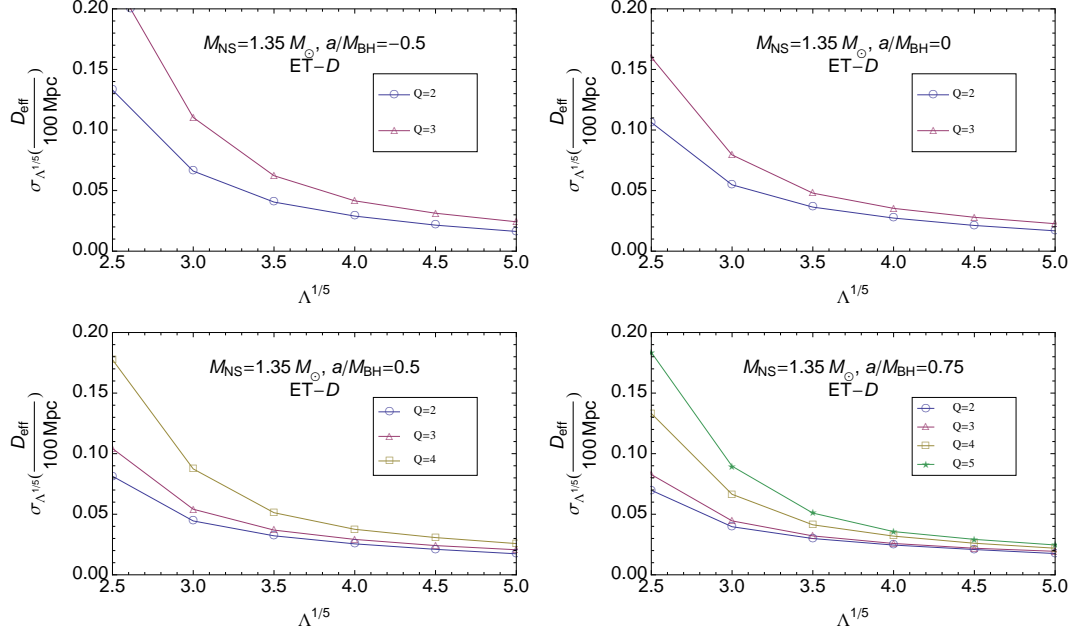


Figure 46 : Same as Fig. 45, but with ET-D noise curve. Uncertainty  $\sigma_{\Lambda^{1/5}}$  is an order of magnitude smaller.

combining the EOS information for the complete IMR waveform dramatically improves the measurability  $\Lambda$  by up to a factor of  $\sim 3$  in some cases over just the merger and ringdown.

In order to examine the correlations between  $\Lambda$  and the other parameters, we constructed an analytic IMR waveform based on the frequency domain PhenomC aligned-spin waveform model [72], and we calibrated this waveform model to our hybridized numerical waveforms. Although  $\Lambda$  does correlate with the other parameters, the correlations are not nearly as strong as correlations between the other parameters.

The frequency domain analytic waveform presented here can be, without too much difficulty, incorporated into Markov Chain Monte Carlo and Nested Sampling algorithms used for Bayesian parameter estimation for networks of gravitational-wave detectors. A full Bayesian analysis will then make it possible to assess the true nature of the probability distribution for the waveform parameters as well as the accuracy of the Fisher matrix approximation.

## Appendix A

# Analytic fits to tabulated EOS

### A.1 Low-density equation of state

We use an analytic form of the (SLy) low-density EOS that closely matches its tabulated values. With rms residual less than 0.03,  $p(\rho)$  for SLy is approximated between  $\rho = 10^3 \text{ g/cm}^3$  and  $\rho = 10^{14} \text{ g/cm}^3$  by four polytropic pieces. The four regions correspond roughly to a nonrelativistic electron gas, a relativistic electron gas, neutron drip, and the density range from neutron drip to nuclear density. Using the notation of Sect. 2.3, the analytic form of the SLy EOS is set by the values of  $K_i, \Gamma_i$  and  $\rho_i$  listed in Table 7.

Table 7 : An analytic representation of  $p(\rho)$  for the SLy EOS below nuclear density uses polytropes specified by the constants listed here.  $\Gamma_i$  is dimensionless,  $\rho_i$  is in  $\text{g/cm}^3$ , and  $K_i$  is in cgs units for which the corresponding value of  $p$  is in units of  $\text{dyne/cm}^2$ . The last dividing density is the density where the low density EOS matches the high density EOS and depends on the parameters  $p_1$  and  $\Gamma_1$  of the high density EOS.

$K_i/c^2$	$\Gamma_i$	$\rho_i$
6.80110e-09	1.58425	2.44034e+07
1.06186e-06	1.28733	3.78358e+11
5.32697e+01	0.62223	2.62780e+12
3.99874e-08	1.35692	–

### A.2 Comparison table

Table 8 compares neutron-star properties for each EOS to their values for the best-fit piecewise polytrope. The parameters for the three-piece polytropic core EOS, the corresponding

residuals, as well as the observable properties of these EOSs and the error in using the best fit parameterized EOS instead of the tabulated EOS are listed in Table 8. The parameterized EOS systematically overestimates the maximum speed of sound.

Table 8: Comparison of candidate EOSs and their best fits. The parameters that provide the best fit to the candidate EOSs as well as the residual are given.  $p_1$  is in units of dyne/cm<sup>2</sup>. Values for observables calculated using the tabulated EOSs are also given.  $v_{s,\max}$  is the maximum adiabatic speed of sound below the central density of the maximum mass neutron star.  $M_{\max}$  is the maximum nonrotating mass configuration in units of  $M_{\odot}$ .  $z_{\max}$  is the corresponding maximum gravitational redshift.  $f_{\max}$  is the maximum rotation frequency in Hz, as calculated using the rotating neutron-star code `rms`.  $I_{1.338}$  is the moment of inertia for a  $1.338 M_{\odot}$  star in units of  $10^{45} \text{ g cm}^2$ .  $R_{1.4}$  is the radius of a  $1.4 M_{\odot}$  star in units of km. The difference in calculated values for each observable when using the tabulated EOS ( $O_{\text{tab}}$ ) versus the best fit parameterized EOS ( $O_{\text{fit}}$ ) is calculated with  $(O_{\text{fit}}/O_{\text{tab}} - 1)100$ . The last entry gives the mean and standard deviation of the errors for each observation.

EOS	$\log(p_1)$	$\Gamma_1$	$\Gamma_2$	$\Gamma_3$	residual	$v_{s,\max}$	%	$M_{\max}$	%	$z_{\max}$	%	$f_{\max}$	%	$I_{1.338}$	%	$R_{1.4}$	%
PAL6	34.380	2.227	2.189	2.159	0.0011	0.693	1.37	1.477	-0.47	0.374	-0.51	1660	-0.97	1.051	-2.03	10.547	-0.54
SLy	34.384	3.005	2.988	2.851	0.0020	0.989	1.41	2.049	0.02	0.592	0.81	1810	0.10	1.288	-0.08	11.736	-0.21
AP1	33.943	2.442	3.256	2.908	0.019	0.924	9.94	1.683	-1.60	0.581	2.79	2240	1.05	0.908	-2.57	9.361	-1.85
AP2	34.126	2.643	3.014	2.945	0.0089	1.032	0.42	1.808	-1.50	0.605	0.33	2110	-0.02	1.024	-2.34	10.179	-1.57
AP3	34.392	3.166	3.573	3.281	0.0091	1.134	2.72	2.390	-1.00	0.704	0.57	1810	-0.14	1.375	-1.59	12.094	-0.96
AP4	34.269	2.830	3.445	3.348	0.0068	1.160	1.45	2.213	-1.08	0.696	0.22	1940	0.05	1.243	-1.36	11.428	-0.90
FPS	34.283	2.985	2.863	2.600	0.0050	0.883	2.29	1.799	-0.03	0.530	0.67	1880	0.11	1.137	0.03	10.850	0.12
WFF1	34.031	2.519	3.791	3.660	0.018	1.185	7.86	2.133	-0.29	0.739	2.21	2040	0.30	1.085	0.10	10.414	0.02
WFF2	34.233	2.888	3.475	3.517	0.017	1.139	7.93	2.198	-0.14	0.717	0.71	1990	0.03	1.204	-0.59	11.159	-0.28
WFF3	34.283	3.329	2.952	2.589	0.017	0.835	8.11	1.844	-0.48	0.530	2.26	1860	0.59	1.160	-0.25	10.926	-0.12
BBB2	34.331	3.418	2.835	2.832	0.0055	0.914	7.75	1.918	0.10	0.574	0.97	1900	0.47	1.188	0.17	11.139	-0.29
BPAL12	34.358	2.209	2.201	2.176	0.0010	0.708	1.03	1.452	-0.18	0.382	-0.29	1700	-1.03	0.974	0.20	10.024	0.67
ENG	34.437	3.514	3.130	3.168	0.015	1.000	10.71	2.240	-0.05	0.654	0.39	1820	-0.44	1.372	-0.97	12.059	-0.69
MPA1	34.495	3.446	3.572	2.887	0.0081	0.994	4.91	2.461	-0.16	0.670	-0.05	1700	-0.18	1.455	-0.41	12.473	-0.26
MS1	34.858	3.224	3.033	1.325	0.019	0.888	12.44	2.767	-0.54	0.606	-0.52	1400	1.67	1.944	-0.09	14.918	0.06
MS2	34.605	2.447	2.184	1.855	0.0030	0.582	3.96	1.806	-0.42	0.343	2.57	1250	2.25	1.658	0.46	14.464	-2.69
MS1b	34.855	3.456	3.011	1.425	0.015	0.889	11.38	2.776	-1.03	0.614	-0.56	1420	1.38	1.888	-0.64	14.583	-0.32
PS	34.671	2.216	1.640	2.365	0.028	0.691	7.36	1.755	-1.53	0.355	-1.45	1300	-2.39	2.067	-3.06	15.472	3.72
GS1 <sup>1</sup>	34.504	2.350	1.267	2.421	0.018	0.695	0.49	1.382	-1.00	0.395	-0.64	1660	9.05	0.766	-3.13		<sup>2</sup>
GS2 <sup>1</sup>	34.642	2.519	1.571	2.314	0.026	0.592	16.10	1.653	-0.30	0.339	7.71	1340	3.77	1.795	-3.33	14.299	0.07

Table 8 – Continued

EOS	$\log(p_1)$	$\Gamma_1$	$\Gamma_2$	$\Gamma_3$	residual	$v_{s,\max}$	%	$M_{\max}$	%	$z_{\max}$	%	$f_{\max}$	%	$I_{1.338}$	%	$R_{1.4}$	%
BGN1H1	34.623	3.258	1.472	2.464	0.029	0.878	-7.42	1.628	0.39	0.437	-3.55	1670	-2.08	1.504	0.56	12.901	-1.96
GNH3	34.648	2.664	2.194	2.304	0.0045	0.750	2.04	1.962	0.13	0.427	0.37	1410	-0.04	1.713	0.38	14.203	-0.28
H1	34.564	2.595	1.845	1.897	0.0019	0.561	2.81	1.555	-0.92	0.311	-1.47	1320	-1.46	1.488	-1.45	12.861	-0.03
H2	34.617	2.775	1.855	1.858	0.0028	0.565	1.38	1.666	-0.77	0.322	-0.55	1280	-1.29	1.623	-0.82	13.479	0.29
H3	34.646	2.787	1.951	1.901	0.0070	0.564	7.05	1.788	-0.79	0.343	1.07	1290	-0.88	1.702	-1.18	13.840	0.31
H4	34.669	2.909	2.246	2.144	0.0028	0.685	4.52	2.032	-0.85	0.428	-1.01	1400	-1.28	1.729	-1.18	13.774	1.34
H5	34.609	2.793	1.974	1.915	0.0050	0.596	1.65	1.727	-1.00	0.347	-0.82	1340	-1.55	1.615	-1.31	13.348	0.68
H6 <sup>1</sup>	34.593	2.637	2.121	2.064	0.0087	0.598	11.71	1.778	0.07	0.346	8.65	1310	5.33	1.623	-2.19	13.463	0.37
H7	34.559	2.621	2.048	2.006	0.0046	0.630	1.82	1.683	-1.12	0.357	-0.57	1410	-1.52	1.527	-2.33	12.992	0.23
PCL2	34.507	2.554	1.880	1.977	0.0069	0.600	1.74	1.482	-0.79	0.326	-2.25	1440	-1.87	1.291	-3.27	11.761	-1.15
ALF1	34.055	2.013	3.389	2.033	0.040	0.565	18.59	1.495	-0.53	0.386	3.52	1730	2.44	0.987	-0.40	9.896	-0.22
ALF2	34.616	4.070	2.411	1.890	0.043	0.642	1.50	2.086	-5.26	0.436	-0.62	1440	1.01	1.638	-6.94	13.188	-3.66
ALF3	34.283	2.883	2.653	1.952	0.017	0.565	11.29	1.473	-0.06	0.358	2.46	1620	1.79	1.041	0.76	10.314	-0.25
ALF4	34.314	3.009	3.438	1.803	0.023	0.685	14.78	1.943	-0.93	0.454	0.59	1590	0.52	1.297	-2.38	11.667	-1.20
Mean error							5.68		-0.71		0.74		0.43		-1.26		-0.37
Standard deviation of error							5.52		0.96		2.42		2.25		1.57		1.29

<sup>1</sup>The tables for GS1, GS2, and H6 do not go up to the central density of the maximum mass star. For most observables, the EOS can be safely extrapolated to higher density with minimal error. However, the maximum speed of sound is highly sensitive to how this extrapolation is done. Thus, we only use the maximum speed of sound up to the last tabulated point when comparing the values for the table and fit.

<sup>2</sup>GS1 has a maximum mass less than  $1.4 M_{\odot}$ .

## Appendix B

# Accuracy of the tidal correction model

To assess the accuracy of the simple phase evolution model, we compute the corrections to the tidal phase perturbation due to several EOS-dependent effects: the leading order finite mode-frequency terms, higher order tidal effects, and nonlinear hydrodynamic couplings. For simplicity, we will only derive the phase corrections for one star with internal degrees of freedom coupled to a point mass. The terms for the other star simply add. For such a binary system, the Lagrangian can then be written as

$$\begin{aligned}
 L = & \frac{1}{2}\eta M\dot{r}^2 + \frac{1}{2}\eta M r^2 \dot{\varphi}^2 + \frac{\eta M^2}{r} - \frac{1}{2}Q_{ij}\mathcal{E}_{ij} + \frac{1}{4\lambda\omega_0^2}\left(\dot{Q}_{ij}\dot{Q}_{ij} - \omega_0^2 Q_{ij}Q_{ij}\right) \\
 & - \frac{1}{6}Q_{ijk}\mathcal{E}_{ijk} + \frac{1}{12\lambda_3\omega_{03}^2}\left(\dot{Q}_{ijk}\dot{Q}_{ijk} - \omega_{03}^2 Q_{ijk}Q_{ijk}\right) - \frac{\alpha}{\lambda^3}Q_{ij}Q_{jk}Q_{ki}. \quad (\text{B.1})
 \end{aligned}$$

Here, the star's static mass quadrupole  $Q_{ij}$  parameterizes the  $l = 2$  modes of the star, which can be treated as harmonic oscillators that are driven below their resonant frequency by the companion's tidal field. The tensor  $Q_{ijk}$  parameterizes the star's mass octupole degrees of freedom, and  $\mathcal{E}_{ij}$  and  $\mathcal{E}_{ijk}$  are the  $l = 2$  and  $l = 3$  tidal tensors respectively, which are given by  $\mathcal{E}_{ij} = \partial_i\partial_j(-m_2/r)$  and  $\mathcal{E}_{ijk} = \partial_i\partial_j\partial_k(-m_2/r)$  in Newtonian gravity. The  $l = 3$  deformability constant  $\lambda_3$  is defined by  $Q_{ijk} = -\lambda_3\mathcal{E}_{ijk}$ . The quantities  $\omega_0$  and  $\omega_{03}$  are the  $l = 2$  and  $l = 3$   $f$ -mode frequencies, and  $\alpha$  is a coupling constant for the leading order nonlinear hydrodynamic interactions. In general, one would need to sum over the contributions from all the modes, but other modes contribute negligibly in the regime of interest for the above model (see [86]). Post-Newtonian effects on the Lagrangian for the binary are derived in Refs. [85, 111] and can simply be added to those derived here.

We will be interested in finding an effective description of the dynamics of the system

for quasi-circular inspirals in the adiabatic limit, where the radiation reaction timescale is long compared to the orbital timescale. From equilibrium solutions to the Euler-Lagrange equations derived from this Lagrangian, the following radius-frequency relation is obtained:

$$r(\omega) = M^{1/3}\omega^{-2/3} \left[ 1 + \frac{3\lambda m_2 \omega^{10/3}}{M^{5/3} m_1} + \frac{9\lambda m_2 \omega^{10/3}}{M^{5/3} m_1} \frac{\omega^2}{\omega_0^2} + \frac{20\lambda_3 m_2 \omega^{14/3}}{M^{7/3} m_1} - \frac{27\alpha m_2^2 \omega^{16/3}}{2M^{8/3} m_1} - \frac{27\lambda^2 m_2^2 \omega^{20/3}}{M^{10/3} m_1^2} \right], \quad (\text{B.2})$$

The equilibrium energy, obtained by reversing the signs of the potential energy terms in the Lagrangian, is given by:

$$E = -\frac{1}{2}\eta M^{5/3}\omega^{2/3} \left[ 1 - \frac{9\lambda m_2 \omega^{10/3}}{M^{5/3} m_1} - \frac{45\lambda m_2 \omega^{10/3}}{M^{5/3} m_1} \frac{\omega^2}{\omega_0^2} - \frac{65\lambda_3 m_2 \omega^{14/3}}{M^{7/3} m_1} + \frac{42\alpha m_2^2 \omega^{16/3}}{M^{8/3} m_1} + \frac{63\lambda^2 m_2^2 \omega^{20/3}}{M^{10/3} m_1^2} \right]. \quad (\text{B.3})$$

The energy flux  $\dot{E} = -\frac{1}{5}\langle \ddot{Q}_{ij}^T \ddot{Q}_{ij}^T \rangle$ , where  $Q_{ij}^T = \mu r^2 (n^i n^j - \frac{1}{3}\delta_{ij}) + Q_{ij}$  is the total quadrupole moment, is

$$\dot{E} = -\frac{32}{5}\eta^2 M^{10/3}\omega^{10/3} \left[ 1 + \frac{6\lambda \omega^{10/3}}{M^{2/3} m_1} \left( 2\frac{m_2}{M} + 1 \right) + \frac{12\lambda \omega^{10/3}}{M^{2/3} m_1} \frac{\omega^2}{\omega_0^2} \left( 3\frac{m_2}{M} + 2 \right) + \frac{80\lambda_3 m_2 \omega^{14/3}}{M^{7/3} m_1} - \frac{36\alpha m_2 \omega^{16/3}}{M^{5/3} m_1} \left( \frac{3m_2}{2M} + 1 \right) + \frac{9\lambda^2 \omega^{20/3}}{M^{4/3} m_1^2} \left( 1 - \frac{2m_2}{M} - \frac{6m_2^2}{M^2} \right) \right]. \quad (\text{B.4})$$

Using the formula  $d^2\Psi/d\omega^2 = 2(dE/d\omega)/\dot{E}$  in the stationary phase approximation and integrating twice leads to the final expression for the tidal phase correction:

$$\delta\Psi = -\frac{9\lambda x^{5/2}}{16\eta M^5} \left( \frac{m_1 + 12m_2}{m_1} \right) - \frac{45\lambda x^{5/2}}{1408\eta M^5 \omega_0^2} \frac{\omega^2}{\omega_0^2} \left( \frac{8m_1 + 155m_2}{m_1} \right) - \frac{125}{12} \frac{\lambda_3 x^{9/2}}{\eta M^7} \frac{m_2}{m_1} + \frac{135\alpha m_2 x^{11/2}}{352\eta M^8} \left( \frac{m_1 + 13m_2}{m_1} \right) - \frac{3\lambda^2 x^5}{64\eta M^{10}} \left( \frac{M^2 - 2m_2 M - 83m_2^2}{m_1^2} \right). \quad (\text{B.5})$$

We will analyze the information contained in the portion of the signal at frequencies  $f \leq 450$  Hz. This is slightly higher than previously considered, and we now argue that in this frequency band, the simple model of the phase correction is still sufficiently accurate for our purposes. We will evaluate all of the corrections for the case of equal masses  $m_1 = m_2 \equiv m$ . An estimate of the fractional errors for the case of  $m = 1.4 M_\odot$  and  $R = 15$  km is given in parentheses.

1. *Post-1-Newtonian corrections* ( $\sim 10\%$ ).

These corrections give rise to terms  $\propto \lambda x^{7/2}$  that add to those in Eq. (B.5). The explicit form of these terms is computed in Refs. [85, 111] and they depend on the NS physics only via the same parameter  $\lambda$  as the Newtonian tidal terms, so they can easily be incorporated into the data analysis method. Preliminary estimates indicate that for equal masses, these post-1 Newtonian effects will increase the tidal signal.

2. *Adiabatic approximations* ( $\sim 1\%$ ).

The approximation that the radiation reaction time is much longer than the orbital time is extremely accurate, to better than 1%; see Fig. 2 of Ref. [86], which compares the phase error obtained from numerically integrating the equations of motion supplemented with the leading order gravitational wave dissipation terms to that obtained analytically using the adiabatic approximation.

The accuracy of the approximation  $\omega \ll \omega_0$  can be estimated from the fractional correction to (B.5), which is  $\sim (815/1144)(\omega/\omega_0)^2 \sim 0.18(f/f_0)^2$ , where  $f = \omega/\pi$  and  $f_0 = \omega_0/(2\pi)$ . For typical NS models the  $l = 2$   $f$ -mode frequency is [170]

$$\frac{f_0}{\text{kHz}} \approx 0.78 + 1.64 \left( \frac{m}{1.4 M_\odot} \right)^{1/2} \left( \frac{R}{10 \text{ km}} \right)^{-3/2}, \quad (\text{B.6})$$

so that the fractional correction is  $\sim 0.012$  for  $f = 450$  Hz and for a conservatively low  $f$ -mode frequency of  $f_0 = 1700$  Hz.

3. *Higher order tidal effects* ( $\sim 0.7\%$ ).

The  $l = 3$  correction to the gravitational wave phase (B.5) is smaller than the  $l = 2$  contribution by a factor of  $\sim (25/351)(k_3/k_2)(m/R)^{-2}x^2 \sim 0.007$ , for  $m/R = 0.14$  and a stiff  $n = 0.5$  polytrope. Here, we have defined the  $l = 3$  Love number  $k_3 = (15/2)\lambda_3 R^{-7}$  and used the values  $k_2 = 0.17$  and  $k_3 = 0.06$  from Ref. [110].

4. *Nonlinear hydrodynamic corrections* ( $\sim 0.1\%$ ).

The leading nonlinear hydrodynamic corrections are characterized by the coupling coefficient  $\alpha/\lambda^3$  in the action. The size of this parameter can be estimated by comparing the Newtonian  $k_2$  to the coupling constants in Lai's ellipsoidal models (e.g. Table 1 of [171]) to be  $\omega^2\alpha/\lambda \sim 2 \times 10^{-3}$ . The nonlinear self-coupling term in Eq. (B.5) is smaller than the leading  $l = 2$  term by a factor  $-285\alpha\omega^2/(572\lambda) \sim 0.001$ .

5. *Spin corrections* ( $\lesssim 0.3\%$ ).

Fractional corrections to the tidal signal due to spin scale as

$$\frac{\delta\Psi_{\text{spin}}}{\delta\Psi_{\text{tidal}}} \propto \left( \frac{\omega_{\text{spin}}}{\omega_{\text{max}}} \right)^2, \quad (\text{B.7})$$

where  $\omega_{\max}$  is the maximum rotational frequency the star can have before breakup, which for most NS models is  $> 2\pi(1000 \text{ Hz})$ . The observed NS-NS binaries which will merge within a Hubble time have spin periods of  $\sim 23 - 104 \text{ ms}$ , and near the coalescence they will have slowed down due to e.g. magnetic braking, with final spin periods of  $\sim 50 - 130 \text{ ms}$ . The fractional corrections to the tidal signal due to the spin are then  $\lesssim 0.3\%$ .

If the stars have spin, there will also be a spin-induced correction to the phase, as discussed in Refs. [104, 106]. In the slow rotation limit (which is likely to be the relevant regime for the binaries we consider), the effect of spin on the phasing can be computed using similar methods as for the tidal corrections. The resulting spin-induced phase correction scales as  $\delta\Psi_s \sim 345n_2R^2/(32\eta M^2x^{1/2})\omega_{\text{spin}}^2/(m_1/R^3)$ , where  $\omega_{\text{spin}}$  the spin frequency and  $n_2$  is the rotational Love number, which for Newtonian stars is the same as the tidal Love number  $k_2$ . The scaling of the spin term as  $\propto x^{-1/2}$  shows that only at large separation do spin effects dominate over tidal effects, which scale as  $\propto x^{5/2}$ . For spin periods of  $\sim 50 \text{ ms}$  and  $R \sim 5m$ , the spin-induced phase correction  $\delta\Psi_s$  becomes smaller than the tidal correction at frequencies above  $\sim 170 \text{ Hz}$ . This agrees with the results of the more detailed analysis of the relative importance of spin and tidal effects in Ref. [106].

6. *Nonlinear response to the tidal field* ( $\sim 3\%$ ).

We have linearized in  $\lambda$ . Including terms  $\propto \lambda^2$  gives a fractional correction in Eq. (B.5) of  $-(83/7488)k_2R^5x^{5/2}/m^5 = -4.8 \times 10^{-11}k_2(m/M_\odot)^{-10/3}(R/\text{km})^5(f/\text{Hz})^{5/3} = -0.31k_2$ .

7. *Viscous dissipation* (negligible).

There have been several analytical and numerical studies of the effect of viscosity during the early part of the inspiral, e.g. [103, 104]. They found that viscous dissipation is negligible during the early inspiral if the volume-averaged shear viscosity  $\eta_{\text{shear}}$  is

$$\eta_{\text{shear}} \lesssim 10^{29} \left(\frac{r}{R}\right)^2 \text{ g cm}^{-1}\text{s}^{-1}. \quad (\text{B.8})$$

The expected microscopic viscosity of NSs is [172]

$$\eta_{\text{micr}} \sim 10^{22} \left(\frac{\rho}{10^{14} \text{ g cm}^{-3}}\right)^{9/4} \left(\frac{T}{10^6 \text{ K}}\right)^{-2} \text{ g cm}^{-1}\text{s}^{-1}, \quad (\text{B.9})$$

which is orders of magnitude too small to lead to any significant effect. A variety of other likely sources of viscosity, e. g. the breaking or crumpling of the crust, are also insignificant [104, 103] in the regime of interest to us.

Thus, systematic errors in the measured value of  $\lambda$  due to errors in the model should be  $O(10\%)$ , which is small compared to the current uncertainty of an order of magnitude in  $\lambda$ .

## Appendix C

# Numerically evaluating the Fisher matrix

When an analytical representation of a waveform is not available, the partial derivatives in the Fisher matrix Eq. (8.14) must be evaluated numerically. There are several possible methods one can use, and we will examine their accuracy below.

### C.1 Finite differencing of $h(t; \theta)$

The simplest method, and that used in Ref. [16], is straightforward finite differencing of the signal  $h = F_+ h_+ + F_\times h_\times$ . For example, for five waveforms with values of an EOS parameter  $\theta$  given by  $\{\theta_{-2}, \theta_{-1}, \theta_0, \theta_1, \theta_2\}$  with equal spacing  $\Delta\theta$ , the three and five point central differences are given by

$$\begin{aligned} \frac{dh}{d\theta} &= \frac{\Delta_2 h}{\Delta\theta} + \mathcal{O}((\Delta\theta)^2), \text{ where} \\ \frac{\Delta_2 h}{\Delta\theta} &:= \frac{-\frac{1}{2}h(t; \theta_{-1}) + \frac{1}{2}h(t; \theta_1)}{\Delta\theta} \end{aligned} \quad (\text{C.1})$$

$$\begin{aligned} \frac{dh}{d\theta} &= \frac{\Delta_4 h}{\Delta\theta} + \mathcal{O}((\Delta\theta)^4), \text{ where} \\ \frac{\Delta_4 h}{d\theta} &:= \frac{\frac{1}{12}h(t; \theta_{-2}) - \frac{2}{3}h(t; \theta_{-1}) + \frac{2}{3}h(t; \theta_1) - \frac{1}{12}h(t; \theta_2)}{\Delta\theta}. \end{aligned} \quad (\text{C.2})$$

This finite differencing method is useful when waveforms differ only slightly: at each time  $t$ , on the scale  $\Delta\theta$  the function  $h(t; \theta)$  is well approximated by the low order interpolating polynomials used to generate the finite differencing formulas.

This assumption fails when the waveforms used in the finite differencing are significantly

out of phase with each other<sup>1</sup>. The tidal interaction leads to a monotonically accumulating phase difference relative to a BBH waveform, implying that at a fixed time  $t$  the function  $h(\theta; t)$  is an oscillating function of  $\theta$ . Now if an oscillating function  $h[\Phi(\theta)] = \cos[\Phi(\theta)]$  has wavenumber  $k = \Phi'(\theta)$  that varies slowly compared to  $\Phi$ , then  $h'(\theta)$  is better approximated by  $-\sin(\Phi)\Delta\Phi/\Delta\theta$  than by  $\Delta\cos[\Phi(\theta)]/\Delta\theta$ . The assumption that  $k$  is slowly varying is  $k' \ll k^2$ ,  $k'' \ll k^3$ , and the error in, for example, each of the two second-order discretizations is given to order  $\Delta\theta^2$  by

$$\begin{aligned} \frac{dh}{d\theta} - \frac{\Delta_2 h}{\Delta\theta} &= h(\theta) \left[ \frac{1}{6} k^3 + O(kk', k'') \right] \Delta\theta^2, \\ \frac{dh}{d\theta} + \sin[\Phi(\theta)] \frac{\Delta_2 \Phi}{\Delta\theta} &= h(\theta) \frac{1}{6} k'' \Delta\theta^2, \end{aligned} \quad (\text{C.3})$$

with the error in the second expression much smaller than that in the first. We consider two ways to take advantage of this difference in accuracy.

## C.2 Finite differencing of amplitude and phase

The first is to decompose each complex waveform into an amplitude  $A$  and accumulated phase  $\Phi$

$$h_+(t; \theta) - ih_\times(t; \theta) = A(t; \theta) e^{-i\Phi(t; \theta)}, \quad (\text{C.4})$$

where the accumulated phase of each waveform is a continuous function defined by  $\Phi = -\arg(h_+ - ih_\times) \pm 2n\pi$  for some integer  $n$ , and at the starting time  $t_i$  the accumulated phase of each waveform is chosen to be on the branch  $n = 0$ . The advantage of this method is that, at a fixed time, the functions  $A(t; \theta)$  and  $\Phi(t; \theta)$  are non-oscillatory functions of  $\theta$  even when the accumulated phase difference between two waveforms is significantly more than a radian.

With this decomposition the gravitational wave signal is

$$h(t; \theta) = A(t; \theta) (F_+ \cos \Phi(t; \theta) + F_\times \sin \Phi(t; \theta)), \quad (\text{C.5})$$

and the derivative of  $h$  is approximated by

$$\begin{aligned} \frac{dh}{d\theta} &= \frac{\Delta A}{\Delta\theta} (F_+ \cos \Phi + F_\times \sin \Phi) \\ &\quad + A(-F_+ \sin \Phi + F_\times \cos \Phi) \frac{\Delta\Phi}{\Delta\theta}. \end{aligned} \quad (\text{C.6})$$

---

<sup>1</sup>The dephasing of numerical waveforms is even more significant for BNS inspiral. We believe that Ref. [16] which used this method underestimated the derivatives in some cases by a factor of  $\sim 2$  or more, and thus overestimated the uncertainty in EOS parameters by the same factor.

If an intermediate waveform is not available to provide the functions  $A(t; \theta_0)$  and  $\Phi(t; \theta_0)$ , they can be evaluated by e.g.  $A(t; \theta_0) = (A(t; \theta_{-1}) + A(t; \theta_1))/2$ .

We have found that this method works reasonably well for the inspiral waveform. If, however, the amplitude of one of the numerical waveforms drops to zero, then the phase of the waveform becomes undefined. Because the amplitude of the numerical BHNS waveforms fall to zero at different times for different EOS, as shown in Fig. 27, the finite difference  $\Delta\Phi/\Delta\theta$  becomes meaningless towards the end when the average amplitude is still nonzero. It is likely one could work around this difficulty. However, we choose instead to use another more robust method.

### C.3 Finite differencing of Fourier transform

Because we will need to calculate the Fourier transform of the derivative  $\partial h/\partial\theta^A$  to find the Fisher matrix, we first Fourier transform each waveform and then evaluate the numerical derivative. Since the derivative  $\partial/\partial\theta^A$  commutes with the Fourier transform, the Fisher matrix can be written explicitly as

$$\left( \frac{\partial h}{\partial\theta^A} \middle| \frac{\partial h}{\partial\theta^B} \right) = 4\text{Re} \int_{f_i}^{f_f} \frac{\partial\tilde{h}}{\partial\theta^A} \frac{\partial\tilde{h}^*}{\partial\theta^B} \frac{df}{S_n(f)}, \quad (\text{C.7})$$

where the contribution to the integral below  $f_i$  and above  $f_f$  is negligible.

As in the second method we break up each Fourier transformed waveform into amplitude  $A(f; \theta)$  and accumulated phase  $\Phi(f; \theta)$

$$\tilde{h}(f; \theta) = A(f; \theta)e^{-i\Phi(f; \theta)}, \quad (\text{C.8})$$

where the phase of each waveform at  $f_i$  is on the  $n = 0$  branch cut. As demonstrated by Figs. 29 and 30, both the amplitude and phase are non-oscillatory functions of  $\theta$  at a fixed frequency  $f$ , and can be well approximated by a low-order polynomial. In contrast to the accumulated phase of the complex numerical waveform  $h_+ - ih_\times$ , the accumulated phase of the Fourier transform of the strain  $\tilde{h}$  is always well defined for numerical BHNS waveforms in the frequency range  $f_i$  to  $f_f$ .

Finally, we find that one obtains better accuracy by differentiating  $\ln A$  instead of  $A$ , decomposing  $\tilde{h}$  as

$$\tilde{h}(f; \theta) = e^{\ln A(f; \theta) - i\Phi(f; \theta)}. \quad (\text{C.9})$$

The derivative is now approximated by

$$\frac{d\tilde{h}}{d\theta} = e^{\ln A - i\Phi} \left( \frac{\Delta \ln A}{\Delta\theta} - i \frac{\Delta\Phi}{\Delta\theta} \right). \quad (\text{C.10})$$

interpolating when needed to evaluate  $\ln A$  and  $\Phi$  at the midpoint.

We find that methods 1–3 for calculating uncertainties in  $\Lambda^{1/5}$  and  $R$  agree with each other to  $\sim 10\%$  when the EOS parameters are closely separated by  $\Delta \log(p_1/(\text{dyne cm}^{-2})) = 0.1$ . However, for larger EOS spacing, when the accumulated phase difference between two waveforms is as large as 2 radians (see Fig. 28), method 1 will give a result as much as 50% larger than for the smaller spacing while method 2 may fail completely for the reasons discussed above. Method 3, however, gives the same result to within  $\sim 20\%$  when  $\Delta \log(p_1/(\text{dyne cm}^{-2}))$  is varied between 0.1 and 0.4. We also note that errors in the quadrature in Eq. C.7 from discrete sampling are negligible compared to the errors from the finite differencing.

#### C.4 Parameter spacing and numerical resolution

Finally, we note that the EOS parameter spacing must be carefully chosen. If two waveforms are too close in parameter space, the error in each waveform will dominate over the truncation error due to finite differencing. The most significant source of this error comes from the spurious oscillations in the amplitude of the Fourier transform in the frequency range  $\sim 500\text{--}800$  Hz (see Fig. 29) that result from joining the EOB and numerical waveforms which are not exactly the same in the matching window. We find that the integrand of the Fisher matrix is often erratic in the range  $\sim 500\text{--}800$  Hz when using the smallest parameter spacing available. However, when the spacing is increased, the integrand is smoother in this frequency range and its contribution to the integral is significantly reduced. For the mass ratio  $Q = 2$ , we find that a spacing between waveforms of  $\Delta \log(p_1/(\text{dyne cm}^{-2})) = 0.1$  for the first EOS parameter is often sufficiently large to reduce this problem, while a spacing of  $\Delta \Gamma = 0.6$  for the second EOS parameter is the minimum spacing one can use. For  $Q = 3$ , we have found that a spacing of  $\Delta \log(p_1/(\text{dyne cm}^{-2})) \geq 0.2$  is necessary to reduce this problem.

In addition, if the EOS parameters of two waveforms lie near the same degenerate contour where waveforms are identical (e.g. a contour of constant  $\Lambda$  which can be nearly identical to a line of constant  $\Gamma$ ), the error in each waveform will again dominate the truncation error even if the EOS parameters are widely spaced. For our two-dimensional EOS parameter space, this problem can be solved by transforming the parameter space such that points that originally formed a  $\times$  pattern now form a  $+$  pattern, and in the transformed parameter space the new axes are not aligned with a degenerate contour. The Fisher matrix can be calculated in the transformed parameter space then transformed back to the original parameter space.

We find that as long as these two requirements are met, the uncertainties in  $\sigma_{\Lambda^{1/5}}$  and  $\sigma_R$  have only an  $\sim 20\%$  fractional dependence on the EOS parameter spacing. However, the dependence of the orientation of the error ellipses on the EOS parameter spacing does not allow one to distinguish between  $\Lambda$  and  $R$  as the best extracted parameter.

The resolution in the simulation also has an effect on the Fisher matrix. For the two waveforms  $\{Q = 2, M_{\text{NS}} = 1.35M_{\odot}, p.4\Gamma3.0\}$  and  $\{Q = 3, M_{\text{NS}} = 1.35M_{\odot}, p.5\Gamma3.0\}$  we performed three different resolution runs with  $N = \{36, 42, 50\}$  as defined in Ref. [137], where the grid size is proportional to  $1/N$ . All other simulations used  $N = 50$ . We find that when using the  $N = 42$  resolution simulation instead of  $N = 50$ , the uncertainties  $\sigma_{\Lambda^{1/5}}$  and  $\sigma_R$  change by no more than  $\sim 25\%$ .

# Bibliography

- [1] S. L. Shapiro and S. A. Teukolsky. *Black holes, white dwarfs, and neutron stars*. John Wiley and Sons, New York, 1983.
- [2] F. Reif. *Fundamentals of statistical and thermal physics*, pages 314–315. McGraw-Hill, Boston, 1965.
- [3] J. L. Friedman and N. Stergioulas. *Rotating relativistic stars*. In Preparation, 2012.
- [4] L. Lindblom. Determining the nuclear equation of state from neutron-star masses and radii. *ApJ*, 398:569–573, October 1992.
- [5] P. Haensel and A. Y. Potekhin. Analytical representations of unified equations of state of neutron-star matter. *A&A*, 428:191–197, December 2004.
- [6] James B. Hartle. Slowly rotating relativistic stars. 1. Equations of structure. *Astrophys. J.*, 150:1005–1029, 1967.
- [7] L. Engvik, G. Bao, M. Hjorth-Jensen, E. Osnes, and E. Østgaard. Asymmetric nuclear matter and neutron star properties. *Astrophysical Journal*, 469:794, 1996.
- [8] J. M. Lattimer and M. Prakash. Neutron Star Structure and the Equation of State. *ApJ*, 550:426–442, March 2001.
- [9] J. M. Lattimer and M. Prakash. Equation of state, neutron stars and exotic phases. *Nuclear Physics A*, 777:479–496, October 2006.
- [10] T. Klähn, D. Blaschke, S. Typel, E. N. E. van Dalen, A. Faessler, C. Fuchs, T. Gaitanos, H. Grigorian, A. Ho, E. E. Kolomeitsev, M. C. Miller, G. Röpke, J. Trümper, D. N. Voskresensky, F. Weber, and H. H. Wolter. Constraints on the high-density nuclear equation of state from the phenomenology of compact stars and heavy-ion collisions. *Phys. Rev. C*, 74(3):035802, September 2006.

- [11] D. Page and S. Reddy. Dense Matter in Compact Stars: Theoretical Developments and Observational Constraints. *Annual Review of Nuclear and Particle Science*, 56:327–374, November 2006.
- [12] C. Vuille and J. Ipser. On the Maximum Mass of Neutron Stars. In C. P. Burgess and R. C. Myers, editors, *General Relativity and Relativistic Astrophysics*, volume 493, page 60, College Park MD, 1999. American Institute of Physics.
- [13] J. L. Zdunik, M. Bejger, P. Haensel, and E. Gourgoulhon. Phase transitions in rotating neutron stars cores: back bending, stability, corequakes, and pulsar timing. *A&A*, 450:747–758, May 2006.
- [14] M. Bejger, P. Haensel, and J. L. Zdunik. Mixed-phase induced core-quakes and the changes in neutron-star parameters. *MNRAS*, 359:699–706, May 2005.
- [15] Masaru Shibata, Keisuke Taniguchi, and Koji Uryu. Merger of binary neutron stars with realistic equations of state in full general relativity. *Physical Review D*, 71:084021, 2005.
- [16] J. S. Read, C. Markakis, M. Shibata, K. Uryū, J. D. E. Creighton, and J. L. Friedman. Measuring the neutron star equation of state with gravitational wave observations. *Phys. Rev. D*, 79(12):124033, June 2009.
- [17] B. D. Lackey, M. Nayyar, and B. J. Owen. Observational constraints on hyperons in neutron stars. *Phys. Rev. D*, 73(2):024021, January 2006.
- [18] J. M. Lattimer and B. F. Schutz. Constraining the Equation of State with Moment of Inertia Measurements. *ApJ*, 629:979–984, August 2005.
- [19] M. Bejger, T. Bulik, and P. Haensel. Constraints on the dense matter equation of state from the measurements of PSR J0737-3039A moment of inertia and PSR J0751+1807 mass. *MNRAS*, 364:635–639, December 2005.
- [20] M. Prakash, T. L. Ainsworth, and J. M. Lattimer. Equation of state and the maximum mass of neutron stars. *Phys. Rev. Lett.*, 61(22):2518–2521, Nov 1988.
- [21] F. Douchin and P. Haensel. A unified equation of state of dense matter and neutron star structure. *A&A*, 380:151–167, December 2001.
- [22] A. Akmal, V. R. Pandharipande, and D. G. Ravenhall. Equation of state of nucleon matter and neutron star structure. *Phys. Rev. C*, 58(3):1804–1828, Sep 1998.

- [23] B. Friedman and V. R. Pandharipande. Hot and cold, nuclear and neutron matter. *Nuclear Physics A*, 361:502–520, 1981.
- [24] R. B. Wiringa, V. Fiks, and A. Fabrocini. Equation of state for dense nucleon matter. *Phys. Rev. C*, 38(2):1010–1037, Aug 1988.
- [25] M. Baldo, I. Bombaci, and G. F. Burgio. Microscopic nuclear equation of state with three-body forces and neutron star structure. *A&A*, 328:274–282, December 1997.
- [26] W. Zuo, I. Bombaci, and U. Lombardo. Asymmetric nuclear matter from an extended brueckner-hartree-fock approach. *Phys. Rev. C*, 60(2):024605, Jul 1999.
- [27] H. Muther, M. Prakash, and T. L. Ainsworth. The nuclear symmetry energy in relativistic Brueckner-Hartree-Fock calculations. *Physics Letters B*, 199:469–474, 1987.
- [28] H. Müller and B. D. Serot. Relativistic mean-field theory and the high-density nuclear equation of state. *Nuclear Physics A*, 606:508–537, February 1996.
- [29] V. R. Pandharipande and R. A. Smith. A model neutron solid with  $\pi^0$  condensate. *Nuclear Physics A*, 237:507–532, January 1975.
- [30] Norman K. Glendenning and Jürgen Schaffner-Bielich. First order kaon condensate. *Phys. Rev. C*, 60(2):025803, Jul 1999.
- [31] S. Balberg and A. Gal. An effective equation of state for dense matter with strangeness. *Nuclear Physics A*, 625:435–472, February 1997.
- [32] N. K. Glendenning. Neutron stars are giant hypernuclei? *ApJ*, 293:470–493, June 1985.
- [33] M. Prakash, J. R. Cooke, and J. M. Lattimer. Quark-hadron phase transition in protonneutron stars. *Phys. Rev. D*, 52:661–665, July 1995.
- [34] M. Alford, M. Braby, M. Paris, and S. Reddy. Hybrid Stars that Masquerade as Neutron Stars. *ApJ*, 629:969–978, August 2005.
- [35] J. W. Negele and D. Vautherin. Neutron star matter at sub-nuclear densities. *Nuclear Physics A*, 207:298–320, June 1973.
- [36] Norman K. Glendenning and Christiane Kettner. Non-Identical Neutron Star Twins. *Astron. Astrophys.*, 353:L9, 2000.

- [37] J. M. Lattimer and M. Prakash. Neutron star observations: Prognosis for equation of state constraints. *Phys. Rep.*, 442:109–165, April 2007.
- [38] Scott M. Ransom et al. Twenty-One Millisecond Pulsars in Terzan 5 Using the Green Bank Telescope. *Science*, 307:892–896, 2005.
- [39] P. C. C. Freire, A. Wolszczan, M. van den Berg, and J. W. T. Hessels. A Massive Neutron Star in the Globular Cluster M5. *ApJ*, 679:1433–1442, June 2008.
- [40] D. J. Champion, S. M. Ransom, P. Lazarus, F. Camilo, C. Bassa, V. M. Kaspi, D. J. Nice, P. C. C. Freire, I. H. Stairs, J. van Leeuwen, B. W. Stappers, J. M. Cordes, J. W. T. Hessels, D. R. Lorimer, Z. Arzoumanian, D. C. Backer, N. D. R. Bhat, S. Chatterjee, I. Cognard, J. S. Deneva, C.-A. Faucher-Giguère, B. M. Gaensler, J. Han, F. A. Jenet, L. Kasian, V. I. Kondratiev, M. Kramer, J. Lazio, M. A. McLaughlin, A. Venkataraman, and W. Vlemmings. An Eccentric Binary Millisecond Pulsar in the Galactic Plane. *Science*, 320:1309–, June 2008.
- [41] J. P. W. Verbiest, M. Bailes, W. van Straten, G. B. Hobbs, R. T. Edwards, R. N. Manchester, N. D. R. Bhat, J. M. Sarkissian, B. A. Jacoby, and S. R. Kulkarni. Precision Timing of PSR J0437-4715: An Accurate Pulsar Distance, a High Pulsar Mass, and a Limit on the Variation of Newton’s Gravitational Constant. *ApJ*, 679:675–680, May 2008.
- [42] P. C. C. Freire, S. M. Ransom, S. Bégin, I. H. Stairs, J. W. T. Hessels, L. H. Frey, and F. Camilo. Eight New Millisecond Pulsars in NGC 6440 and NGC 6441. *ApJ*, 675:670–682, March 2008.
- [43] P. B. Demorest, T. Pennucci, S. M. Ransom, M. S. E. Roberts, and J. W. T. Hessels. A two-solar-mass neutron star measured using Shapiro delay. *Nature*, 467:1081–1083, October 2010.
- [44] P. Haensel, J.L. Zdunik, and F. Douchin. Equation of state of dense matter and the minimum mass of cold neutron stars. *Astronomy and Astrophysics*, 385:301–307, 2002.
- [45] J. Cottam, F. Paerels, and M. Mendez. Gravitationally redshifted absorption lines in the X-ray burst spectra of a neutron star. *Nature*, 420:51–54, 2002.
- [46] J. Cottam et al. The Burst Spectra of EXO 0748-676 during a Long 2003 XMM-Newton Observation. *Astrophys. J.*, 672:504–509, 2008.

- [47] J. Lin, F. Özel, D. Chakrabarty, and D. Psaltis. The Incompatibility of Rapid Rotation with Narrow Photospheric X-ray Lines in EXO 0748-676. *ApJ*, 723:1053–1056, November 2010.
- [48] F. Özel. Soft equations of state for neutron-star matter ruled out by EXO 0748 - 676. *Nature*, 441:1115–1117, June 2006.
- [49] Jason W. T. Hessels et al. A Radio Pulsar Spinning at 716 Hz. *Science*, 311:1901–1904, 2006.
- [50] Philip Kaaret et al. Evidence of 1122 Hz X-Ray Burst Oscillations from the Neutron Star X-Ray Transient XTE J1739-285. *Astrophys. J.*, 657:L97–100, 2007.
- [51] S. Koranda, N. Stergioulas, and J. L. Friedman. Upper Limits Set by Causality on the Rotation and Mass of Uniformly Rotating Relativistic Stars. *ApJ*, 488:799, October 1997.
- [52] N. K. Glendenning. Limiting rotational period of neutron stars. *Phys. Rev. D*, 46:4161–4168, November 1992.
- [53] N. Stergioulas. <http://www.gravity.phys.uwm.edu/rns>. UWM Centre for Gravitation and Cosmology, 2000.
- [54] J. S. Read, B. D. Lackey, B. J. Owen, and J. L. Friedman. Constraints on a phenomenologically parametrized neutron-star equation of state. *Phys. Rev. D*, 79(12):124032, June 2009.
- [55] P. Haensel and J. L. Zdunik. A submillisecond pulsar and the equation of state of dense matter. *Nature*, 340:617–619, August 1989.
- [56] P. Haensel, M. Salgado, and S. Bonazzola. Equation of state of dense matter and maximum rotation frequency of neutron stars. *A&A*, 296:745, April 1995.
- [57] J. L. Friedman, L. Parker, and J. R. Ipser. Rapidly rotating neutron star models. *ApJ*, 304:115–139, May 1986.
- [58] J. M. Lattimer, M. Prakash, D. Masak, and A. Yahil. Rapidly rotating pulsars and the equation of state. *ApJ*, 355:241–254, May 1990.
- [59] G. B. Cook, S. L. Shapiro, and S. A. Teukolsky. Rapidly rotating neutron stars in general relativity: Realistic equations of state. *ApJ*, 424:823–845, April 1994.

- [60] I. A. Morrison, T. W. Baumgarte, S. L. Shapiro, and V. R. Pandharipande. The Moment of Inertia of the Binary Pulsar J0737-3039A: Constraining the Nuclear Equation of State. *ApJ*, 617:L135–L138, December 2004.
- [61] F. Özel, T. Güver, and D. Psaltis. The Mass and Radius of the Neutron Star in EXO 1745-248. *ApJ*, 693:1775–1779, March 2009.
- [62] T. Güver, F. Özel, A. Cabrera-Lavers, and P. Wroblewski. The Distance, Mass, and Radius of the Neutron Star in 4U 1608-52. *ApJ*, 712:964–973, April 2010.
- [63] Luc Blanchet. Gravitational radiation from post-newtonian sources and inspiralling compact binaries. *Living Reviews in Relativity*, 9(4), 2006.
- [64] M. Maggiore. *Gravitational Waves Volume 1: Theory and Experiments*. Oxford University Press, Oxford, UK, 2008.
- [65] S. Chandrasekhar. *The Mathematical Theory of Black Holes*, pages 40–43. Oxford University Press, Oxford, UK, 1983.
- [66] W. B. Campbell. Tensor and Spinor Spherical Harmonics and the Spin-s Harmonics  ${}_sY_{lm}(\theta, \phi)$ . *Journal of Mathematical Physics*, 12:1763–1770, August 1971.
- [67] J. D. E. Creighton and W. G. Anderson. *Gravitational-Wave Physics and Astronomy*. Wiley-VCH, Weinheim, Germany, 2011.
- [68] L. Blanchet, G. Faye, B. R. Iyer, and S. Sinha. The third post-Newtonian gravitational wave polarizations and associated spherical harmonic modes for inspiralling compact binaries in quasi-circular orbits. *Classical and Quantum Gravity*, 25(16):165003, August 2008.
- [69] L. E. Kidder. Using full information when computing modes of post-Newtonian waveforms from inspiralling compact binaries in circular orbit. *Phys. Rev. D*, 77(4):044016, February 2008.
- [70] M. Boyle, D. A. Brown, L. E. Kidder, A. H. Mroué, H. P. Pfeiffer, M. A. Scheel, G. B. Cook, and S. A. Teukolsky. High-accuracy comparison of numerical relativity simulations with post-Newtonian expansions. *Phys. Rev. D*, 76(12):124038, December 2007.
- [71] A. Buonanno, B. R. Iyer, E. Ochsner, Y. Pan, and B. S. Sathyaprakash. Comparison of post-Newtonian templates for compact binary inspiral signals in gravitational-wave detectors. *Phys. Rev. D*, 80(8):084043, October 2009.

- [72] L. Santamaría, F. Ohme, P. Ajith, B. Brügmann, N. Dorband, M. Hannam, S. Husa, P. Mösta, D. Pollney, C. Reisswig, E. L. Robinson, J. Seiler, and B. Krishnan. Matching post-Newtonian and numerical relativity waveforms: Systematic errors and a new phenomenological model for nonprecessing black hole binaries. *Phys. Rev. D*, 82(6):064016, September 2010.
- [73] P. Ajith, S. Babak, Y. Chen, M. Hewitson, B. Krishnan, A. M. Sintes, J. T. Whelan, B. Brügmann, P. Diener, N. Dorband, J. Gonzalez, M. Hannam, S. Husa, D. Pollney, L. Rezzolla, L. Santamaría, U. Sperhake, and J. Thornburg. Template bank for gravitational waveforms from coalescing binary black holes: Nonspinning binaries. *Phys. Rev. D*, 77(10):104017, May 2008.
- [74] P. Ajith, M. Hannam, S. Husa, Y. Chen, B. Brügmann, N. Dorband, D. Müller, F. Ohme, D. Pollney, C. Reisswig, L. Santamaría, and J. Seiler. Inspiral-Merger-Ringdown Waveforms for Black-Hole Binaries with Nonprecessing Spins. *Physical Review Letters*, 106(24):241101, June 2011.
- [75] A. Buonanno and T. Damour. Effective one-body approach to general relativistic two-body dynamics. *Phys. Rev. D*, 59(8):084006, April 1999.
- [76] T. Damour and A. Nagar. Improved analytical description of inspiralling and coalescing black-hole binaries. *Phys. Rev. D*, 79(8):081503, April 2009.
- [77] T. Damour and A. Nagar. The Effective One Body description of the Two-Body problem. *ArXiv e-prints*, June 2009.
- [78] T. Damour, B. R. Iyer, and A. Nagar. Improved resummation of post-Newtonian multipolar waveforms from circularized compact binaries. *Phys. Rev. D*, 79(6):064004, March 2009.
- [79] E. Berti, V. Cardoso, and C. M. Will. Gravitational-wave spectroscopy of massive black holes with the space interferometer LISA. *Phys. Rev. D*, 73(6):064030, March 2006.
- [80] T. Damour and A. Nagar. Faithful effective-one-body waveforms of small-mass-ratio coalescing black hole binaries. *Phys. Rev. D*, 76(6):064028, September 2007.
- [81] T. Damour and A. Gopakumar. Gravitational recoil during binary black hole coalescence using the effective one body approach. *Phys. Rev. D*, 73(12):124006, June 2006.

- [82] A. Nagar. Private communication, 2010.
- [83] T. Damour, A. Nagar, E. N. Dorband, D. Pollney, and L. Rezzolla. Faithful effective-one-body waveforms of equal-mass coalescing black-hole binaries. *Phys. Rev. D*, 77(8):084017, April 2008.
- [84] A. Buonanno and T. Damour. Transition from inspiral to plunge in binary black hole coalescences. *Phys. Rev. D*, 62(6):064015, September 2000.
- [85] J. Vines and É. É. Flanagan. Post-1-Newtonian quadrupole tidal interactions in binary systems. *ArXiv e-prints*, September 2010.
- [86] É. É. Flanagan and T. Hinderer. Constraining neutron-star tidal Love numbers with gravitational-wave detectors. *Phys. Rev. D*, 77(2):021502, January 2008.
- [87] T. Hinderer. Tidal Love Numbers of Neutron Stars. *ApJ*, 677:1216–1220, April 2008.
- [88] É. Racine and É. É. Flanagan. Post-1-Newtonian equations of motion for systems of arbitrarily structured bodies. *Phys. Rev. D*, 71(4):044010, February 2005.
- [89] R. N. Lang. *Observable signatures of general relativistic dynamics in compact binaries*. PhD thesis, Massachusetts Institute of Technology, 2009.
- [90] K. S. Thorne and A. Campolattaro. Non-Radial Pulsation of General-Relativistic Stellar Models. I. Analytic Analysis for  $L \geq 2$ . *ApJ*, 149:591, September 1967.
- [91] T. Regge and J. A. Wheeler. Stability of a Schwarzschild Singularity. *Physical Review*, 108:1063–1069, November 1957.
- [92] J. B. Hartle and K. S. Thorne. Slowly Rotating Relativistic Stars. III. Static Criterion for Stability. *ApJ*, 158:719, November 1969.
- [93] T. Damour and A. Nagar. Relativistic tidal properties of neutron stars. *Phys. Rev. D*, 80(8):084035, October 2009.
- [94] J. Veitch and A. Vecchio. Bayesian coherent analysis of in-spiral gravitational wave signals with a detector network. *Phys. Rev. D*, 81(6):062003, March 2010.
- [95] F. Feroz, J. R. Gair, M. P. Hobson, and E. K. Porter. Use of the MULTINEST algorithm for gravitational wave data analysis. *Classical and Quantum Gravity*, 26(21):215003, November 2009.

- [96] T. B. Littenberg and N. J. Cornish. Bayesian approach to the detection problem in gravitational wave astronomy. *Phys. Rev. D*, 80(6):063007, September 2009.
- [97] W. G. Anderson, P. R. Brady, J. D. Creighton, and É. É. Flanagan. Excess power statistic for detection of burst sources of gravitational radiation. *Phys. Rev. D*, 63(4):042003, February 2001.
- [98] L. S. Finn and D. F. Chernoff. Observing binary inspiral in gravitational radiation: One interferometer. *Phys. Rev. D*, 47:2198–2219, March 1993.
- [99] W. H. Press, S. A. Teukolsky, W. T. Vetterling, and B. P. Flannery. *Numerical recipes: the art of scientific computing*. Cambridge University Press, Cambridge, UK, 2007.
- [100] M. van der Sluys, V. Raymond, I. Mandel, C. Röver, N. Christensen, V. Kalogera, R. Meyer, and A. Vecchio. Parameter estimation of spinning binary inspirals using Markov chain Monte Carlo. *Classical and Quantum Gravity*, 25(18):184011, September 2008.
- [101] D. A. Leahy, S. M. Morsink, and C. Cadeau. Limits on Mass and Radius for the Millisecond-Period X-Ray Pulsar SAX J1808.4-3658. *ApJ*, 672:1119–1126, January 2008.
- [102] D. A. Leahy, S. M. Morsink, Y.-Y. Chung, and Y. Chou. Constraints on the Properties of the Neutron Star XTE J1814-338 from Pulse-Shape Models. *ApJ*, 691:1235–1242, February 2009.
- [103] C. S. Kochanek. Coalescing binary neutron stars. *ApJ*, 398:234–247, October 1992.
- [104] L. Bildsten and C. Cutler. Tidal interactions of inspiraling compact binaries. *ApJ*, 400:175–180, November 1992.
- [105] D. Lai and A. G. Wiseman. Innermost stable circular orbit of inspiraling neutron-star binaries: Tidal effects, post-Newtonian effects, and the neutron-star equation of state. *Phys. Rev. D*, 54:3958–3964, September 1996.
- [106] D. Lai, F. A. Rasio, and S. L. Shapiro. Hydrodynamic instability and coalescence of binary neutron stars. *ApJ*, 420:811–829, January 1994.
- [107] R. A. Brooker and T. W. Olle. Apsidal-motion constants for polytropic models. *MNRAS*, 115:101, 1955.

- [108] T. Mora and C. M. Will. Post-Newtonian diagnostic of quasiequilibrium binary configurations of compact objects. *Phys. Rev. D*, 69(10):104021, May 2004.
- [109] E. Berti, S. Iyer, and C. M. Will. Post-Newtonian diagnosis of quasiequilibrium configurations of neutron star neutron star and neutron star black hole binaries. *Phys. Rev. D*, 77(2):024019, January 2008.
- [110] T. Binnington and E. Poisson. Relativistic theory of tidal Love numbers. *Phys. Rev. D*, 80(8):084018, October 2009.
- [111] J. Vines, T. Hinderer, and É. É. Flanagan. Post-1-Newtonian tidal effects in the gravitational waveform from binary inspirals. *ArXiv e-prints*, January 2011.
- [112] S. Ransom, P. Demorest, V. Kaspi, R. Ramachandran, and D. Backer. GBT Exploratory Time Observations of the Double-Pulsar System PSR J0737-3039. In F. A. Rasio & I. H. Stairs, editor, *Binary Radio Pulsars*, volume 328 of *Astronomical Society of the Pacific Conference Series*, page 73, July 2005.
- [113] T. Bulik, D. Gonddek-Rosinska, and K. Belczynski. Expected masses of merging compact object binaries observed in gravitational waves. *MNRAS*, 352:1372–1380, August 2004.
- [114] D. Shoemaker. *Advanced LIGO anticipated sensitivity curves*. LSC, 2009.
- [115] S. Hild, S. Chelkowski, and A. Freise. Pushing towards the ET sensitivity using ‘conventional’ technology. *ArXiv e-prints*, October 2008.
- [116] Eric Poisson and Clifford M. Will. Gravitational waves from inspiraling compact binaries: Parameter estimation using second-post-newtonian waveforms. *Phys. Rev. D*, 52(2):848–855, Jul 1995.
- [117] I. H. Stairs. Pulsars in Binary Systems: Probing Binary Stellar Evolution and General Relativity. *Science*, 304:547–552, April 2004.
- [118] R. O’Shaughnessy, V. Kalogera, and K. Belczynski. Binary compact object coalescence rates: The role of elliptical galaxies. *ArXiv e-prints*, August 2009.
- [119] C. Cutler and É. É. Flanagan. Gravitational waves from merging compact binaries: How accurately can one extract the binary’s parameters from the inspiral waveform? *Phys. Rev. D*, 49:2658–2697, March 1994.

- [120] J. Abadie, B. P. Abbott, R. Abbott, M. Abernathy, T. Accadia, F. Acernese, C. Adams, R. Adhikari, P. Ajith, B. Allen, and et al. TOPICAL REVIEW: Predictions for the rates of compact binary coalescences observable by ground-based gravitational-wave detectors. *Classical and Quantum Gravity*, 27(17):173001, September 2010.
- [121] K. Belczynski, M. Dominik, T. Bulik, R. O’Shaughnessy, C. Fryer, and D. E. Holz. The Effect of Metallicity on the Detection Prospects for Gravitational Waves. *ApJ*, 715:L138–L141, June 2010.
- [122] K. Belczynski, V. Kalogera, and T. Bulik. A Comprehensive Study of Binary Compact Objects as Gravitational Wave Sources: Evolutionary Channels, Rates, and Physical Properties. *ApJ*, 572:407–431, June 2002.
- [123] T. Hinderer, B. D. Lackey, R. N. Lang, and J. S. Read. Tidal deformability of neutron stars with realistic equations of state and their gravitational wave signatures in binary inspiral. *Phys. Rev. D*, 81(12):123016, June 2010.
- [124] F. Pannarale, L. Rezzolla, F. Ohme, and J. S. Read. Will black hole-neutron star binary inspirals tell us about the neutron star equation of state? *Phys. Rev. D*, 84(10):104017, November 2011.
- [125] J. S. Read, L. Baiotti, J. D. E. Creighton, J. L. Friedman, B. Giacomazzo, K. Kyutoku, C. Markakis, L. Rezzolla, M. Shibata, and K. Taniguchi. Matter effects on double neutron star binary waveforms. *in progress*, 2012.
- [126] T. Damour and A. Nagar. Effective one body description of tidal effects in inspiralling compact binaries. *Phys. Rev. D*, 81(8):084016, April 2010.
- [127] Luca Baiotti, Thibault Damour, Bruno Giacomazzo, Alessandro Nagar, and Luciano Rezzolla. Analytic modeling of tidal effects in the relativistic inspiral of binary neutron stars. *Phys. Rev. Lett.*, 105(26):261101, Dec 2010.
- [128] L. Baiotti, T. Damour, B. Giacomazzo, A. Nagar, and L. Rezzolla. Accurate numerical simulations of inspiralling binary neutron stars and their comparison with effective-one-body analytical models. *Phys. Rev. D*, 84(2):024017, July 2011.
- [129] Masaru Shibata and Koji Uryū. Merger of black hole-neutron star binaries: Nonspinning black hole case. *Phys. Rev. D*, 74(12):121503, Dec 2006.

- [130] Z. B. Etienne, J. A. Faber, Y. T. Liu, S. L. Shapiro, K. Taniguchi, and T. W. Baumgarte. Fully general relativistic simulations of black hole-neutron star mergers. *Phys. Rev. D*, 77(8):084002, April 2008.
- [131] M. Shibata and K. Uryu. Merger of black hole neutron star binaries in full general relativity. *Classical and Quantum Gravity*, 24:125, June 2007.
- [132] Masaru Shibata and Keisuke Taniguchi. Merger of black hole and neutron star in general relativity: Tidal disruption, torus mass, and gravitational waves. *Phys. Rev. D*, 77(8):084015, Apr 2008.
- [133] M. D. Duez, F. Foucart, L. E. Kidder, H. P. Pfeiffer, M. A. Scheel, and S. A. Teukolsky. Evolving black hole-neutron star binaries in general relativity using pseudospectral and finite difference methods. *Phys. Rev. D*, 78(10):104015, November 2008.
- [134] Z. B. Etienne, Y. T. Liu, S. L. Shapiro, and T. W. Baumgarte. General relativistic simulations of black-hole-neutron-star mergers: Effects of black-hole spin. *Phys. Rev. D*, 79(4):044024, February 2009.
- [135] M. Shibata, K. Kyutoku, T. Yamamoto, and K. Taniguchi. Gravitational waves from black hole-neutron star binaries: Classification of waveforms. *Phys. Rev. D*, 79(4):044030, February 2009.
- [136] M. Shibata and K. Kyutoku. Constraining Nuclear-Matter Equations of State by Gravitational Waves from Black Hole-Neutron Star Binaries. *Progress of Theoretical Physics Supplement*, 186:17–25, 2010.
- [137] K. Kyutoku, M. Shibata, and K. Taniguchi. Gravitational waves from nonspinning black hole-neutron star binaries: Dependence on equations of state. *Phys. Rev. D*, 82(4):044049, August 2010.
- [138] M. D. Duez, F. Foucart, L. E. Kidder, C. D. Ott, and S. A. Teukolsky. Equation of state effects in black hole-neutron star mergers. *Classical and Quantum Gravity*, 27(11):114106, June 2010.
- [139] F. Foucart, M. D. Duez, L. E. Kidder, and S. A. Teukolsky. Black hole-neutron star mergers: Effects of the orientation of the black hole spin. *Phys. Rev. D*, 83(2):024005, January 2011.

- [140] K. Kyutoku, H. Okawa, M. Shibata, and K. Taniguchi. Gravitational waves from spinning black hole-neutron star binaries: dependence on black hole spins and on neutron star equations of state. *ArXiv e-prints*, August 2011.
- [141] M. Vallisneri. Prospects for Gravitational-Wave Observations of Neutron-Star Tidal Disruption in Neutron-Star-Black-Hole Binaries. *Physical Review Letters*, 84:3519–3522, April 2000.
- [142] Koutarou Kyutoku, Masaru Shibata, and Keisuke Taniguchi. Quasiequilibrium states of black hole-neutron star binaries in the moving-puncture framework. *Phys. Rev. D*, 79(12):124018, Jun 2009.
- [143] LORENE website.
- [144] Tetsuro Yamamoto, Masaru Shibata, and Keisuke Taniguchi. Simulating coalescing compact binaries by a new code (*sacra*). *Phys. Rev. D*, 78(6):064054, Sep 2008.
- [145] M. Shibata. Axisymmetric general relativistic hydrodynamics: Long-term evolution of neutron stars and stellar collapse to neutron stars and black holes. *Phys. Rev. D*, 67(2):024033, January 2003.
- [146] C. Reisswig and D. Pollney. Notes on the integration of numerical relativity waveforms. *Classical and Quantum Gravity*, 28(19):195015, October 2011.
- [147] T. Nakamura, K. Oohara, and Y. Kojima. General Relativistic Collapse to Black Holes and Gravitational Waves from Black Holes. *Progress of Theoretical Physics Supplement*, 90:1–218, 1987.
- [148] D. Lai, F. A. Rasio, and S. L. Shapiro. Hydrodynamic instability and coalescence of close binary systems. *ApJ*, 406:L63–L66, April 1993.
- [149] R. Sturani, S. Fischetti, L. Cadonati, G. M. Guidi, J. Healy, D. Shoemaker, and A. Viceré. Complete phenomenological gravitational waveforms from spinning coalescing binaries. *Journal of Physics Conference Series*, 243(1):012007, August 2010.
- [150] R. Sturani, S. Fischetti, L. Cadonati, G. M. Guidi, J. Healy, D. Shoemaker, and A. Viceré. Phenomenological gravitational waveforms from spinning coalescing binaries. *ArXiv e-prints*, December 2010.
- [151] H. P. Pfeiffer, D. A. Brown, L. E. Kidder, L. Lindblom, G. Lovelace, and M. A. Scheel. Reducing orbital eccentricity in binary black hole simulations. *Classical and Quantum Gravity*, 24:59, June 2007.

- [152] L A Wainstein and V D Zubakov. *Extraction of signals from noise*. Prentice-Hall, Englewood Cliffs, NJ, 1962.
- [153] S. Hild, M. Abernathy, F. Acernese, P. Amaro-Seoane, N. Andersson, K. Arun, F. Barone, B. Barr, M. Barsuglia, M. Beker, N. Beveridge, S. Birindelli, S. Bose, L. Bosi, S. Braccini, C. Bradaschia, T. Bulik, E. Calloni, G. Cella, E. Chassande Motin, S. Chelkowski, A. Chincarini, J. Clark, E. Coccia, C. Colacino, J. Colas, A. Cumming, L. Cunningham, E. Cuoco, S. Danilishin, K. Danzmann, R. De Salvo, T. Dent, R. De Rosa, L. Di Fiore, A. Di Virgilio, M. Doets, V. Fafone, P. Falferi, R. Flaminio, J. Franc, F. Frasconi, A. Freise, D. Friedrich, P. Fulda, J. Gair, G. Gemme, E. Genin, A. Gennai, A. Giazotto, K. Glampedakis, C. Gräf, M. Granata, H. Grote, G. Guidi, A. Gurkovsky, G. Hammond, M. Hannam, J. Harms, D. Heinert, M. Hendry, I. Heng, E. Hennes, J. Hough, S. Husa, S. Huttner, G. Jones, F. Khalili, K. Kokeyama, K. Kokkotas, B. Krishnan, T. G. F. Li, M. Lorenzini, H. Lück, E. Majorana, I. Mandel, V. Mandic, M. Mantovani, I. Martin, C. Michel, Y. Minenkov, N. Morgado, S. Mosca, B. Mours, H. Müller-Ebhardt, P. Murray, R. Nawrodt, J. Nelson, R. Oshaughnessy, C. D. Ott, C. Palomba, A. Paoli, G. Parguez, A. Pasqualetti, R. Passaquieti, D. Passuello, L. Pinard, W. Plastino, R. Poggiani, P. Popolizio, M. Prato, M. Punturo, P. Puppò, D. Rabeling, P. Rapagnani, J. Read, T. Regimbau, H. Rehbein, S. Reid, F. Ricci, F. Richard, A. Rocchi, S. Rowan, A. Rüdiger, L. Santamaría, B. Sassolas, B. Sathyaprakash, R. Schnabel, C. Schwarz, P. Seidel, A. Sintes, K. Somiya, F. Speirits, K. Strain, S. Strigin, P. Sutton, S. Tarabrin, A. Thüring, J. van den Brand, M. van Veggel, C. van den Broeck, A. Vecchio, J. Veitch, F. Vetrano, A. Vicere, S. Vyatchanin, B. Willke, G. Woan, and K. Yamamoto. Sensitivity studies for third-generation gravitational wave observatories. *Classical and Quantum Gravity*, 28(9):094013, May 2011.
- [154] S. Hild, S. Chelkowski, A. Freise, J. Franc, N. Morgado, R. Flaminio, and R. DeSalvo. A xylophone configuration for a third-generation gravitational wave detector. *Classical and Quantum Gravity*, 27(1):015003, January 2010.
- [155] B.J. Meers. RECYCLING IN LASER INTERFEROMETRIC GRAVITATIONAL WAVE DETECTORS. *Phys.Rev.*, D38:2317–2326, 1988.
- [156] Alessandra Buonanno and Yan-bei Chen. Quantum noise in second generation, signal recycled laser interferometric gravitational wave detectors. *Phys.Rev.*, D64:042006, 2001.
- [157] L. S. Finn. Gravitational wave interferometer noise calculator, 2011.

- [158] S. A. Hughes. Tuning gravitational-wave detector networks to measure compact binary mergers. *Phys. Rev. D*, 66(10):102001, November 2002.
- [159] L. Lindblom. Spectral representations of neutron-star equations of state. *Phys. Rev. D*, 82(10):103011, November 2010.
- [160] Feryal Özel and Dimitrios Psaltis. Reconstructing the neutron-star equation of state from astrophysical measurements. *Phys. Rev. D*, 80(10):103003, Nov 2009.
- [161] A. W. Steiner, J. M. Lattimer, and E. F. Brown. The Equation of State from Observed Masses and Radii of Neutron Stars. *ApJ*, 722:33–54, October 2010.
- [162] F. Özel, G. Baym, and T. Güver. Astrophysical measurement of the equation of state of neutron star matter. *Phys. Rev. D*, 82(10):101301, November 2010.
- [163] Y. Pan, A. Buonanno, M. Boyle, L. T. Buchman, L. E. Kidder, H. P. Pfeiffer, and M. A. Scheel. Inspiral-merger-ringdown multipolar waveforms of nonspinning black-hole binaries using the effective-one-body formalism. *Phys. Rev. D*, 84(12):124052, December 2011.
- [164] Y. Pan, A. Buonanno, L. T. Buchman, T. Chu, L. E. Kidder, H. P. Pfeiffer, and M. A. Scheel. Effective-one-body waveforms calibrated to numerical relativity simulations: Coalescence of nonprecessing, spinning, equal-mass black holes. *Phys. Rev. D*, 81(8):084041, April 2010.
- [165] Y. Pan, A. Buonanno, R. Fujita, E. Racine, and H. Tagoshi. Post-Newtonian factorized multipolar waveforms for spinning, nonprecessing black-hole binaries. *Phys. Rev. D*, 83(6):064003, March 2011.
- [166] D. Bini, T. Damour, and G. Faye. Effective action approach to higher-order relativistic tidal interactions in binary systems and their effective one body description. *ArXiv e-prints*, February 2012.
- [167] T. Damour, A. Nagar, and L. Villain. Measurability of the tidal polarizability of neutron stars in late-inspiral gravitational-wave signals. *ArXiv e-prints*, March 2012.
- [168] S. Bernuzzi, A. Nagar, M. Thierfelder, and B. Bruegmann. Tidal effects in binary neutron star coalescence. *ArXiv e-prints*, May 2012.
- [169] B. D. Lackey, K. Kyutoku, M. Shibata, P. R. Brady, and J. L. Friedman. Extracting equation of state parameters from black hole-neutron star mergers: Nonspinning black holes. *Phys. Rev. D*, 85(4):044061, February 2012.

- [170] K. Kokkotas and B. Schmidt. Quasi-Normal Modes of Stars and Black Holes. *Living Reviews in Relativity*, 2:2, September 1999.
- [171] D. Lai, F. A. Rasio, and S. L. Shapiro. Ellipsoidal figures of equilibrium - Compressible models. *ApJS*, 88:205–252, September 1993.
- [172] C. Cutler and L. Lindblom. The effect of viscosity on neutron star oscillations. *ApJ*, 314:234–241, March 1987.

## Curriculum Vitae

### Benjamin D. Lackey

Place of Birth: Poughkeepsie, New York

#### Education

B.S., Pennsylvania State University 2006

Major: Physics with honors

Ph.D., University of Wisconsin–Milwaukee 2012

Major: Physics

Dissertation Title: The Neutron-Star Equation of State and Gravitational Waves from Compact Binaries

#### Refereed Publications:

“Extracting equation of state parameters from black hole-neutron star mergers: Nonspinning black holes.” Benjamin D. Lackey, Koutarou Kyutoku, Masaru Shibata, Patrick R. Brady, John L. Friedman. *Phys. Rev. D* 85, 044061 (2012).

“Tidal deformability of neutron stars with realistic equations of state and their gravitational wave signatures in binary inspiral.” Tanja Hinderer, Benjamin D. Lackey, Ryan N. Lang, Jocelyn S. Read. *Phys. Rev. D* 81, 123016 (2010).

“Constraints on a phenomenologically parameterized neutron-star equation of state.” Jocelyn S. Read, Benjamin D. Lackey, Benjamin J. Owen, John L. Friedman. *Phys. Rev. D* 79, 124032 (2009).

“Observational constraints on hyperons in neutron stars.” Benjamin D. Lackey, Mohit Nayyar, Benjamin J. Owen. *Phys. Rev. D* 73, 024021 (2006).

#### Awards and Fellowships:

UWM Papastamatiou Award in Theoretical Physics 2012

UWM Graduate School Dissertation Fellowship 2011–2012

APS Blue Apple Award, Midwest Relativity Meeting 2010

UWM Graduate School Fellowship 2010–2011

Wisconsin Space Grant Consortium Graduate Fellowship	2009–2011
Penn State Brickwedde Research Award in Physics	2005, 2006
Penn State Teas Scholarship	2004–2006
Penn State President's Freshman Award for 4.0 GPA	2003